Alma Mater Studiorum – Università di Bologna

DOTTORATO DI RICERCA
in
SCIENZE CHIMICHE

XXIV Ciclo
03/B1
CHIM/03

Dye Doped, Core/Shell Silica Nanoparticles: Synthesis, Characterization, & Biotechnological Applications

Presentata da:
Riccardo Juris

Relatore
Prof. Luca Prodi

Coordinatore Dottorato
Prof. Adriana Bigi

Esame finale anno 2012

Contents

Part I – Synthesis & Characterization

A mia madre e mio padre,

per le piccole cose:
quelle importanti.

Part I

Synthesis & Characterization

Chapter 1
Introduction

1.1 Nanotechnology

Nanotechnology refers to a field of applied science and technology whose aim is the control over matter on the molecular level, usually between 1 and 100 nm. A whole new kind of materials can be fabricated, characterized by original and peculiar properties, which cannot be found in the bulk, as already predicted decades ago.[1-3] These new features rise from (and strongly depend on) their small size: the behavior of these systems can be fully described only by quantum mechanics – that is why this phenomenon is often called *quantum size effect*.

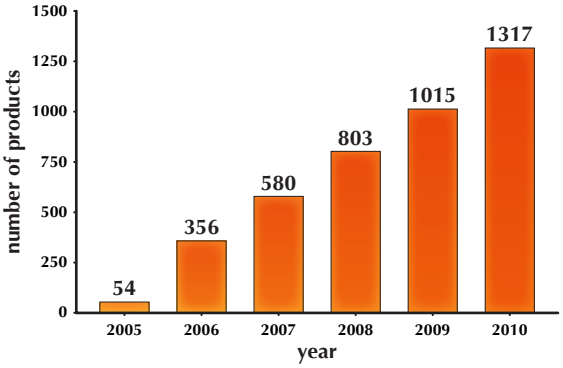

Figure 1 Number of total products listed in *The Project on Emerging Nanotechnologies*, by date of inventory update.

Molecular nanotechnology is regarded as the most advanced frontier of research in many fields such as medicine, biology, chemistry, physics, engineering, and electronics. However, it is not exclusively confined to the realm of science: many consumers may be unaware, but nanotechnology is already affecting our everyday life. Started in 2005, *The Project on Emerging Nanotechnologies*[4] is still operative: its main goal is to monitor as thoroughly and objectively

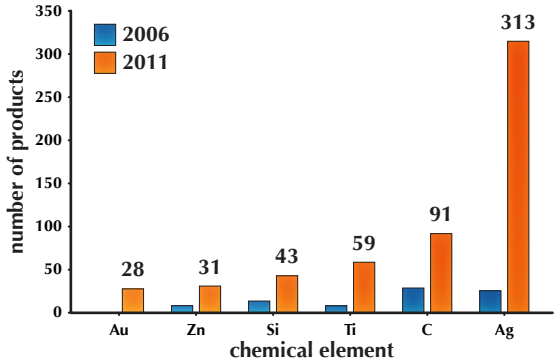

Figure 2 Numbers of products associated with specific materials, in the above mentioned project list. C includes fullerenes, Ti titanium dioxide, Si silica, and Zn zinc oxide.

1. H. Fröhlich, *Physica* **1937**, *4*, 406.
2. (a) R. Kubo, *J. Phys. Soc. Jpn.* **1962**, *17*, 975; (b) R. Kubo, *Phys. Lett.* **1962**, *1*, 49.
3. I. Giaever, H. R. Zeller, *Phys. Rev. Lett.* **1968**, *20*, 1504.
4. http://www.nanotechproject.org

as possible the progress in this field, in order to stimulate the public opinion and minimize any related risks. An inventory of nanotechnology based products currently on the market is provided: more than a thousand items are listed, belonging to very diverse categories, ranging from electronics to automotive, from food to personal care, even goods for children.

It must be stressed that nanotechnology is a very general term that encompasses many different materials, which share the same small size, but otherwise completely unrelated to each other. For example, nanoparticles can be synthesized[5] starting from carbon,[6-8] metals (gold,[9,10] silver,[11] platinum,[12,13] nickel,[14] etc.), metal oxides (titanium,[15] iron,[16,17] zinc,[18,19] etc.), semiconductors[20] (cadmium selenide, zinc sulfide, etc. – usually referred to as *quantum dots*), silica,[21] surfactants, polymers,[22] lipids, etc., and almost any feasible combination among them, without considering the range of possible post-synthetic modifications.

There should be no surprise if scientific debate has arisen over the toxicity of nanoparticles,[23-27] relating not only to their chemical composition, but rather to their inherently small size. However, a definitive answer has not yet been found: too many factors have to be accounted for, due to the fact that every material has his own specific characteristics and behavior, sometimes depending also on the methods employed for its preparation.

The main safety concern related to nanoparticles is the fact that, given their tiny dimensions, they may penetrate easily in the human body by inhalation or absorption through the skin or

5. B. L. Cushing, V. L. Kolesnichenko, C. J. O'Connor, *Chem. Rev.* **2004**, *104*, 3893.
6. Y.-P. Sun, B. Zhou, Y. Lin, W. Wang, K. A. S. Fernando, P. Pathak, M. J. Meziani, B. A. Harruff, X. Wang, H. Wang, P. G. Luo, H. Yang, M. E. Kose, B. Chen, L. M. Veca, S.-Y. Xie, *J. Am. Chem. Soc.* **2006**, *128* , 7756.
7. H. Liu, T. Ye, C. Mao, *Angew. Chem. Int. Ed.* **2007**, *46*, 6473.
8. S.-L. Hu, K.-Y. Niu, J. Sun, J. Yang, N.-Q. Zhao, X.-W. Du, *J. Mater. Chem.* **2009**, *19*, 484.
9. M. Brust, M. Walker, D. Bethell, D. J. Schiffrin, R. Whyman, *Chem. Soc., Chem. Commun* **1994**, 801.
10. M.-C. Daniel, D. Astruc, *Chem. Rev.* **2004**, *104*, 293.
11. M. Rycenga, C. M. Cobley, J. Zeng, W. Li, C. H. Moran, Q. Zhang, D. Qin, Y. Xia, *Chem. Rev.* **2011**, *111*, 3669.
12. S. Giuffrida, G. Ventimiglia, F. L. Callari, S. Sortino, *Eur. J. Inorg. Chem.* **2006**, 4022.
13. E. G. Castro, R. V. Salvatierra, W. H. Schreiner, M. M. Oliveira, A. J. G. Zarbin, *Chem. Mater.* **2010**, *22*, 360.
14. H. Winnischofer, T. C. R. Rocha, W. C. Nunes, L. M. Socolovsky, M. Knobel, D. Zanchet, *Acs Nano* **2008**, *2*, 1313.
15. X. Chen, S. S. Mao, *Chem. Rev.* **2007**, *107*, 2891.
16. T. Hyeon, *Chem. Commun.* **2003**, 927.
17. S. Singamaneni, V. N. Bliznyuk, C. Binek, E. Y. Tsymbal, *J. Mater. Chem.* **2011**, *21*, 16819.
18. D. W. Bahnemann, C. Kormann, M. R. Hoffman, *J. Phys. Chem.* **1987**, *91*, 3789.
19. E. M. Wong, J. E. Bonevich, P. C. Searson, *J. Phys. Chem. B* **1998**, *102*, 7770.
20. See notes 11-37 of chapter 2.
21. See chapter 2 – Silica nanoparticles.
22. C. Vauthier, K. Bouchemal, *Pharm. Res.* **2009**, *26*, 1025.
23. C. Buzea, I. I. Pacheco, K. Robbie, *Biointerphases* **2007**, *2*, MR17.
24. W. H. Suh, K. S. Suslick, G. D. Stucky, Y.-H. Suh, *Prog. Neurobiol.* **2009**, *87*, 133.
25. S. M. Hussain, L. K. Braydich-Stolle, A. M. Schrand, R. C. Murdock, K. O. Yu, D. M. Mattie, J. J. Schlager, M. Terrones, *Adv. Mater.* **2009**, *21*, 1549.
26. K. L. Aillon, Y. Xie, N. El-Gendy, C. J. Berkland, M. L. Forrest, *Adv. Drug. Deliv. Rev.* **2009**, *61*, 457.
27. R. Landsiedel, L. Ma-Hock, A. Kroll, D. Hahn, J. Schnekenburger, K. Wiench, W. Wohlleben, *Adv. Mater.* **2010**, *22*, 2601.

digestive tract,[28,29] yet little is known about their biodistribution, accumulation or excretion. Despite these concerns, nanoparticles have been increasingly important for the advancement of biomedical sciences and have found several and diverse applications in biology and medicine, from *in vitro* and *in vivo* imaging to drug delivery.[30-38] Recently, gold nanoparticles have reached in-human phase I clinical trial stage in the treatment of patients affected with solid cancer.[39]

1.2 Fluorescence

1.2.1 Chemosensors & Labels

The scope of this thesis is to design, synthesize and develop a nanoparticle based system to be used as a chemosensor or as a label in bioanalytical applications.

A ***chemosensor*** is defined as "a device that transforms chemical information, ranging from the concentration of a specific sample component to total composition analysis, into an analytically useful signal".[40] From a supramolecular point of view,[41-43] the system consists of three main parts (figure 3): a receptor, a signaling unit and, in most cases, a linker between them. The receptor is responsible for the molecular recognition of the analyte, while the signaling unit converts this

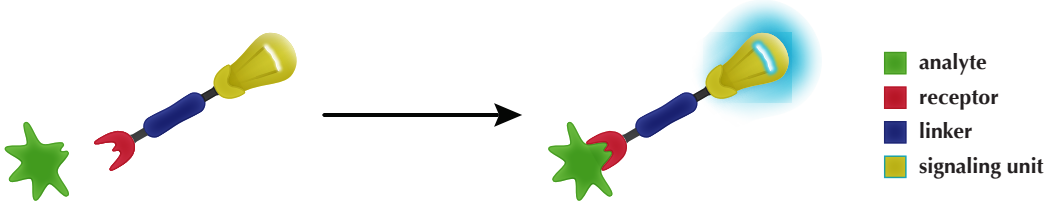

Figure 3 Schematic representation of a chemosensor.

28. M. Crosera, M. Bovenzi, G. Maina, G. Adami, C. Zanette, C. Florio, F. Filon Larese, *Int. Arch. Occup. Environ. Health* **2009**, *82*, 1043.
29. N. A. Monteiro-Riviere, J. E. Riviere, *Nanotoxicology* **2009**, *3*, 188.
30. A. G. Cuenca, H. Jiang, S. N. Hochwald, M. Delano, W. G. Cance, S. R. Grobmyer, *Cancer* **2006**, *107*, 459.
31. J. Cheon, J.-H. Lee, *Acc. Chem. Res.* **2008**, *41*, 1630.
32. K. Riehemann, S. W. Schneider, T. A. Luger, B. Godin, M. Ferrari, H. Fuchs, *Angew. Chem. Int. Ed.* **2009**, *48*, 872.
33. (a) O. C. Farokhzad, R. Langer, *Acs Nano* **2009**, *3*, 16; (b) N. Kamaly, Z. Xiao, P. M. Valencia, A. F. Radovic-Moreno, O. C. Farokhzad, *Chem. Soc. Rev.* **2012**, DOI: 10.1039/C2CS15344K.
34. J. LaRocque, D. J. Bharali, S. A. Mousa, *Mol. Biotechnol.* **2009**, *42*, 358.
35. E. Boisselier, D. Astruc, *Chem. Soc. Rev.* **2009**, *38*, 1759.
36. D. K. Kim, J. Dobson, *J. Mater. Chem.* **2009**, *19*, 6294.
37. J. Kim, Y. Piao, T. Hyeon, *Chem. Soc. Rev.* **2009**, *38*, 372.
38. T. D. Schladt, K. Schneider, H. Schild, W. Tremel, *Dalton Trans.* **2011**, *40*, 6315.
39. M. E. Davis, J. E. Zuckerman, C. H. J. Choi, D. Seligson, A. Tolcher, C. A. Alabi, Y. Yen, J. D. Heidel, A. Ribas, *Nature* **2010**, *464*, 1067.
40. Quote is taken from: A. Hulanicki, S. Głab, F. Ingman, *Pure & Appl. Chem.* **1991**, *63*, 1247.
41. J.-M. Lehn, *Supramolecular chemistry: concepts and perspectives*, 1st ed., **1995**, Wiley-VCH (Weinheim, Germany).
42. A. B. Descalzo, R. Martínez-Máñez, F. Sancenón, K. Hoffmann, K. Rurack, *Angew. Chem. Int. Ed.* **2006**, *45*, 5924.
43. V. Balzani, A. Credi, M. Venturi, *Molecular devices and machines: concepts and perspectives for the nanoworld*, 2nd ed., **2008**, Wiley-VCH (Weinheim, Germany).

recognition event into a detectable signal. In other words, the reaction between the probe and the analyte leads to a measurable change in the properties of the signaling moiety.

A ***label*** – or tag – is a device that provides a measurable trace, allowing the collection of information about the spatial and temporal distribution of an analyte. The signaling unit of a label is not affected by the recognition event.

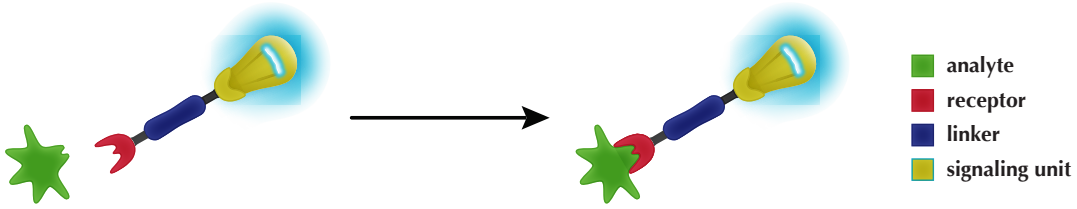

Figure 4 Schematic representation of a label.

Among the different analytical methods that can be used in chemical sensing applications,[44,45] fluorescence based techniques are well suited to investigate the fundamental processes in life sciences, thanks to their high sensitivity (in particular condition, down to the single molecule),[46-48] broad versatility, ability to provide spatial and temporal resolution, low cost, simple equipment, and even the possibility of remote sensing by means of optical fibers.[49] In the next section, the basic principles of fluorescence are discussed, with emphasis on the parameters useful in the design and optimization of fluorescent systems.

1.2.2 Mechanism of fluorescence[50]

The absorption of a ultraviolet or visible photon by a molecule causes one of its electron to be promoted to a higher energy level: the molecule is considered to be in an electronically excited state.

The excess energy is not stored indefinitely: the excited state is metastable, and eventually will relax back to the ground state by following three main paths (scheme 1):

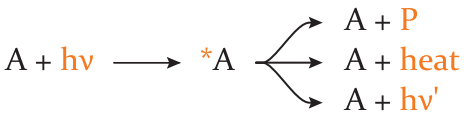

Scheme 1 Monomolecular decay pathways.

- Photochemical reaction: it is a light induced chemical reaction, which leads to the formation of a generic product (for simplicity, it will be omitted from here on);
- Non-radiative decay: the excess energy is converted into heat, through collisions with the surrounding molecules (usually the solvent);
- Radiative decay: the return to the ground state happens through emission of a photon.

44. *Chemical sensors*, A. B. Ellis, D. R. Walt (eds.), *Chem. Rev.* **2000**, *100*, issue 7.
45. *Modern topics in chemical sensing*, J. Janata (ed.), *Chem. Rev.* **2008**, *108*, issue 2.
46. Ph. Tamarat, A. Maali, B. Lounis, M. Orrit, *J. Phys. Chem. A* **2000**, *104*, 1.
47. P. V. Cornish, T. Ha, *ACS Chem. Bio.* **2007**, *2*, 53.
48. S. J. Lord, H.-I. D. Lee, W. E. Moerner, *Anal. Chem.* **2010**, *82*, 2192.
49. O. S. Wolfbeis, *Anal. Chem.* **2006**, *78*, 3859.
50. Main bibliography: (a) B. Valeur, *Molecular fluorescence: principles and applications*, 1st ed., **2001**, Wiley-VCH (Weinheim, Germany); (b) J. R. Lakovicz, *Principles of fluorescence spectroscopy*, 3rd ed., **2006**, Springer (New York, NY); (c) P. Klán, J. Wirz, *Photochemistry of organic compounds: from concepts to practice*, 1st ed., **2009**, Wiley-VCH (Weinheim, Germany).

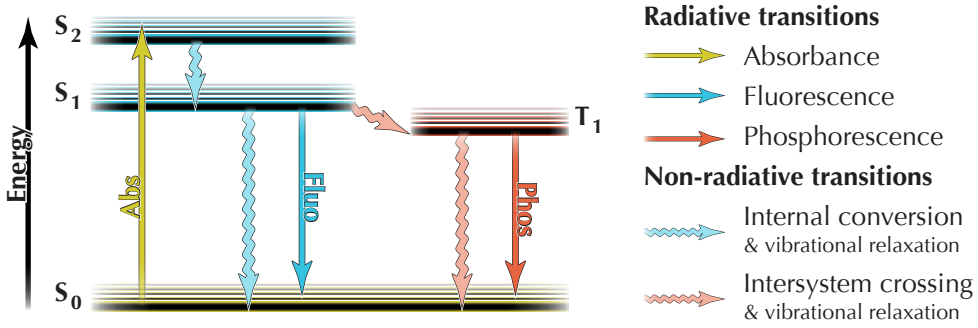

Figure 5 Typical simplified Jablonski diagram for an organic dye (simple vibrational relaxation transitions are omitted).

The Jablonski diagram[51] of figure 5 gives a more detailed description of the processes that can occur in the excited state. The singlet states are denoted as $\mathbf{S_0}$ – the ground state, $\mathbf{S_1}$ and $\mathbf{S_2}$ – the excited states; while only the first triplet excited state ($\mathbf{T_1}$) is shown. Each electronic level is characterized by different vibrational energy levels. According to the Franck-Condon principle, electronic transition between states are depicted as vertical lines, because are essentially instantaneous (10^{-15} s) compared to the time scale of nuclear motions.

Following light absorption, the fluorophore is excited to a vibrationally excited level of an excited state – for simple organic dyes, usually $\mathbf{S_1}$ or $\mathbf{S_2}$ – and it rapidly transfers this excess vibrational energy to the surrounding solvent molecules through collisions (*vibrational relaxation*). Eventually, the system will evolve from $\mathbf{S_2}$ to $\mathbf{S_1}$ via *internal conversion, i.e.*, a non-radiative transition between two electronic states of the same spin multiplicity, quickly followed by vibrational relaxation. These processes are very fast and typically occur in less than 10^{-12} s.

From $\mathbf{S_1}$, the excited molecule can relax to the ground state through an internal conversion/vibrational relaxation pathway or through the emission of a photon, defined as *fluorescence*, *i.e.*, a radiative transition between states of the same multiplicity. Fluorescence time scale is generally in the range 10^{-9}-10^{-6} s, thus slower than aforementioned processes: for this reason, fluorescence takes place only from the lowest vibrational level of $\mathbf{S_1}$ (known also as Kasha's rule)[52] and, as a consequence, fluorescence spectra are the mirror image of the $\mathbf{S_0}$-$\mathbf{S_1}$ transition. Photons emitted by fluorescence are typically at higher wavelengths than the photons absorbed, because of the energy lost during vibrational relaxation.

An additional pathway is represented by *intersystem crossing*, i.e., a non-radiative transition between two isoenergetic vibrational levels of electronic states of different multiplicity. As in the case of internal conversion, intersystem crossing is quickly followed by vibrational relaxation, leaving the excited molecule in the lowest vibrational level of $\mathbf{T_1}$. Theoretically, the spin selection rule forbids this kind of transition, but it can be favored for molecules containing heavy atoms such as bromine, iodine, etc.,[53] or for transition metal complexes,[54] thanks to spin-orbit coupling,[55] whose efficiency has a Z^4 dependence (where Z is the atomic number).

Emission from $\mathbf{T_1}$ is called *phosphorescence* and is generally shifted to longer wavelengths with respect to fluorescence; the time scale for this transition is in the range 10^{-2}-10^{2} s, because it is spin forbidden as well as intersystem crossing. Despite its long lifetime, it is difficult to

51. A. Jabłoński, *Z. Phys.* **1935**, *94*, 38.
52. "The emitting level of a given multiplicity is the lowest excited level of that multiplicity", which means that also phosphorescence takes place only from the lowest vibrational level of $\mathbf{T_1}$ (see below). Quote is taken from: M. Kasha, *Discuss. Faraday Soc.* **1950**, *9*, 14.
53. D. S. McClure, *J. Chem. Phys.* **1949**, *17*, 905.
54. P. Yuster, S. I. Weissman, *J. Chem. Phys.* **1949**, *17*, 1182.
55. S. P. McGlynn, J. Daigre, F. J. Smith, *J. Chem. Phys.* **1963**, *39*, 675.

observe this transition in solution at room temperature: the non-radiative intersystem crossing/vibrational relaxation pathway is usually predominant, even without taking into account the quenching by molecular oxygen.

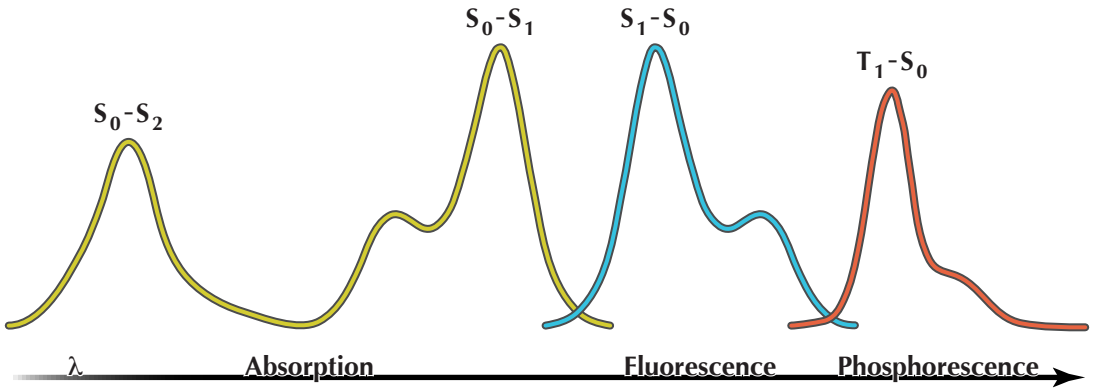

Figure 6 Typical shapes and positions of absorption and emission spectra.

1.2.3 Molecular fluorophores

One of the first efficient fluorescent chemosensors was reported by Tsien in 1980, for the detection of Ca^{2+};[56] since then, research, design, and synthesis of these system has been in constant evolution.[57-65] For example, biologists are very interested in the detection of cations – *e.g.*, Na^{2+}, K^{+}, Mg^{2+}, Ca^{2+}, to name a few – because they are involved in many biological processes such as transmission of nerve impulses, regulation of cell activity, or muscle contraction; while environmental analysts require ultrasensitive detection of toxic species, like Hg^{2+} or Cd^{2+}.On the other hand, fluorescent labeling is one of the most popular approach used in molecular imaging[66-69] to tag biomolecules – such as single amino acids, peptides, whole proteins, antibodies, and DNA or RNA strands – in order to monitor biological processes.

Molecular organic dyes are still commonly employed as signal transduction tools. Besides their chemical properties (such as reactivity, polarity, thermal stability, etc.), they can described by many photophysical parameters: the most relevant in our discussion will be briefly presented.

---

56. R. Y. Tsien, *Biochem.* **1980**, *19*, 2396.
57. (a) R. A. Bissell, A. P. de Silva, H. Q. N. Gunaratne, P. L. M. Lynch, G. E. M. Maguire, K. R. A. S. Sandanayake, *Chem. Soc. Rev.* **1992**, *21*, 187; (b) A. P. de Silva, H. Q. N. Gunaratne, T. Gunnlaugsson, A. J. M. Huxley, C. P. McCoy, J. T. Rademacher, T. E. Rice, *Chem. Rev.* **1997**, *97*, 1515; (c) J. F. Callan, A. P. de Silva, D. C. Magri, *Tetrahedron* **2005**, *61*, 8551.
58. *Luminescent Sensors*, L. Fabbrizzi (ed.), *Coord. Chem. Rev.* **2000**, *205*, issue 1.
59. L. Fabbrizzi, M. Licchelli, A. Taglietti, *Dalton Trans.* **2003**, 3471.
60. L. Prodi, *New. J. Chem.* **2005**, *29*, 20.
61. F. Mancin, E. Rampazzo, P. Tecilla, U. Tonellato, *Chem. Eur. J.* **2006**, *12*, 1844.
62. R. McRae, P. Bagchi, S. Sumalekshmy, C. J. Fahrni, *Chem. Rev.* **2009**, *109*, 4780.
63. C. Lodeiro, J. L. Capelo, J. C. Mejuto, E. Oliveira, H. M. Santos, B. Pedras, C. Nuñez, *Chem. Soc. Rev.* **2010**, *39*, 2948.
64. E. M. Nolan, S. J. Lippard, *Acc. Chem. Res.* **2009**, *42*, 193.
65. T. Doussineau, A. Schulz, A. Lapresta-Fernandez, A. Moro, S. Körsten, S. Trupp, G. J. Mohr, *Chem. Eur. J.* **2010**, *16*, 10290.
66. B. N. G. Giepmans, S. R. Adams, M. H. Ellisman, R. Y. Tsien, *Science* **2006**, *312*, 217.
67. L. D. Lavis, R. T. Raines, *ACS Chem. Biol.* **2008**, *3*, 142.
68. M. S. T. Gonçalves, *Chem. Rev.* **2009**, *109*, 190.
69. *Concepts and strategies for molecular imaging*, *Chem. Rev.* **2010**, *100*, issue 5.

First, ***molar absorption coefficient*** $\varepsilon(\lambda)$ expresses the probability of a fluorophore to absorb a photon at a given wavelength, and in a given solvent. Experimentally, is defined by the Beer-Lambert law:

$$A(\lambda) = \text{Log}\,\frac{I^0}{I} = \varepsilon(\lambda)\,b\,c \qquad [1]$$

where $A(\lambda)$ is the measured absorbance; I^0 and I are the intensities of the beams entering and leaving the sample, respectively; b is the absorption pathlenght; and c the concentration. Typically b is expressed in cm and c in M, so that $\varepsilon(\lambda)$ results in $M^{-1}\cdot cm^{-1}$, being A a dimensionless quantity. Clearly, $\varepsilon(\lambda)$ varies as a function of the wavelength: u sually, unless otherwise specified, the reported values for organic dyes are those measured at the maximum absorption wavelength; ε values for allowed $\mathbf{S_0}$-$\mathbf{S_1}$ transitions are typically greater than $10^4\ M^{-1}\cdot cm^{-1}$.

Second, ***fluorescence quantum yield*** Φ is the fraction of excited molecules in $\mathbf{S_1}$ that return directly to the ground state with emission of photons, *i.e.*, the ratio between the number of emitted and the number of absorbed photons; commonly it is determined by comparison with a reference molecule.[70] It is generally accepted that molecular oxygen quenches fluorescence[71] – and phosphorescence as well[72] – but only compounds with long excited state lifetimes are affected (depending on the medium), because oxygen operates through a diffusion-controlled collisional mechanism.

In diluted solution, the intensity of emitted light is directly proportional both to ε – that accounts for the probability of the molecule to be excited – and to Φ – the efficiency of the fluorescence radiative decay – so in the design of new systems, it is recommended to maximize these parameters.

Last, ***Stokes shift*** is the difference between the first absorption band and the maximum of the fluorescence spectrum; the name comes from George Gabriel Stokes, who was the first in 1852[73] to observe the fact that the maximum emission wavelength is usually higher than the absorption. Experimentally, the detection of a fluorescent species is easier when the Stokes shift is larger; moreover, organic dyes with small values of Stokes shift are more subject to self-quenching, because the absorption spectrum overlaps to some extent the fluorescence spectrum.

As previously stated, molecular fluorophores are still very popular and frequently exploited in chemosensor and labels, thanks to their low cost, versatility, availability and ease of use. Among all the different kinds of dyes available, it is worth mentioning coumarins,[74-77] fluoresceins,[78-80]

---

70. See equation [1] of chapter 8 – Experimental section.
71. K. Kikuchi, C. Sato, M. Watabe, H. Ikeda, Y. Takahashi, T. Miyashi, *J. Am. Chem. Soc.* **1993**, *115*, 5180.
72. (a) K. Kawaoka, A. U. Khan, D. R. Kearns, *J. Chem. Phys.* **1967**, *46*, 1842; (b) D. R. Kearns, A. J. Stone, *J. Chem. Phys.* **1971**, *55*, 3383.
73. G. G. Stokes, *Phil. Trans. R. Soc. Lond.* **1852**, *142*, 463. In this same paper, it was him who coined the term *fluorescence*.
74. R. O. Clinton, S. C. Laskows, *J. Am. Chem. Soc.* **1949**, *71*, 3602.
75. W.-C. Sun, K. R. Gee, R. P. Haugland, *Bioorg. & Med. Chem. Lett.* **1998**, *8*, 3107.
76. J. E. T. Corrie, V. R. N. Munasinghe, W. Rettig, *J. Heterocycl. Chem.* **2000**, *37*, 1447.
77. J. Gordo, J. Avó, A. J. Parola, J. C. Lima, A. Pereira, P. S. Branco, *Org. Lett.* **2011**, *13*, 5112.
78. A. Baeyer, *Ber. Dtsch. Chem. Ges.* **1871**, *4*, 555.
79. W.-C. Sun, K. R. Gee, D. H. Klaubert, R. P. Haugland, *J. Org. Chem.* **1997**, *62*, 6469.
80. L. D. Lavis, T. J. Rutkoski, R. T. Raines, *Anal. Chem.* **2007**, *79*, 6775.

rhodamines,[81-84] BODIPY[85] dyes,[86-88] benzophenoxazines,[89] squaraines,[90-92] and cyanines.[93-95] There is a particular interest for red and near infrared emitting dyes,[96-99] especially for imaging applications,[100] thanks to the reduced scattering; improved signal to noise ratio – due to the minimal tissue autofluorescence; enhanced tissue penetration depth (biological components such as hemoglobin, water, and lipids have their lowest ε between 650 and 900 nm); and reduced damage in experiments involving live cells.

However, small molecule organic dyes show several drawbacks:

- Only one fluorophore at a time can signal the analyte recognition event;
- Usually they are susceptible to photobleaching,[101] especially under continuous irradiation;
- Many interfering species can quench their fluorescence;
- The synthesis of the supramolecular system can be demanding, time-consuming, and expensive;
- Most of them are highly hydrophobic species, limiting their use in biocompatible aqueous mediums.[102]

---

81. T. Nguyen, M. B. Francis, *Org. Lett.* **2003**, *5*, 3245.
82. H. N. Kim, M. H. Lee, H. J. Kim, J. S. Kim, J. Yoon, *Chem. Soc. Rev.* **2008**, *37*, 1465.
83. M. Beija, C. A. M. Afonso, J. M. G. Martinho, *Chem. Soc. Rev.* **2009**, *38*, 2410.
84. M. V. Kvach, I. A. Stepanova, I. A. Prokhorenko, A. P. Stupak, D. A. Bolibrukh, V. A. Korshun, V. V. Shmanai, *Bioconj. Chem.* **2009**, *20*, 1673.
85. BODIPY is a registered trademark of Life Technologies Corporation.
86. A. Treibs, F.-H. Kreuzer, *Justus Liebigs Ann. Chem.* **1968**, *718*, 208.
87. A. Loudet, K. Burgess, *Chem. Rev.* **2007**, *107*, 4891.
88. (a) R. Ziessel, G. Ulrich, A. Harriman, *New J. Chem.* **2007**, *31*, 496; (b) G. Ulrich, R. Ziessel, A. Harriman, *Angew. Chem. Int. Ed.* **2008**, *47*, 1184.
89. J. Jose, K. Burgess, *Tetrahedron* **2006**, *62*, 11021.
90. B. Oswald, L. Patsenker, J. Duschl, H. Szmacinski, O. S. Wolfbeis, E. Terpetschnig, *Bioconj. Chem.* **1999**, *10*, 925.
91. A. L. Tatarets, I. A. Fedyunyayeva, T. S. Dyubko, Y. A. Povrozin, A. O. Doroshenko, E. A. Terpetschnig, L. D. Patsenker, *Anal. Chim. Acta* **2006**, *570*, 214.
92. L. Beverina, P. Salice, *Eur. J. Org. Chem.* **2010**, 1207.
93. (a) A. Mishra, R. K. Behera, P. K. Behera, B. K. Mishra, G. B. Behera, *Chem. Rev.* **2000**, *100*, 1973; (b) M. Panigrahi, S. Dash, S. Patel, B. K. Mishra, *Tetrahedron* **2012**, *68*, 781.
94. M. Levitus, S. Ranjit, *Q. Rev. Biophys.* **2011**, *44*, 123.
95. A. S. Tatikolov, *J. Photochem. Photobiol. C: Photochem. Rev.* **2012**, *13*, 55.
96. J. Fabian, H. Nakazumi, M. Matsuoka, *Chem. Rev.* **1992**, *92*, 1197.
97. V. Buschmann, K. D. Weston, M. Sauer, *Bioconj. Chem.* **2003**, *14*, 195.
98. A. Gómez-Hens, M. P. Aguilar-Caballos, *Trends Anal. Chem.* **2004**, *23*, 127.
99. J. O. Escobedo, O. Rusin, S. Lim, R. M Strongin, *Curr. Op. Biol. Chem.* **2010**, *14*, 64.
100. (a) R. Weissleder, V. Ntziachristos, *Nat. Med.* **2003**, *9*, 123; (b) S. A Hilderbrand, R. Weissleder, *Curr. Op. Biol. Chem.* **2010**, *14*, 71.
101. For example, fluorescein: L. Song, E. J. Hennink, T. Young, H. J. Tanke, *Biophys. J.* **1995**, *68*, 2588.
102. There is much research around the water solubilization of organic dyes, mainly via introduction of sulfonate groups – see for example: (a) C. Bouteiller, G. Clavé, A. Bernardin, B. Chipon, M. Massonneau, P.-Y. Renard, A. Romieu, *Bioconj. Chem.* **2007**, *18*, 1303; (b) A. Romieu, D. Brossard, M. Hamon, H. Outaabout, C. Portal, P.-Y. Renard, *Bioconj. Chem.* **2008**, *19*, 279; (c) A. Romieu, D. Tavernier-Lohr, S. Pellet-Rostaing, M. Lemaire, P.-Y. Renard, *Tetrahedron Lett.* **2010**, *51*, 3304; (d) A. Romieu, T. Bruckdorfer, G. Clavé, V. Grandclaude, C. Massif, P.-Y. Renard, *Org. Biomol. Chem.* **2011**, *9*, 5337 – but the purification of such compounds is all but straightforward.

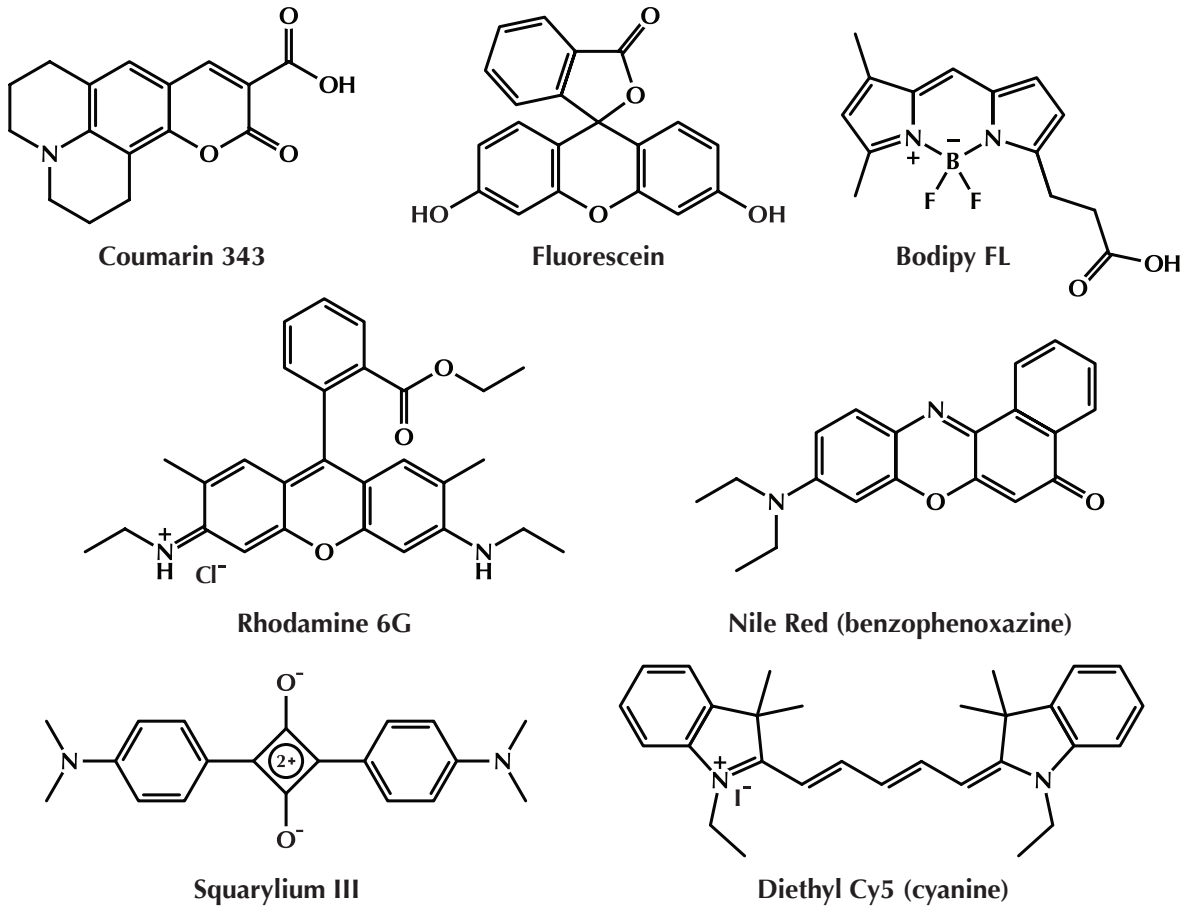

Scheme 2 Representative examples of molecular fluorophores.

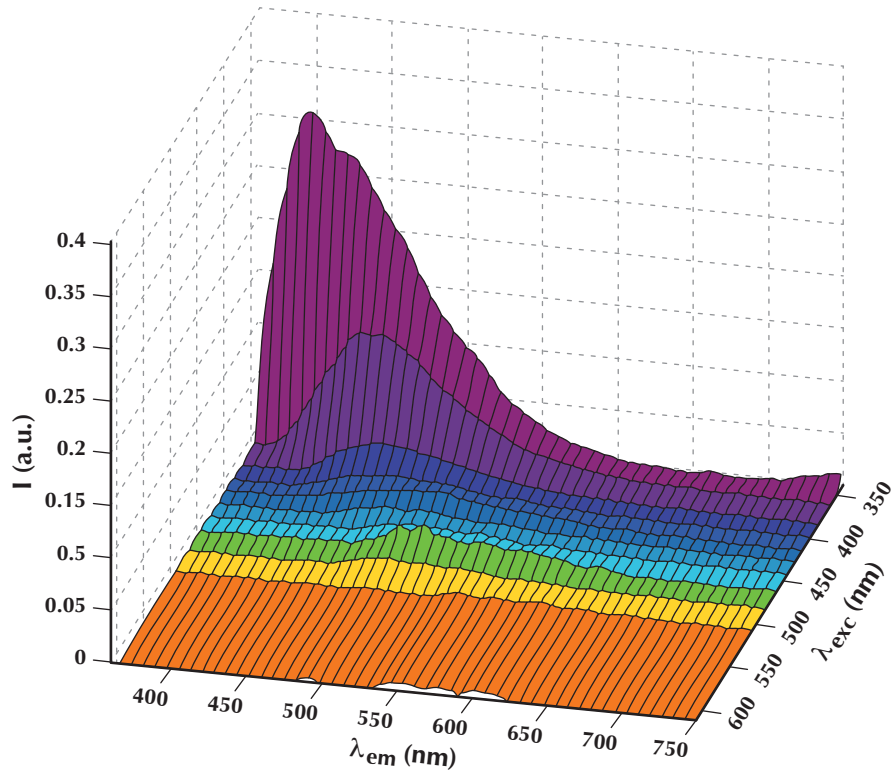

Figure 7 Autofluorescence spectra (λ_{em} = 360-750 nm) obtained *in vivo* at different excitation wavelengths (λ_{exc} = 337-610 nm). Adapted from reference 100a.

1.2.4 Fluorescent nanoparticles

Molecular fluorophores can be conveniently replaced with dye doped nanoparticles as signaling moieties in chemosensor and labels. Their overall photophysical behavior, as in the case of rigorously supramolecular systems,[41-43] depends on the type, strength, and efficiency of the interactions between the constituent molecular units at the ground or excited state.[103] Due to the close proximity of the active moieties, energy and/or electron transfer are likely to arise, resulting in collective effects, that confers to the nanoparticle new properties or improved performances with respect to single molecules, beside the fact that the its matrix acts as a protective shell against interfering species.[60,104,105]

On the other hand, if no intramolecular interactions occurred, the photophysical features of a nanoparticle would be merely the combination of those of the included molecular units. Nevertheless this can be still an attractive characteristic: *e.g.*, the molar absorption coefficient of heavily doped nanoparticles is the result of the sum of all the trapped absorbing moieties, and thus can be extremely higher than a single molecular fluorophore.

All the above mentioned factors lead to an increase in both ε and Φ, and thus to a great signal enhancement, showing that dye doped nanoparticles possess improved features with respect to molecular fluorophores. Moreover, the overall solubility of a nanosystem depends on its surface properties, which can be suitably tailored to match the specific needs of a particular application, overcoming the limitation of hydrophobic fluorescent molecules.

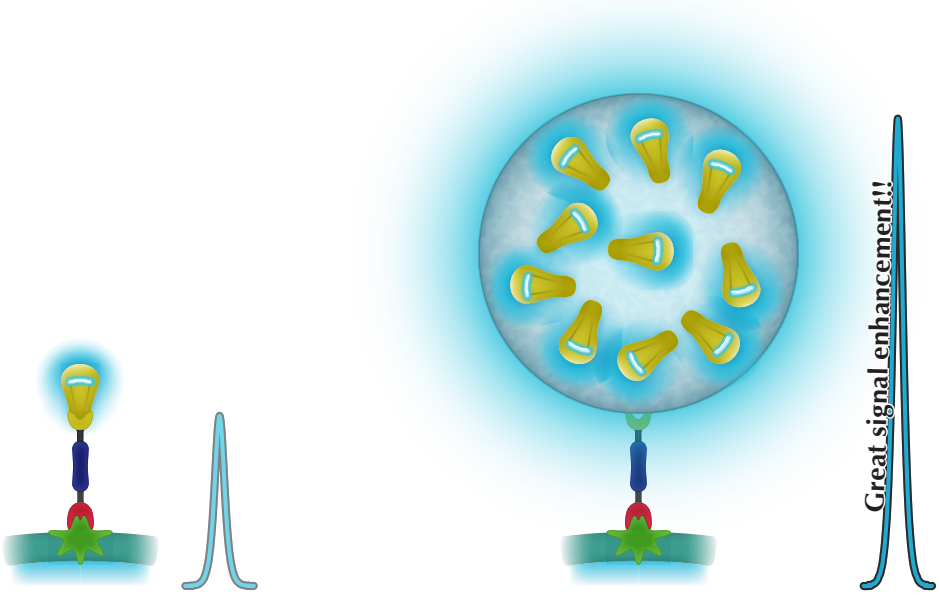

Figure 8 Schematic comparison between molecular fluorophores and fluorescent nanoparticles.

In the next chapter, we will describe the methods available for the fabrication of silica nanosystems, with particular emphasis on a surfactant mediated protocol we have developed for the synthesis of silica-core/PEG-shell nanoparticles.

103. K. E. Sapsford, L. Berti, I. L. Medintz, *Angew. Chem. Int. Ed.* **2006**, *45*, 4562.
104. E. Rampazzo, S. Bonacchi, M. Montalti, L. Prodi, N. Zaccheroni, *J. Am. Chem. Soc.* **2007**, *129*, 14251.
105. A. Pedone, G. Prampolini, S. Monti, V. Barone, *Chem. Mater.* **2011**, *23*, 5016.

Chapter 2
Silica nanoparticles

2.1 Introduction

In general terms, there are two main approaches in the synthesis of nanoparticles:[1]

- ***Top-down***:[2] starting from bulk materials, the nanosystems are obtained through a series of degradation processes; however, this method lacks in reproducibility and is unable to gain an accurate control over the size and shape of the final products;
- ***Bottom-up***:[3] complex nanostructures are created by spontaneous self-assembly, either with an atom-by-atom or molecule-by-molecule procedure; the control over the morphological properties of the final material can be excellent, therefore this approach is usually preferred in the nanometer scale, even if a complete understanding of the synthetic mechanism is often puzzling.

Nowadays, silicon dioxide – or simply *silica* – nanoparticles represent one of the most widespread systems employed in nanotechnology research, development and applications.[4] In the field of fluorescence, silica has proven to be an excellent platform, thanks to the fact that it is photophysically inert, *i.e.*, it is transparent to ultraviolet and visible radiation, and it is not involved in energy or electron transfer processes. As a consequence, all the photochemical properties of silica nanoparticles are conferred by the molecules doped inside the system or grafted on its surface. On the contrary, photoactive materials may be subject to or cause photodecomposition (titania)[5,6] or may induce the quenching of the luminescence of bound chromophores via electron or energy transfer processes (gold)[7-9].

1. G. A. Ozin, *Adv. Mater.* **1992**, *4*, 612.
2. "There's plenty of room at the bottom.": R. P. Feynman, *Eng. Sci.* **1960**, *23*, 22.
3. "There is even more room at the top.": J.-M. Lehn, *Supramolecular chemistry: concepts and perspectives*, 1st ed., **1995**, Wiley-VCH (Weinheim, Germany).
4. *Colloidal silica: Fundamentals and applications*, H. E. Bergna, W. O. Roberts (eds.), **2006**, CRC Press (Boca Raton, FL).
5. J.-M. Wu, T.-W. Zhang, *Langmuir* **2005**, *21*, 6995.
6. X. Chen, S. S. Mao, *Chem. Rev.* **2007**, *107*, 2891.
7. K. G. Thomas, P. V. Kamat, *Acc. Chem. Res.* **2003**, *36*, 888.
8. T. L. Jennings, M. P. Singh, G. F. Strouse, *J. Am. Chem. Soc.* **2006**, *128*, 5462.
9. S. Kühn, G. Mori, M. Agio, V. Sandoghdar, *Mol. Phys.* **2008**, *106*, 893.

Another advantage of silica is that it is intrinsically non-toxic,[10] in particular if compared to other nanomaterials such as quantum dots,[11-17] which are still widely researched[18-22] and employed in bioanalytical applications,[23-27] even *in vivo*,[28-30] despite the well know toxicity[31-34] (but sometimes disputed)[35] of its constituent materials,[36] and their blinking behavior.[37] Preliminary experiments seems to support the benign nature of silica nanoparticles,[38] but there are evidences of possible harmful effects as well, due to tissue accumulation, caused by endocytosis by macrophages[39] (fortunately, there are ways to overcome this uptake – see below).

10. Clearly, we are referring to amorphous phase silica; it has been established that prolonged exposure to crystalline silica dust by inhalation eventually leads to long-term, irreversible lung disease (silicosis).
11. M. L. Steigerwald, L. E. Brus, *Acc. Chem. Res.* **1990**, *23*, 183.
12. A. P. Alivisatos, *Science*, **1996**, *271*, 933.
13. T. Trindade, P. O'Brien, N. L. Pickett, *Chem. Mater.* **2001**, *13*, 3843.
14. J. Park, J. Joo, S. G. Kwon, Y. Jang, T. Hyeon, *Angew. Chem. Int. Ed.* **2007**, *46*, 4630.
15. U. Resch-Genger, M. Grabolle, S. Cavaliere-Jaricot, R. Nitschke, T. Nann, *Nat. Meth.* **2008**, *5*, 763.
16. A. M. Smith, S. Nie, *Acc. Chem. Res.* **2010**, *43*, 190.
17. M. D. Regulacio, M.-Y. Han, *Acc. Chem. Res.* **2010**, *43*, 621.
18. J. M. Costa-Fernández, R. Pereiro, A. Sanz-Medel, *Trends Anal. Chem.* **2006**, *25*, 207.
19. W. W. Yu, E. Chang, J. C. Falkner, J. Zhang, A. M. Al-Somali, C. M. Sayes, J. Johns, R. Drezek, V. L. Colvin, *J. Am. Chem. Soc.* **2007**, *129*, 2871.
20. K. Susumu, H. T. Uyeda, I. L. Medintz, T. Pons, J. B. Delehanty, H. Mattoussi, *J. Am. Chem. Soc.* **2007**, *129*, 13987.
21. R. E. Galian, M. de la Guardia, *Trends Anal. Chem.* **2009**, *28*, 279.
22. H. Shen, A. M. Jawaid, P. T. Snee, *ACS Nano* **2009**, *3*, 915.
23. (a) W. C. W. Chan, S. Nie, *Science* **1998**, *281*, 2016; (b) A. M. Smith, S. Nie, *Nat. Biotech.* **2009**, *27*, 732.
24. (a) A. P. Alivisatos, W. Gu, C. Larabell, *Annu. Rev. Biomed. Eng.* **2005**, *7*, 55; (b) A. P. Alivisatos, *Nat. Biotech.* **2004**, *22*, 47.
25. (a) I. L. Medintz, H. T. Uyeda, E. R. Goldman, H. Mattoussi, *Nat. Mater.* **2005**, *4*, 435; (b) I. L. Medintz, H. Mattoussi, *Phys. Chem. Chem. Phys.* **2009**, *11*, 17; (c) J. B. Delehanty, H. Mattoussi, I. L. Medintz, *Anal. Bioanal. Chem.* **2009**, *393*, 1091.
26. R. Gill, M. Zayats, I. Willner, *Angew. Chem. Int. Ed.* **2008**, *47*, 7602.
27. (a) M. F. Frasco, N. Chaniotakis, *Sensors* **2009**, *9*, 7266; (b) M. F. Frasco, N. Chaniotakis, *Anal. Bioanal. Chem.* **2010**, *396*, 229.
28. B. Dubertret, P. Skourides, D. J. Norris, V. Noireaux, A. H. Brivanlou, A. Libchaber, *Science* **2002**, *298*, 1759.
29. X. Michalet, F. F. Pinaud, L. A. Bentolila, J. M. Tsay, S. Doose, J. J. Li, G. Sundaresan, A. M. Wu, S. S. Gambhir, S. Weiss, *Science* **2005**, *307*, 538.
30. W. Cai, D.-W. Shin, K. Chen, O. Gheysens, Q. Cao, S. X. Wang, S. S. Gambhir, X. Chen, *Nano Lett.* **2006**, *6*, 669.
31. A. M. Derfus, W. C. W. Chan, S. N. Bhatia, *Nano Lett.* **2004**, *4*, 11.
32. C. Kirchner, T. Liedl, S. Kudera, T. Pellegrino, A. Muñoz Javier, H. E. Gaub, S. Stölzle, N. Fertig, W. J. Parak, *Nano Lett.* **2005**, *5*, 331.
33. A. Hoshino, K. Fujioka, T. Oku, M. Suga, Y. F. Sasaki, T. Ohta, M. Yasuhara, K. Suzuki, K. Yamamoto, *Nano Lett.* **2004**, *4*, 2163.
34. J. Lovrić, H. S. Bazzi, Y. Cuie, G. R. A. Fortin, F. M. Winnik, D. Maysinger, *J. Mol. Med.* **2005**, *83*, 377.
35. T. S. Hauck, R. E. Anderson, H. C. Fischer, S. Newbigging, W. C. W. Chan, *Small* **2010**, *6*, 138.
36. The debate is still open; see also: (a) J. L. Pelley, A. S. Daar, M. A. Saner, *Toxicol. Sci.* **2009**, *112*, 276; (b) M. Bottrill, M. Green, *Chem. Commun.* **2011**, *47*, 7039; and (c) W. Cai, A. R. Hsu, Z.-B. Li, X. Chen, *Nanoscale Res. Lett.* **2007**, *2*, 265.
37. J. Yao, D. R. Larson, H. D. Vishwasrao, W. R. Zipfel, W. W. Webb, *Proc. Natl. Acad. Sci. USA* **2005**, *102*, 14284.
38. Y. Jin, S. Kannan, M. Wu, J. X. Zhao, *Chem. Res. Toxicol.* **2007**, *20*, 1126.
39. G. Xie, J. Sun, G. Zhong, L. Shi, D. Zhang, *Arch. Toxicol.* **2010**, *84*, 183.

From a synthetic point of view, besides the fact that it is rather inexpensive, silica is a very appealing material: the preparation of nanoparticles usually requires mild condition and does not involve complicated purification procedures, while size is tunable with few adjustments in the reaction conditions. Moreover design of these systems can be based on a modular approach, thanks to their extreme flexibility and versatility, making them adaptable for diverse applications.

For all these reasons, the chemistry of silica has been extensively researched: nanoparticles can be obtained according to three different major protocols – the Stöber method, the reverse microemulsion synthesis, and the aqueous micellar system – which will be discussed in more detail in the following sections.

2.2 Stöber method

This method takes its name from Werner Stöber, who discovered the controlled synthesis of colloidal silica in 1968,[40] based on a previous work by Kolbe,[41] and later further developed by van Blaaderen.[42] It involves the ammonia catalyzed hydrolysis and condensation of tetraethyl orthosilicate (TEOS) in an ethanol/water mixture.

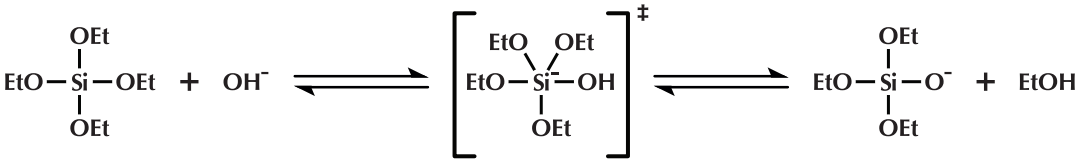

Scheme 1 Reaction mechanism for the base catalyzed hydrolysis of TEOS.

The ***hydrolysis*** step (scheme 1) is thought to proceed through a bimolecular nucleophilic substitution (S_N2) on the silicon atom, characterized by a negatively charged, pentacoordinate transition state.[42,43] The nucleophile involved in this step is OH^-, therefore an increase in the concentration of NH_3 and/or H_2O leads to an increase in the reaction rate. Moreover, since the hydrolysis decreases the electron density on the silicon atom – OH is more electron-withdrawing than OEt – the negative charge of the transition state is more stabilized for each subsequent step; for this reason, the rate-determining step for monomers is the hydrolysis of the first ethoxy group.

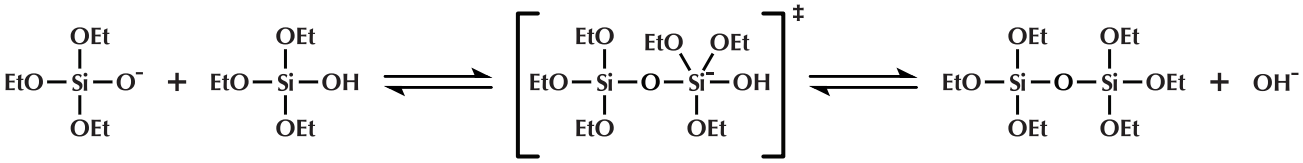

Scheme 2 Reaction mechanism for the base catalyzed hydrolysis of TEOS.

The ***condensation*** step (scheme 2) is very similar to hydrolysis: it proceeds through a S_N2 type nucleophilic substitution at the silicon atom, which results in a negatively charged, pentacoordinate transition state; the nucleophile is a deprotonated silanol group, so the reaction rate is still influenced by the concentration of NH_3 and/or H_2O; and it decreases the electron density on the silicon atom – OSi is more electron withdrawing than OH.

This implies that more condensed species are more susceptible both to hydrolysis and to condensation, because the acidity of the silanol groups are increased as well. Since it has been

40. W. Stöber, A. Fink, E. Bohn, *J. Colloid Interface Sci.* **1968**, *26*, 62.
41. G. Kolbe, *Ph. D. Thesis*, **1956**, Jena (Germany).
42. A. van Blaaderen, A. Vrij, *J. Colloid Interface Sci.* **1993**, *156*, 1.
43. B. L. Cushing, V. L. Kolesnichenko, C. J. O'Connor, *Chem. Rev.* **2004**, *104*, 3893.

observed that the rate of condensation is much faster than the rate of hydrolysis, the most probable reaction in solution is between a monomer and a higher polymerized species (condensation between large siloxane moieties is hindered by steric effects), which leads to the formation of a spheroidal particle.

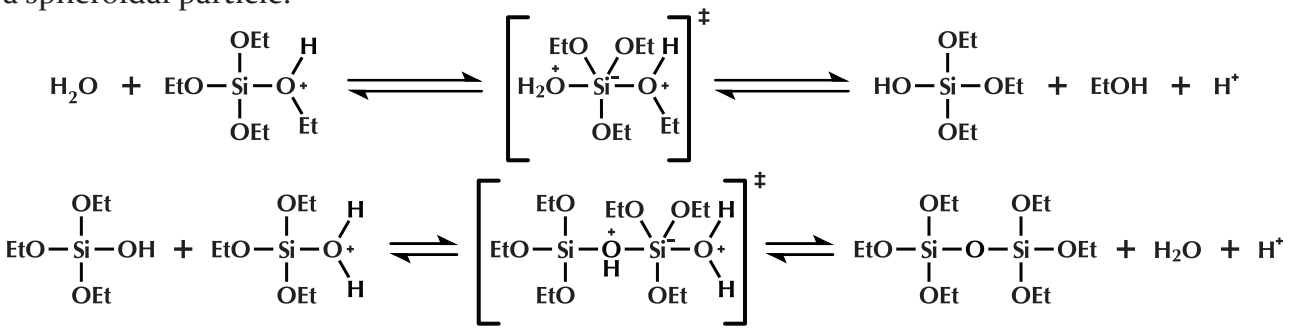

Scheme 3 Reaction mechanism for the acid catalyzed hydrolysis (above) and condensation (below) of TEOS.

As a matter of fact, these two reactions may occur in acidic solution as well (scheme 3). With acid catalysis, the above mentioned effects are reversed: the transition state is now positively charged and therefore is less stabilized for each hydrolysis or condensation step, whose rates decrease as the polymerization process proceeds; moreover, hydrolysis becomes the faster process. As a consequence, instead of spheroidal agglomerates, chains and branches are preferentially formed, that will eventually cross-link at later stages. It is clear that the morphology of the final structure is strongly dependent on the catalysis employed.[44]

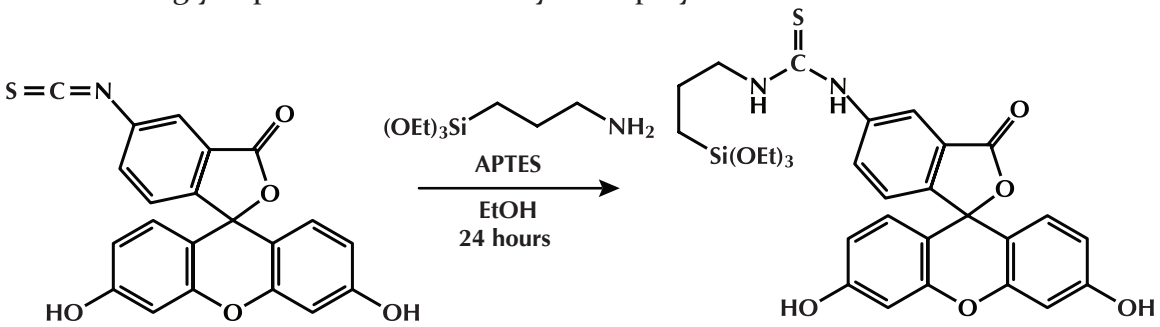

Scheme 4 Exemplifying synthesis of a trialkoxysilane functionalized fluorophore: coupling of fluorescein isothiocyanate with APTES as in reference 45.

The preparation of the first ***dye doped*** silica nanoparticles was possible thanks to van Blaaderen's idea of modifying the structure of fluorophores, by coupling (3-aminopropyl)triethoxysilane (APTES) with fluorescein isothiocyanate[45] (scheme 4) and rhodamine B isothiocyanate.[46] The resulting triethoxysilane derivatized molecules are then able to co-condense with TEOS during

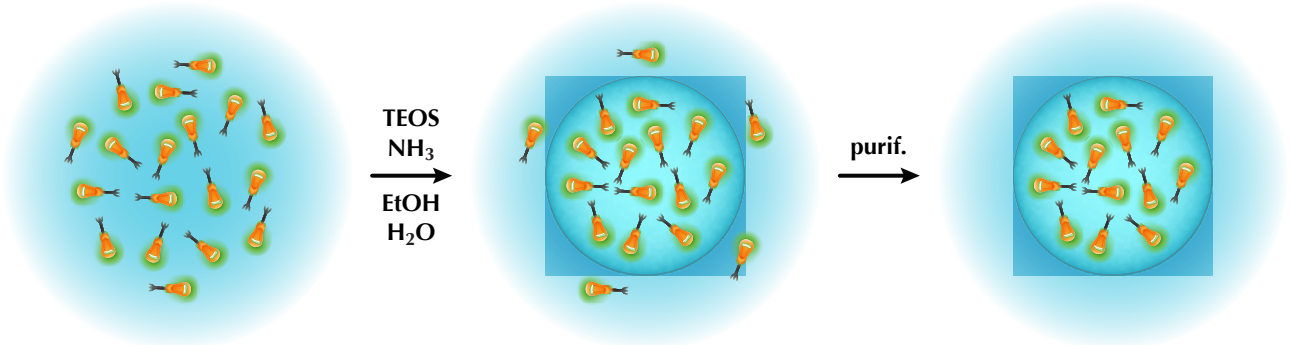

Figure 1 Schematic representation of the Stöber synthesis of fluorescein isothiocyanate doped silica nanoparticles.

44. D. Gallagher, T. A. Ring, *Chimia* **1989**, *43*, 298.
45. A. van Blaaderen, A. Imhof, W. Hage, A. Vrij, *Langmuir* **1992**, *8*, 1514.
46. N. A. M. Verhaegh, A. van Blaaderen, *Langmuir* **1994**, *10*, 1427.

the nanoparticle growth, yielding systems in which the organic dyes are covalently grafted to the silica matrix (figure 1). This is a fundamental improvement, because, apart from minimizing leaching issues, allows to reach very high doping levels.

Even if already mentioned in chapter 1, it should be stressed that the inclusion inside the nanoparticles leads to an improvement of the photophysical properties of the fluorophores, such as quantum yield or photostability.[47,48] This segregation, in fact, reduces the interaction of the dyes with external interfering agents – *e.g.*, the solvent or molecular oxygen, that is often responsible for luminescence quenching – as well as their excited state conformational mobility.[49] In most cases, these factors inhibit non-radiative decay pathways and could prevent photoreactions that result in the irreversible degradation of the fluorophores. Moreover, thanks to the water compatibility of silica, many hydrophobic fluorophores can be successfully transferred in water – and thus their properties exploited – as a consequence of their insertion within the nanoparticle.

2.3 Reverse microemulsion synthesis

This method was developed by Arriagada and Osseo-Asare,[50] and later improved by Tan and co-workers.[51] The fundamental reactions at the basis of this process are the same described in the previous section; the difference lies in the medium where hydrolysis and condensation of TEOS take place, *i.e.*, in the core of a reverse microemulsion. This peculiar system originates when a surfactant, along with a controlled amount of water, is dispersed in a hydrocarbon, under certain conditions.

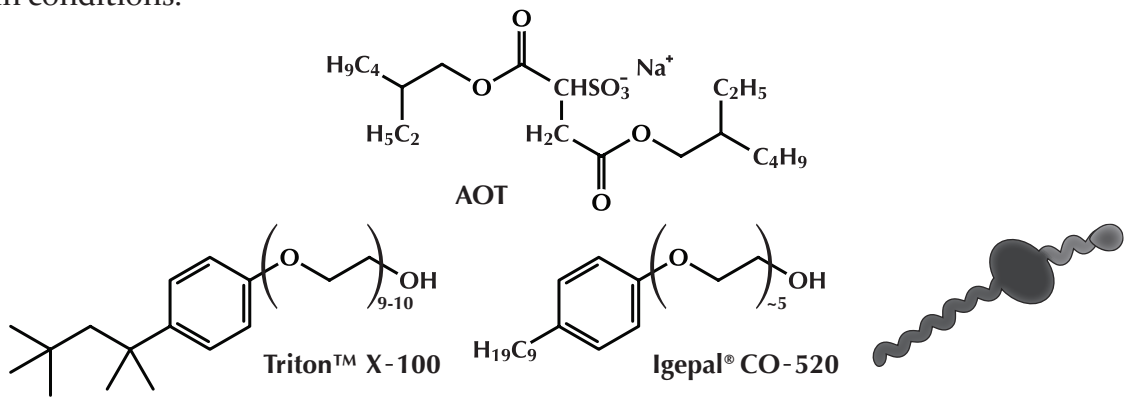

Scheme 5 Molecular structures of commonly used surfactants in the reverse microemulsion synthesis of silica nanoparticles.

Surfactants are amphiphilic long-chain organic compounds (scheme 5), miscible both in hydrocarbons and in water, characterized by two fundamental parameters: the critical micelle concentration (CMC) and the critical micelle temperature (CMT). Above these threshold values,

47. (a) H. Ow, D. R. Larson, M. Srivastava, B. A. Baird, W. W. Webb, U. Wiesner, *Nano Lett.* **2005**, *5*, 113; (b) A. Burns, H. Ow, U. Wiesner, *Chem. Soc. Rev.* **2006**, *35*, 1028; (c) D. R. Larson, H. Ow, H. D. Vishwasrao, A. A. Heikal, U. Wiesner, W. W. Webb, *Chem. Mater.* **2008**, *20*, 2677; (d) E. Herz, H .Ow, D. Bonner, A. Burns, U. Wiesner, *J. Mater. Chem.* **2009**, *19*, 6341; (e) B. Cohen, C. Martin, S. K. Iyer, U. Wiesner, A. Douhal, *Chem. Mater.* **2012**, *24*, 361.

48. A. Pedone, G. Prampolini, S. Monti, V. Barone, *Chem. Mater.* **2011**, *23*, 5016.

49. E. Rampazzo, S. Bonacchi, M. Montalti, L. Prodi, N. Zaccheroni, *J. Am. Chem. Soc.* **2007**, *129*, 14251.

50. (a) F. J. Arriagada, K. Osseo-Asare, *J. Colloid Interface Sci.* **1995**, *170*, 8; (b) F. J. Arriagada, K. Osseo-Asare, *J. Colloid Interface Sci.* **1999**, *211*, 210; (c) K. Osseo-Asare, F. J. Arriagada, *J. Colloid Interface Sci.* **1999**, *218*, 68.

51. (a) X. Zhao, R. P. Bagwe, W. Tan, *Adv. Mater.* **2004**, *16*, 173; (b) R. P. Bagwe, C. Yang, L. R. Hilliard, W. Tan, *Langmuir* **2004**, *20*, 8336.

when they are dissolved in a hydrocarbon solution, they create a macroscopically isotropic dispersion, but the orientation of the surfactant molecules is not random: spherical aggregates are formed, where the hydrophilic heads are aligned toward the center, while the hydrophobic tails extend into the bulk oil phase. If water is added to this system, it places itself at the center of these aggregates: these stabilized water droplets then act as small nanoreactors, where the hydrolysis and condensation of TEOS is confined (figure 2), yielding highly monodisperse, spherical particles with diameters ranging from 20 to 100 nm. The parameters that control the size and monodispersity of the resulting nanoparticles are the nature of the surfactant and the amount of water, because evidently these are the main factors that influence the dimensions and stability of the reverse micellar aggregates.

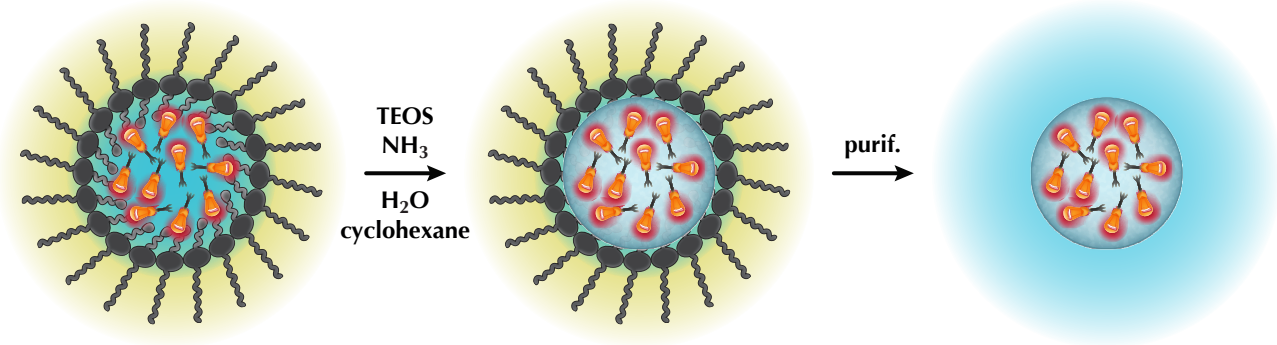

Figure 2 Schematic representation of the reverse microemulsion synthesis of tris(bipyridine)ruthenium(II) doped silica nanoparticles.

The reverse microemulsion synthesis may be preferred over Stöber method when the photoactive species is well soluble in water, so that it can be directly added during the growth of the nanoparticles, to be physically entrapped in the structure by means of non covalent interactions, with no need of derivatization.[50b] By including more than one type of dye, it is possible to prepare fluorescent nanoparticles with multiple emissions, suitable for multiplex bioanalysis.[52] Nevertheless, it is always recommended to modify the dyes with trialkoxysilane moieties, to allow their covalent binding to the silica matrix, and to avoid leaching over time.[53]

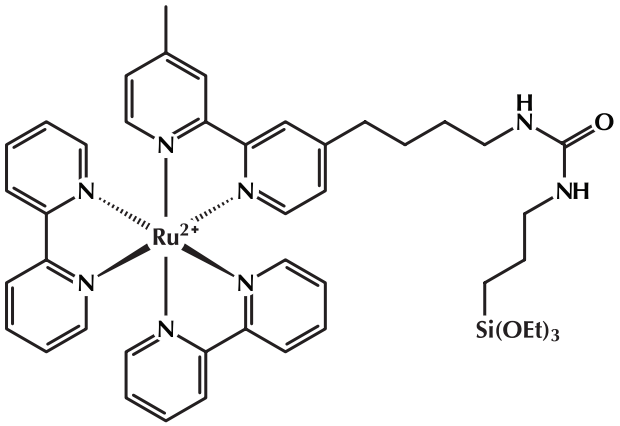

Scheme 6 Molecular structure of the triethoxysilane derivative of tris(bipyridine)ruthenium(II) used in reference 53.

Thanks to the versatility of the chemistry of silica, several functional groups can be easily introduced onto the nanoparticle surface, in order to exploit them in biotechnology applications, and to ensure the covalent conjugation with biomolecules – such as peptides, antibodies or

52. (a) L. Wang, C. Yang, W. Tan, *Nano. Lett.* **2005**, *5*, 37; (b) L. Wang, W. Tan, *Nano. Lett.* **2006**, *6*, 84.
53. S. Zanarini, E. Rampazzo, L. Della Ciana, M. Marcaccio, E. Marzocchi, M. Montalti, F. Paolucci, L. Prodi, *J. Am. Chem. Soc.* **2009**, *131*, 2260.

nucleic acids.[54] This functionalization can be achieved by performing an additional coating step (before purification procedures) by means of readily available silane reagents, such as N^1-(3-trimethoxysilylpropyl)diethylenetriamine[55] or APTES[56] itself for amino groups, (3-mercaptopropyl) trimethoxysilane for thiol groups,[57] or carboxyethyl silanetriol[56] for carboxylic acid groups.

2.4 Aqueous micellar system

2.4.1 ORMOSIL nanoparticles

As an alternative to the reverse microemulsion synthesis, the formation of silica nanoparticles can occur in direct micelles as well, using lipophilic trialkoxysilanes. In an aqueous solution spherical aggregates are formed as well, but the orientation of the surfactants is reversed, with respect to the previous case: the hydrophilic heads are in contact with the surrounding water molecules, while the hydrophobic tails associate together in the core, in order to avoid contact with the solvent. This method was first proposed by Maitra and co-workers,[58] condensing octyltriethoxysilane in Triton™ X-100 micelles, and later deeply investigated by Prasad and co-workers, with vinyltriethoxysilane (VTES) and AOT[59] or Tween® 80[60] as surfactant.

The resulting nanoparticles, usually referred as ORMOSIL (*or*ganic *mo*dified *sil*ica), show diameters ranging from 20 to 30 nm and some degree of mesoporosity. These systems too have been succesfully surface functionalized with the same reagents described before,[61] and employed in bioimaging applications, both *in vitro*[59a,60,62] and *in vivo*.[63]

Very recently, Mancin and co-workers further refined this methodology,[64] using VTES and Brij® 35, obtaining – in a one-pot procedure – highly PEGylated, NIR fluorescent, surface functionalized silica nanoparticles, with a tunable diameter from 5 to 100 nm.

---

54. (a) W. Tan, K. Wang, X. He, X. J. Zhao, T. Drake, L. Wang, R. P. Bagwe, *Med. Res. Rev.* **2004**, *24*, 621; (b) L. Wang, K. Wang, S. Santra, X. Zhao, L. R. Hilliard, J. E. Smith, Y. Wu, W. Tan, *Anal. Chem.* **2006**, *78*, 648; (c) G. Yao, L. Wang, Y. Wu, J. Smith, J. Xu, W. Zhao, E. Lee, W. Tan, *Anal. Bioanal. Chem.* **2006**, *385*, 518; (d) J. Yan, M. C. Estévez, J. E. Smith, K. Wang, X. He, L. Wang, W. Tan, *Nano Today* **2007**, *2*, 44.
55. (a) S. Santra, P. Zhang, K. Wang, R. Tapec, W. Tan, *Anal. Chem.* **2001**, *73*, 4988; (b) M. Qhobosheane, S. Santra, P. Zhang, W. Tan, *Analyst* **2001**, *126*, 1274.
56. (a) R. P. Bagwe, L. R. Hilliard, W. Tan, *Langmuir* **2006**, *22*, 4357; (b) L. Wang, C. Lofton, M. Popp, W. Tan, *Bioconj. Chem.* **2007**, *18*, 610.
57. L. R. Hilliard, X. Zhao, W. Tan, *Anal. Chim. Acta* **2002**, *470*, 51.
58. S. Das, T. K. Jain, A. Maitra, *J. Colloid Interface Sci.* **2002**, *252*, 82.
59. (a) I. Roy, T. Y. Ohulchanskyy, H. E. Pudavar, E. J. Bergey, A. R. Oseroff, J. Morgan, T. J. Dougherty, P. N. Prasad, *J. Am. Chem. Soc.* **2003**, *125*, 7860; (b) I. Roy, T. Y. Ohulchanskyy, D. J. Bharali, H. E. Pudavar, R. A. Mistretta, N. Kaur, P. N. Prasad, *Proc. Natl. Acad. Sci. USA* **2005**, *102*, 279; (c) S. Kim, H. E. Pudavar, P. N. Prasad, *Chem. Commun.* **2006**, 2071.
60. T. Y. Ohulchanskyy, I. Roy, L. N. Goswami, Y. Chen, E. J. Bergey, R. K. Pandey, A. R. Oseroff, P. N. Prasad, *Nano Lett.* **2007**, *7*, 2835.
61. R. Kumar, I. Roy, T. Y. Ohulchanskyy, L. N. Goswami, A. C. Bonoiu, E. J. Bergey, K. M. Tramposch, A. Maitra, P. N. Prasad, *ACS Nano* **2008**, *2*, 449.
62. (a) S. Kim, T. Y. Ohulchanskyy, H. E. Pudavar, R. K. Pandey, P. N. Prasad, *J. Am. Chem. Soc.* **2007**, *129*, 2669; (b) S. Kim, H. Huang, H. E. Pudavar, Y. Cui, P. N. Prasad, *Chem. Mater.* **2007**, *19*, 5650; (c) S. Kim, H. E. Pudavar, A. Bonoiu, P. N. Prasad, *Adv. Mater.* **2007**, *19*, 3791; (d) S. Kim, T. Y. Ohulchanskyy, A. Baev, P. N. Prasad, *J. Mater. Chem.* **2009**, *19*, 3181.
63. R. Kumar, I. Roy, T. Y. Ohulchanskyy, L. A. Vathy, E. J. Bergey, M. Sajjad, P. N. Prasad, *ACS Nano* **2010**, *4*, 699.
64. I. M. Rio-Echevarria, F. Selvestrel, D. Segat, G. Guarino, R. Tavano, V. Causin, E. Reddi, E. Papini, F. Mancin, *J. Mater. Chem.* **2010**, *20*, 2780.

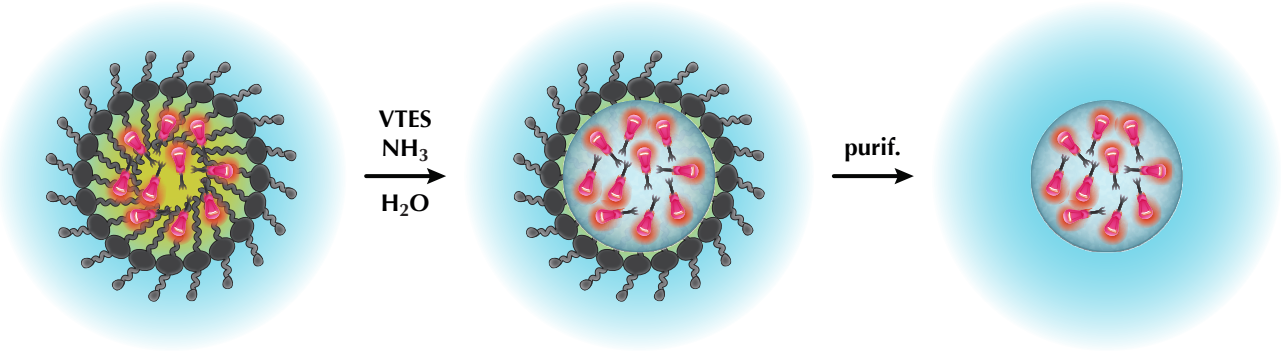

Figure 3 Schematic representation of the direct micelles synthesis of rhodamine doped silica nanoparticles.

2.4.2 Pluronic® F127 nanoparticles

The methods described so far require the removal of the surfactants at the end of the synthesis. However, it is known that nanostructures can be also obtained via intramicellar cross-linking between the polymeric chains that form the micelle.[65] In fact, these aggregates are dynamic in nature: their main drawback is that they collapse upon dilution, *i.e.*, below the CMC value. Thus, the cross-linking process provides stability for the nanosystem, by strengthening the weak intermolecular interactions that enable its self-assembly and existence. Depending on the chemical nature of the surfactant, there are different ways to cross-link the micellar core, such as photochemical irradiation – butadiene[66,67] or cinnamate;[68,69] radical polymerization – methacrylate[70] or maleate;[71] and carbodiimide coupling – poly(methacrylic acid).[72]

In this context, our research group has adapted a synthetic protocol proposed by Liu and co-workers for the development of nanoparticles suitable for drug delivery,[73] to obtain a versatile fluorescent functionalizable nanoarchitecture,[74] which can be advantageously employed in electrochemiluminescence applications,[75] reversible photoswitching experiments,[76] live cell

65. R. K. O'Reilly, C. J. Hawkerb, K. L. Wooley, *Chem. Soc. Rev.* **2006**, *35*, 1068.
66. (a) K. Procházka, M. K. Baloch, Z. Tuzar, *Makromol. Chem.* **1979**, *180*, 2521; (b) Z. Tuzar, B. Bednář, Č. Koňák, M. Kubín, Š. Svobodová, K. Procházka, *Makromol. Chem.* **1982**, *183*, 399.
67. D. J. Wilson, G. Riess, *Eur. Polym. J.* **1988**, *24*, 617.
68. (a) A. Guo, G. Liu, J. Tao, *Macromolecules* **1996**, *29*, 2487; (b) F. Henselwood, G. Liu, *Macromolecules* **1997**, *30*, 488; (c) J. Tao, G. Liu, J. Ding, M. Yang, *Macromolecules* **1997**, *30*, 4084; (d) G. Wang, F. Henselwood, G. Liu, *Langmuir* **1998**, *14*, 1554; (e) F. Henselwood, G. Liu, *Macromolecules* **1998**, *31*, 4213; (f) J. Zhou, Z. Li, G. Liu, *Macromolecules* **2002**, *35*, 3690; (g) G. Liu, J. Zhou, *Macromolecules* **2002**, *35*, 8167; (h) G. Liu, J. Zhou, *Macromolecules* **2003**, *36*, 5279.
69. M. Jamróz-Piegza, W. Wałach, A. Dworak, B. Trzebicka, *J. Colloid Interface Sci.* **2008**, *325*, 141.
70. M. Iijima, Y. Nagasaki, T. Okada, M. Kato, K. Kataoka, *Macromolecules* **1999**, *32*, 1140.
71. X. Shuai, T. Merdan, A. K. Schaper, F. Xi, T. Kissel, *Bioconj. Chem.* **2004**, *15*, 441.
72. T. K. Bronich, P. A. Keifer, L. S. Shlyakhtenko, A. V. Kabanov, *J. Am. Chem. Soc.* **2005**, *127*, 8236.
73. Q. Huo, J. Liu, L.-Q. Wang, Y. Jiang, T. N. Lambert, E. Fang, *J. Am. Chem. Soc.* **2006**, *128*, 6447.
74. (a) E. Rampazzo, S. Bonacchi, R. Juris, M. Montalti, D. Genovese, N. Zaccheroni, L. Prodi, D. C. Rambaldi, A. Zattoni, P. Reschiglian, *J. Phys. Chem. B* **2010**, *114*, 14605; (b) S. Bonacchi, D. Genovese, R. Juris, M. Montalti, L. Prodi, E. Rampazzo, N. Zaccheroni, *Angew. Chem. Int. Ed.* **2011**, *50*, 4056.
75. S. Zanarini, E. Rampazzo, S. Bonacchi, R. Juris, M. Marcaccio, M. Montalti, F. Paolucci, L. Prodi, *J. Am. Chem. Soc.* **2009**, *131*, 14208.
76. D. Genovese, M. Montalti, L. Prodi, E. Rampazzo, N. Zaccheroni, O. Tosic, K. Altenhöner, F. May, J. Mattay, *Chem. Commun.* **2011**, *47*, *10975*.

fluorescence imaging,[77] and *in vivo* imaging.[78] It has also been reported that this method can be effectively used for the coating of iron oxide nanoparticles.[79]

This synthetic strategy is based on the formation of direct micelles of Pluronic® F127 in water. Pluronic® block copolymers are a family of non-ionic triblock surfactants, presenting a poly(ethylene glycol)$_x$-poly(propylene oxide)$_y$-poly(ethylene glycol)$_x$ structure (PEG$_x$-PPO$_y$-PEG$_x$), terminating in primary hydroxyl groups;[80] in particular, Pluronic® F127 has an average molecular weight of about 12 600 – where x = 100, and y = 65 (scheme 6). The core of Pluronic® F127 micelles is made up of the hydrophobic PPO portion of the copolymer, while the shell is formed by the PEG chains extending into water.[81]

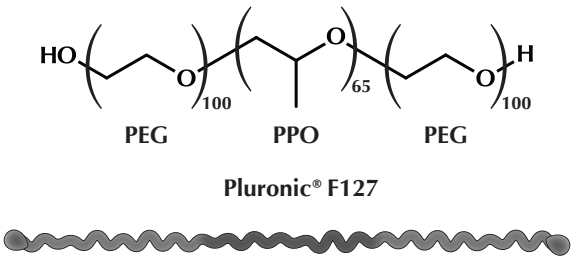

Scheme 6 Molecular structure of Pluronic® F127.

TEOS is a rather apolar species, therefore it is reasonable to argue that, when added to a micelle solution, it would spontaneously diffuse and accumulate inside the hydrophobic PPO core, where the hydrolysis and condensation reactions are bound to occur, leading to the formation of the silica nanoparticle (figure 4). Moreover, the surfactant molecules remain trapped in the silica matrix: the micellar structure is blocked and do not collapse upon dilution.

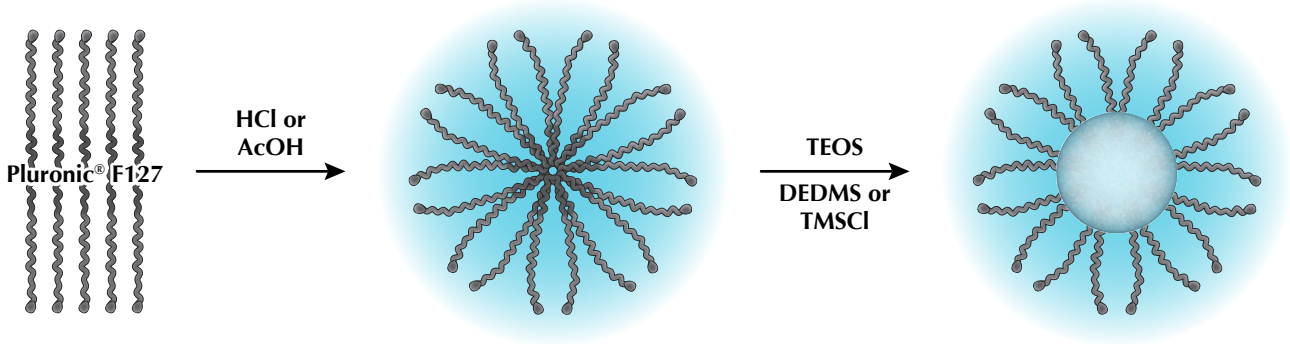

Figure 4 Schematic representation of the Pluronic® F127 mediated synthesis of silica nanoparticles.

This process operates only under acid catalysis: it is likely that, since the reaction is confined in the core of the micelle, the chains and branches – whose formation is favored in these conditions

77. See chapter 5, adapted from: E Rampazzo, S. Bonacchi, D. Genovese, R. Juris, M. Sgarzi, M. Montalti, L. Prodi, N. Zaccheroni, G. Tomaselli, S. Gentile, C. Satriano, E. Rizzarelli, *Chem. Eur. J.* **2011**, *17*, 13429.
78. See chapter 6, adapted from: E. Rampazzo, F. Boschi, S. Bonacchi, R. Juris, M. Montalti, N. Zaccheroni, L. Prodi, L. Calderan, B. Rossi, S. Becchi, A. Sbarbati, *Nanoscale* **2012**, *4*, 824.
79. Z. Liu, J. Ding, J. Xue, *New. J. Chem.* **2009**, *33*, 88.
80. A. V. Kabanov, E. V. Batrakova, V. Yu. Alakhov, *J. Control. Release* **2002**, *82*, 189.
81. There is much confusion in the literature regarding the parameters characterizing this system: for example, CMC values are reported ranging from $2.8 \cdot 10^{-6}$ M (M. Yu. Kozlov, N. S. Melik-Nubarov, E. V. Batrakova, A. V. Kabanov, *Macromolecules* **2000**, *33*, 3305) to $5.5 \cdot 10^{-4}$ M (P. Alexandridis, J. F. Holzwarth, T. A. Hatton, *Macromolecules* **1994**, *27*, 2414) – depending on the temperature, concentration, technique employed and even manufacturer's batch number. It is not in the scope of this thesis to organize and clarify such a large amount of conflicting data.

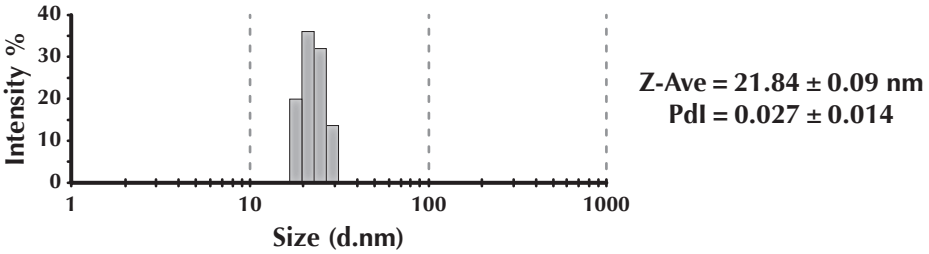

Figure 5 Dynamic light scattering diameter distribution of silica-core/PEG-shell nanoparticles. A detailed description of the synthesis is provided in chapter 8 – Experimental section. This sample was prepared in HCl with TMSCl as terminating agent.

– eventually cross-link together in this restricted region, forced into a spheroidal shape, and at the same time secure the surfactant molecules in a fixed position.

Nevertheless, the condensation of TEOS must be controlled and stopped at some point, to avoid the inclusion in the matrix of the PEG chains as well and, in the end, to prevent aggregation through intermicellar polymerization. This can be achieved by adding to the reaction mixture, with careful timing, a suitable terminating agent, such as diethoxydimethylsilane (DEDMS) or trimethylsilyl chloride (TMSCl), that bears alkyl substituents on the silicon atom, which are unable to hydrolyze and condense.

The morphology of the nanoparticles has been analyzed by dynamic light scattering (DLS) and transmission electron microscopy (TEM). DLS measurements provide a hydrodynamic diameter of about 22 nm (figure 5), in accordance with experiments performed with Pluronic® F127 micelles solutions.[82]

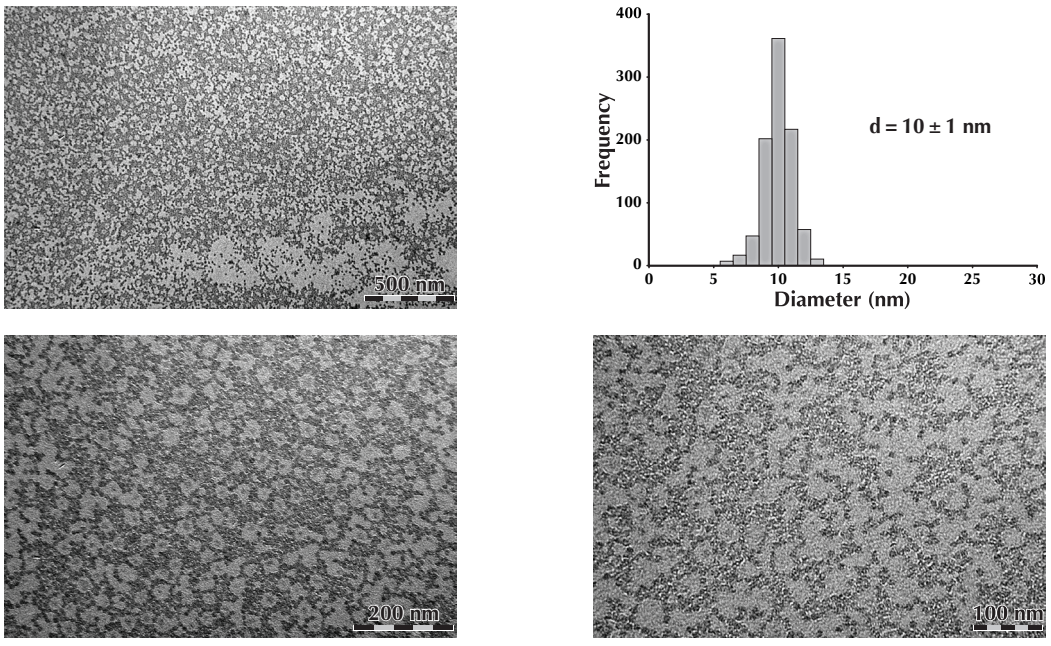

Figure 6 TEM images of silica-core/PEG-shell nanoparticles.

TEM images (figure 6) on the same sample show very uniform round particles, with a diameter of 10 nm. This value is smaller than the one obtained with DLS: this is due to the fact that by means of TEM it is possible to observe only the silica core of the nanoparticles, because the Pluronic® chains are too soft and do not give enough contrast to be detected. This is a clear evidence that this systems presents a core/shell type architecture, with a nucleus of silica and the flexible PEG segments of Pluronic® extending in water.

82. P. R. Desai, N. J. Jain, R. K. Sharma, P. Bahadur, *Colloids Surf. A* **2001**, *178*, 57.

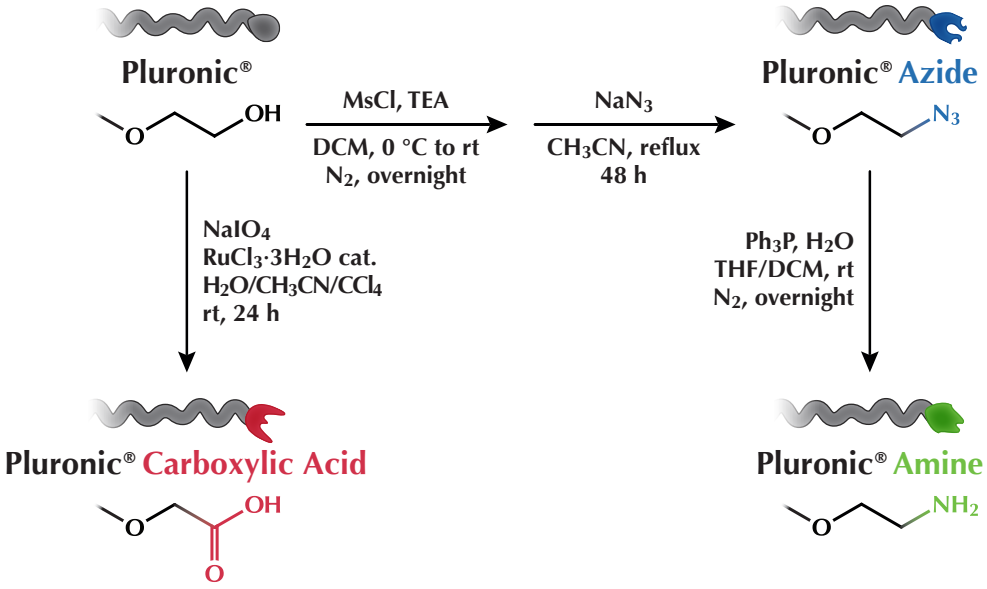

Scheme 7 Chemical modifications of Pluronic® F127.

The PEG chains play an important role, preventing the particle agglomeration and granting to the system an excellent water solubility and stability over time: no precipitate or flocculation could be detected – even after years (!) – with no loss in monodispersity. Moreover, this PEG coating is an appealing feature looking toward *in vitro* and *in vivo* bioanalytical applications, because it may act as a stealth layer. In fact, nanoparticles, when injected in the blood stream, are rapidly captured by macrophages of the reticuloendothelial system (RES) and in consequence cleared from circulation,[83,84] or worse, they may accumulate in tissue.[39] To avoid RES uptake, and to extend the blood circulation times,[85,86] PEG surface passivation is a widely employed strategy.[87,88]

Surface functionalization of these nanoparticles is possible by modifying the hydroxyl ends of Pluronic® F127. Carboxylic acid, azide and amino terminated surfactants have been successfully synthesized[89] (scheme 7). Micelles formed by mixing commercial Pluronic® F127 with the modified surfactant exhibit on the outside shell the functional groups; the following hydrolysis

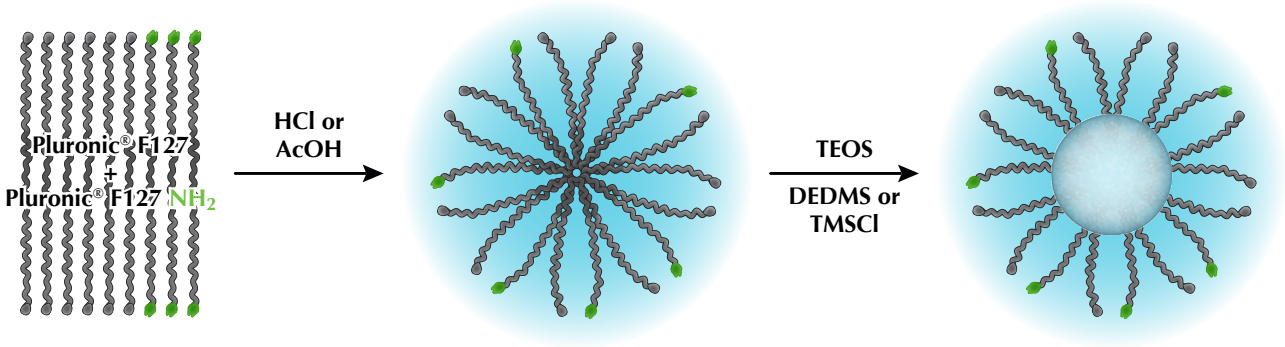

Figure 7 Schematic representation of the Pluronic® F127 mediated synthesis of silica nanoparticles.

83. S. Greenberg, *Trends Cell Biol.* **1995**, 5, 93.
84. M. A. Dobrovolskaia, P. Aggarwal, J. B. Hall, S. E. McNeil, *Mol. Pharmaceutics* **2008**, 5, 487.
85. S. M. Moghimi, A. C. Hunter, J. C. Murray, *Pharmacol. Rev.* **2001**, 53, 283.
86. M. M. van Schooneveld, E. Vucic, R. Koole, Y. Zhou, J. Stocks, D. P. Cormode, C. Y. Tang, R. E. Gordon, K. Nicolay, A. Meijerink, Z. A. Fayad, W. J. M. Mulder, *Nano Lett.* **2008**, *8*, 2517.
87. K. Knop, R. Hoogenboom, D. Fischer, U. S. Schubert, *Angew. Chem. Int. Ed.* **2010**, *49*, 6288.
88. X. He, H. Nie, K. Wang, W. Tan, X. Wu, P. Zhang, *Anal. Chem.* **2008**, *80*, 9597.
89. A detailed description of the synthesis and characterization of modified Pluronic® F127 is provided in chapter 8 – Experimental section.

and condensation of TEOS yield surface functionalized silica nanoparticles in a one-pot procedure (figure 7).

Table 1 reports DLS measurements of nanoparticles synthesized with increasing amount of Pluronic® F127 amine.[90] Results show that the modified surfactant does not perturb significantly the micellar equilibrium; the same behavior has been observed with azide or carboxylic acid functionalization (data not shown).

Table 1 Morphological properties of amino functionalized nanoparticles.

Modified surfactant (%)	Z-AVE[a]	PdI[b]
5	21.49 ± 0.10	0.055 ± 0.006
10	22.14 ± 0.18	0.017 ± 0.010
17.5	22.96 ± 0.14	0.036 ± 0.013
25	23.92 ± 0.04	0.022 ± 0.005

[a] diameter of nanoparticles, nm; [b] polydispersity index.

2.5 Conclusions

In the preparation of silica nanoparticles, a careful control of the reaction medium is absolutely necessary to obtain smaller and extremely monodisperse systems. Pluronic® F127 micelles mediated synthesis proved to be a reliable and highly reproducible method for the formation of silica-core/PEG-shell nanoparticles. Chemical modifications of the surfactant allow the introduction of functional groups on the surface of these systems in a one-pot procedure, with the view of employing them as bioanalytical tools. In the next chapter, we will describe the techniques that enable the doping of these nanoparticles with fluorescent molecules.

90. These sample were prepared in AcOH with TMSCl as terminating agent.

Chapter 3
Fluorescent nanoparticles

3.1 Early attempts

In the previous chapter, we described the synthesis of highly monodisperse, water soluble, silica-core/PEG-shell nanoparticles. In this chapter we are going to explain how it is possible to make those particles luminescent, by inserting fluorescent molecules in their core. We will be referring often to the dye doping percentage (δδ%), that represents the moles of fluorophore employed in the synthesis of nanoparticles with respect to the moles of TEOS.

All the syntheses of the molecules – as well as of the nanoparticles – discussed within this chapter will be described in detail in chapter 8 – Experimental section.

3.1.1 Spontaneous entrapment

There are two viable ways to place luminescent dyes inside silica nanoparticles. The first method is by spontaneous entrapment: if a certain molecule is highly hydrophobic, it is probable that, once dissolved in the micelle solution, it would locate itself in the core, because it possess a more lipophilic character (figure 1); all the dyes that have not been included will be removed during the purification step. With this procedure, commercial fluorophores may be used as they are, without the need of any further synthetic functionalization.

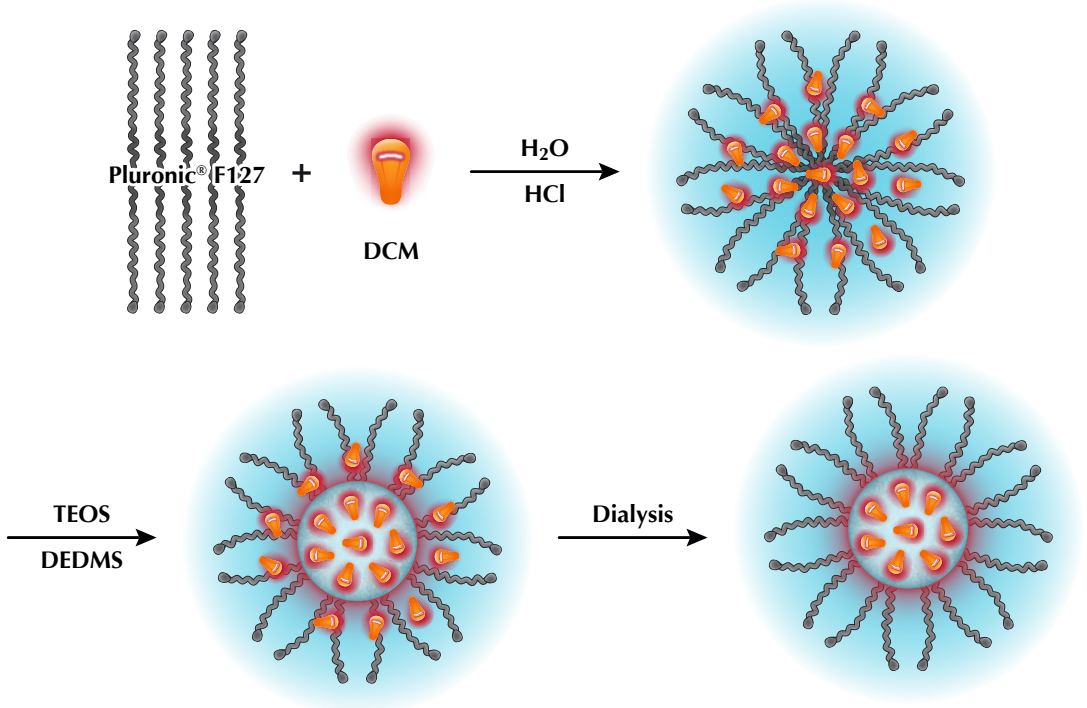

Figure 1 Schematic representation of the process of doping nanoparticles by spontaneous entrapment with **DCM** (see below).

A representative example is given by the commercial fluorophore 4-(dicyanomethylene)-2-methyl-6-(4-dimethylaminostyryl)-4H-pyran (abbreviated as **DCM** – see scheme 1), which is completely insoluble in water.

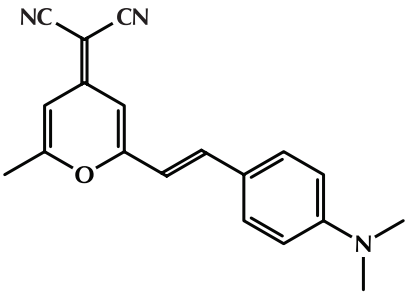

DCM

Scheme 1 Molecular structure of **DCM**.

The photochemical properties of nanoparticles doped with **DCM** ($\delta\delta\% = 0.075$) have been compared with the free molecule in ethanol solution (figure 2).

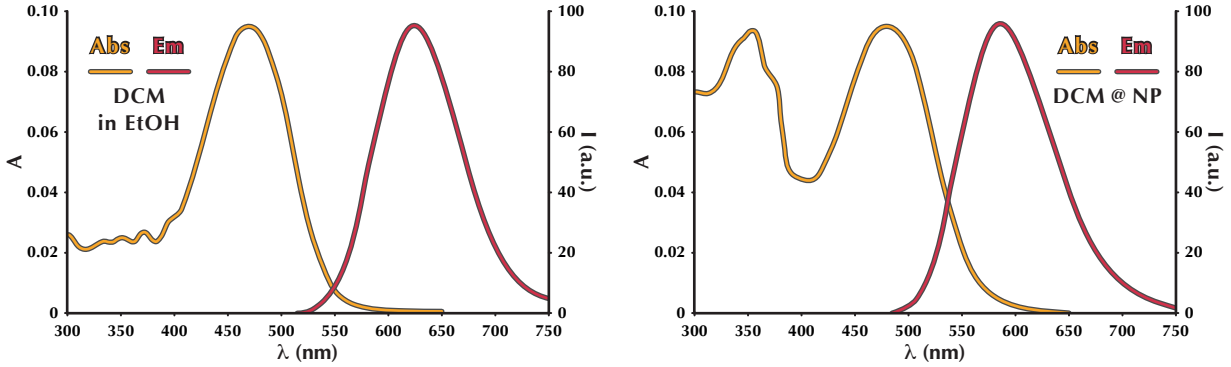

Figure 2 Absorption and emission spectra of **DCM** in ethanol solution (left) or encapsulated within nanoparticles (right).

The shape of the emission band is the same for both samples, but the introduction inside the silica matrix leads to a blue shift of the maximum (580 nm versus 620 nm in ethanol solution). On the contrary the absorption band is centered around 470 nm in both cases, but in the nanoparticles sample a new band at 355 nm rises, due to the protonation of the dimethylamino moiety of **DCM** (scheme 2): in fact, the synthesis of these systems is carried out under strong acidic conditions.

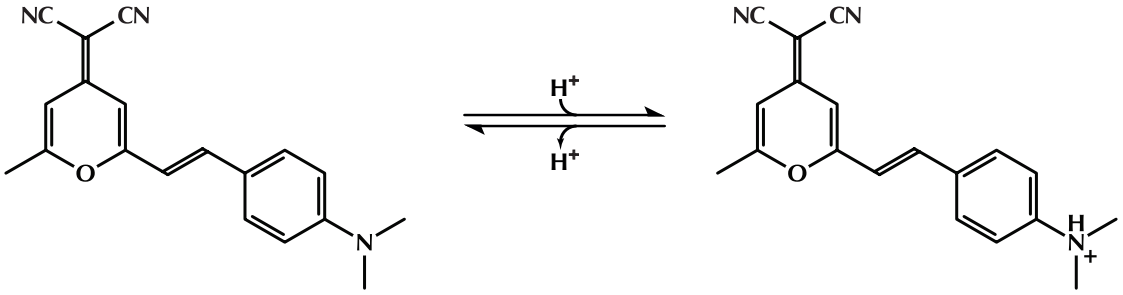

Scheme 2 Acid-base equilibrium of **DCM**.

Unfortunately, the protonated form of **DCM** is not luminescent; however, this is evidence of the fact that there is a region inside the core of the nanoparticle which is completely secluded from the outside environment: the proton cannot be exchanged even after extensive dialysis. As a consequence, it is safe to say that the molecule is efficiently entrapped in the silica matrix.

From a morphological point of view, dynamic light scattering revealed no significant anomalies (figure 3).

To sum up, with this method, it is possible to transfer in water a highly insoluble molecule, while retaining its fluorescent properties (at least partially). Since the majority of fluorophores are hydrophobic in nature, this technique could be in principle employed to synthesize a wide range of differently colored nanoparticles. Unfortunately, after several experiments, this method

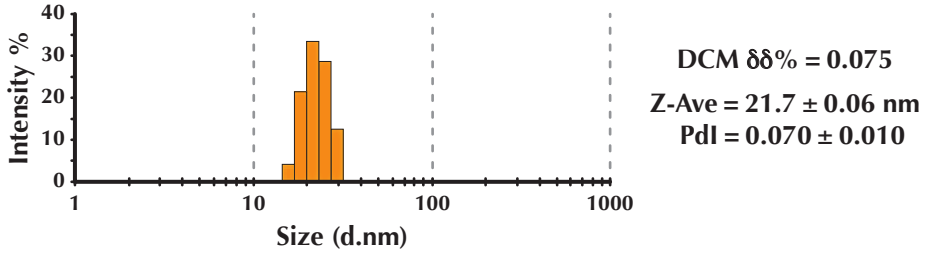

Figure 3 Dynamic light scattering diameter distribution of nanoparticles doped with **DCM**.

we found has revealed itself not particularly reliable, based on a mere trial-and-error behavior, without any evident relation between structure and effective dye inclusion. Furthermore, no high doping levels can be reached and a certain degree of fluorophore leaching was observed over time (typically after months), probably due to molecules located on the more external part of the silica network.

3.1.2 Triethoxysilane derivatization

In order to avoid these limitations, it is essential to permanently attach in some way the dye to the core of the nanoparticle. Following van Blaaderen's idea,[1] this can be achieved by chemically modifying the fluorophores, in particular by introducing a triethoxysilane moiety on the molecular framework, able to hydrolyze and co-condense along with TEOS during the formation of the particle, resulting in a covalent linkage to the silica matrix (figure 4).

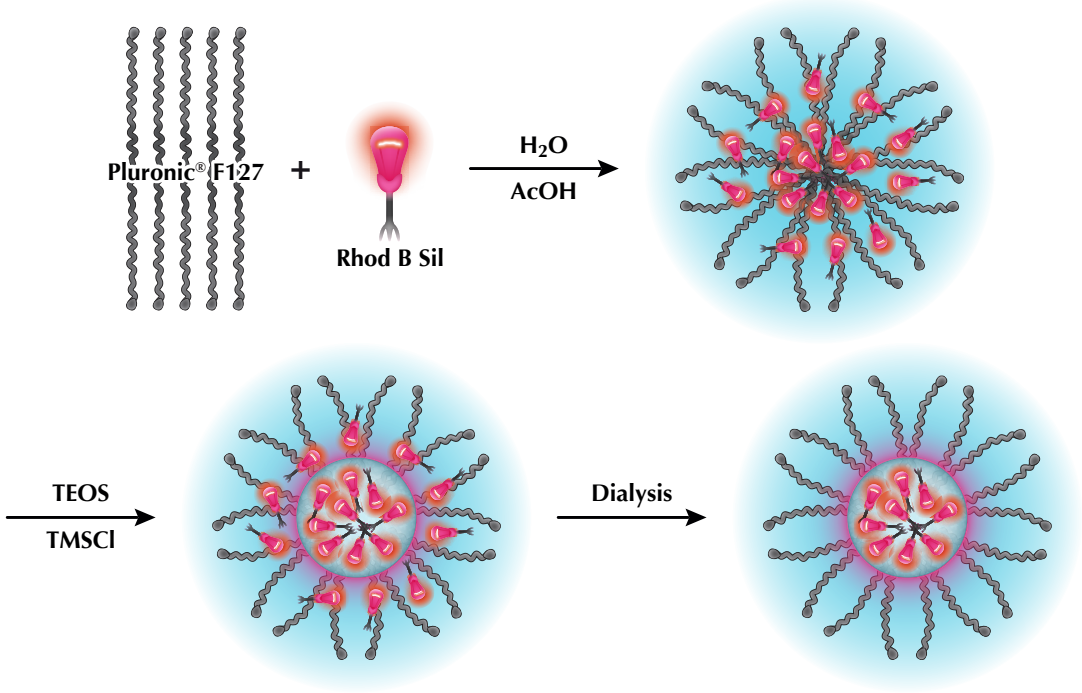

Figure 4 Schematic representation of the process of nanoparticles doping with a triethoxysilane derivatized molecule, in particular **Rhod B Sil** (see below).

Besides, this synthetic functionalization must be performed on molecules that are to some extent water soluble, because they will not spontaneously place themselves in the hydrophobic region of the micelle. For example, rhodamine B – a well known xanthene dye,[2] extensively employed in biotechnology applications – has been derivatized, obtaining **Rhod B Sil** (scheme 3).

1. (a) A. van Blaaderen, A. Imhof, W. Hage, A. Vrij, *Langmuir* **1992**, *8*, 1514; (b) N. A. M. Verhaegh, A. van Blaaderen, *Langmuir* **1994**, *10*, 1427.
2. See notes 81-84 of chapter 1.

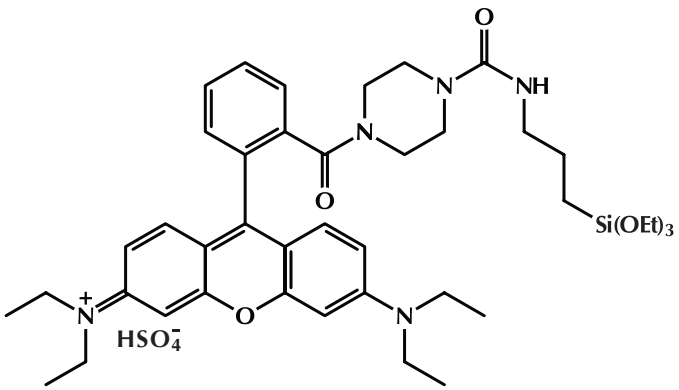

Rhod B Sil

Scheme 3 Molecular structure of **Rhod B Sil**.

As in the previous case, the photochemical properties of nanoparticles doped with **Rhod B Sil** ($\delta\delta\% = 0.1$) have been compared with rhodamine B in ethanol solution (figure 5).

Free rhodamine B in ethanol displays an absorption maximum around 575 nm and an emission peak at 590 nm. No significant differences are detectable in the nanoparticles sample, only a small hypsochromic shift of both bands. Morphological characterization shows typical size and monodispersity (figure 6).

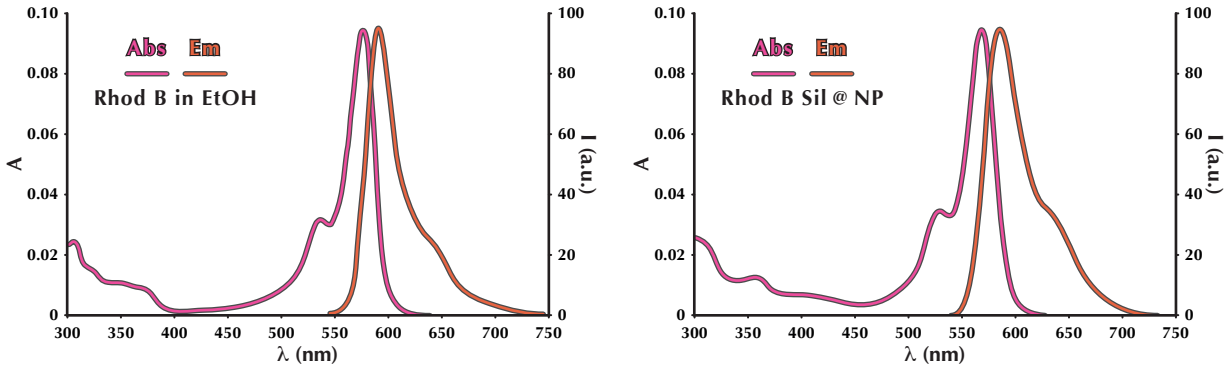

Figure 5 Absorption and emission spectra of rhodamine B in ethanol solution (left) and **Rhod B Sil** encapsulated within nanoparticles (right).

Although this method requires a much higher synthetic effort, triethoxysilane derivatization is considerably superior with respect to spontaneous entrapment, because it ensures the covalent inclusion of the molecules (no dye leaching even after years!) and allows to reach easily higher levels of doping.

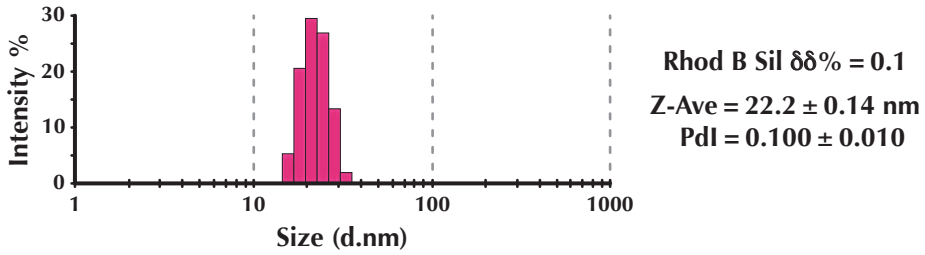

Figure 6 Dynamic light scattering diameter distribution of nanoparticles doped with **Rhod B Sil**.

3.2 Triethoxysilane functionalized dyes – A systematic approach

Having established the need for triethoxysilane functionalization, it is important not only to evaluate the changes in photophysical properties upon increasing δδ%, but also to broaden the library of fluorophores, in order to cover the whole visible spectral range. For this reason, a small group of dyes have been synthesized and derivatized with a triethoxysilane moiety; then, several nanoparticles samples have been prepared, varying the type of fluorophore and the degree of doping (usually 0.1%, 0.2% and 0.4%, except for the first case). In the next section, absorption and emission spectra of all the nanosystem created will be presented in increasing order of wavelength and their photochemical parameters will be discussed and compared.

3.2.1 DEAC Sil

The first nanoparticles that will be described are doped with **DEAC Sil** (scheme 4), which comes from the functionalization of the commercial fluorophore 7-(diethylamino)coumarin-3-carboxylic acid.

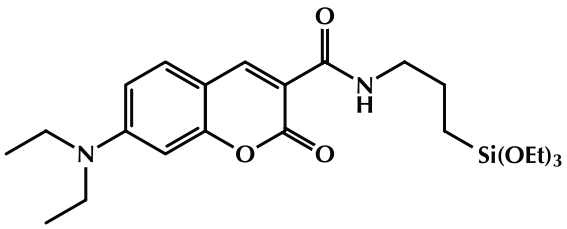

DEAC Sil

Scheme 4 Molecular structure of **DEAC Sil**.

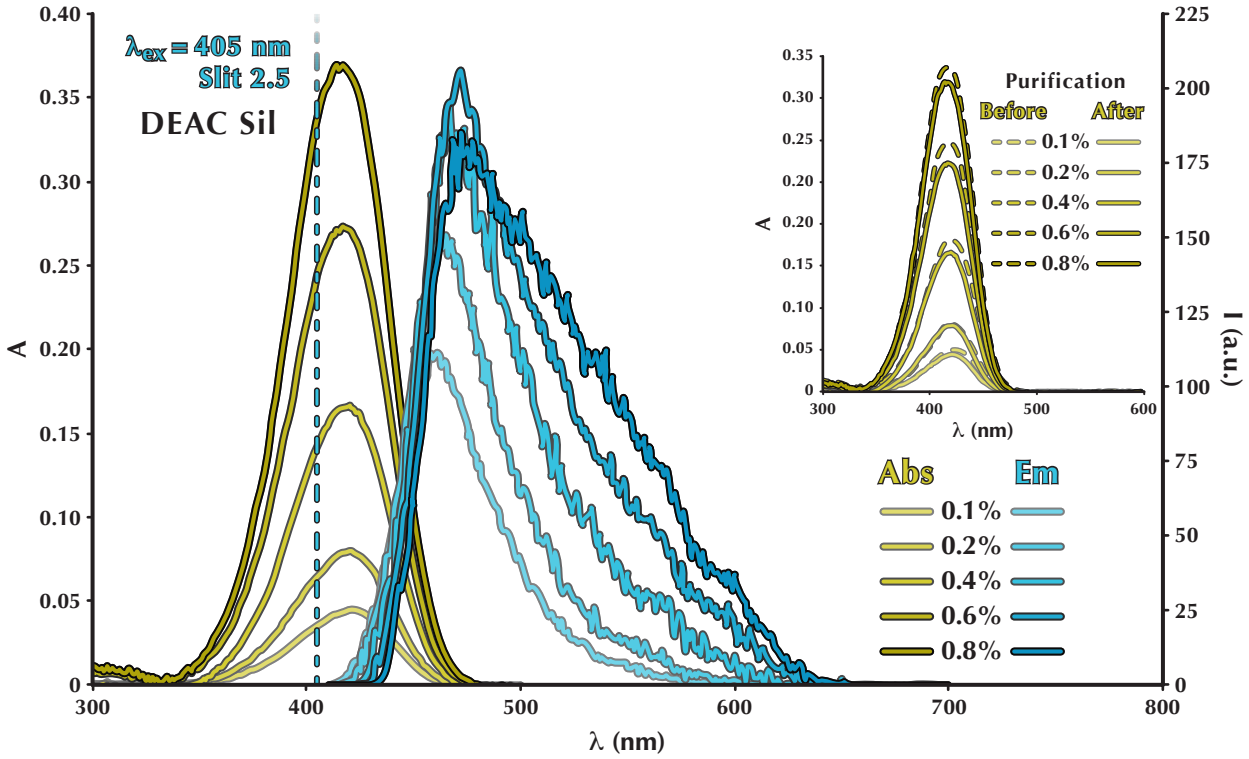

Figure 7 Absorption (yellow-green) and emission (light blue) spectra of **DEAC Sil** doped nanoparticles. Inset shows the absorption spectra before (dashed) and after (solid) dialysis/filtration treatment.

Table 1 Spectroscopic and morphological properties of **DEAC Sil** doped nanoparticles.

Dye	δδ%	mg	ε/fluo[a]	ε/NP[a]	λ abs[b]	λ em[b]	S S[c]	Φ[d]	Z-Ave[e]	PdI[f]
DEAC Sil	**0.1**	0.37	29500	200000	420	461	41	0.66	20.98 ± 0.07	0.090 ± 0.009
	0.2	0.74	23500	355000	421	462	41	0.51	21.57 ± 0.14	0.071 ± 0.012
	0.4	1.49	26300	741000	420	462	47	0.33	21.45 ± 0.19	0.12 ± 0.03
	0.6	2.23	29100	1228000	417	472	55	0.25	21.90 ± 0.08	0.086 ± 0.010
	0.8	2.97	28400	1650000	417	472	58	0.19	22.06 ± 0.09	0.089 ± 0.008

[a] $M^{-1} \cdot cm^{-1}$; [b] nm; [c] Stokes shift, nm; [d] quinine sulfate in H_2SO_4 0.05 M (Φ = 0.53) was used as reference; [e] diameter of nanoparticles, nm; [f] polydispersity index.

Since the difference between the spectra recorded before and after purification of the nanoparticles – that is, right after the synthesis and after the dialysis/filtration processes, respectively – is practically negligible, as one can note in the inset of figure 7, it can be definitely stated that the dye is quantitatively included inside the core of the nanosystem as expected.

DEAC Sil doped nanoparticles show an absorption maximum around 420 nm. The molar absorption coefficient of the nanosystem increases linearly with increasing δδ% and the shape of the band remains unchanged – clear evidence of the fact that there is no interaction between the fluorophores in the ground state. On the contrary, the maximum of the emission band varies between 461 and 472 nm: in fact, as the doping level gets higher, a new band grows at longer wavelengths. Because no dimers or aggregates are detected in the absorption spectra, this new emission band can be attributed to an excimer[3] (a short-lived dimeric species, which originates from the relaxation of **DEAC Sil** excited state). These excimers appear to be less emissive, as the dramatic drop of the quantum yield indicates: this fact leads to the quenching of the overall emission.

The δδ% only slightly affects the morphological properties of the nanoparticles: the mean diameter keeps in the range of 21-22 nm, while the polydispersity index is always excellent.

3.2.2 Bodipy – TM Sil series

Three different types of tetramethyl (**TM**) Bodipy were prepared, by varying the length of the alkyl chain bearing the triethoxysilane group at the 8-position of the indacene ring – namely ethyl, propyl, and butyl (scheme 5).

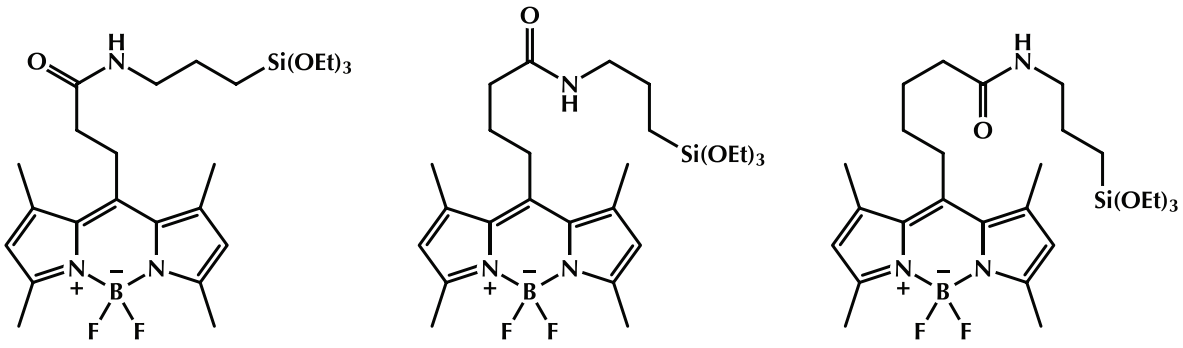

Scheme 5 Molecular structures of triethoxysilane dyes, belonging to the **TM Sil** series of Bodipy.

3. J. B. Birks, *Rep. Prog. Phys.* **1975**, *38*, 903.

The absorption spectra in figure 8 show a maximum around 500 nm – only slightly blue shifted by the lengthening of the alkyl chain – assigned to the S_0-S_1 (0-0) transition of the BODIPY core; the shoulder is considered to be corresponding to the 0-1 vibrational band of the same transition.[4-6]

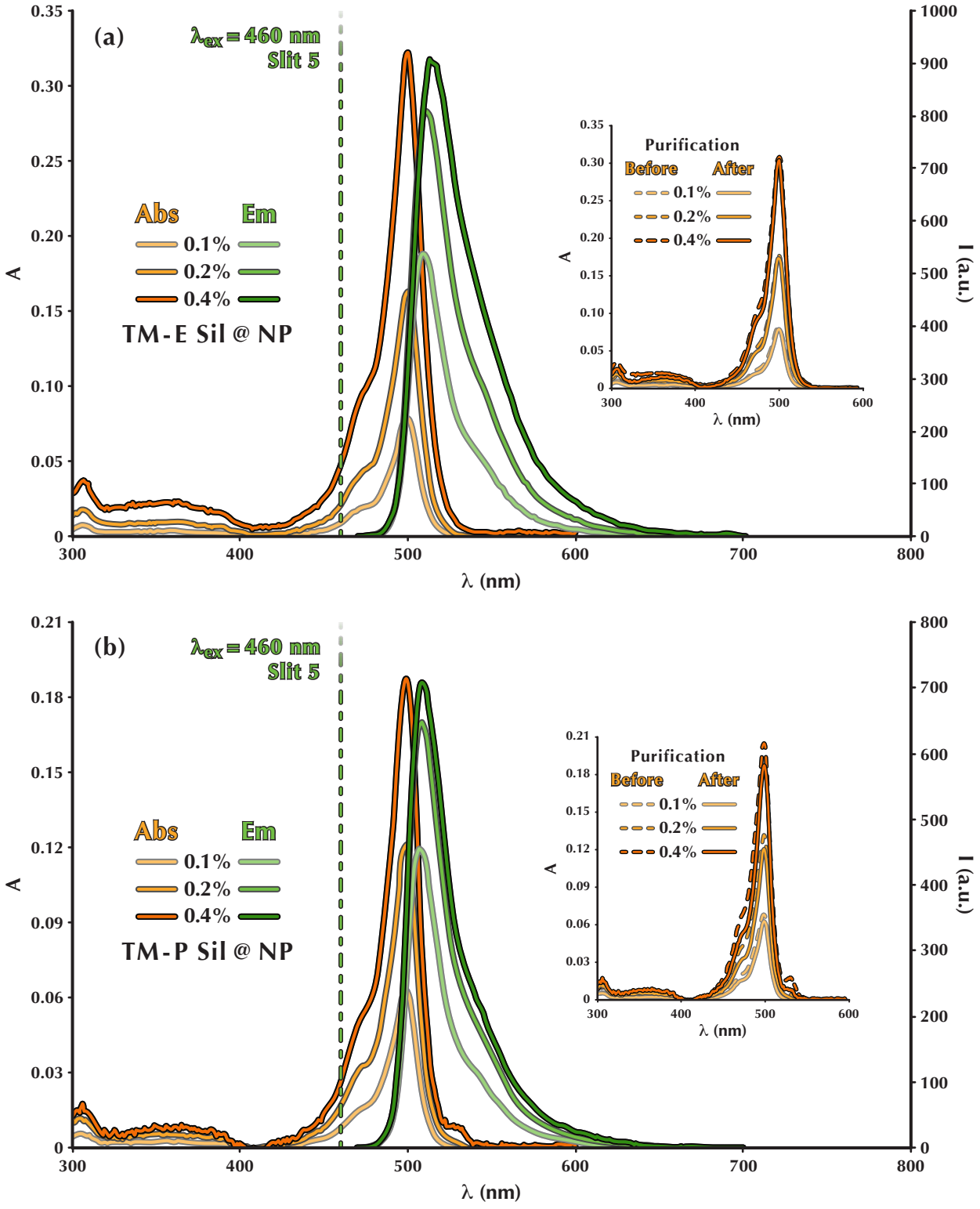

4. J. Karolin, L. B.-A. Johansson, L. Strandberg, T. Ny, *J. Am. Chem. Soc.* **1994**, *116*, 7801.
5. M. Kollmannsberger, K. Rurack, U. Resch-Genger, J. Daub, *J. Phys. Chem. A* **1998**, *102*, 10211.
6. (a) W. Qin, M. Baruah, M. Van der Auweraer, F. C. De Schryver, N. Boens, *J. Phys. Chem. A* **2005**, *109*, 7371; (b) W. Qin, T. Rohand, W. Dehaen, J. N. Clifford, K. Driesen, D. Beljonne, B. Van Averbeke, M. Van der Auweraer, N. Boens, *J. Phys. Chem. A* **2007**, *111*, 8588.

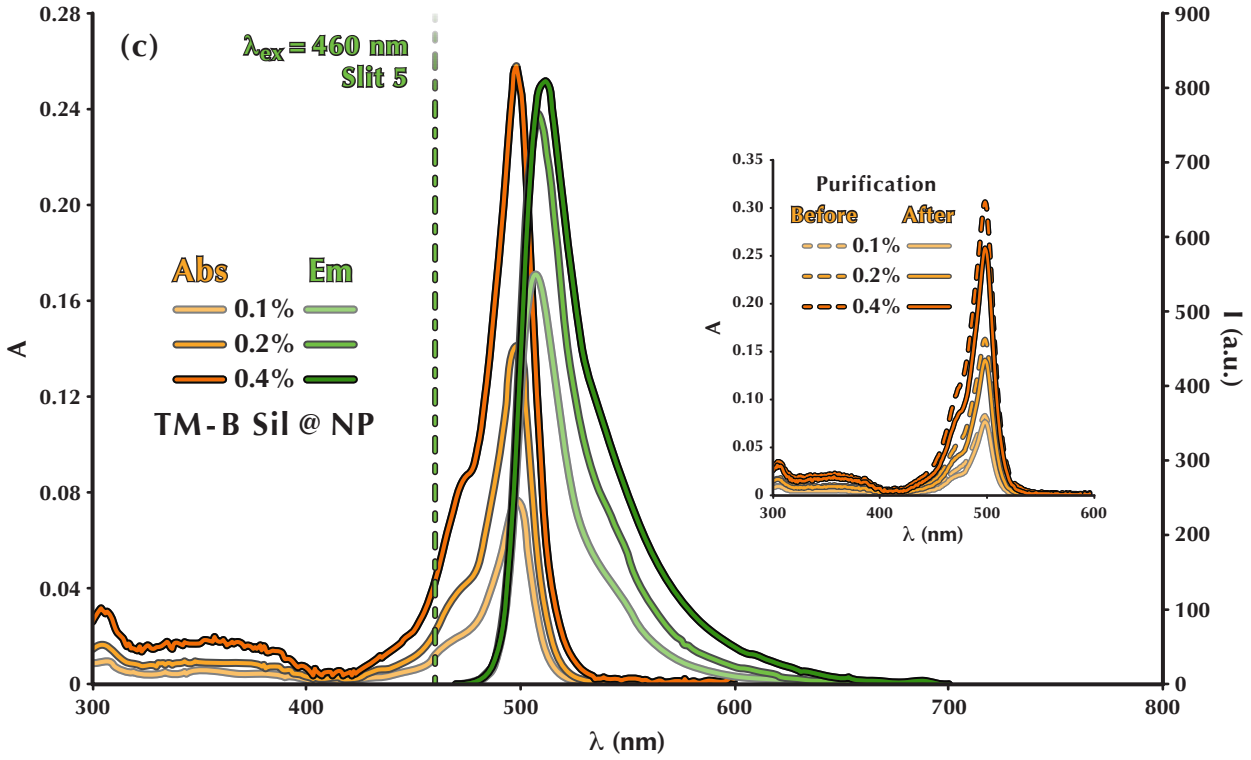

Figure 8 Absorption (orange) and emission (green) spectra of (a) **TM-E Sil**, (b) **TM-P Sil**, and (c) **TM-B Sil** doped nanoparticles. Insets show the absorption spectra before (dashed) and after (solid) dialysis/filtration treatment.

The emission peak is narrow; its maximum is located around 510 nm. With respect to **DEAC Sil**, BODIPY dyes exhibit higher quantum yields (the 0.1% sample almost reaches unity), sharper peaks, but smaller Stokes shifts.

Other spectroscopic features seems to follow the trend shown before: there is a linear correspondence between the nanoparticles molar absorption coefficient and the δδ%, while the emission maximum intensities deviate from this linearity, due to self-quenching processes, which partially compete with the radiative relaxation pathway.

Table 2 Spectroscopic and morphological properties of **TM Sil** doped nanoparticles.

Dye	δδ%	mg	ε/fluo[a]	ε/NP[a]	λ abs[b]	λ em[b]	S S[c]	Φ[d]	Z-Ave[e]	PdI[f]
TM-E Sil	**0.1**	0.42	48200	358000	500	509	9	0.93	20.86 ± 0.17	0.121 ± 0.012
	0.2	0.84	51900	780000	500	511	11	0.71	22.23 ± 0.09	0.100 ± 0.007
	0.4	1.68	45600	1358000	500	513	13	0.43	22.77 ± 0.19	0.099 ± 0.011
TM-P Sil	**0.1**	0.43	39700	281000	499	507	8	0.93	20.91 ± 0.18	0.045± 0.005
	0.2	0. 86	38500	540000	499	508	9	0.70	23.06 ± 0.09	0.009 ± 0.007
	0.4	1.72	27600	837000	499	509	10	0.49	25.1 ± 0.2	0.195 ± 0.005
TM-B Sil	**0.1**	0.44	48600	346000	498	507	9	0.95	19.50 ± 0.08	0.064 ± 0.004
	0.2	0.88	47400	631000	498	508	10	0.75	20.20 ± 0.07	0.062 ± 0.009
	0.4	1.77	44200	1152000	498	512	15	0.48	21.53 ± 0.09	0.124 ± 0.007

[a] $M^{-1} \cdot cm^{-1}$; [b] nm; [c] Stokes shift, nm; [d] Rhodamine 6G in ethanol (Φ = 0.94) was used as standard for nanoparticles at 0.1% δδ, which were used in turn as reference for the others; [e] diameter of nanoparticles, nm; [f] polydispersity index.

Morphological properties of nanoparticles doped with **TM Sil** are similar to those doped with **DEAC Sil**, with the exception of **TM-P Sil** at the higher doping level: in the inset of figure 8b, an extra band can be observed, reasonably due to the formation of J-aggregates,[7] which disrupt to some extent the micellar self-organization during the synthesis, and prevent the fluorophore to co-condense correctly in the appropriate position (as a matter of fact, the ε value of the highest doped sample is substantially lower).

3.2.3 BODIPY – DE Sil series

Similarly as for the **TM** series, three different types of tetramethyl-diethyl (**DE**) BODIPY were synthesized, modifying the length of the alkyl chain at the 8 position (scheme 6).

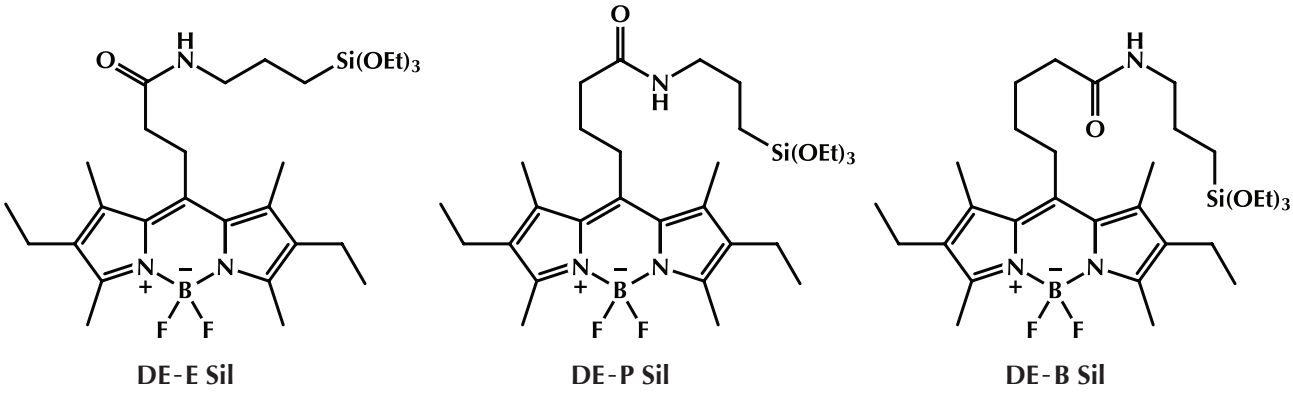

DE-E Sil **DE-P Sil** **DE-B Sil**

Scheme 6 Molecular structures of triethoxysilane dyes, belonging to the **DE Sil** series of BODIPY.

Apart from a red shift of both the absorption and the emission spectra of about 25 nm with respect of **TM Sil** doped nanoparticles, resulting from the extra ethyl chains at the 2- and 6-position of the indacene ring, the **DE Sil** series shares the same spectroscopic behavior described before. From a morphological point of view, it is **DE-B Sil** that forms J-aggregates at the higher doping level.

Table 3 Spectroscopic and morphological properties of **DE Sil** doped nanoparticles.

Dye	δδ%	mg	ε/fluo[a]	ε/NP[a]	λ abs[b]	λ em[b]	S S[c]	Φ[d]	Z-AVE[e]	PdI[f]
DE-E Sil	**0.1**	0.46	50700	381000	523	535	12	0.80	20.40 ± 0.12	0.038 ± 0.014
	0.2	0.93	47700	705000	523	538	15	0.67	22.09 ± 0.12	0.042 ± 0.012
	0.4	1.86	47500	1385000	523	539	16	0.43	22.73 ± 0.13	0.066 ± 0.008
DE-P Sil	**0.1**	0.48	45300	343000	522	534	12	0.85	21.83 ± 0.06	0.058 ± 0.007
	0.2	0.95	44700	660000	523	535	13	0.74	22.13 ± 0.14	0.082 ± 0.009
	0.4	1.90	43800	1224000	523	537	14	0.47	22.99 ± 0.04	0.13 ± 0.02
DE-B Sil	**0.1**	0.49	49400	368000	521	533	11	0.91	19.52 ± 0.08	0.047 ± 0.008
	0.2	0.97	49900	714000	522	534	12	0.72	19.78 ± 0.02	0.066 ± 0.017
	0.4	1.95	32900	962000	521	534	13	0.74	22.19 ± 0.14	0.055 ± 0.007

[a] $M^{-1} \cdot cm^{-1}$; [b] nm; [c] Stokes shift, nm; [d] Rhodamine 6G in ethanol (Φ = 0.94) was used as standard for nanoparticles at 0.1% δδ, which were used in turn as reference for the others; [e] diameter of nanoparticles, nm; [f] polydispersity index.

7. E. E. Jelley, *Nature* **1936**, *138*, 1009.

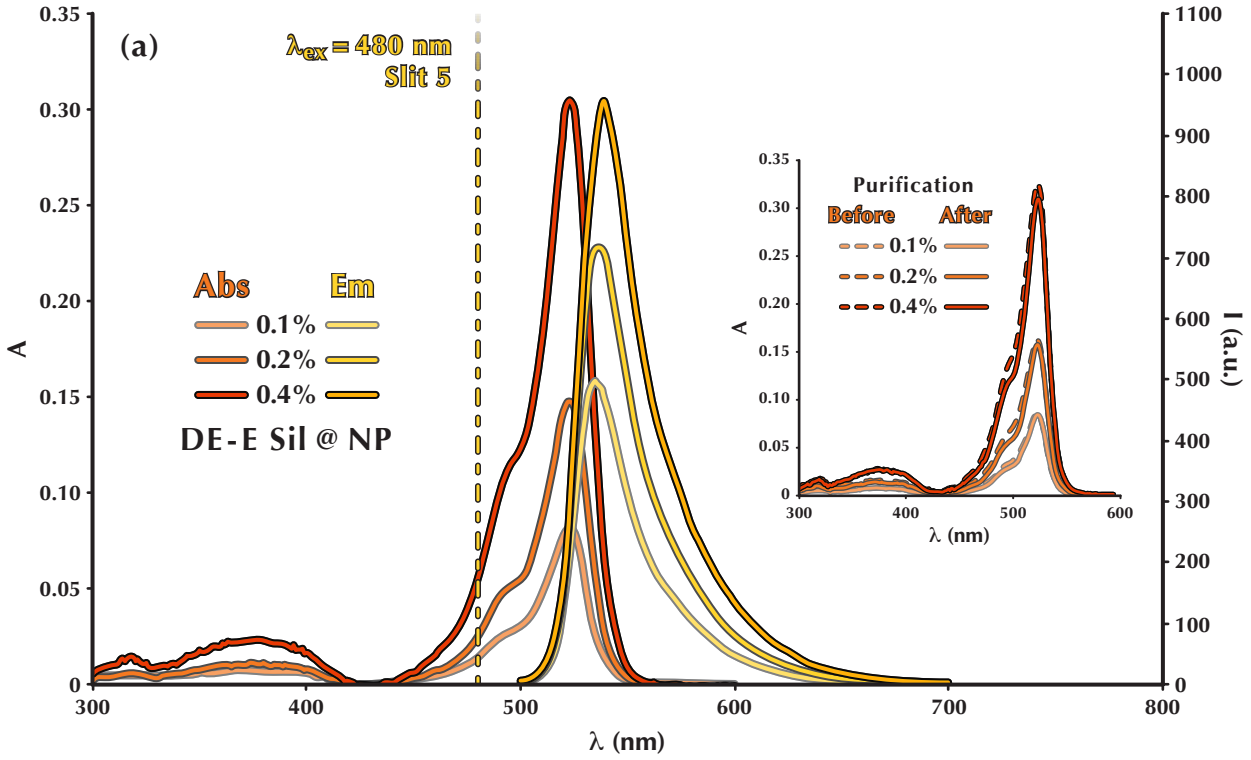
(a)
λex = 480 nm
Slit 5
Abs
Em
0.1%
0.2%
0.4%
DE-E Sil @ NP
Purification
Before
After
0.1%
0.2%
0.4%
A
I (a.u.)
λ (nm)

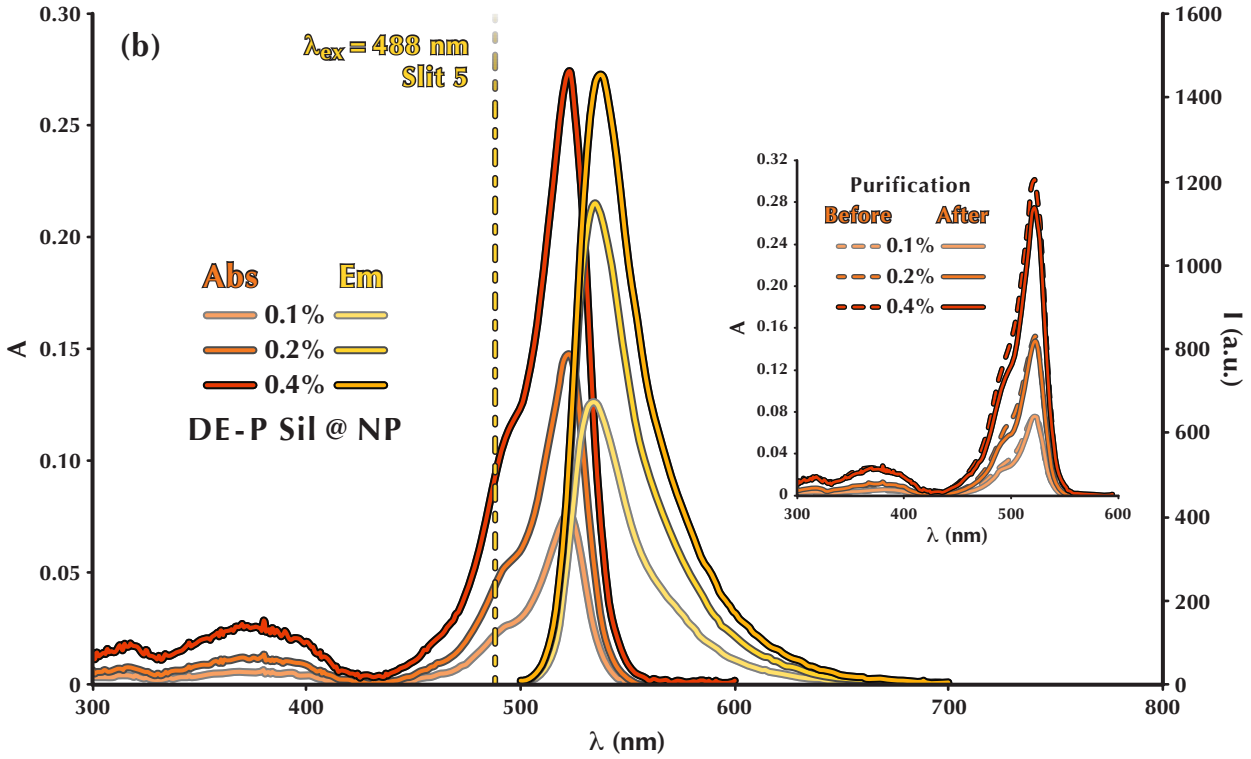
(b)
λex = 488 nm
Slit 5
Abs
Em
0.1%
0.2%
0.4%
DE-P Sil @ NP
Purification
Before
After
0.1%
0.2%
0.4%
A
I (a.u.)
λ (nm)

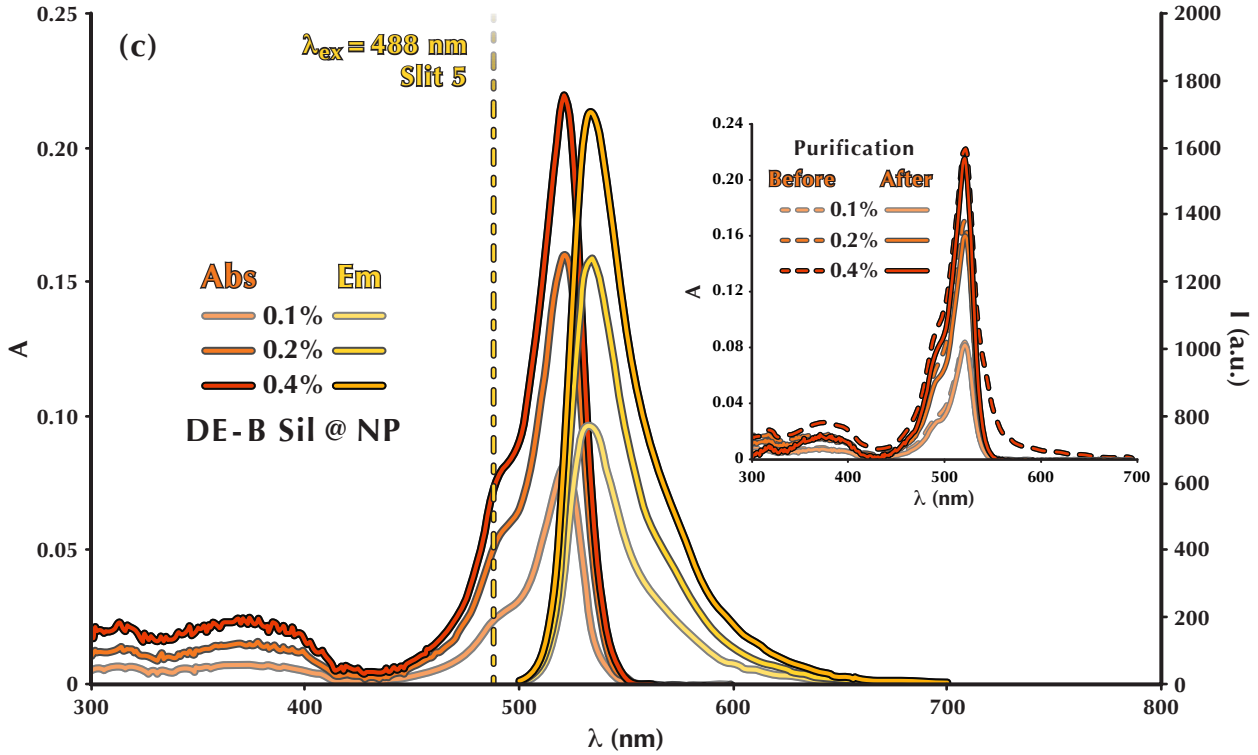

Figure 9 Absorption (dark orange) and emission (yellow) spectra of (a) **DE-E Sil**, (b) **DE-P Sil**, and (c) **DE-B Sil** doped nanoparticles. Insets show the absorption spectra before (dashed) and after (solid) dialysis/filtration treatment.

3.2.4 Rhod B Sil

Rhod B Sil has been studied once more: new nanoparticles were synthesized, increasing the dye doping level (figure 10).

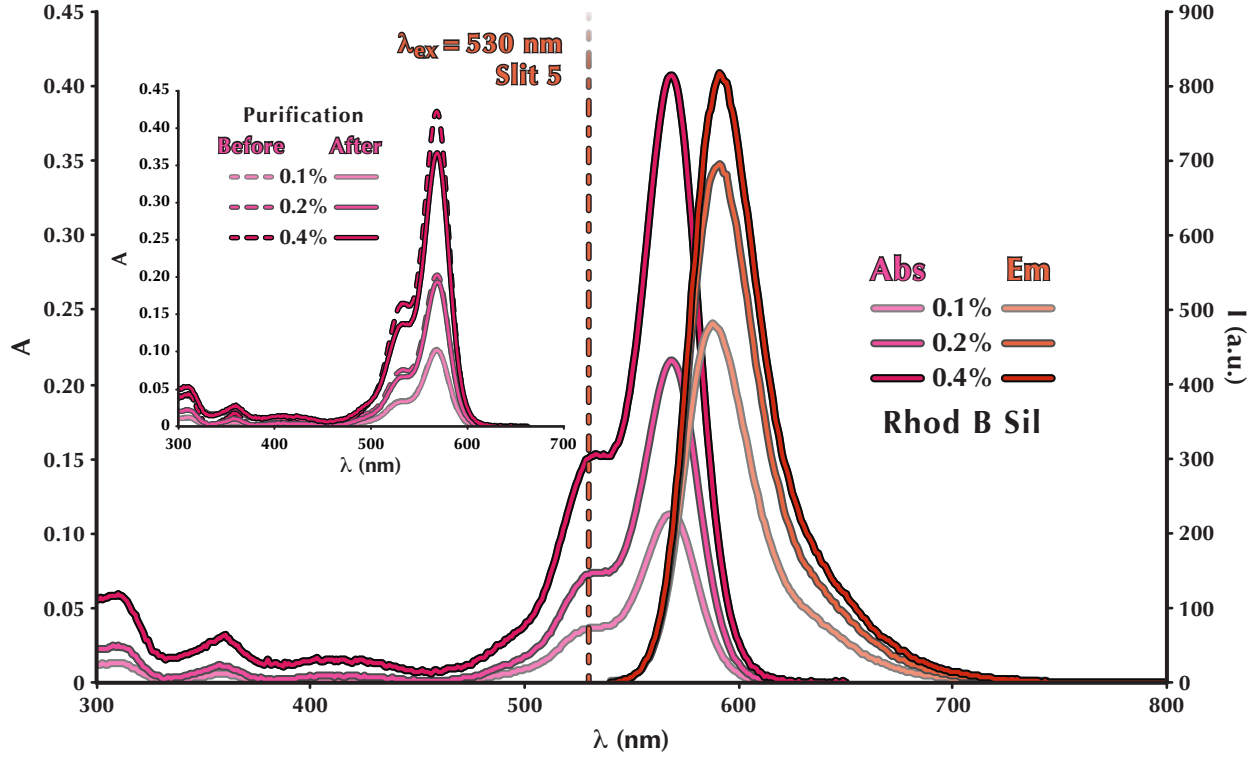

Figure 10 Absorption (pink) and emission (light red) spectra of **Rhod B Sil** doped nanoparticles. Insets show the absorption spectra before (dashed) and after (solid) dialysis/filtration treatment.

Table 4 Spectroscopic and morphological properties of **Rhod B Sil** doped nanoparticles.

Dye	δδ%	mg	ε/fluo[a]	ε/NP[a]	λ abs[b]	λ em[b]	S S[c]	Φ[d]	Z-Ave[e]	PdI[f]
Rhod B Sil	**0.1**	0.69	67400	507000	568	588	20	0.85	21.72 ± 0.09	0.021 ± 0.011
	0.2	1.37	65700	972000	569	591	22	0.63	22.16 ± 0.07	0.058 ± 0.017
	0.4	2.74	67300	1835000	568	591	23	0.37	20.82 ± 0.14	0.034 ± 0.015

[a] $M^{-1} \cdot cm^{-1}$; [b] nm; [c] Stokes shift, nm; [d] Cresyl violet perchlorate in methanol (Φ = 0.54) was used as standard; [e] diameter of nanoparticles, nm; [f] polydispersity index.

The absorption band has a maximum at 568 nm, while the emission band around 590 nm. With respect to Bodipy dyes, **Rhod B Sil** has slightly smaller quantum yields, but it exhibits a moderately broader Stokes shift, but not as wide as **DEAC Sil**. Like the previous cases, the absorbance follows a linear correlation with the doping level, while the quantum yield decreases.

Dynamic light scattering measurements show the typical diameter size of about 22 nm, with excellent polydispersity index values.

3.2.5 Bodipy – DE mSA Sil series

Two monostyryl adducts were successfully synthesized – and then derivatized – starting from **DE** Bodipy dyes and 4-methoxybenzaldehyde by means of Knoevenagel condensation: **DE-P mSA Sil** and **DE-B mSA Sil** (scheme 7).

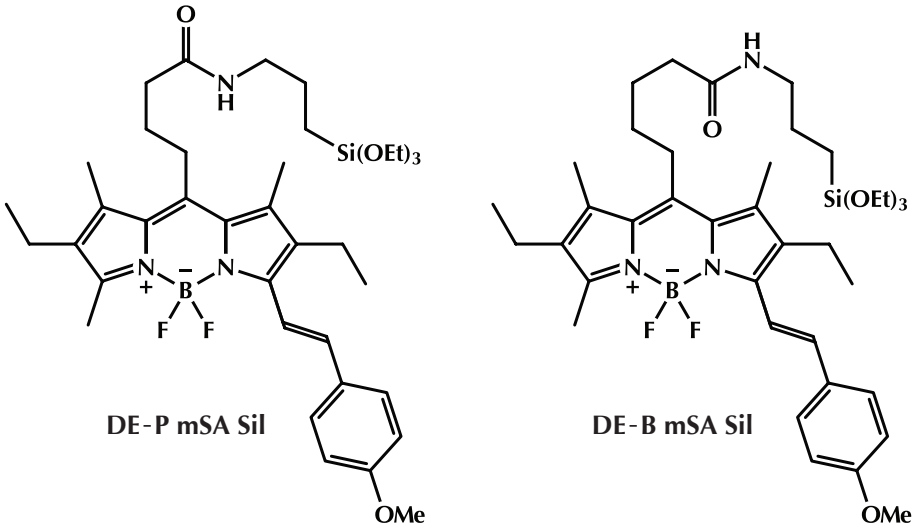

Scheme 7 Molecular structures of the two monostyryl triethoxysilane adducts.

The introduction of a single 4-methoxystyryl group results in an extension of the conjugation, which leads to a bathochromic shift of about 60-65 nm with respect to the parent molecules (**DE-P Sil** and **DE-B Sil**), regarding both the absorption and the emission properties of the fluorophores. The new band appearing around 335 nm is typical of these monoadducts[8] and is likely due to the π-π* transition of the styryl moiety. Quantum yields remain very high, but are lower at higher doping levels, as already observed with the other fluorophores.

On the other hand, the added styryl moiety confers to the molecule diminished solubility, as experienced during its synthesis: this reflects in the fact that the fluorophore have some

8. (a) W. Qin, M. Baruah, W. Dehaen, W. M. De Borggraeve, N. Boens, *J. Photochem. Photobiol. A: Chem.* **2006**, *183*, 190; (b) M. Baruah, W. Qin, C. Flors, J. Hofkens, R. A. L. Vallée, D. Beljonne, M. Van der Auweraer, W. M. De Borggraeve, N. Boens, *J. Phys. Chem. A* **2006**, *110*, 5998.

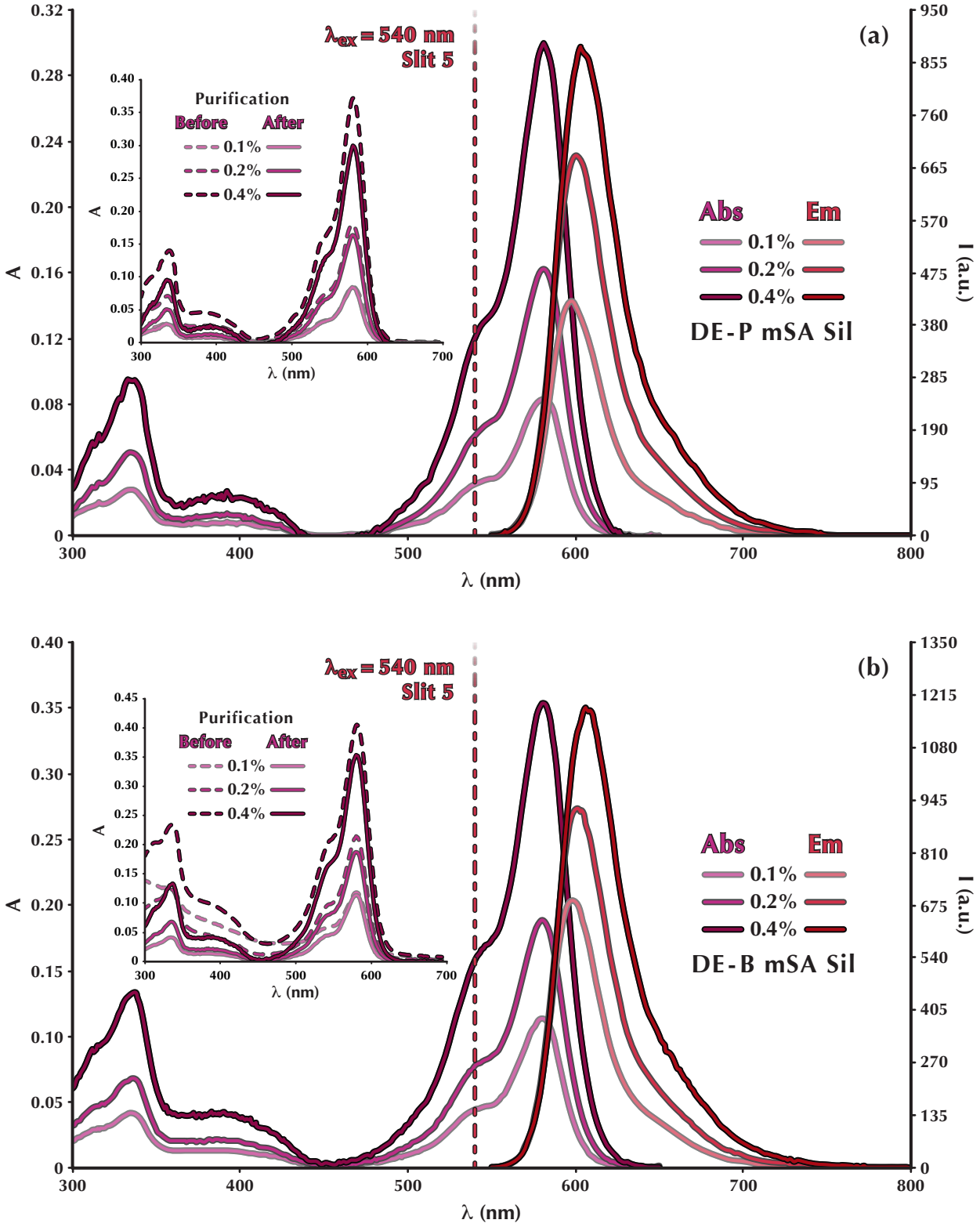

Figure 11 Absorption (purple) and emission (crimson red) spectra of (a) **DE-P mSA Sil** and (b) **DE-B mSA Sil** doped nanoparticles. Insets show the absorption spectra before (dashed) and after (solid) dialysis/filtration treatment.

difficulty in dissolving in the micelle water solution and has a moderate tendency to precipitate, especially at high concentrations. As can be noted in the insets of figure 11 – in particular for **DE-B mSA Sil**, a fraction of the dye does not co-condense properly, but fortunately the extent of this loss in not very pronounced.

Table 5 Spectroscopic and morphological properties of **DE mSA Sil** doped nanoparticles.

Dye	δδ%	mg	ε/fluo[a]	ε/NP[a]	λ abs[b]	λ em[b]	S S[c]	Φ[d]	Z-Ave[e]	PdI[f]
DE-P mSA Sil	**0.1**	0.57	49900	376000	580	597	17	1.00	22.58 ± 0.18	0.03 ± 0.02
	0.2	1.14	52100	755000	581	601	20	0.87	–[g]	–[g]
	0.4	2.28	52300	1349000	581	603	22	0.62	–[g]	–[g]
DE-B mSA Sil	**0.1**	0.58	69100	509000	580	597	17	0.99	22.0 ± 0.5	0.05 ± 0.03
	0.2	1.16	61400	848000	580	600	20	0.86	–[g]	–[g]
	0.4	2.32	58600	1592000	580	606	26	0.59	–[g]	–[g]

[a] $M^{-1} \cdot cm^{-1}$; [b] nm; [c] Stokes shift, nm; [d] Cresyl violet perchlorate in methanol (Φ = 0.54) was used as standard; [e] diameter of nanoparticles, nm; [f] polydispersity index; [g] the sample partially absorbs the incident light beam (633 nm), interfering with the measurement.

3.2.6 Bodipy – TM-P dSB Sil

Only one triethoxysilane distyryl adduct was effectively synthesized, starting from a **TM** Bodipy dye and 4-(*tert*-butyloxy)benzaldehyde via Knoevenagel condensation: **TM-P dSB Sil** (scheme 8).

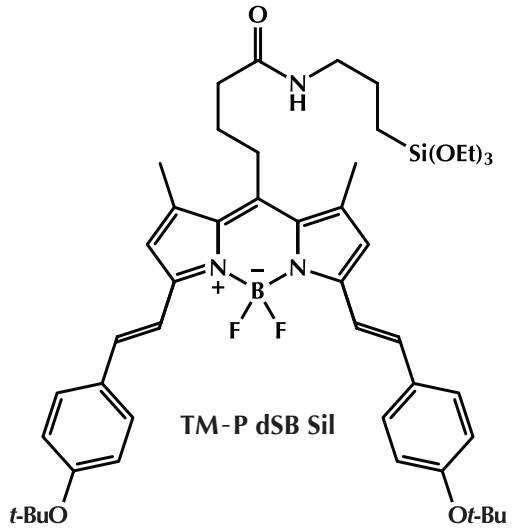

Scheme 8 Molecular structure of the distyryl triethoxysilane adduct.

The two 4-(*tert*-butyloxy)styryl groups shift bathochromically the absorption and emission bands of about 135 nm with respect to the parent molecule, **TM-P Sil**. The absorption band due to the π-π* transition of the styryl moiety lies at 355 nm and is consistently much stronger, as

Table 6 Spectroscopic and morphological properties of **TM-P dSB Sil** doped nanoparticles.

Dye	δδ%	mg	ε/fluo[a]	ε/NP[a]	λ abs[b]	λ em[b]	S S[c]	Φ[d]	Z-Ave[e]	PdI[e]
TM-P dSB Sil	**0.1**	0.69	51300	383000	631	644	13	0.44	–	–
	0.2	1.37	48200	697000	631	647	16	0.31	–	–
	0.4	2.75	31500	822000	632	645	13	0.16	–	–

[a] $M^{-1} \cdot cm^{-1}$; [b] nm; [c] Stokes shift, nm; [d] Cresyl violet perchlorate in methanol (Φ = 0.54) was used as standard; [e] the samples absorb the incident light beam (633 nm), interfering with the measurement.

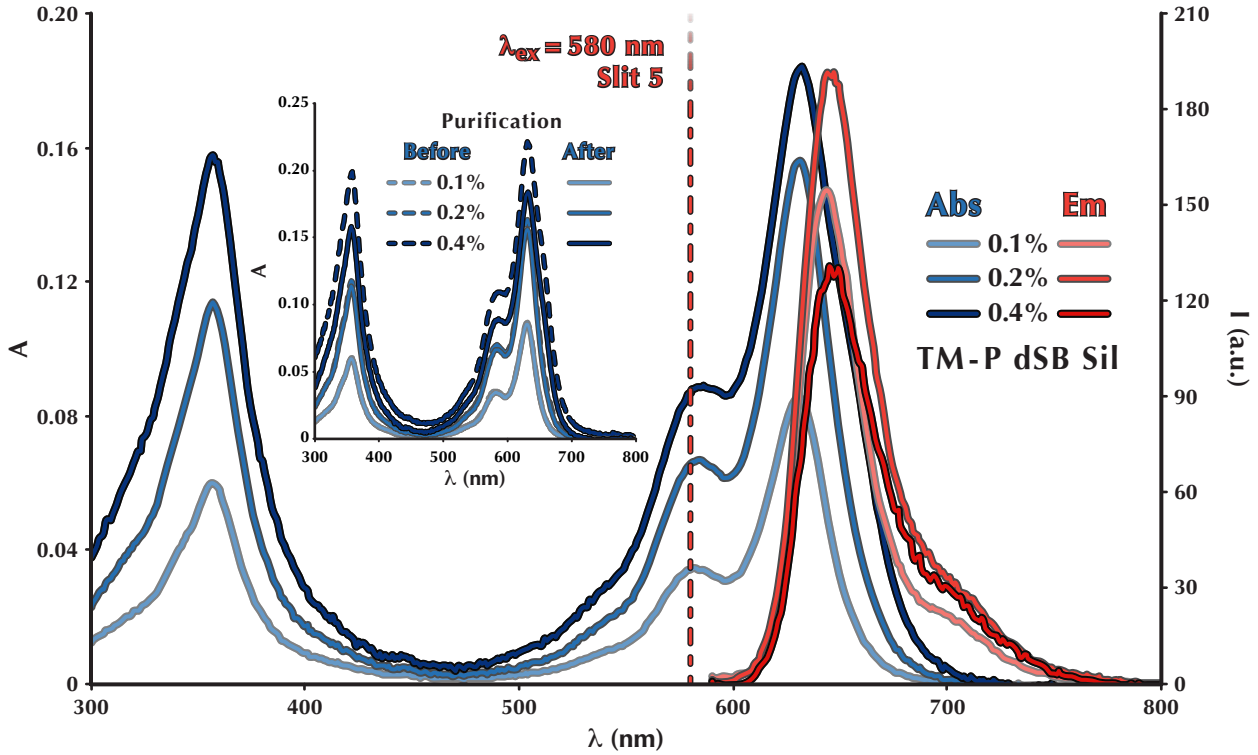

Figure 12 Absorption (blue) and emission (red) spectra of **TM dSB Sil** doped nanoparticles. Insets show the absorption spectra before (dashed) and after (solid) dialysis/filtration treatment.

already observed for other distyryl BODIPY dyes.[9] The values of quantum yield are the smallest compared to all other fluorophores, but it is quite common for red emitting dyes to have lower efficiencies.

Apart from the established problems of self-quenching processes, solubility issues are more serious than before: as the absorption spectrum of the most doped sample clearly indicates, most of the dye fails to be incorporated in the nanoparticles.

3.3 Conclusions

A whole library of fluorophore, encompassing the whole visible spectrum has been synthesized.

The triethoxysilane derivatization of the fluorophores allows a higher degree of doping inside the nanoparticles. In general, there is a good – almost linear – correlation between the amount of dye included and the molar absorption coefficient of the nanoparticle. Moreover, since the shape of the bands in the absorption spectra does not significantly change (only **TM-P Sil** shows a little band after purification), it is possible to rule out the presence of intermolecular interactions in the ground state and the formation of dimers or aggregates.

However, fluorescence properties are strongly affected by the δδ%: in fact, the close proximity of the molecules inside the silica matrix leads to the formation of excimers and the development of self-quenching processes, which function as an alternative, non-radiative energy decay pathway, that happens to be faster than the emission of photons, thus resulting in a dramatic decrease of the quantum yield. It must be stressed that it is necessary to choose carefully the degree of doping, in order to maximize the intensity of the luminescence signal arising from the nanoparticles.

9. K. Rurack, M. Kollmannsberger, J. Daub, *New J. Chem.* **2001**, *25*, 289.

Besides, it is not possible to augment indefinitely the doping degree of the fluorophore for synthetic reasons. First, the presence of an extraneous molecule perturbs the micellar structure and hence the nanoparticles formation, as it can be observed from the increase in the polydispersity index and mean diameter along with the increment of the δδ%. Second, BODIPY dyes in particular have the tendency to self-aggregate – the distyryl adduct at a very high extent – forming precipitates prior to their inclusion inside the nanosystem; that is the reason why in most of the cases, the 0.4% samples have the lowest ε value.

Chapter 4
Energy transfer

4.1 Principles of energy transfer

In the previous chapter, we discussed the photophysical properties of dye doped silica nanoparticles, in which it was included only one type of fluorophore. As far as fluorescence is concerned, the main drawback can be ascribed to the loss of quantum yield with increasing doping, because of the occurrence of self-quenching processes. In order to bypass this parasite phenomenon and to improve the performance of the nanoparticles, it is reasonable to introduce another relaxation pathway (figure 1), *i.e.*, an additional molecule – called acceptor (**A**) – capable of intercepting the excitation energy of the excited molecule – called donor, or (**D**).[1] Before entering the heart of the discussion, describing multichromophoric nanoparticles, it is necessary to recall the basics of energy transfer.[2]

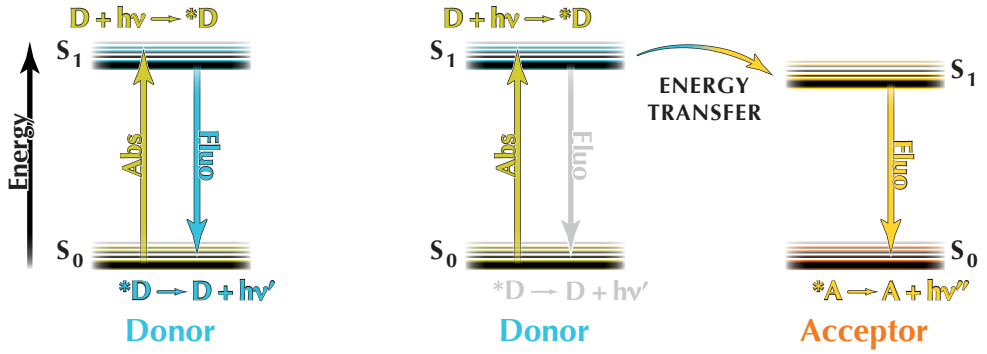

Figure 1 Simplified Jablonski diagram for donor alone (left) or in presence of a suitable acceptor (right).

4.1.1 Mechanisms of energy transfer

Energy transfer is a bimolecular process between a donor molecule in the excited state (denoted as ***D**) and an acceptor molecule in the ground state (see equation [1]). The excitation energy can be transferred both in a radiative or non-radiative way, but nevertheless this phenomenon obeys the law of conservation of energy, so that the energy level of ***A** (that is the acceptor molecule in the excited state) must be equal or lower than the one of ***D**.

$$*D + A \xrightarrow{k_{et}} D + *A \qquad [1]$$

The ***radiative energy transfer*** involves the emission of a photon from ***D**, which is then reabsorbed by **A**. In this mechanism, that is responsible for inner filter effects, no electronic interactions are required: the acceptor merely intercepts the photon before its detection. This is why it is usually referred to as *trivial mechanism*: it depends on the optical properties of the

1. Silica nanoparticles are known to be suitable platforms for energy transfer processes, *e.g.*: S. Bonacchi, D. Genovese, R. Juris, E. Marzocchi, M. Montalti, L. Prodi, E. Rampazzo, N. Zaccheroni, *Reviews in fluorescence 2008, chapter 5*, C. D. Geddes (ed.), **2010**, Springer (New York, NY) and references therein.
2. For a more extensive treatment on this subject, see: J. R. Lakovicz, *Principles of fluorescence spectroscopy*, 3rd ed., **2006**, Springer (New York, NY).

sample – for instance the size and shape of the cuvette or the path followed by the excitation and emission light – therefore no specific information on the structure or the energetics of the molecules can be obtained.

On the other hand, ***non-radiative energy transfer*** does not require the participation of photons, but is the consequence of an electronic dipole-dipole interaction between **D** and **A**. It may be further divided into two components: the *exchange interaction* (also called Dexter mechanism) and the *Coulombic interaction* (commonly known as FRET – Förster resonance energy transfer).

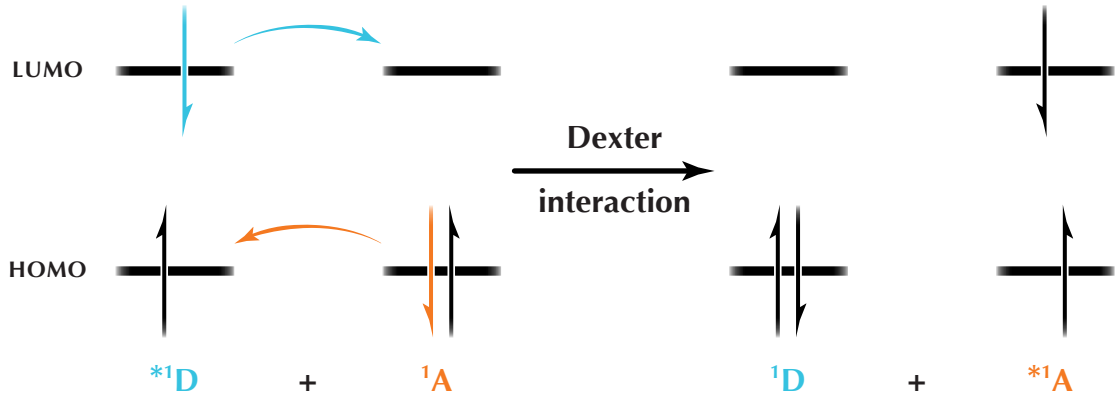

Figure 2 Schematic representation of the exchange mechanism.

The ***Dexter mechanism***[3] is described as a double electron transfer reaction (it can be either stepwise or concerted): the electron in the LUMO of ***D** is transferred into the LUMO of **A**, while an electron in the HOMO of **A** jumps back into the HOMO of ***D** (figure 2).

This kind of interaction requires the overlap of the electron clouds: for this reason the Dexter mechanism is efficient only at short range (between 6 and 20 Å); the rate constant k_D has an exponential dependence on distance, expressed by:

$$k_D = A e^{-\beta(r - r_c)} \qquad [2]$$

where r is the distance between the centers of **D** and **A** and r_c is the sum of the van der Waals radii of the two molecules. The values of β are typically close to 1 $Å^{-1}$ – they decrease if **D** and **A** are connected through a conjugated bridge – while those of A can be up to 10^{13} s^{-1}.

With regard to spin selection rules, the spin must be conserved by taking into account the two molecules **D** and **A** as a pair, so both singlet-singlet and triplet-triplet transition are permitted. This is very important, because it is at the basis of quenching of excited triplets by molecular oxygen[4] and consequently of photosensitized generation of singlet oxygen:[5]

$$^{*3}D + {}^{3}O_2 \longrightarrow {}^{1}D + {}^{*1}O_2 \qquad [3]$$

On the contrary, the ***Förster mechanism***[6] is a through-space long-range dipole-dipole interaction. There is no physical contact between the molecules, but it is the oscillating field of ***D** that induces a dipole oscillation in A (figure 3): the excited electron on the LUMO of **D** relaxes to the HOMO and the released energy migrates to **A** by means of coulombic interactions, resulting in the promotion of one electron into the empty LUMO and the formation of ***A**.

3. D. L. Dexter, *J. Chem. Phys.* **1953**, *21*, 836.
4. (a) K. Kawaoka, A. U. Khan, D. R. Kearns, *J. Chem. Phys.* **1967**, *46*, 1842; (b) D. R. Kearns, A. J. Stone, *J. Chem. Phys.* **1971**, 55, 3383.
5. M. C. DeRosa, R. J. Crutchley, *Coord. Chem. Rev.* **2002**, *233-234*, 351.
6. (a) T. Förster, *Ann. Phys.* **1948**, *2*, 55; (b) T. Förster, *Discuss. Faraday Soc.* **1959**, *27*, 7.

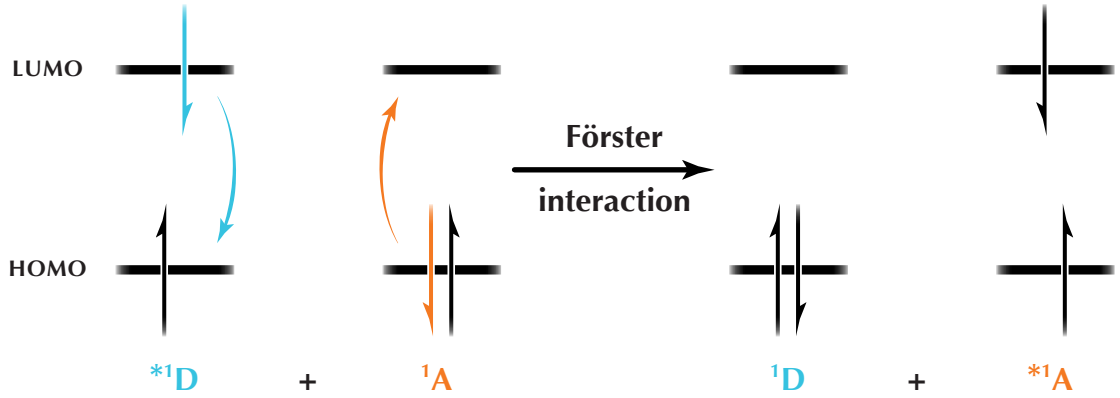

Figure 3 Schematic representation of the FRET process.

The rate constant k_F for the Förster mechanism can be calculated from:

$$k_F = \frac{\Phi_D \kappa^2}{\tau_D r^6} \left(\frac{9000 (\ln 10)}{128 \pi^5 N n^4} \right) J(\lambda) \qquad [4]$$

where N is the Avogadro's number, n the refractive index of the solvent, r the distance between **D** and **A**, Φ_D and τ_D the emission quantum yield and lifetime of the donor in the absence of acceptor. κ^2 is a geometric factor that depends on the relative orientation of the dipoles; for a dynamic random orientation (condition which can be applied to dyes inserted in nanoparticles, since we do not control their disposition) it is generally assumed to be ⅔. $J(\lambda)$ represents the overlap integral between the normalized emission spectrum of **D** – $F_D(\lambda)$, where $\int F_D(\lambda) d\lambda = 1$ – and the absorption spectrum of **A** – $\varepsilon_A(\lambda)$; it is given by:

$$J(\lambda) = \int_0^\infty F_D(\lambda)\, \varepsilon_A(\lambda)\, \lambda^4\, d\lambda \qquad [5]$$

The Förster distance R_0 is defined as the distance at which the energy transfer has an efficiency of 50% and it can be predicted from:

$$R_0^6 = \Phi_D \kappa^2 \frac{9000 (\ln 10)}{128 \pi^5 N n^4} J(\lambda) \qquad [6]$$

Combining equation [4] and [6], one can obtain:

$$k_F = \frac{1}{\tau_D} \left(\frac{R_0}{r} \right)^6 \qquad [7]$$

Equation [7] clearly states that, apart from the extent of the spectral overlap $J(\lambda)$ and the quantum yield of the donor Φ_D (nested inside R_0), the rate of FRET depends strongly on the distance between **D** and **A** and it can be demonstrated that is efficient even over large distances, up to 100 Å. This implies that, if there is a large spectral overlap between **D** and **A**, FRET will occur before the Dexter exchange; moreover Dexter requires high concentrations of reactant to be observable. On the other hand, with regard to spin selection rules, Förster mechanism is limited to singlet-singlet transitions, because radiative transitions involving triplet states have usually weak oscillator strengths.

4.1.2 Evaluation of FRET

In the next section, the method to calculate the efficiency of energy transfer will be explained, focusing first on the case of nanoparticles doped with two type of fluorophores, then extending

to three. As far as the donor is concerned, we will be referring to quenching efficiency η_Q, *i.e.*, how much the presence of **A** leads to the extinction of the fluorescence of **D**; while regarding the acceptor, we will be dealing with the sensitization efficiency η_S, *i.e.*, how many excited states of **D** transfer their energy to **A**, *at a given excitation wavelength*.

4.1.2.1 Energy transfer in two dye doped nanoparticles

In order to calculate the extent of energy transfer, one needs to record not only the absorption and emission spectra of nanoparticles doped with both dyes (denoted by A_X and E_X), but also those of nanoparticles doped with only one type of fluorophore (designated with A_D, A_A, E_D, and E_A). It is not necessary for the samples to have the same concentration, but all emission spectra must be obtained at the same excitation wavelength.

First, A_X is fitted as a linear combination of A_D and A_A:

$$A_X = \alpha_D \cdot A_D + \alpha_A \cdot A_A = A_{D,X} + A_{A,X} \quad [8]$$

where $A_{D,X}$ and $A_{A,X}$ are the contributions of each fluorophore in the bicolor nanoparticles.

The same process is applied to the E_X:

$$E_X = \beta_D \cdot E_D + \beta_A \cdot E_A = E_{D,X} + E_{A,X} \quad [9]$$

The ***quenching efficiency of D*** can be calculated from:

$$\eta_Q = 1 - \frac{E_{D,X}}{E^o_{D,X}} \quad [10]$$

where

$$E_{D,X} = \beta_D \cdot E_D \quad [11]$$

is the *observed* residual emission of the donor in the two fluorophore system in the *presence* of energy transfer; while

$$E^o_{D,X} = \frac{E_D}{A_D} \cdot A_{D,X} = E_D \cdot \alpha_D \quad [12]$$

is the *hypothetical* emission in the *absence* of energy transfer (the last step comes from the fact that $A_{D,X} = \alpha_D \cdot A_D$).

Substituting equations [11] and [12] into equation [10], one can obtain:

$$\eta_Q = 1 - \frac{\beta_D}{\alpha_D} \quad [13]$$

On the other hand, the ***sensitization efficiency of A*** can be calculated from:

$$\eta_S = \frac{E_{A,X} - E^o_{A,X}}{E^{MAX}_{A,X} - E^o_{A,X}} \quad [14]$$

where

$$E_{A,X} = \beta_A \cdot E_A \quad [15]$$

is the *observed* emission of the acceptor in the two fluorophore system in the *presence* of energy transfer; while

$$E^o_{A,X} = \frac{E_A}{A_A} \cdot A_{A,X} = E_A \cdot \alpha_A \quad [16]$$

is the *hypothetical* emission in the *absence* of energy transfer (the last step comes from the fact that $A_{A,X} = \alpha_A \cdot A_A$); and last

$$E^{MAX}_{A,X} = \frac{E_A}{A_A} \cdot A_X \qquad [17]$$

is the *hypothetical highest possible* emission, *i.e.*, if energy transfer efficiency were equal to 1. Substituting equations [15], [16] and [17] into equation [14], one can obtain:

$$\eta_S = A_A \cdot \frac{\beta_A - \alpha_A}{A_X - \alpha_A \cdot A_A} = A_A \cdot \frac{\beta_A - \alpha_A}{\alpha_D \cdot A_D} \qquad [18]$$

In the last step, equation [8] has been substituted as well. The absorbance values refer to the absorbance of the samples at the excitation wavelength.[7]

4.1.2.2 Energy transfer in three dye doped nanoparticles

The previous analysis can be extended if an additional type of dye is inserted in the nanoparticles, a dye (which will be noted as $\mathbf{A_2}$) capable of acting as an acceptor toward the former acceptor **A** (which from now on will be noted as $\mathbf{A_1}$).

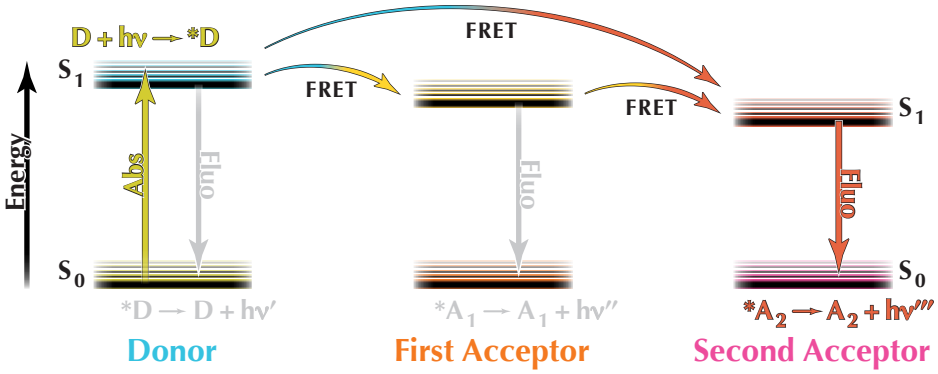

Figure 4 Simplified Jablonski diagram of a FRET process taking place in a three component system.

Even if only three molecules are involved, the whole picture reaches a complexity intricate to fathom in every detail: *e.g.*, from the point of view of **D** alone, we would have to consider the amount of energy passed on to $\mathbf{A_1}$, the energy transmitted directly to $\mathbf{A_2}$, and the energy that reaches $\mathbf{A_2}$ via hopping through $\mathbf{A_1}$. Luckily, to quantify the FRET process, it is sufficient to evaluate the overall quenching of **D**, the overall quenching of $\mathbf{A_1}$, and the overall sensitization of $\mathbf{A_2}$, without concerning about the exact path taken by the energy.

The first and the last case are simpler, because we can reduce the discussion to a two dye doped nanoparticle. Regarding the ***overall quenching efficiency of D***, $\mathbf{A_1}$ and $\mathbf{A_2}$ can be grouped together and treated as if they were one molecule: we are interested in assessing the extent to which the excited state of **D** transfers energy to $\mathbf{A_1}$ and to $\mathbf{A_2}$, but not its accurate allocation. Equations [8] and [9] become:

$$A_X = \alpha_D \cdot A_D + \alpha_{A_1A_2} \cdot A_{A_1A_2} = A_{D,X} + A_{A_1A_2,X} \qquad [19]$$

7. The measure of sensitization efficiency is the most prone to error, because the absorbance of the acceptor at the excitation wavelength (A_A) is very low (the absorbance on the whole spectrum must be inferior to 0.1, to avoid problems in evaluating the emission) and most of the times is indistinguishable from the background noise. To bypass this limitation, it is necessary to record an additional absorption spectrum of the acceptor at higher concentration.

$$E_X = \beta_D \cdot E_D + \beta_{A_1A_2} \cdot E_{A_1A_2} = E_{D,X} + E_{A_1A_2,X} \quad [20]$$

while the quenching efficiency is still calculated from equation [13], once α_D and β_D parameters have been derived. Evidently, apart from nanoparticles doped with only one type of fluorophore as before, a sample containing both $\mathbf{A_1}$ and $\mathbf{A_2}$ is also required.

Similarly, for the ***overall sensitization efficiency of A_2***, **D** and $\mathbf{A_1}$ can be grouped together (we need to evaluate how much energy $\mathbf{A_2}$ receives, but not its origin) and equations [8] and [9] change into:

$$A_X = \alpha_{DA_1} \cdot A_{DA_1} + \alpha_{A_2} \cdot A_{A_2} = A_{DA_1,X} + A_{A_2,X} \quad [21]$$

$$E_X = \beta_{DA_1} \cdot E_{DA_1} + \beta_{A_2} \cdot E_{A_2} = E_{DA_1,X} + E_{A_2,X} \quad [22]$$

while equation [18]:

$$\eta_S = A_{A_2} \cdot \frac{\beta_{A_2} - \alpha_{A_2}}{\alpha_{DA_1} \cdot A_{DA_1}} \quad [23]$$

In this case we need to synthesize a sample containing both **D** and $\mathbf{A_1}$.[8]

On the contrary, in calculating the ***overall quenching efficiency of A_1***, the analysis gets more complicated, because the absorbance spectrum can be deconvolved with equation [21], but in emission each fluorophore must be considered individually:

$$E_X = \beta_D \cdot E_D + \beta_{A_1} \cdot E_{A_1} + \beta_{A_2} \cdot E_{A_2} = E_{D,X} + E_{A_1,X} + E_{A_2,X} \quad [24]$$

The quenching efficiency is given by:

$$\eta_Q = 1 - \frac{E_{A_1,X}}{E^0_{A_1,X}} \quad [25]$$

where

$$E_{A_1,X} = \beta_{A_1} \cdot E_{A_1} \quad [26]$$

is the *observed* emission of $\mathbf{A_1}$ in the three fluorophore system in the *presence* of energy transfer toward $\mathbf{A_2}$; while

$$E^0_{A_1,X} = \frac{E_{A_1,2}}{A_{DA_1}} \cdot A_{DA_1,X} \quad [27]$$

is the *hypothetical* emission in the *absence* of energy transfer. In equation [27]

$$E_{A_1,2} = \beta_{A_1,2} \cdot E_{A_1} \quad [28]$$

is the *observed* emission of $\mathbf{A_1}$ in the *two dye sample* containing only **D** and $\mathbf{A_1}$ in the *presence* of energy transfer (the parameter β refers to the deconvolution in the two dye system and it is different from the one of equation [24]). Knowing from equation [21] that:

$$A_{DA_1,X} = \alpha_{DA_1} \cdot A_{DA_1} \quad [29]$$

equation [27] becomes:

$$E^0_{A_1,X} = \beta_{A_1,2} \cdot E_{A_1} \cdot \alpha_{DA_1} \quad [30]$$

8. Clearly, the same issue applies in this case: supplementary absorption spectrum must be recorded of both $\mathbf{A_1}$ and $\mathbf{A_2}$ at higher concentration.

Substituting equations [30] and [26] into equation [25], one can finally obtain:

$$\eta_Q = 1 - \frac{\beta_{A_1}}{\beta_{A_1,2} \cdot \alpha_{DA_1}} \qquad [31]$$

4.2 Multichromophoric nanoparticles

4.2.1 Two dye doped nanoparticles

As discussed in the previous section, FRET depends mainly on the distance between the donor and the acceptor and is efficient up to 100 Å, which correspond to 10 nm, that is exactly the diameter of the silica core. Therefore, if we co-condense two dyes, instead of a single one, during the nanoparticles synthesis, these fluorophores would be located at the proper distance for this mechanism to happen. Previous simulations[9] have shown that the observed efficiencies are consistent with Förster mechanism and that Dexter interaction can be ruled out as the least probable.

4.2.1.1 DEAC Sil & DE-E Sil

Moreover, another requirement for efficient energy transfer is a good spectral overlap between donor emission and acceptor absorption. As figure 5 illustrates, **DEAC Sil** and **DE-E Sil** seem to be suitable candidates for a donor-acceptor pair, respectively. Then, several nanoparticles were prepared, keeping the doping level of the acceptor fixed to a low value, while varying the δδ% of the donor.

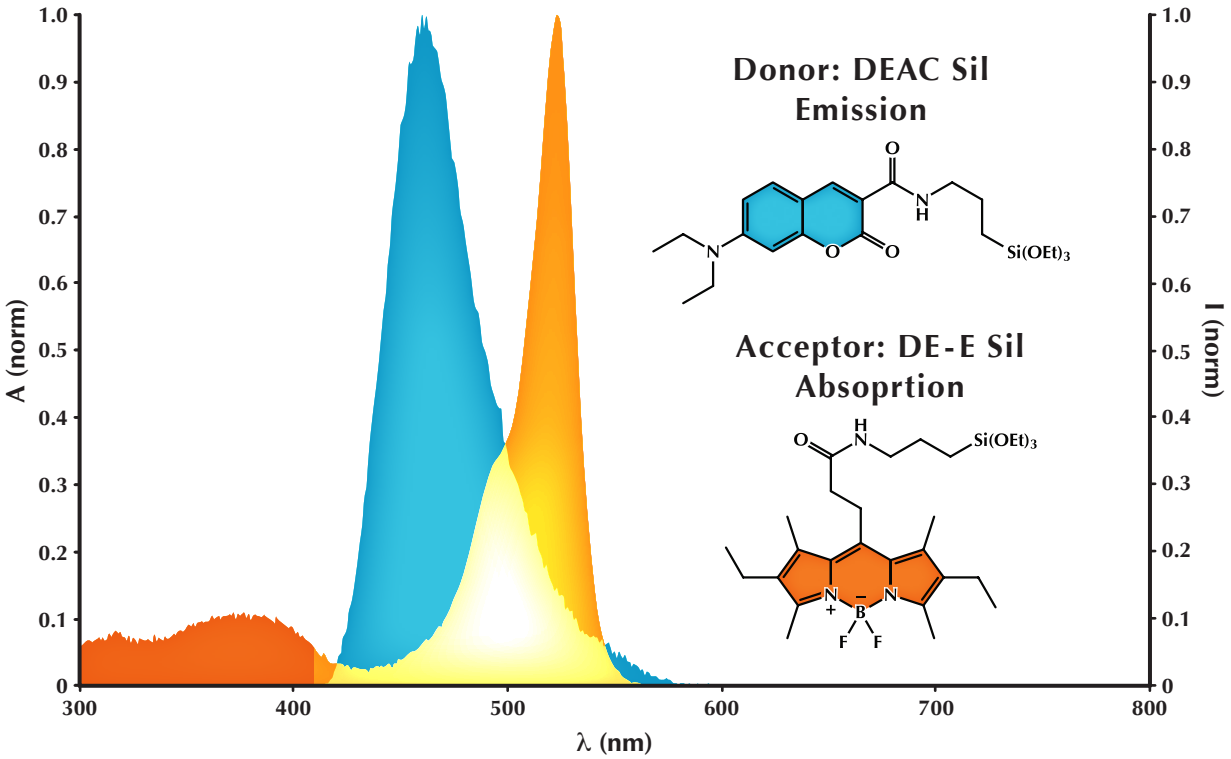

Figure 5 Normalized emission (light blue) of **DEAC Sil** (donor) and normalized absorption (dark orange) of **DE-E Sil** (acceptor) doped nanoparticles. The overlap region is shown in yellow.

9. D. Genovese, *Ph. D. Thesis*, **2011**, Bologna (Italy).

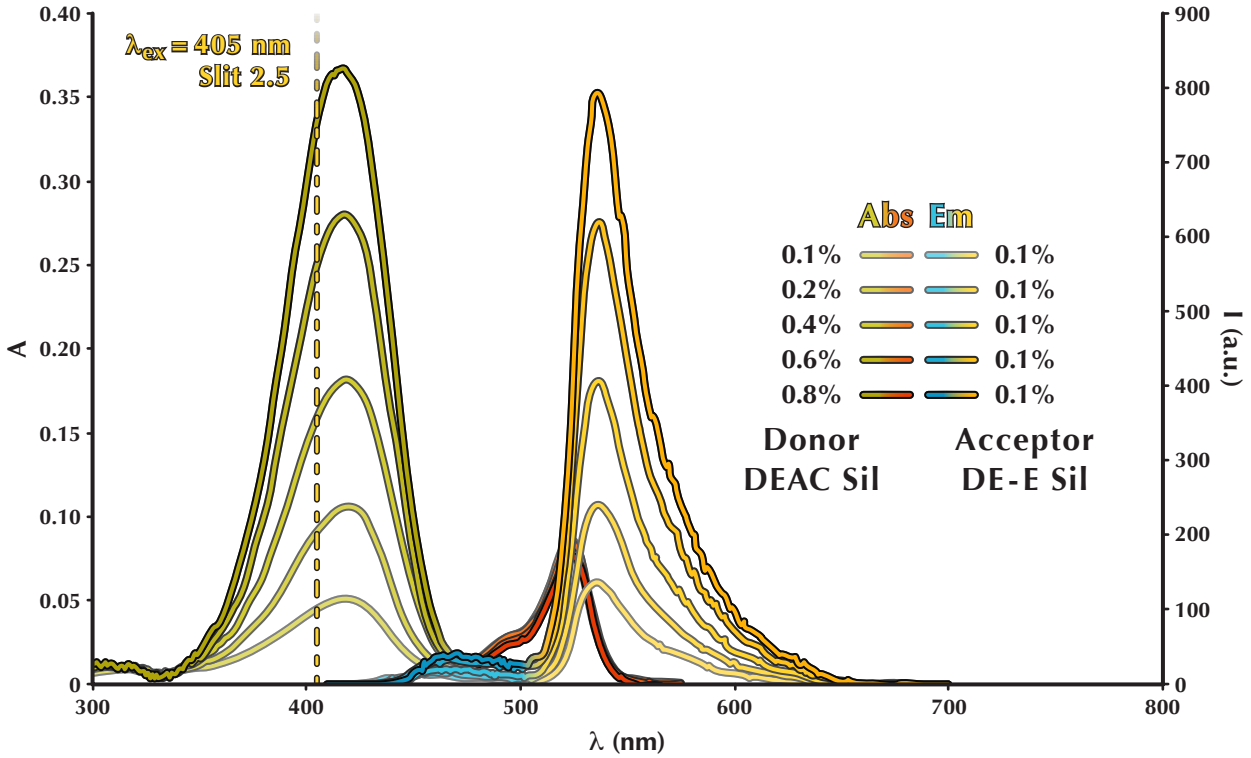

Figure 6 Absorption (yellow-green/dark orange) and emission (light blue/yellow) spectra of **DEAC Sil** (donor) and **DE-E Sil** (acceptor) doped nanoparticles.

Table 1 Spectroscopic properties of **DEAC Sil/DE-E Sil** doped nanoparticles.

Donor	δδ%	λ abs[a]	η_Q	Acceptor	δδ%	λ abs[a]	λ em[a]	η_S	S S[b]
DEAC Sil	**0.1**	420	0.90	DE-E Sil	**0.1**	523	536	0.96	116
	0.2	420	0.88		**0.1**	523	536	0.82	116
	0.4	417	0.86		**0.1**	524	536	0.80	118
	0.6	418	0.77		**0.1**	524	537	0.77	119
	0.8	417	0.65		**0.1**	523	536	0.73	119

[a] nm; [b] Pseudo Stokes shift, nm.

Table 2 Morphological properties of **DEAC Sil/DE-E Sil** doped nanoparticles.

Donor	δδ%	Acceptor	δδ%	Z-Ave[a]	PdI[b]
DEAC Sil	**0.1**	DE-E Sil	**0.1**	21.82 ± 0.09	0.091 ± 0.011
	0.2		**0.1**	21.79 ± 0.15	0.117 ± 0.013
	0.4		**0.1**	21.66 ± 0.10	0.118 ± 0.010
	0.6		**0.1**	22.06 ± 0.12	0.070 ± 0.004
	0.8		**0.1**	23.33 ± 0.17	0.148 ± 0.011

[a] diameter of nanoparticles, nm; [b] polydispersity index.

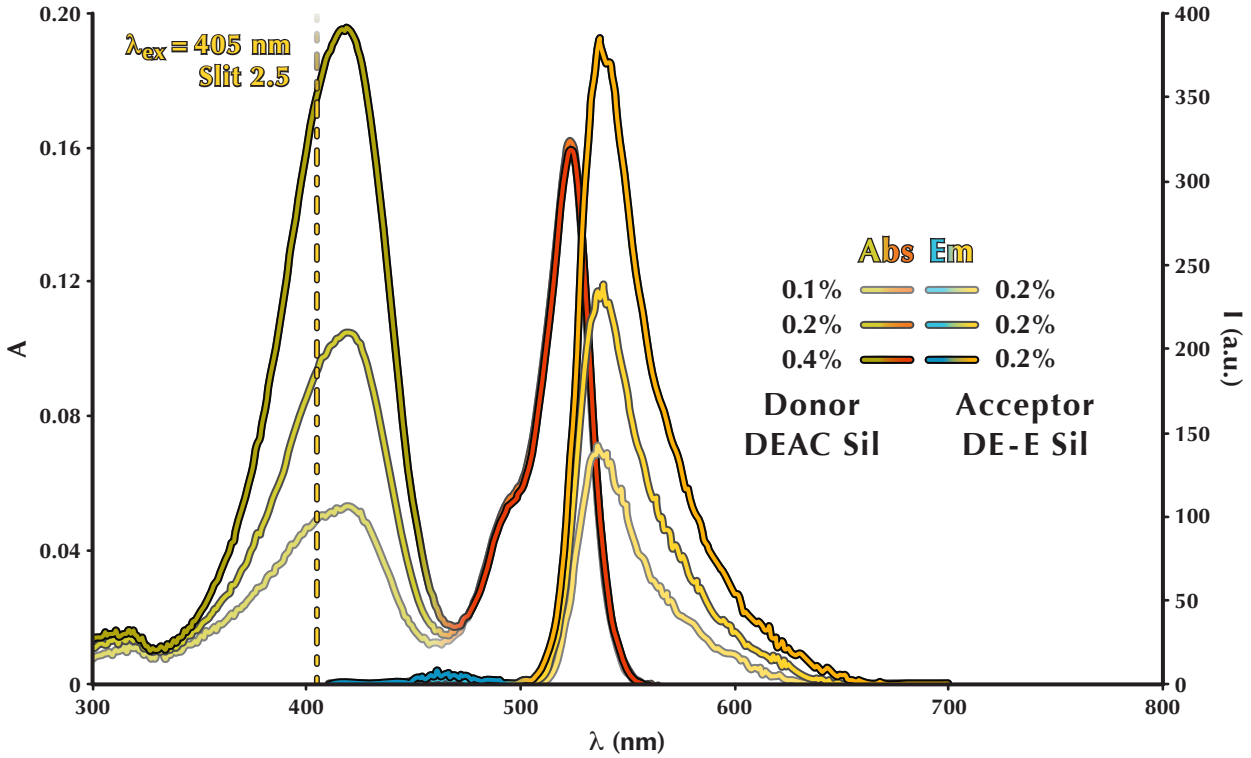

Figure 7 Absorption (yellow-green/dark orange) and emission (light blue/yellow) spectra of **DEAC Sil** (donor) and **DE-E Sil** (acceptor) doped nanoparticles.

Table 3 Spectroscopic properties of **DEAC Sil/DE-E Sil** doped nanoparticles.

Donor	δδ%	λ abs[a]	η_Q	Acceptor	δδ%	λ abs[a]	λ em[a]	η_S	S S[b]
DEAC Sil	**0.1**	420	0.99	DE-E Sil	**0.2**	523	536	0.99	116
	0.2	419	0.97		**0.2**	523	539	0.93	120
	0.4	419	0.93		**0.2**	524	537	0.80	118

[a] nm; [b] Pseudo Stokes shift, nm.

Table 4 Morphological properties of **DEAC Sil/DE-E Sil** doped nanoparticles.

Donor	δδ%	Acceptor	δδ%	Z-Ave[a]	PdI[b]
DEAC Sil	**0.1**	DE-E Sil	**0.2**	22.79 ± 0.14	0.16 ± 0.02
	0.2		**0.2**	22.89 ± 0.15	0.15 ± 0.03
	0.4		**0.2**	22.92 ± 0.14	0.155 ± 0.008

[a] diameter of nanoparticles, nm; [b] polydispersity index.

In the absorption spectra of figure 6, the bands of both dyes are clearly recognizable, denoting their successful inclusion, as expected. In this bichromophoric system, there are two possible relaxation pathways that compete with **DEAC Sil** emission: self-quenching and energy transfer via FRET to **DE-E Sil**. The fact that this emission becomes very weak (with respect to single dye doped nanoparticles), as the emission from the acceptor rises with increasing δδ% of the donor, indicates that FRET is the fastest of all processes, in accordance with the very high values calculated for the quenching and sensitization efficiencies, shown in table 1. Not surprisingly, these values decrease with increasing donor doping, because the self-quenching process, even if kinetically unfavorable, becomes statistically more probable. It is worth noticing that the pseudo Stokes shift[10] – in comparison with the system with **DEAC Sil** alone – is almost three times greater.

Next, another series of nanoparticles were prepared, where the δδ% of the acceptor was still variable, while the doping level of the acceptor was increased to a value of 0.2% (figure 7).

The quenching efficiency is higher than before – almost close to unity – and the residual emission of the donor practically disappears; the intensity of the acceptor emission, though, is very similar to the previous case and there is no significant gain, even if the sensitization efficiency is still excellent,[11] due to the fact that the quantum yield of the acceptor at a doping level of 0.2% is lower than 0.1%.

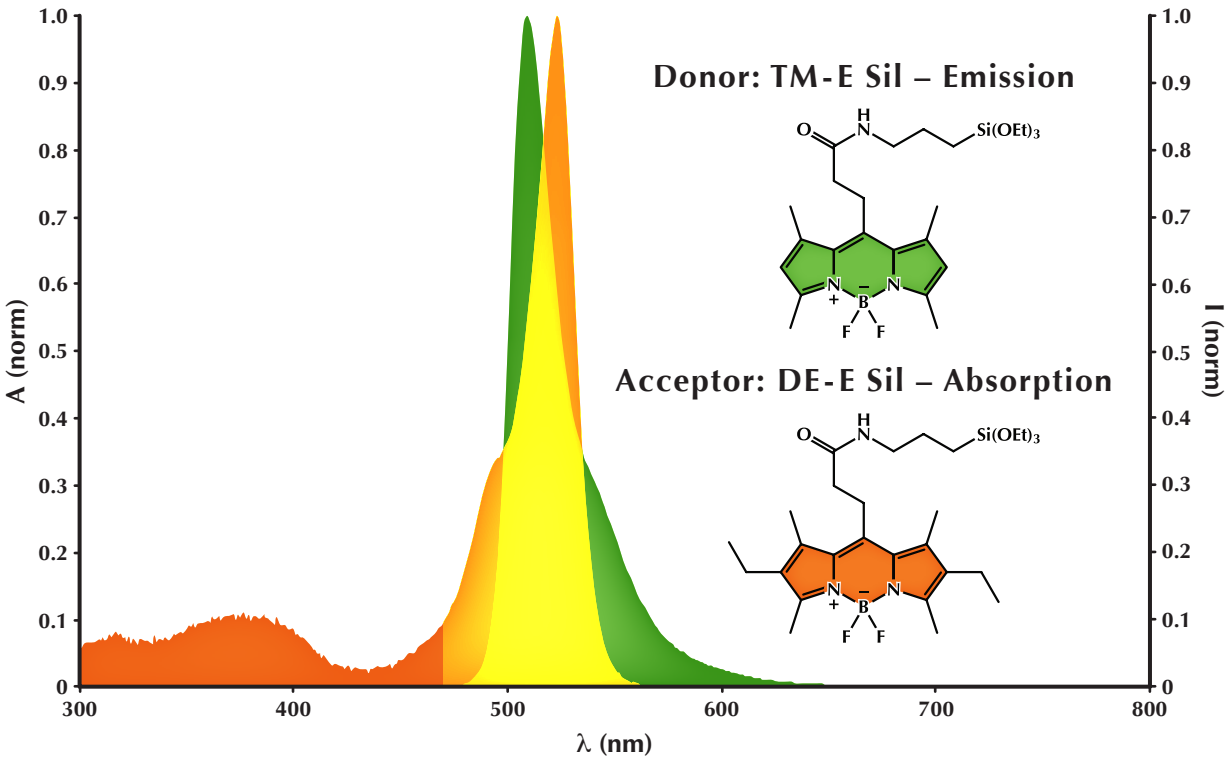

Figure 8 Normalized emission (green) of **TM-E Sil** (donor) and normalized absorption (dark orange) of **DE-E Sil** (acceptor) doped nanoparticles. The overlap region is shown in yellow.

10. Technically, the *Stokes shift* is defined as the "difference [...] between the spectral positions of the Franck–Condon maxima of the lowest energy (highest wavelength) absorption and the luminescence arising from the same electronic transition (the 0-0 bands)", so for multichromophoric systems it is more appropriate to talk about *pseudo Stokes shift*, *i.e.*, the distance between the absorption maximum of the first donor and the emission maximum of the last acceptor. The quote is taken from: S. E. Braslavsky, *Pure & Appl. Chem.* **2007**, *79*, 293.
11. It is safe to make this assumption because all the spectra are compared at the same nanoparticles concentration and were recorded on the same day, on the same instrument, with the same instrumental settings.

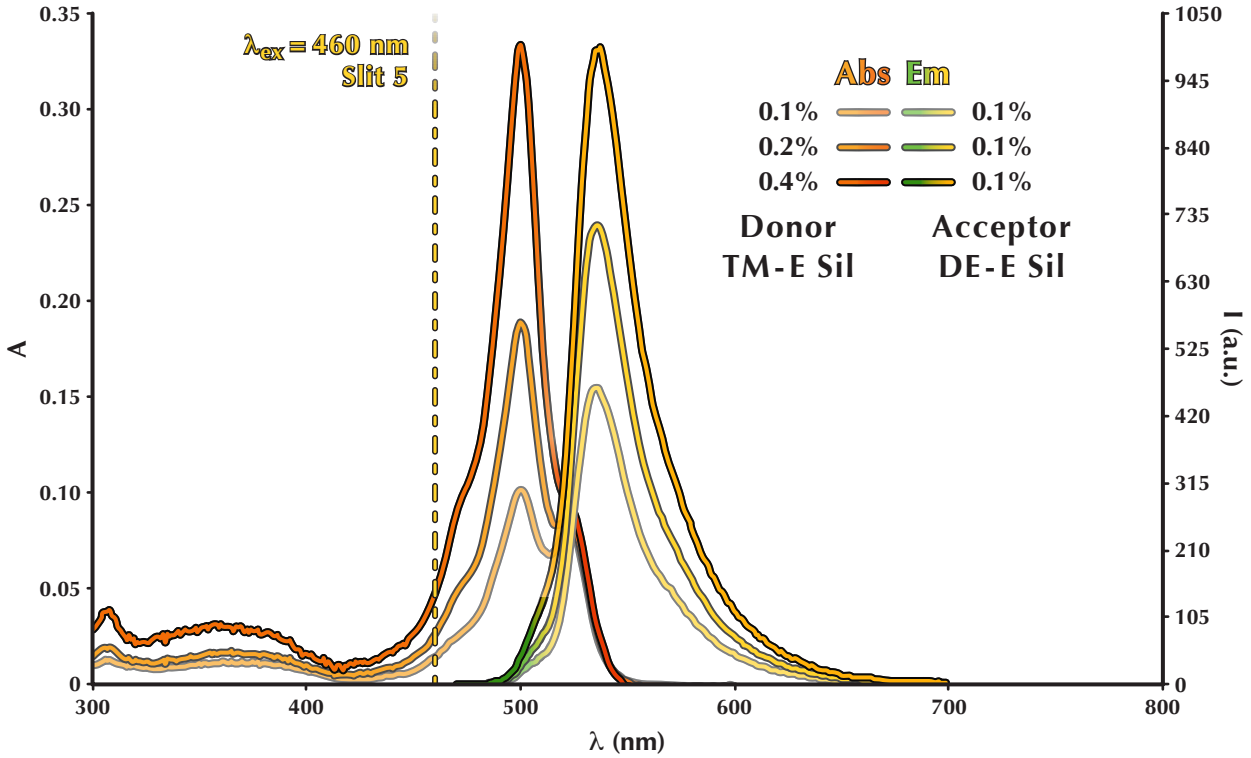

Figure 9 Absorption (orange/dark orange) and emission (green/yellow) spectra of **TM-E Sil** (donor) and **DE-E Sil** (acceptor) doped nanoparticles.

Table 5 Spectroscopic properties of **TM-E Sil/DE-E Sil** doped nanoparticles.

Donor	δδ%	λ abs[a]	η_Q	Acceptor	δδ%	λ abs[a]	λ em[a]	η_S	S S[b]
TM-E Sil	**0.1**	500	0.94	DE-E Sil	**0.1**	523	536	0.99	36
	0.2	500	0.94		**0.1**	522	536	0.84	36
	0.4	500	0.91		**0.1**	–[c]	537	0.60	37

[a] nm; [b] Pseudo Stokes shift, nm; [c] hidden by the absorption band of **TM-E Sil**.

Table 6 Morphological properties of **TM-E Sil/DE-E Sil** doped nanoparticles.

Donor	δδ%	Acceptor	δδ%	Z-Ave[a]	PdI[b]
TM-E Sil	**0.1**	DE-E Sil	**0.1**	23.21 ± 0.17	0.17 ± 0.02
	0.2		**0.1**	22.0 ± 0.2	0.14 ± 0.02
	0.4		**0.1**	23.55 ± 0.15	0.134 ± 0.010

[a] diameter of nanoparticles, nm; [b] polydispersity index.

4.2.1.2 TM-E Sil & DE-E Sil

Given these extremely promising results, another couple of dyes was tested: **TM-E Sil** as donor and again **DE-E Sil** as acceptor; their spectral overlap is shown in figure 8.

As before, the doping level of the acceptor was fixed to 0.1%, while the quantity of the donor was changed, from 0.1 to 0.4%.

Examining the data of table 5, this pair of fluorophores manifests the same behavior of the previous one: the emission of the **TM-E Sil** is almost totally quenched, as the emission of the acceptor is significantly enhanced by increasing the donor doping level.

Table 7 Spectroscopic properties of **TM-B Sil/DE-P Sil** doped nanoparticles.

Donor	δδ%	λ abs[a]	η_Q	Acceptor	δδ%	λ abs[a]	λ em[a]	η_S	S S[b]
TM-B Sil	**0.1**	498	0.94	DE-P Sil	**0.1**	522	534	0.84	36
	0.2	498	0.92		**0.1**	521	534	0.75	36
	0.4	498	0.90		**0.1**	–[c]	534	0.52	36

[a] nm; [b] Pseudo Stokes shift, nm, [c] hidden by the absorption band of **TM-B Sil**.

Table 8 Morphological properties of **TM-B Sil/DE-P Sil** doped nanoparticles.

Donor	δδ%	Acceptor	δδ%	Z-Ave[a]	PdI[b]
TM-B Sil	**0.1**	DE-P Sil	**0.1**	22.28 ± 0.15	0.106 ± 0.008
	0.2		**0.1**	23.08 ± 0.12	0.079 ± 0.016
	0.4		**0.1**	25.5 ± 0.5	0.26 ± 0.03

[a] diameter of nanoparticles, nm; [b] polydispersity index.

4.2.1.3 TM-B Sil & DE-P Sil

After comparing and weighing all the factors – *i.e.*, overall synthetic yield, molar absorption coefficient, quantum yield, and tendency to form aggregates – **TM-B Sil** and **DE-P Sil** seemed to be the fluorophores exhibiting the best performances among each series. For that reason, these dyes were used together in the synthesis of nanoparticles, hoping to further improve the photophysical features. Unfortunately, with respect to the previous case, the **TM-B Sil/DE-P Sil**

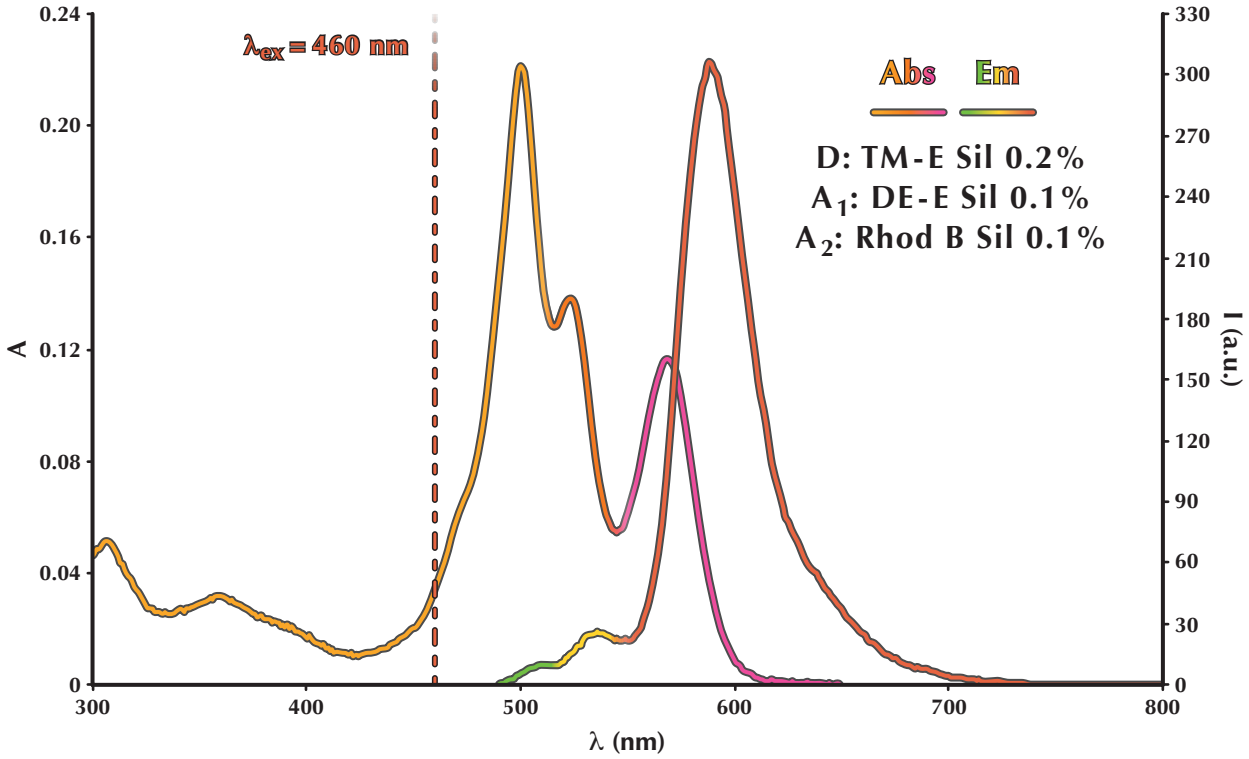

Figure 10 Absorption (orange/dark orange/pink) and emission (green/yellow/light red) spectra of **TM-E Sil** (donor), **DE-E Sil** (first acceptor), and **Rhod B Sil** (second acceptor) doped nanoparticles.

couple seems to be slightly inferior,[12] especially regarding the efficiency of sensitization. In addition, the most doped sample shows a mediocre value of polydispersity.

4.2.2 Three dye doped nanoparticles

4.2.2.1 TM-E Sil, DE-E Sil & Rhod B Sil

In order to get a wider pseudo Stokes shift, a three component system was prepared; the triethoxysilane fluorophores employed in the synthesis are **TM-E Sil**, **DE-E Sil**, and **Rhod B Sil** (doping levels are shown in figure 10 or in tables 9 and 10).

The Förster interaction is still extremely efficient: all the calculated values, both for quenching and sensitization, are close to unity. With respect to the sample containing only **TM-E Sil** and **DE-E Sil**, the presence of **Rhod B Sil** shifts the system emission to 568 nm (versus 536 nm), while the excitation wavelength is kept at 460 nm.

Morphological characterization reveal that the nanoparticles diameter expands a little, but nevertheless the monodispersity remains good.

Table 9 Spectroscopic properties of **TM-E Sil/DE-E Sil/Rhod B Sil** doped nanoparticles.

Donor	λ abs[a]	η_Q	First acceptor	λ abs[a]	η_Q	Second acceptor	λ abs[a]	λ em[a]	η_S	S S[b]
TM-E Sil 0.2%	500	0.99	**DE-E Sil 0.1%**	523	0.95	**Rhod B Sil 0.1%**	568	588	0.96	88

[a] nm; [b] Pseudo Stokes shift, nm.

Table 10 Morphological properties of **TM-E Sil/DE-E Sil/Rhod B Sil** doped nanoparticles.

Donor	δδ%	First acceptor	δδ%	Second acceptor	δδ%	Z-Ave[a]	PdI[b]
TM-E Sil	**0.2**	**DE-E Sil**	**0.1**	**Rhod B Sil**	**0.1**	25.17 ± 0.14	0.14 ± 0.03

[a] diameter of nanoparticles, nm; [b] polydispersity index.

4.2.2.2 TM-B Sil, DE-E Sil & DE-P mSA Sil

Another three component system was synthesized, replacing **Rhod B Sil** with the BODIPY monoadduct **DE-P mSA Sil**, whose emission is slightly red shifted.

In this case, the quenching efficiency of the donor could not be calculated, because the sample containing only the two acceptors (required for its assessment) was not synthesized, due to a lack of enough amount of **DE-P mSA Sil**. Still, taking into account the fact that **DE-E Sil** is totally quenched, and qualitatively judging the emission spectrum in figure 11, where the contribution coming from **TM-B Sil** is insignificant, it is safe to assume the energy transfer from the donor to be complete.

As in the previous case, one can note that nanoparticles seem to be bigger than usual; anyway the polydispersity index is excellent.

12. Absorption and emission spectra are not shown, because they are practically identical to the previous ones.

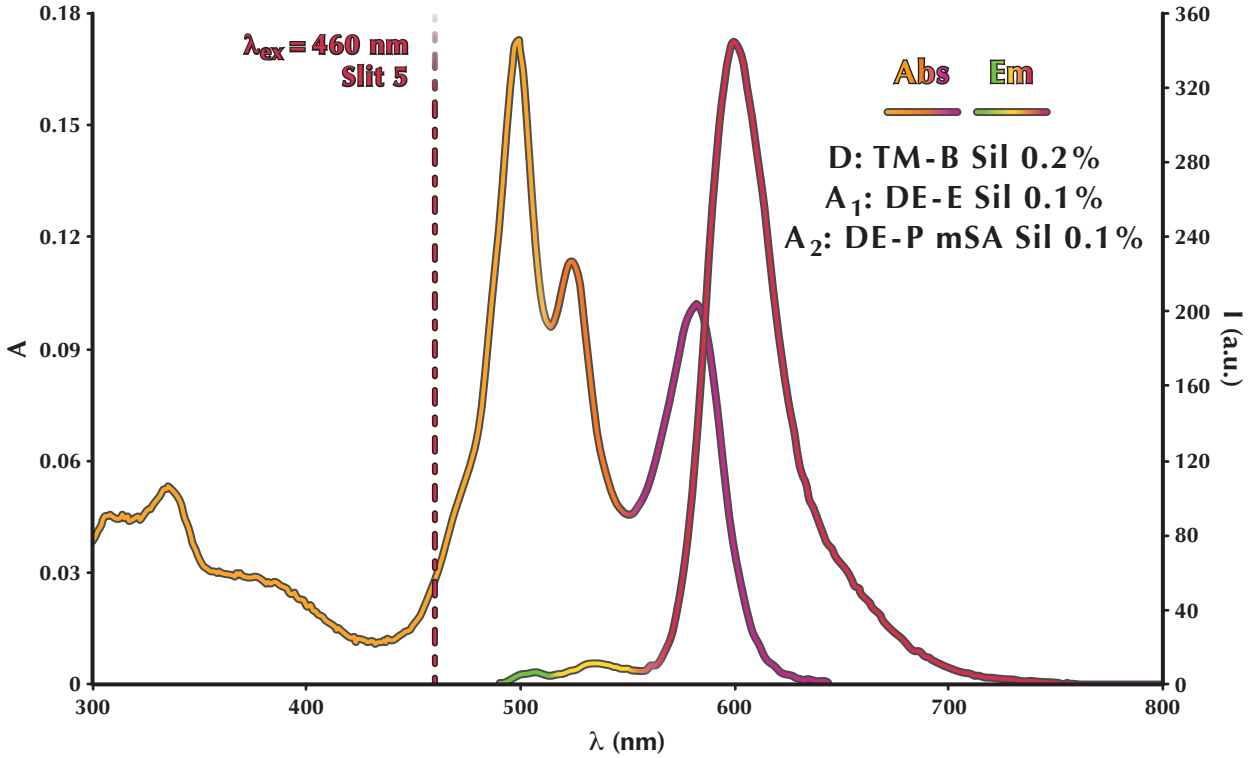

Figure 11 Absorption (orange/dark orange/purple) and emission (green/yellow/crimson red) spectra of **TM-B Sil** (donor), **DE-E Sil** (first acceptor), and **DE-P mSA Sil** (second acceptor) doped nanoparticles.

Table 11 Spectroscopic properties of **TM-B Sil/DE-E Sil/DE-P mSA Sil** doped nanoparticles.

Donor	λ abs[a]	η_Q	First acceptor	λ abs[a]	η_Q	Second acceptor	λ abs[a]	λ em[a]	η_S	S S[b]
TM-B Sil 0.2%	499	–[c]	**DE-E Sil 0.1%**	523	0.99	**DE-P mSA Sil 0.1%**	582	599	0.84	100

[a] nm; [b] Pseudo Stokes shift, nm; [c] not determined.

Table 12 Morphological properties of **TM-B Sil/DE-E Sil/DE-P mSA Sil** doped nanoparticles.

Donor	δδ%	First acceptor	δδ%	Second acceptor	δδ%	Z-Ave[a]	PdI[b]
TM-B Sil	**0.2**	**DE-E Sil**	**0.1**	**DE-P mSA Sil**	**0.1**	26.2±0.6	0.07±0.03

[a] diameter of nanoparticles, nm; [b] polydispersity index.

4.2.3 Four dye doped nanoparticles

Finally, a sample containing four different kinds of dye – namely **TM-E Sil**, **DE-E Sil**, **Rhod B Sil**, and **TM-P dSB Sil**– was synthesized. No quenching or sensitization efficiencies were calculated; this system was prepared to verify qualitatively the possibility to further extend the energy transfer toward the red.

The absorption and emission spectra of figure 12 clearly show that the Förster interaction is still occurring at high rate: the most intense band belongs to the lowest energy emitter, while the others are greatly diminished. Compared to the other samples, the intensity of the emission is weaker, but only because the last acceptor – **TM-P dSB Sil** – has the lowest quantum yield among all the molecules synthesized.

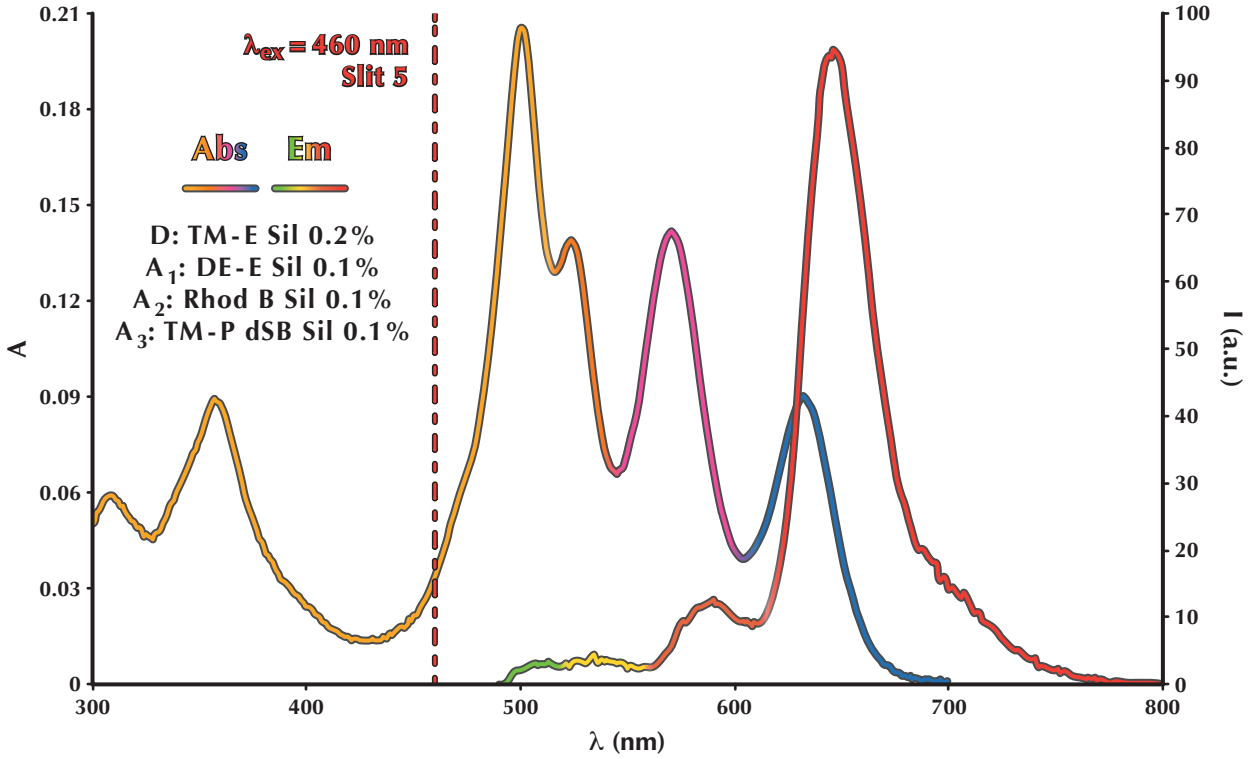

Figure 12 Absorption (orange/dark orange/pink/blue) and emission (green/yellow/light red/red) spectra of **TM-E Sil** (donor), **DE-E Sil** (first acceptor), **Rhod B Sil** (second acceptor) and **TM-P dSB Sil** (third acceptor) doped nanoparticles.

Table 13 Spectroscopic properties of **TM-E Sil/DE-E Sil/Rhod B Sil/TM-P dSB Sil** doped nanoparticles.

Donor	λ abs[a]	First acceptor	λ abs[a]	Second acceptor	λ abs[a]	Third acceptor	λ abs[a]	λ em[a]	S S[b]
TM-E Sil 0.2%	501	**DE-E Sil 0.1%**	524	**Rhod B Sil 0.1%**	570	**TM-P dSB Sil 0.1%**	632	646	145

[a] nm; [b] Pseudo Stokes shift, nm.

4.3 Conclusions

Silica nanoparticles have proven themselves an excellent platform for highly efficient FRET processes, thanks to the close proximity of the molecules grafted onto the silica matrix. The high values calculated for the quenching and sensitization efficiencies – practically at all doping levels – show that these energy pathways are faster than self-quenching, thus overcoming the drawback encountered in the previous chapter regarding the decrease in quantum yield of single dye doped nanoparticles. The residual emission of the donor dyes is almost negligible in all the cases discussed: their excitation energy rapidly moves forward to the acceptor, whose emission band always predominates. By varying the doping level of the donor toward high values, while keeping low that of the acceptor, the intensity of the nanoparticles emission increases almost linearly, limited only by the quantum yield of the lowest energy emitter .

The FRET efficiency remains very high even in three or four dye systems: as a result, the pseudo Stokes shift gets wider and wider. This is an attractive feature for multiplexing analysis: in fact, using the same excitation wavelength, the final emission can be conveniently tuned, simply by choosing the correct mixture of dyes to be included in the nanoparticle. In our case, for example, setting the excitation wavelength at 460 nm, the emission maxima range from 510 nm (**TM** series, single fluorophore system), up to 646 nm (four dye doped nanoparticles).

Part II

Biotechnological applications

Chapter 5
Fluorescent chemosensor†

5.1 Introduction

The design of fluorescent chemosensors for biologically relevant chemical species has important impacts in many applications, and for this reason it has been the subject of active research in many laboratories worldwide. The achievements in this wide research topic have promoted enormous steps forwards, for example, in the field of cell biology, thanks to the comprehension of the role of different chemical species in many biological processes. Recently, researchers have been moving from molecular chemosensors based on two communicating units, a receptor and a dye, toward more complex and sophisticated structures, and have tried to push further the limits of sensitivity and selectivity. Many different solutions have been proposed but, among them, sensing systems based on nanoparticles are certainly one of the most interesting and promising.[1,2]

In particular, the use of dye doped silica nanoparticles can offer intriguing advantages,[1-5] such as high sensitivity enhancement through the occurrence of amplification processes,[1,6] the possibility of an internal reference signal, which avoids further calibrations,[2-5,7] and good water solubility. An additional interesting feature is the possibility to monitor chemical species *in vivo*, since silica is a biocompatible material. This feature could be of crucial importance; metallostasis alteration, namely, zinc and copper homeostatic levels, has already been observed both in biological fluids and tissues of patients affected by breast, prostate, lung and gastrointestinal tumors,[8,9] and in some neurodegenerative disorders, like Parkinsons disease and Alzheimers disease.[10]

---

†. This chapter is taken and adapted from: E. Rampazzo, S. Bonacchi, D. Genovese, R. Juris, M. Sgarzi, M. Montalti, L. Prodi, N. Zaccheroni, G. Tomaselli, S. Gentile, C. Satriano, E. Rizzarelli, *Chem. Eur. J.* **2011**, *17*, 13429.

1. (a) L. Prodi, *New J. Chem.* **2005**, *29*, 20; (b) S. Bonacchi, D. Genovese, R. Juris, M. Montalti, L. Prodi, E. Rampazzo, N. Zaccheroni, *Angew. Chem. Int. Ed.* **2011**, *50*, 4056; (c) S. Bonacchi, D. Genovese, R. Juris, M. Montalti, L. Prodi, E. Rampazzo, M. Sgarzi, N. Zaccheroni, *Top. Curr. Chem.* **2011**, *300*, 93.
2. T. Doussineau, A. Schulz, A. Lapresta-Fernandez, A. Moro, S. Körsten, S. Trupp, G. J. Mohr, *Chem. Eur. J.* **2010**, *16*, 10290.
3. L. Wang, K. Wang, S. Santra, X. Zhao, L. R. Hilliard, J. E. Smith, Y. Wu, W. Tan, *Anal. Chem.* **2006**, *78,* 646.
4. A. Burns, H. Ow, U. Wiesner, *Chem. Soc. Rev.* **2006**, *35*, 1028.
5. K.-T. Yong, I. Roy, M. T. Swihart, P. N. Prasad, *J. Mater. Chem.* **2009**, *19*, 4655.
6. (a) M. Montalti, L. Prodi, N. Zaccheroni, *J. Mater. Chem.* **2005**, *15*, 2810; (b) S. Bonacchi, E. Rampazzo, M. Montalti, L. Prodi, N. Zaccheroni, F. Mancin, P. Teolato, *Langmuir* **2008**, *24*, 8387; (c) E. Oliveira, D. Genovese, R. Juris, N. Zaccheroni, J. L. Capelo, M. M. M. Raposo, S. P. G. Costa, L. Prodi, C. Lodeiro, *Inorg. Chem.* **2011**, *50*, 8834.
7. P. Teolato, E. Rampazzo, M. Arduini, F. Mancin, P. Tecilla, U. Tonellato, *Chem. Eur. J.* **2007**, *13*, 2238.
8. (a) R. B. Franklin, L. C. Costello, *Arch. Biochem. Biophys.* **2007**, *463*, 211; (b) A. Gonzalez, M. Peters, J. W. Lampe, E. White, *Nutr. Cancer* **2009**, *61*, 206.
9. (a) Q. Pasha, S. A. Malik, J. Iqbal, N. Shaheen, M. H. Shah, *Biol. Trace Elem. Res.* **2008**, *125*, 30; (b) M. Yaman, *Curr. Med. Chem.* **2006**, *13,* 2513.
10. (a) A. I. Bush, *Curr. Opin. Chem. Biol.* **2000**, *4*, 184; (b) K. J. Barnham, A. I. Bush, *Curr. Opin. Chem. Biol.* **2008**, *12*, 222.

Specifically, copper has been implicated in Amyloid β peptide aggregation and neurotoxicity, and it is generally accepted that in Alzheimers disease brain tissue there is an excess of Cu^+ in the extracellular space and in amyloid plaques.[11,12] On the other hand, a decrease of intracellular copper, as compared to healthy control brain tissue, has also been reported.[12] All these findings highlight the need for new efficient chemosensors for copper ions.[13]

5.2 Hosting molecules within the shell

In this context – as described in chapter 2 and 3 – we have developed a new one-pot approach for the synthesis of core-shell dye doped silica nanoparticles based on the preparation of micelles of Pluronic® F127 in water.[1b,14] The final material is a versatile multicompartment system characterized by high water solubility, stability, and brightness. Most interestingly, we have also demonstrated the possibility of hosting water-insoluble dyes even in the outer shell, which are able to give rise to very efficient energy transfer processes with the molecules hosted in the core.[15] Thanks to the unique structure and properties of these nanoparticles, their application in sensing can be envisaged to involved a new type of transduction mechanism based on the addition of a hydrophobic chemosensor to a water solution of the nanoparticles (see figure 1). It must be underlined, that the requirement related to the hydrophobicity is not a limitation; rather, it makes possible the use of a large series of systems that are usually precluded due to their insolubility in water-based environments.

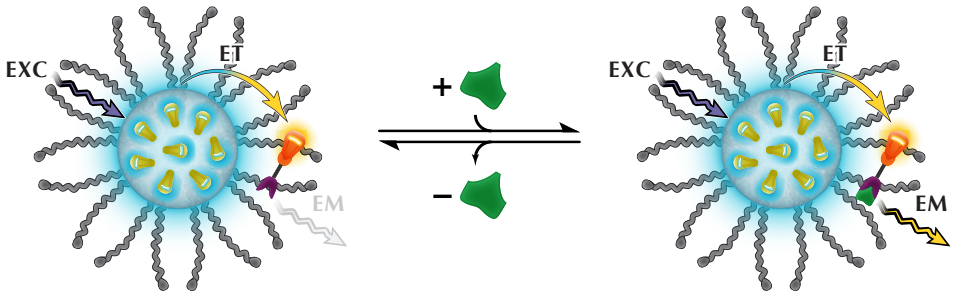

Figure 1 Schematic representation of the proposed transduction mechanism (EXC = excitation, ET = energy transfer, EM = emission).

The fundamental requirement in this case is that, upon complexation with the analyte, an efficient energy transfer should occur between the dyes hosted in the core and in the shell. In order to test, as a first step, the proof of principle for this new strategy, we decided to use **1**, a very selective and promising chemosensor for Cu^+.[13a] Given the spectral properties of the BODIPY dye in the structure of the chemosensor, we decided to synthesize a family of nanoparticles

11. P. J. Crouch, K. J. Barnham, A. I. Bush, A. R. White, *Drug News Perspect.* **2006**, *19*, 469.
12. G. Filiz, K. A. Price, A. Caragounis, T. Du, P. J. Crouch, A. R. White, *Eur. Biophys. J.* **2008**, *37*, 315.
13. (a) L. Zeng, E. W. Miller, A. Pralle, E. Y. Isacoff, C. J. Chang, *J. Am. Chem. Soc.* **2006**, *128*, 10; (b) D. W. Domaille, L. Zeng, C. J. Chang, *J. Am. Chem. Soc.* **2010**, *132*, 1194; (c) A. F. Chaudhry, M. Verma, M. T. Morgan, M. M. Henary, N. Siegel, J. M. Hales, J. W. Perry, C. J. Fahrni, *J. Am. Chem. Soc.* **2010**, *132*, 737; (d) A. F. Chaudhry, S. Mandal, K. I. Hardcastle, C. J. Fahrni, *Chem. Sci.* **2011**, *2*, 1016.
14. S. Zanarini, E. Rampazzo, S. Bonacchi, R. Juris, M. Marcaccio, M. Montalti, F. Paolucci, L. Prodi, *J. Am. Chem. Soc.* **2009**, *131*, 14208.
15. (a) E. Rampazzo, S. Bonacchi, R. Juris, M. Montalti, D. Genovese, N. Zaccheroni, L. Prodi, D. C. Rambaldi, A. Zattoni, P. Reschiglian, *J. Phys. Chem. B* **2010**, *114*, 14605; (b) D. Genovese, M. Montalti, L. Prodi, E. Rampazzo, N. Zaccheroni, K. Altenhöner, F. May, J. Mattay, *Chem. Commun.* **2011**, *47*, 10975.

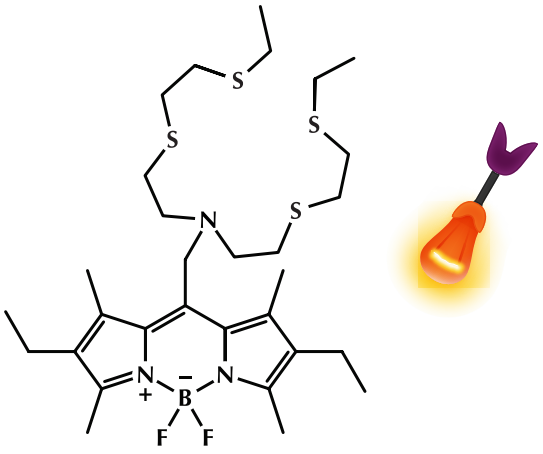

1

Scheme 1 Molecular structure of the BODIPY based Cu^{+}-sensor.

containing an average of ten molecules of **DEAC Sil**,[16] which is a good energy donor for **1**, covalently linked to the silica core (figure 2).

The nanoparticles present a very high absorption coefficient ($\varepsilon = 755000\ M^{-1} \cdot cm^{-1}$) and a very high fluorescence quantum yield ($\Phi = 0.36$). The addition of an increasing amount of **1** (up to 1 equivalent) to the nanoparticle solution ($1.25 \cdot 10^{-7}$ M), buffered at pH 7.2, led to a dramatic decrease of the luminescence intensity of the coumarin dye, with a concomitant linear increase of the fluorescence of the BODIPY moiety (see figure 3). The same results were also observed in the pH range 5.0–8.0; moreover, the addition of bovine serum albumin did not have any influence on these titrations.

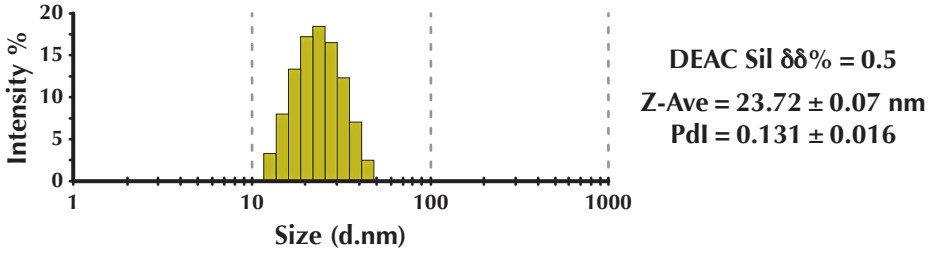

Figure 2 Dynamic light scattering diameter distribution of nanoparticles doped with **DEAC Sil**.

As expected, the fluorescence anisotropy of **1** measured in the absence of nanoparticles is negligible. On the contrary, in the presence of nanoparticles, it becomes as high as 0.25 upon direct excitation of the BODIPY unit ($\lambda_{exc} = 500$ nm); this clearly confirms that **1** is located in the outer shell of the nanoparticles, where it experiences reduced rotational freedom and forms the system **1@NPs**. The measurement of anisotropy can thus be used as an efficient tool to observe whether **1** is inserted in the nanoparticle structure. A negligible value for the fluorescence anisotropy is instead obtained for the same system in the same spectral region (550–700 nm) upon excitation of the coumarin dye ($\lambda_{exc} = 400$ nm). The complete depolarization can be explained, in this case, by the occurrence of an energy transfer process from the coumarin dyes to the BODIPY unit. The efficiency of this process (80%) could be evaluated from the quenching of the coumarin donor, both through analysis of the spectra reported in figure 3 and of the decrease of the donor excited state lifetime. The properties of this system did not change for months, and prove its stability under these conditions.

16. Synthesis and characterization of **DEAC Sil** and preparation of dye doped nanoparticles are described in detail in chapter 8 – Experimental section. Nanoparticles were synthesized in 1 M acetic acid, with TMSCl as terminating agent, using 1.86 mg of **DEAC Sil**.

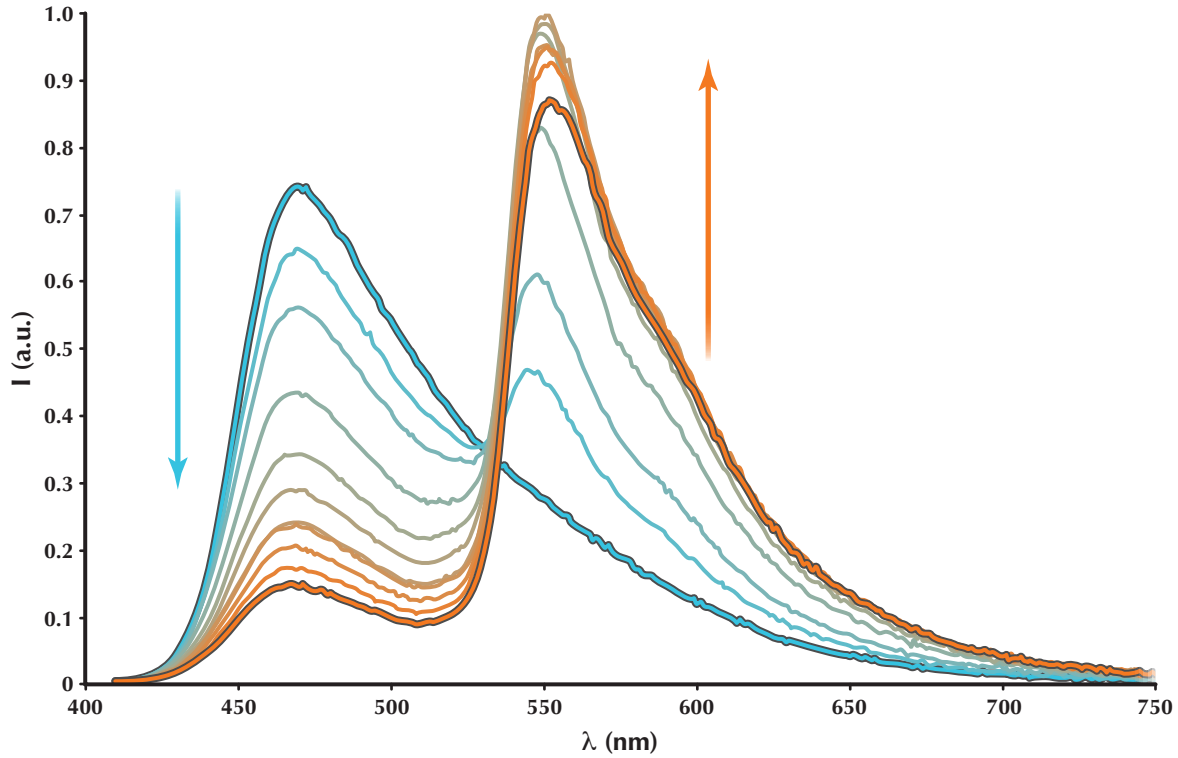

Figure 3 Fluorescence (λ_{exc} = 400 nm) spectra of nanoparticle aqueous solution ($1.25 \cdot 10^{-7}$ M) upon addition of increasing amounts of chemosensor **1**.

5.3 Behavior toward Cu^+

To test the performance of this architecture as a chemosensor, we first added glutathione (1 mM), which has a very high apparent dissociation constant ($9.1 \cdot 10^{-12}$ M) towards Cu^+, in order to mimic cell conditions,[17] without observing any change in the fluorescence intensity. The subsequent addition of Cu^+ ions led to an increase of the absorbance in the 500–600 nm region (see figure 4), as already described[13a] for free **1**.

As far as the fluorescence spectrum is concerned, upon excitation at 400 nm, at which point the light is predominantly absorbed by the coumarin moieties, the complexation process leads to a further decrease of the fluorescence intensity of the coumarin and to an increase of that of the BODIPY unit. This can be seen in figure 5, in which the ratio I_{550}/I_{470} is plotted between the intensities measured at 550 nm (emission of BODIPY) and 470 nm (emission of the coumarin dye) upon excitation at 400 nm versus the equivalents of added metal ion, indicating that this system has a ratiometric nature.

The possibility for the metal ion to be directly involved in the quenching of the fluorescence of the coumarin moieties can be ruled out by the observation that the fluorescence of the coumarin in the nanoparticle is not affected by the addition of Cu^+ in the absence of **1**. Rather, this result can be explained by an increase in the efficiency of the energy transfer process: the observed increase of the absorbance of the acceptor in fact induces an increase of the overlap integral $J(\lambda)$, according to the Förster equation (see chapter 4, equation [4]). This conclusion is further supported by the similarity of the patterns shown by the I_{550}/I_{470} ratio (figure 5, light blue circles) and J^2 (orange circles), which relies on the fact that both the decrease of the coumarin band and the increase of the BODIPY band depend on $J(\lambda)$. We would like to stress that in **1@NPs** the

17. L. Banci, I. Bertini, S. Ciofi-Baffoni, T. Kozyreva, K. Zovo, P. Palumaa, *Nature* **2010**, *465*, 645.

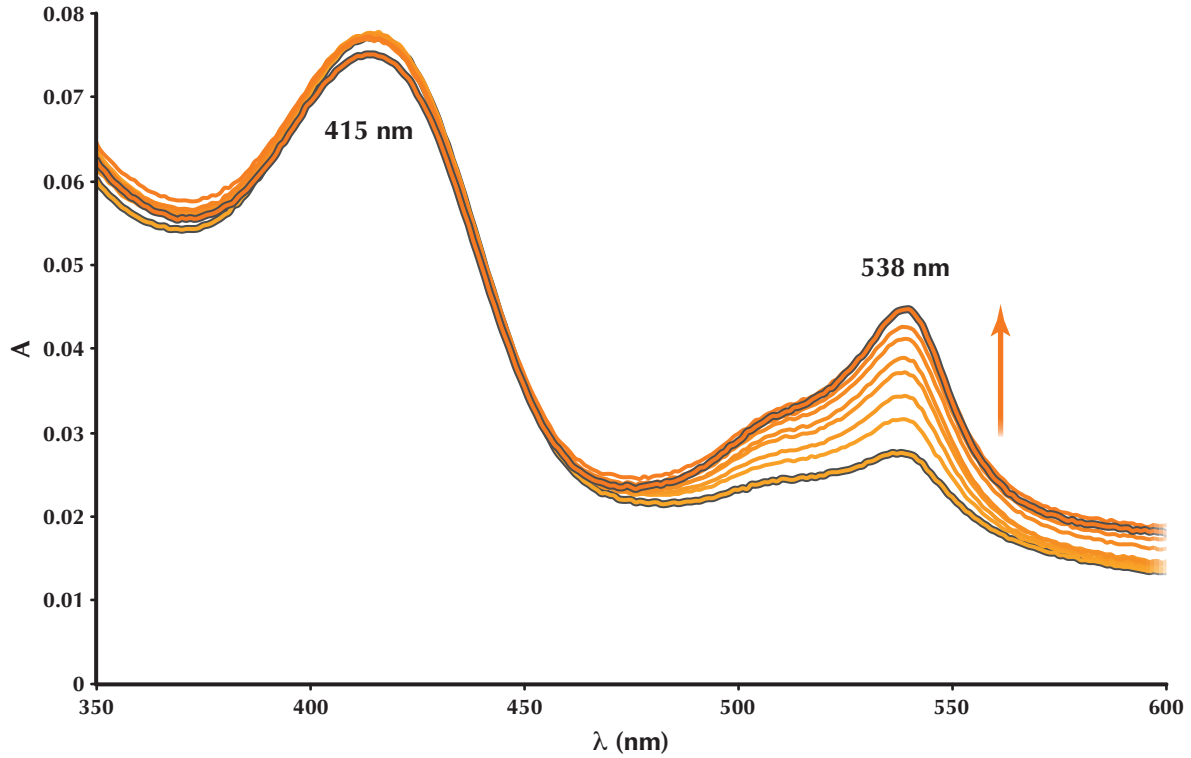

Figure 4 Absorption spectra of an equimolar ($1.25 \cdot 10^{-7}$ M) aqueous solution of nanoparticles and chemosensor **1** upon addition of an increasing amount of Cu^{+} in the presence of glutathione (1 mM).

complexation of a single ion is able to strongly modify the photophysical properties of several dyes (all the coumarin units inside the silica nucleus) at the same time; this induces, among other effects, a very large signal change, which, as in previous cases,[1,6] can be seen as signal amplification.

Interestingly, the dissociation constant between **1** and Cu^{+} was estimated to be $2.2 \cdot 10^{-13}$ M; this indicates that **1@NPs** is able to complex ions with a 16-fold higher affinity than the one shown by free **1** ($K_d = 3.6 \cdot 10^{-12}$ M),[13a] because of the different environment around **1**. Moreover, also the selectivity observed for the free chemosensor was maintained in **1@NPs**; no changes in the absorption and emission spectra were in fact observed upon addition of Cu^{2+}, Zn^{2+}, and Cd^{2+}, even in a 1000-fold excess, both in the presence or absence of glutathione (data not shown). All these results, therefore, show that the assembly **1@NPs**, can compete even with some cytoplasmic copper chaperones and small Cu^{+} ligands in binding copper in a marked selective manner.[18]

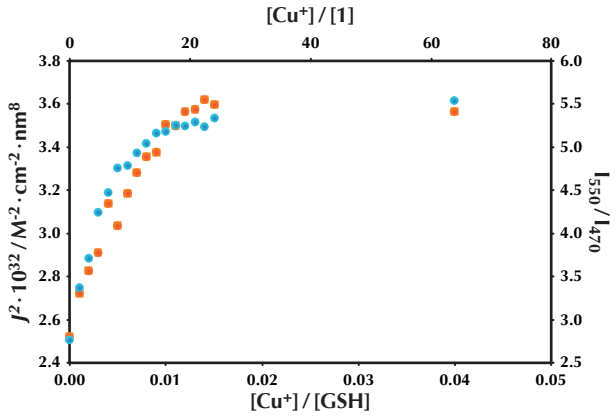

Figure 5 Ratio of the fluorescence intensities measured at 550 and 470 nm ($\lambda_{exc} = 400$ nm, light blue) of an equimolar ($1.25 \cdot 10^{-7}$ M) aqueous solution of nanoparticles and chemosensor **1** upon addition of an increasing amount of Cu^{+} in the presence of glutathione (1 mM) and the square of the overlap integral, J^2, calculated according to the Förster equation (orange).

18. L. A. Finney, T. V. O'Halloran, *Science* **2003**, *300*, 931.

5.4 Live cell fluorescence imaging

This experiment was performed in order to assess whether:

- the newly developed **1@NPs** system is cell permeable, as the free sensor **1**;
- the sensing capability towards intracellular Cu^{+} species, in terms of BODIPY-related emission enhancement ($\lambda_{em} \approx 570$ nm), is changed with respect to the well-established sensor system **1**.[13a]

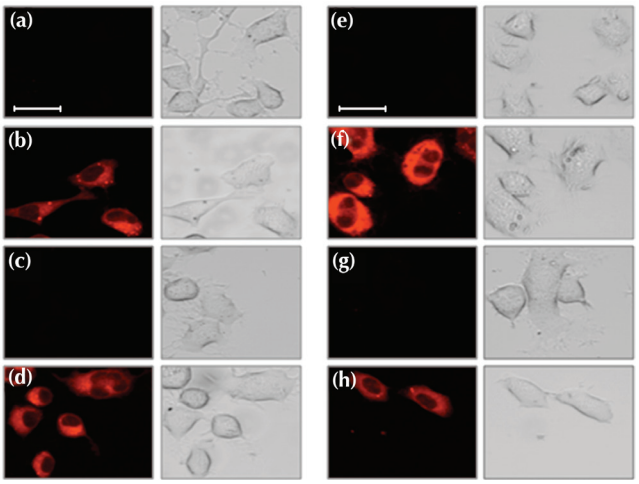

Figure 6 Confocal microscopy emission ($\lambda_{exc} = 543$ nm; $\lambda_{em} = 572$ nm) and corresponding bright-field images for the SHSY5Y cell line: a)–d) cultured in DMEM medium for 24 h, and e)–h) supplemented with $CuCl_2$ (100 μM) for 5 h, incubated at 37 °C. The probe treatments (5 min incubation at 25 °C, then rinsed with PBS) are as follows: a), e) control PBS; b), f) Cu^{+} sensor **1** (5 μM); c), g) nanoparticles (5 μM); d), h) **1@NPs** complex (5 μM; 1:1 molar ratio); scale bar: 30 μm.

Figure 6 shows the fluorescence response of neuroblastoma SHSY5Y cell line, for the different sensor and control treatments, both without exogenous copper addition and with $CuCl_2$ (100 μM) supplemented medium. It is evident that while the cells exposed to the free sensor **1** as well as those incubated with the equimolar **1@NPs** solution exhibit a localized intracellular emission at 570 nm (by excitation at 543 nm), this is not the case for either the cells incubated with nanoparticles or the control samples. These findings point to the fact that **1** in its complexed form with the nanoparticles maintains high selectivity and binds the intracellular Cu^{+}. In fact, due to the absence of emission for the cells treated with the nanoparticles alone, one can rule out the possibility that other intracellular components invoke the observed fluorescence response.

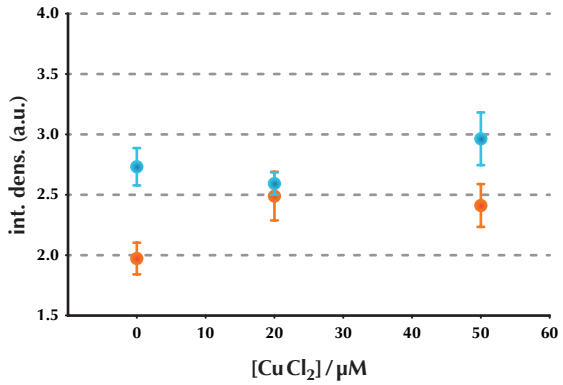

Figure 7 Mean values of integrated density from fluorescence micrographs ($\lambda_{exc} = 552$ nm; $\lambda_{em} = 578$ nm) of SHSY5Y cells after treatment with 5 μM solutions of free **1** sensor (orange circles) or **1@NPs** complex (light blue circles) as function of the Cu^{2+} concentration supplemented in the culture media. Error bars indicate the standard error of means.

Interestingly, the quantitative analysis of fluorescence micrographs shown in figure 7, in the explored Cu^{2+} concentration range (0–50 μM), evidence that the **1@NPs** system is more efficient – up to about 35% of emission enhancement – than the free sensor **1** (while for 100 μM CuCl2 supplemented cells the two probe systems are substantially equivalent).

This is an obvious advantage of the nanoparticle-complexed sensor with respect to the *standard* copper sensor **1**, because under physiological conditions the concentration of copper, in vivo, is typically in the order of tens of μM, and higher levels can be toxic and/or related to a pathological condition for several cell lines.[19]

The observed behavior of the copper sensor complexed with the nanoparticles can be explained in terms of the higher binding affinity to intracellular copper of the **1@NPs** system compared to the free sensor **1**, and takes into account a concentration saturation effect. The apparent Cu^{+} dissociation constant of **1@NPs** is about one order of magnitude lower than that reported for the free **1**. For this reason our system exhibits a higher efficiency in cells upon sensor uptake, without any addition of exogenous copper. A simplified simulation model of species distribution for Cu^{+}-binding ligands in the intracellular environment was carried out by taking into account the recently determined dissociation constants for several copper chaperones and low-mass ligands (see figure 8).[17]

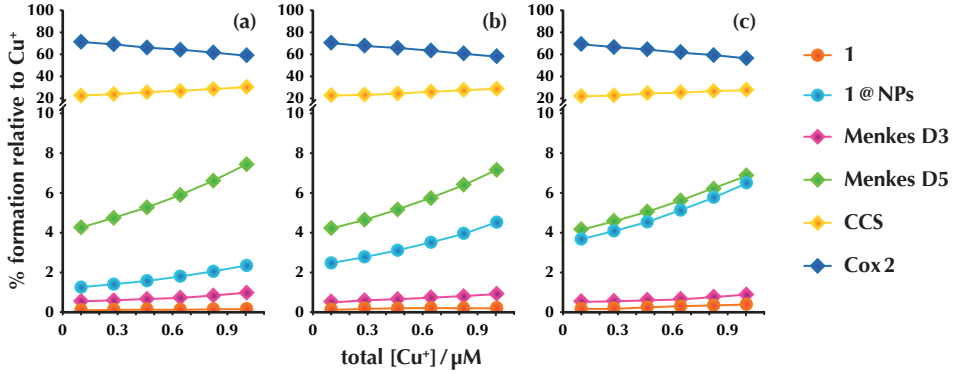

Figure 8 Speciation plots for 5 μM (a), 10 μM (b) and 15 μM (c) solutions of **1@NPs** and free **1** in a simulated intracellular environment with total Cu^{+} concentration ranging from 10^{-7} to 10^{-6} M and some representative copper chaperones and low-mass ligands (Cox2, Ccs, Menkes D5, Menkes D3).

The results show that while copper sensor **1** (5 μM) has always the lowest binding affinity to Cu^{+} at the examined conditions, the **1@NPs** system might compete for Cu^{+} binding with some of the intracellular copper chaperones and/or intracellular ligands at lower binding affinity.[17] This effect is even superior when the **1@NPs** concentration is increased, and could be related to the observed enhancement of intracellular fluorescence without exogenous copper addition compared to the free **1** sensor. Accordingly, for the Cu^{2+} supplemented cells, the **1@NPs**-incubated samples likely suffer from a saturation effect. This interpretation is supported by preliminary measurements performed at higher probe concentrations (10 μM), the results for which show a relative increa se of emission enhancement for the **1@NPs**-treated cells upon exogenous copper addition (see figure 9). Further measurements by systematically varying the concentration of the **1@NPs** system as well as the relative molar ratio between the sensor **1** and the nanoparticles will elucidate this point.

19. (a) L. Tapia, M Gonzalez-Agüero, M. F. Cisternas, M. Suazo, V. Cambiazo, R. Uauy, M. González, *Biochem. J.* **2004**, *378*, 617; (b) H. W. Chan, T. Liu, G. Verdile, G. Bishop, R. J. Haasl, M. A. Smith, G. Perry, R. N. Martins, C. S. Atwood, *Int. J. Clin. Exp. Med.* **2008**, *1*, 76.

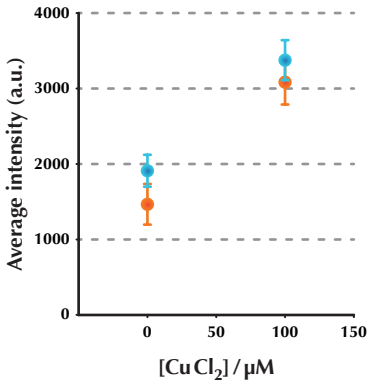

Figure 9 Average intensities of emission measured at 572 nm (λ_{exc} = 543 nm) for regions of interest defined in the intracellular areas and integrated over ten z-stacks (overall depth measured = 7.6 µm) for 10 µM of free **1** sensor (orange circles) or **1@NPs** complex (light blue circles), in the absence of copper addition and with 100 µM $CuCl_2$ addition.

5.5 Conclusions

The strategy for signal amplification that we have described here, for the first time, appears very effective and presents many advantages, such as:

- a significant signal increase due to the much higher absorption of the nanoparticle compared to that of the single chemosensor;
- less noise, because of the larger separation between excitation and emission wavelengths;
- the possibility to apply ratiometric measurements, which avoids external calibration procedures;
- a high versatility that makes it possible to massively enlarge the library of the possible chemosensors to be exploited.

In addition, the advantage of the greater affinity shown by the **1@NPs** system endows it with an enhanced detection capability for intracellular Cu^+ either in the absence or at low concentrations of exogenous metal ion. Moreover, it can suggest its application in proteostasis processes, an additional possibility that will be further examined. For all these reasons, we strongly believe that this concept is very general and can be widely extended in many possible applications to obtain a large increase of the sensitivity in the fundamental field of chemical sensing.

Addendum – Determination of dissociation constant

Apparent value of K_d for Cu^+-**1** complex was calculated according to the following simplified reaction scheme:

$$Cu^+\text{–GSH} \xrightarrow{K_{GSH}} Cu^+ + \text{GSH} \qquad [1]$$

$$Cu^+\text{–}\mathbf{1} \xrightarrow{K_d} Cu^+ + \mathbf{1} \qquad [2]$$

where $K_{GSH} = 9.13 \cdot 10^{-15}$ M is the known dissociation constant for the Cu^+-glutathione complex.[17] In a solution of glutathione at constant concentration, the concentration of free Cu^+ for increasing total concentration of Cu^+ can be calculated from the equilibrium of reaction [1], and then used to calculate K_d. For this purpose we correlate the fluorescence intensity signal (either

decrease of coumarin emission or increase of bodipy emission), which signals the formation of Cu^+-**1** complex, with the concentration of free Cu^+, as previously reported:[20]

$$[Cu^+ - \mathbf{1}] = K_d \cdot \frac{[1]_t \cdot [Cu^+]_f}{1 + K_d \cdot [Cu^+]_f} \qquad [3]$$

where [Cu^+-**1**] is the concentration of the complex, $[\mathbf{1}]_t$ the total concentration of **1**, $[Cu^+]_f$ the concentration of free Cu^+, as calculated from equation [3]. The fitting of experimental fluorescence data with equation [5] provides an estimate for the dissociation constant of **1** in nanoparticles, $K_d = 2.2 \cdot 10^{-13}$ M, which is roughly one order magnitude higher than the dissociation constant for **1** as molecular sensor.

20. L. E. Wilkinson-White, S. B. Easterbrook-Smith, *J. Inorg. Biochem.* **2008**, *102*, 1831.

Chapter 6
Fluorescent label†

6.1 Introduction

Optical imaging of live animals has grown to be an important tool in biomedical research as advances in photonic technology and reporter strategies have led to widespread exploration of biological processes *in vivo*.[1] Fluorescent labeling is, in fact, an ideal tool for understanding the complex spatial-temporal interplay of biomolecules from the cellular to the integrative level.[2-5] Typical limitations of the biological environment due to background signals and low transparency of the tissues can be overcome by performing excitation and detection in the near infrared (NIR) region.[2-8] Nevertheless, although optical memory storage and telecommunication industries provide suitable diode laser sources and detectors for such a spectral window, optimizing the luminescence properties of reporter materials working in this range is far from being a trivial challenge. Semiconductor nano-crystals (quantum dots),[7-11] that are considered at the moment

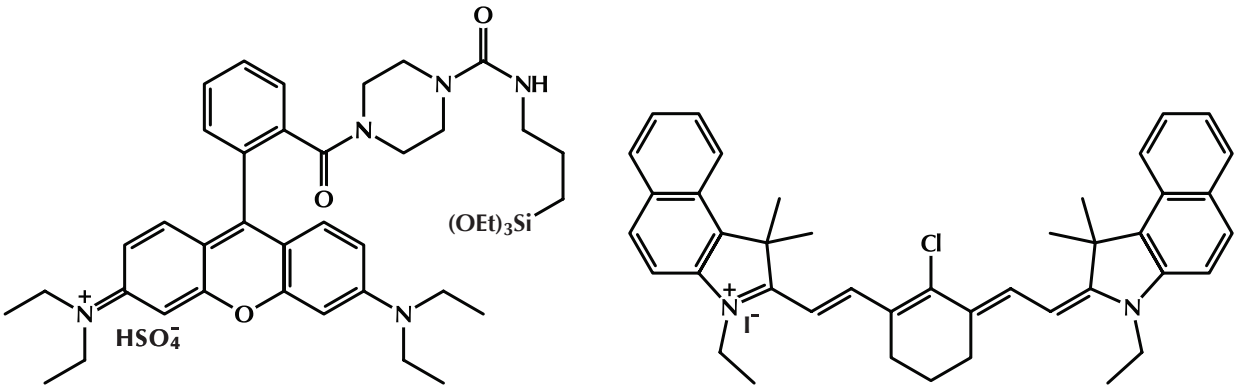

Rhod B Sil **C7**

Scheme 1 Molecular structures of the rhodamine derivative **Rhod B Sil** and of the polymethine dye **C7**.

†. This chapter is taken and adapted from: E. Rampazzo, F. Boschi, S. Bonacchi, R. Juris, M. Montalti, N. Zaccheroni, L. Prodi, L. Calderan, B. Rossi, S. Becchi, A. Sbarbati, *Nanoscale* **2012**, *4*, 824.

1. V. Nziachristos, J. Ripoll, L. V. Wang, R. Weissleder, *Nat. Biotechnol.* **2005**, *23*, 313.
2. J. V. Frangioni, *Curr. Opin. Chem. Biol.* **2003**, *7*, 626.
3. A. Masotti, P. Vicennati, F. Boschi, L. Calderan, A. Sbarbati, G. Ortaggi, *Bioconj. Chem.* **2008**, *19*, 983.
4. J. Rao, A. Dragulescu-Andrasi, *Curr. Opin. Biotechnol.* **2007**, *18*, 17.
5. L. Prodi, *New J. Chem.* **2005**, *29*, 20.
6. M. Montalti, N. Zaccheroni, L. Prodi, N. O'Reilly, S. L. James, *J. Am. Chem. Soc.* **2007**, *129*, 2418.
7. E. H. Sargent, *Adv. Mater.* **2005**, *17*, 515.
8. S. Hinds, S. Myrskog, L. Levina, G. Koleilat, J. Yang, S. O. Kelley, E. H. Sargent, *J. Am. Chem. Soc.* **2007**, *129*, 7218.
9. I. L. Medintz, H. T. Uyeda, E. R. Goldman, H. Mattoussi, *Nat. Mater.* **2005**, *1*, 435.
10. X. Michalet, F. F. Pinaud, L. A. Bentolila, J. M. Tsay, S. Doose, J. J. Li, G. Sundaresan, A. M. Wu, S. S. Gambhir, S. Weiss, *Science* **2005**, *307*, 538.
11. M. Bruchez Jr, M. Moronne, P. Gin, S. Weiss, A. P. Alivisatos, *Science* **1998**, *281*, 2013.

the most promising emitters, typically have a rather high luminescence quantum yield, but their brightness, defined as the product $\varepsilon \cdot \Phi$, is relatively low upon NIR excitation because of their decreasing molar absorption coefficient above 750 nm (less than $2 \cdot 10^5\ M^{-1} \cdot cm^{-1}$).

In this context, dye doped silica nanoparticles are another important class of nanoarchitectures since, together with a high brightness, they present a much lower toxicity related to the constituent materials.[12-19] In this chapter, NIR emitting nanoparticles will be presented, obtained with the method described in chapter 2 and 3, endowed with a high molar absorption coefficient (ε up to $3 \cdot 10^6\ M^{-1} \cdot cm^{-1}$) in the 750-850 nm excitation window and a fluorescence quantum yield comparable to that of quantum dots.

The fluorescence of these nanoparticles is due to the encapsulation of molecules of the poorly water soluble polymethine dye **C7**. This dye was chosen for its particularly suitable photophysical properties to perform in vivo experiments in the best part of the transparency window of the biological tissues (700-900 nm). Water dispersions of these nanoparticles did not show any flocculation or dye leaching even after months from the preparation. Moreover, the inclusion of **C7** in the core-shell nanoparticles prevents self-aggregation of the dyes with a concomitant 50-fold increase of its relatively low fluorescence quantum yield in water solution.

In addition, the versatility of the synthetic methodology allows the insertion of different classes of dyes in the same nanoparticle, and we decided to include, together with dye **C7**, the pH insensitive rhodamine B derivative **Rhod B Sil**. This makes the same nanoparticles suitable also for *ex vivo* imaging, since most common microscopes are generally equipped for monitoring only visible light.

Furthermore, it is important to note that the nanoparticles containing both **C7** and **Rhod B Sil**, upon excitation at 980 nm, showed also an emission band at 610 nm due to two-photon absorption, a very valuable property that could allow two-photon microscopy (TPM) imaging. TPM provides three-dimensional optical sectioning with increased depth penetration as compared to confocal microscopy and, strongly reducing photobleaching and phototoxicity effects, allows long-term visualization of the analyte motility in the living tissue or intact animal specimens.

6.2 Results & Discussion

6.2.1 Synthesis and characterization of nanoparticles

Three different sets of nanoparticles, **Rh@NPs**, **C7@NPs**, and **Rh+C7@NPs** were prepared following the same synthetic procedure, but using different amounts of the dyes **C7** and **Rhod B Sil**.[20] Dye molecules in excess, hence not covalently linked or entrapped in the nanoparticles, were

12. A. Burns, H. Ow, U. Wiesner, *Chem. Soc. Rev.* **2006**, *35*, 1028.
13. E. Herz, H. Ow, D. Bonner, A. Burns, U. Wiesner, *J. Mater. Chem.* **2009**, *19*, 6341.
14. K.-T. Yong, I. Roy, M. T. Swihart, P. N. Prasad, *J. Mater. Chem.* **2009**, *19*, 4655.
15. L. Wang, W. Zhao, W. Tan, *Nano Res.* **2008**, *1*, 99.
16. M.-C. Estevez, M. B. O'Donoghue, X. Chen, W. Tan, *Nano Res.* **2009**, *2*, 448.
17. M. Wang, M. Thanou, *Pharmacol. Res.* **2010**, *62*, 90.
18. S. Bonacchi, D. Genovese, R. Juris, M. Montalti, L. Prodi, E. Rampazzo, M. Sgarzi, N. Zaccheroni, *Top. Curr. Chem.* **2011**, *300*, 93.
19. S. Bonacchi, D. Genovese, R. Juris, M. Montalti, L. Prodi, E. Rampazzo, N. Zaccheroni, *Angew. Chem. Int. Ed.* **2011**, *50*, 4056.
20. Synthesis of dye doped nanoparticles is described in detail in chapter 8 – Experimental section. These samples were prepared in 1 M acetic acid, with DEDMS as terminating agent, using 0.69 mg of **Rhod B Sil**, and/or 1.18 mg of **C7.**

Table 1 Morphological and photophysical properties of the different silica nanoparticles and their doping dyes.

Sample	Solvent	d_H[a]	d_C[b] (PdI)[c]	n° dyes[d]	λ abs[e]	ε[f]	λ em[e]	Φ[g]
Rhod B Sil	EtOH	–	–	–	562	$1.0 \cdot 10^5$	580	0.35
Rh@NPs	H_2O	11 ± 3	24 (0.03)	3.7	570	$3.7 \cdot 10^5$	588	0.47
C7	EtOH	–	–	–	820	$2.1 \cdot 10^5$	845	0.043
C7@NPs	H_2O	11 ± 3	24 (0.03)	3.1	830	$6.5 \cdot 10^5$	855	0.040
Rh+C7 @NPs	H_2O	11 ± 3	25 (0.03)	3.0[h] 3.5[i]	570[h] 830[i]	$3.0 \cdot 10^5$[h] $7.4 \cdot 10^5$[i]	587[h] 855[i]	0.12[h] 0.040[i]
QDs 800	H_2O	–	36 (0.04)[j]	–	750	$1.3 \cdot 10^5$	800	0.13

[a] diameter (nm) of the silica core (TEM); [b] hydrodinamic diameter (nm) of the nanoparticle (DLS); [c] polydispersity index; [d] mean number of dyes per nanoparticle; [e] nm; [f] $M^{-1} \cdot cm^{-1}$; [g] rhodamine B in ehtanol (Φ = 0.49) and cyanine IR-125 in dimethyl sulfoxide (Φ = 0.13) were used as reference; [h] related to **Rhod B Sil**; [i] related to **C7**; [j] after filtration with a 0.20 μm regenerated cellulose filter.

removed by ultrafiltration. The concentration of nanoparticles was determined with static light scattering measurements as previously reported,[21] and in this way it was possible to determine their absorption coefficient. The mean number of dyes per nanoparticle was then calculated assuming that the absorption coefficient of the dyes remains unchanged upon inclusion in the silica matrix.

Very interestingly, the hydrodynamic radius, d_H, measured by dynamic light scattering (see figure 1 for **Rh+C7@NPs**), and the diameter of the silica nuclei, d_C, observed by TEM (see figure 2 for **Rh+C7@NPs**), resulted to be independent on the doping degree (see table 1). Worth noticing is the very low polydispersity index (PdI) for all the samples observed, indicating that this synthetic strategy leads to a highly reproducible, very monodisperse nanomaterial. This is an additional advantage compared to quantum dots, whose production reproducibility represents a major concern.[22]

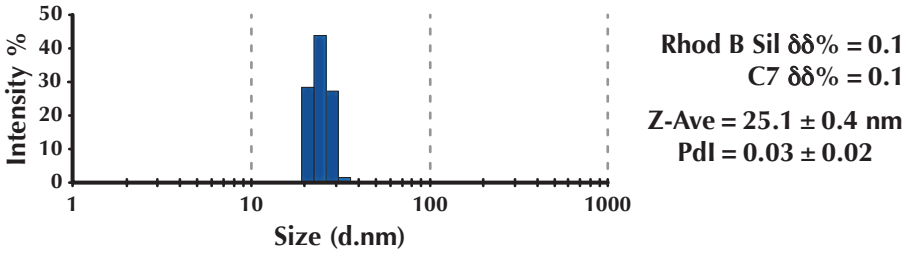

Figure 1 Dynamic light scattering diameter distribution of **Rh+C7@NPs** ($5 \cdot 10^{-8}$ M in PBS 1X, pH 7.4, 25 °C).

The presence of the outer polyethylene glycol (PEG) shell in these nanosystems is of great importance especially in view of biological applications. PEG is, in fact, an FDA approved substance and it is the gold standard for stealth polymers in the emerging field of polymer-based drug delivery.[23] Moreover, this outer shell can be advantageously used to host molecules in order to obtain nanostructured sensors and switches.[21,24]

21. E. Rampazzo, S. Bonacchi, R. Juris, M. Montalti, D. Genovese, N. Zaccheroni, L. Prodi, D. C. Rambaldi, A. Zattoni, P. Reschiglian, *J. Phys. Chem. B* **2010**, *114*, 14605.
22. Q. Huo, *Colloids Surf. B* **2007**, *59*, 1.
23. K. Knop, R. Hoogenboom, D. Fischer, U. S. Schubert, *Angew. Chem. Int. Ed.* **2010**, *49*, 6288.
24. (a) D. Genovese, M. Montalti, L. Prodi, E. Rampazzo, N. Zaccheroni, K. Altenhöner, F. May, J. Mattay, *Chem. Commun.* **2011**, *47*, 10975; (b) E. Oliveira, D. Genovese, R. Juris, N. Zaccheroni, J. L. Capelo, M. M. M. Raposo, S. P. G. Costa, L. Prodi, C. Lodeiro, *Inorg. Chem.* **2011**, *50*, 8834; (c) E. Rampazzo, S. Bonacchi,

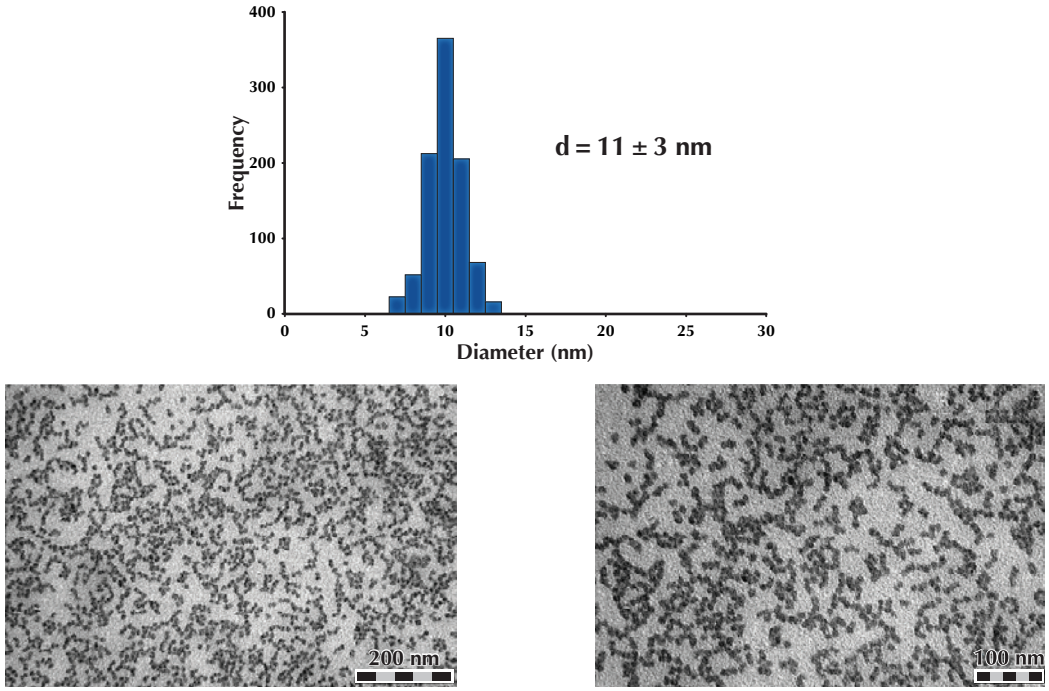

Figure 2 Size distribution of **Rh+C7@NPs** (above), and TEM pictures evidencing the nanoparticles silica core (below).

It is important to underline that these silica-core/PEG-shell nanoparticles are stable for months, also under simulated physiological conditions (phosphate-buffered saline and bovine serum albumin, PBS-BSA), and in the typical environments of most immunochemical protocols. The absence of dye leakage under these conditions demonstrates that beside what was reported by Liu and co-workers,[25] Pluronic® F127 based core-shell nanoparticles with low doping levels are suitable to irreversibly trap an organic dye and thus to prepare NIR emitting nanosized luminescent labels.

In this context, we have studied their possible interactions with BSA, also in comparison with the behavior of Qtracker® 800, non-targeted, pegylated, quantum dots from Invitrogen (**QDs 800**), under the same conditions. Nanoparticles and **QDs 800** (PBS 1X buffer, pH 7.4, 25 °C) present rather different hydrodynamic diameters, 24 and 36 nm respectively (see figure 1 for **Rh+C7@NPs** and figure 3 for **QDs 800**), both with very monodisperse size distributions. As can be seen from figure 4, nanoparticles are less prone to interact with BSA compared to **QDs 800**, that are known to interact with plasmatic proteins and, in particular, with fibrinogen.[26] The aggregation curves, in fact, indicate that for the two systems in the presence of different (increasing) amounts of BSA, the difference between the hydrodynamic diameter is always greater (up to 56 nm) than

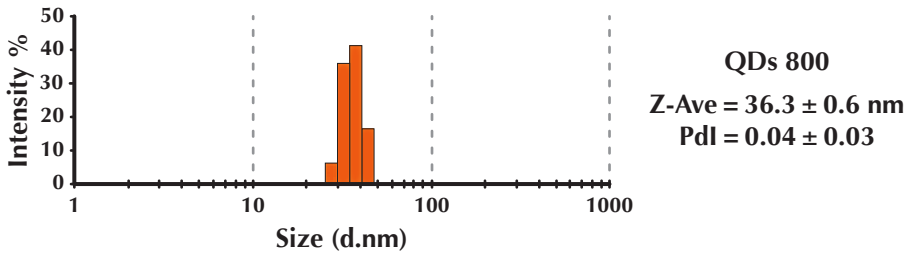

Figure 3 Dynamic light scattering diameter distribution of **QDs 800** ($5 \cdot 10^{-8}$ M in PBS 1X, pH 7.4, 25 °C) after filtration with a 0.20 µm regenerated cellulose filter.

D. Genovese, R. Juris, M. Sgarzi, M. Montalti, L. Prodi, N. Zaccheroni, G. Tomaselli, S. Gentile, C. Satriano, E. Rizzarelli, *Chem. Eur. J.* 2011, *17*, 13429.

25. Q. Huo, J. Liu, L.-Q. Wang, Y. Jiang, T. N. Lambert, E. Fang, *J. Am. Chem. Soc.* **2006**, *128*, 6447.
26. S. Pozzi-Mucelli, F. Boschi, L. Calderan, A. Sbarbati, F. Osculati, *J. Phys.: Conf. Ser.* **2009**, *170*, 1.

the pristine size difference (12 nm) in the absence of BSA. These results suggest that, especially at high concentration regimes, BSA molecules could act as bridging units between two nanoparticles, a behavior that is very evident with non-targeted **QDs 800**.

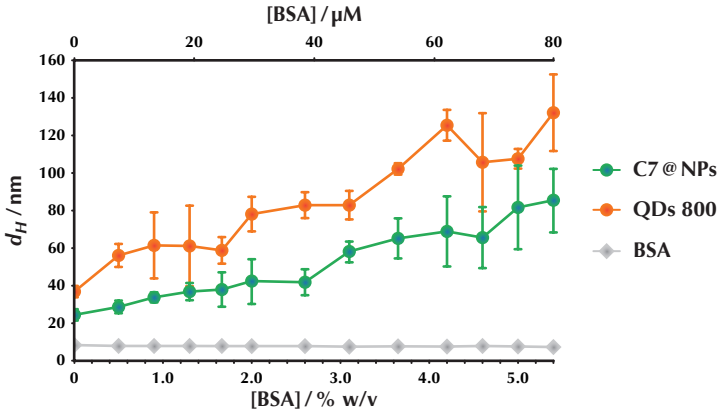

Figure 4 Hydrodynamic diameters measured during aggregation experiments of **QDs 800** and **C7@NPs** in the presence of increasing amounts of BSA (PBS buffer 1x, pH 7.4, 25 °C). The hydrodynamic diameter of BSA measured under the same conditions is reported as the control (d_H=8.3 nm, PdI 0.2). Error bars are calculated as the standard deviation of five different measurements.

6.2.2 Photophysical properties

The main data relative to the photophysical properties of the nanoparticles and of **QDs 800** in water, and of the free dyes in ethanol solutions are shown in table 1. They evidence that, from the ethanol solution to the silica matrix, both the absorption and the emission spectra undergo a small red-shift, without noticeable changes in the band shape and, in particular, in the band width. Such a similarity indicates that, at these doping degrees, the interactions at the ground state between the encapsulated dyes are almost negligible, making it possible to rule out the formation of appreciable quantities of aggregates.[27,28]

A further support to this conclusion comes from the fact that the fluorescence quantum yield of **C7** does not change upon its insertion in the nanoparticles while, in the case of **Rhod B Sil**, it increases considerably. This higher quantum yield can be explained by the fact that in the rigid silica matrix the dyes are segregated from external chemicals, thus increasing their (photo) stability and, in many cases, their luminescence quantum yield. These are not trivial results and explain why these nanoparticles have impressively high brightness.[5] Self-quenching mechanisms cannot be ruled out in this confined environment; although they could explain the different behavior of **C7** and **Rhod B Sil** upon inclusion in the nanoparticles, the effects of this parasite mechanism are efficiently counterbalanced by the increased rigidity of the matrix.

We would like to underline at this point that, since the absorption coefficient of **QDs 800**, as all quantum dots, decreases rapidly in the red part of the spectrum (see figure 5a), **C7@NPs** have comparable brightness at 750 nm (12 000 and 16 900 $M^{-1} \cdot cm^{-1}$ for **C7@NPs** and **QDs 800**, respectively), and even a superior brightness above 775 nm (13 000 and 12 000 $M^{-1} \cdot cm^{-1}$, respectively). Moreover, a renowned and precious characteristic of quantum dots is the sharpness of their emission spectra. Also concerning this aspect, the system based on silica-PEG nanoparticles presents comparable values (figure 5b).

The **Rh+C7@NPs** system, *i.e.*, the nanoparticles including both **Rhod B Sil** and **C7**, is worth a separate discussion. As already mentioned, our aim was to prepare a single bio-label suitable

27. A. Mishra, R. K. Behera, P. K. Behera, B. K. Mishra, G. B. Behera, *Chem. Rev.* **2000**, *100*, 1973.
28. M. Montalti, L. Prodi, N. Zaccheroni, A. Zattoni, P. Reschiglian, G. Falini, *Langmuir*, **2004**, *20*, 2989.

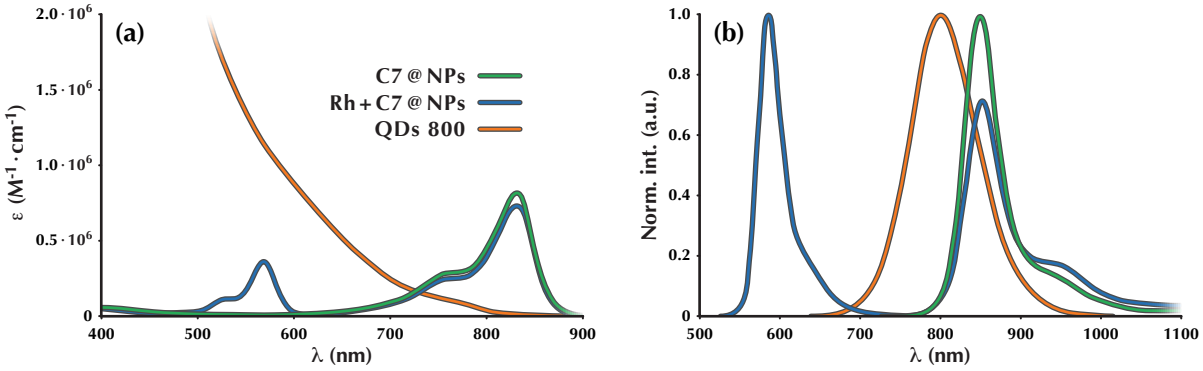

Figure 5 (a) Absorption spectra of **QDs 800** (orange), **C7@NPs** (green) and **Rh+C7@NPs** (blue) in PBS solution; (b) Normalized emission spectra of **QDs 800** (orange, λ_{exc} = 550 nm), **C7@NPs** (green, λ_{exc} =750 nm), and **Rh+C7@NPs** (blue, λ_{exc} =550 nm) in PBS solution.

to be used first for *in vivo* imaging and, later, for *in vitro* microscopy on the same animal. As a matter of fact, while for *in vivo* experiments it is important to use fluorescent labels absorbing and emitting in the NIR region, optical microscopes for tissue investigation are usually equipped with light sources and detectors operating in the visible region. **Rh+C7@NPs** were thus conceived to avoid a complete energy transfer process from one dye to the other, in order to maintain both signals. In these nanoparticles, it was possible to observe a 75% efficiency both of the fluorescence quenching of **Rhod B Sil** and of the fluorescence sensitization of **C7**

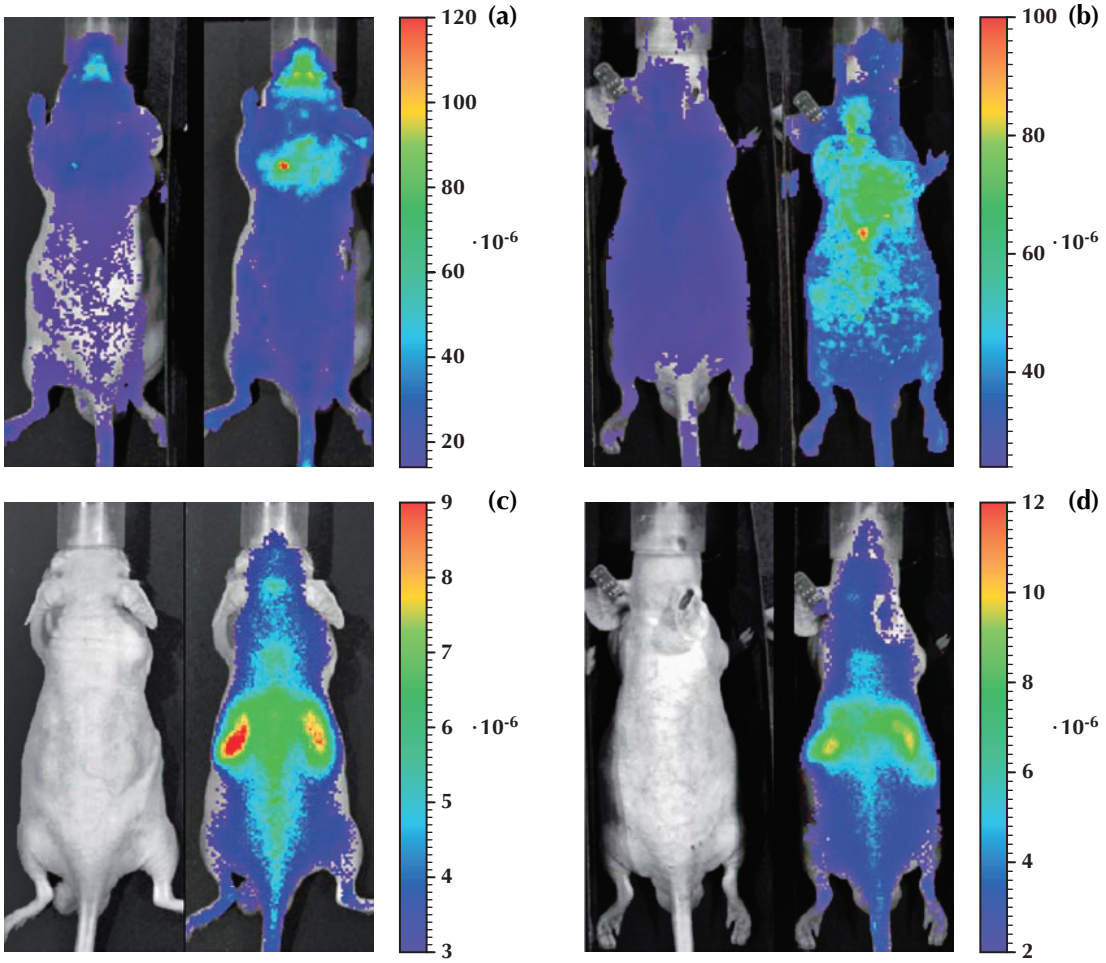

Figure 6 Average efficiency pre- and post-injection of nanoparticles: (a) **Rh@NPs** imaged with DsRed/DsRed filters, (b) **Rh+C7@NPs** imaged with DsRed/DsRed filters, (c) **C7@NPs** imaged with ICG/ICG filters, and (d) **Rh+C7@NPs** imaged with ICG/ICG filters.

(see table 1 and figure 5b). The residual 25% of the luminescence of **Rhod B Sil** is sufficient to have a high signal in the 550-650 nm region (comparable to a fluorophore having an absorption coefficient $\varepsilon = 10^5\ M^{-1} \cdot cm^{-1}$ and a quantum yield $\Phi \geq 0.1$) and the highly efficient sensitization allows a 300 nm separation among the excitation (590 nm, absorption maximum of **Rhod B Sil**) and the emission (860 nm, emission maximum of **C7**) wavelengths.

6.2.3 *In vivo* total body imaging

In vivo images reveal just after the tail vein injection an increase of the signal well above the background emission measured in the pre-injection images with all the three kinds of nanoparticles. Three hours after injection the signal remains higher than the background and the biodistribution is well detectable (figure 6). Regions of interest (ROIs), traced manually on the planar images in correspondence with brain, lungs, and liver, were analyzed to measure the average efficiency (fraction of fluorescent photons relative to the number of incident excitation photons). The average efficiency for each ROI is given with the standard error of the mean (SEM) in figure 7 and 8.

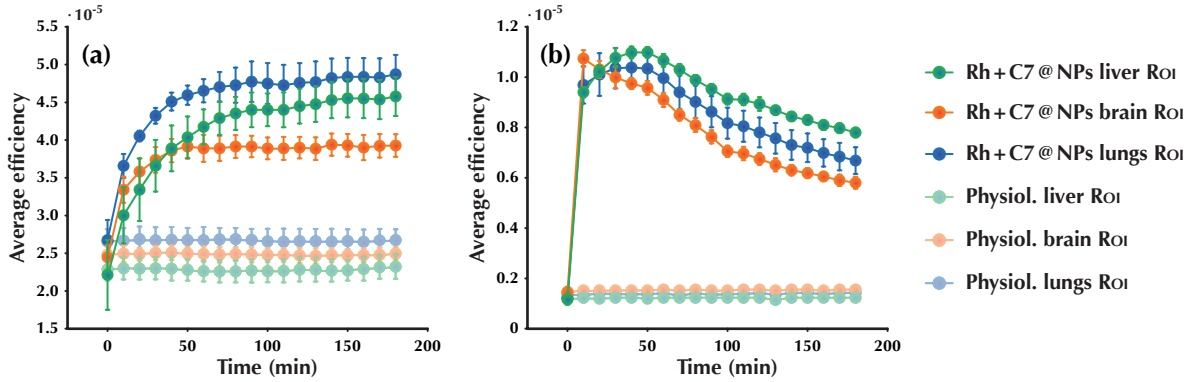

Figure 7 Average efficiency for ROIs measured in the brain, liver and lungs before and after injection of nanoparticles: (a) **Rh+C7@NPs** imaged with DsRed/DsRed filters and (b) **Rh+C7@NPs** imaged with ICG/ICG filters.

Rh@NPs and **Rh+C7@NPs** imaged with DsRed/DsRed (500-550/575-650 nm) filters showed a continuous increase of the intensity of the signal during the observation time. **C7@NPs** and **Rh+C7@NPs** imaged with ICG/ICG (710-760/810-875 nm) filters showed a peak in the fluorescence emission during the first hour after the injection and a subsequent decrease with time. It is important to recall here that the intensity of the observed fluorescence depends on the tissue penetration, and that this dependence is related to the excitation and emission wavelengths, thus leading to the different behavior as observed in fugure 7. These data can be used to better

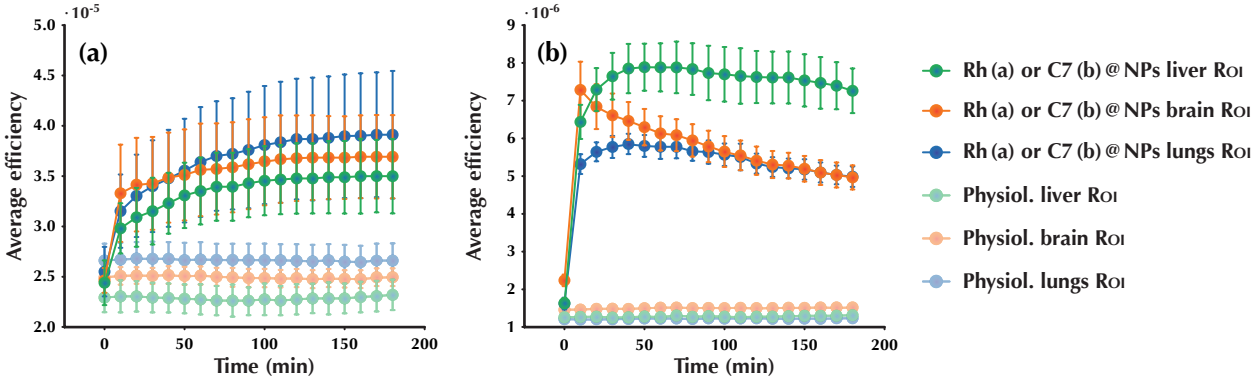

Figure 8 Average efficiency for ROIs measured in the brain, liver and lungs before and after injection of nanoparticles: (a) **Rh@NPs** imaged with DsRed/DsRed filters and (b) **C7@NPs** imaged with ICG/ICG filters.

localize the fluorescence source in depth. Experiments with chicken breasts revealed that at 1 cm of depth the particles can be well localized within the normal experimental errors.[29]

C7@NPs and **Rh+C7@NPs** imaged with ICG/ICG filters showed lower average efficiencies with respect to **Rh@NPs** and **Rh+C7@NPs** imaged with DsRed/DsRed filters but a higher signal to background ratio, due to the very low autofluorescence emission of the biological tissues in the ICG/ICG range (as shown in figure 6).

Measurements of the total flux (p/s) emitted from the extracted organs with SEM are reported in figure 9. Using DsRed/DsRed filters **Rh+C7@NPs** showed a significantly higher (paired Student's t-test) fluorescent signal with respect to the physiological solution in all the organs except the kidneys. **Rh@NPs** showed no statistical differences with the physiological solution in all the organs.

Using ICG/ICG filters **Rh+C7@NPs** showed a significantly higher fluorescent signal with respect to physiological solutions in all the organs and the same occurred with **C7@NPs** except in brain and testicles. Further investigations are needed to localize the nanoparticles at the cellular scale. In any case all these results clearly confirm that these nanoparticles can be used in preclinical imaging in the visible and NIR transparency window of the biological tissues. The washout of the nanoparticles in living organisms and their toxicity need to be investigated in greater detail.

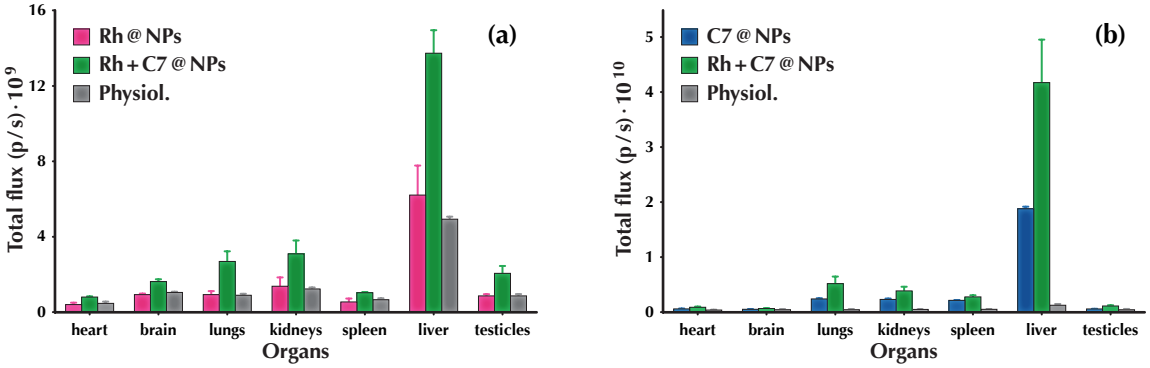

Figure 9 Total flux (p/s) measured from the extracted organs of animals treated with (a) **Rh@NPs** and **Rh+C7@NPs** imaged with DsRed/DsRed filters and (b) **C7@NPs** and **Rh+C7@NPs** imaged with ICG/ICG filters.

6.2.4 *In vivo* microscopy

At the present time intravital imaging allowing the visualization of the local microscopic structure is considered very informative and, since the first application of TPM in immunology ten years ago, the number of studies using this advanced technology has increased dramatically. For example, the blood vessel structures are commonly visualized by intravenous injection of dye-conjugated dextrans.[30] An alternative method for the blood stream imaging came with the commercial introduction of quantum dots with a special coating that improves their half-life in the circulation.[31] TPM images of the samples of nanoparticles excited at 800 nm revealed a peak of emission at 610 nm, and for this reason the best signal was obtained in the 560-630 nm emission window. This setup was maintained for the *in vivo* acquisitions. In ear and in derma the nanoparticles remained in the blood stream during the experimental period and the vessels can be easily detected. In particular very small vessels in the ear are well defined and their shape can be appreciated (figure 10b). In contrast, microscopic images of **Rh+C7@NPs** show

29. O. Coquoz, T. L. Troy, D. Jekic-McMullen, B. W. Rice, *Proc. SPIE-Int. Soc. Opt. Eng.* **2003**, *4967*, 37.
30. T. R. Mempel, S. E. Henrickson, U. H. von Andrian, *Nature* **2004**, *427*, 154.
31. G. Shakhar, R. L. Lindquist, D. Skokos, D. Dudziak, J. H. Huang, M. C. Nussenzweig, M. L. Dustin, *Nat. Immunol.* **2005**, *6*, 707.

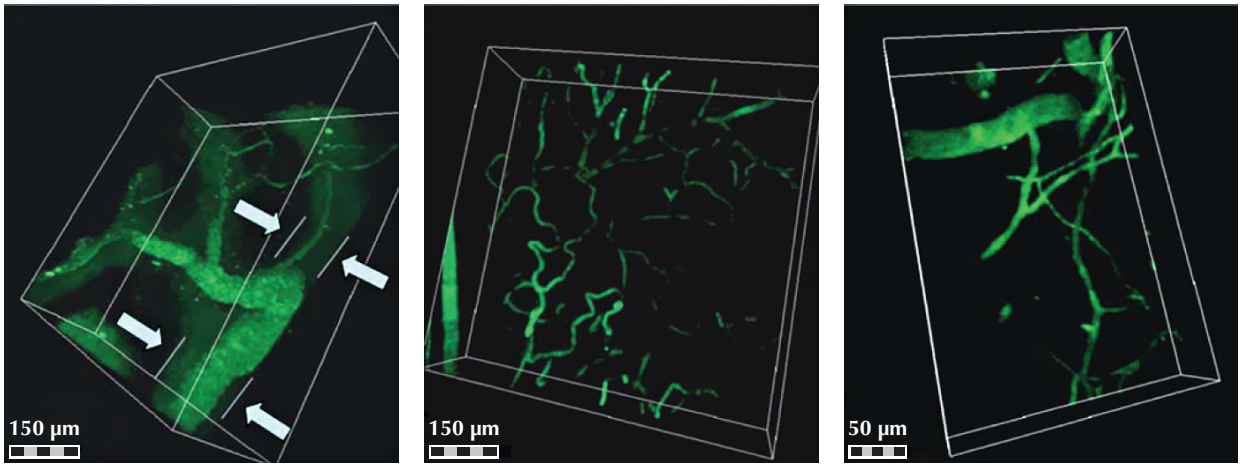

Figure 10 In vivo microscopic images of **Rh+C7@NPs** (a) in tumor, (b) in ear, (c) and in derma; respectively 10, 30, and 60 minutes after the injection of the nanoparticles.

a diffuse emission around tumor vessels just a few minutes after the injection of the nanoparticles (figure 10a). The diffuse emission is visible both around large and small vessels and can be evaluated in fully 3D images. These results clearly demonstrate that these silica nanoparticles can also be used to investigate the integrity of the biological barriers with promising results.

6.3 Conclusions

To conclude, we reported the synthesis and characterization of a new family of core-shell nanoparticles, highly reproducible and very monodisperse nanomaterials, that show an outstanding brightness in the NIR region and long time stability in water under physiological conditions. All these features make them suitable for *in vivo* optical imaging. The possibility of covalently binding two or more different luminophores inside the same nanoparticle core with a one-pot reaction leads to systems allowing a 300 nm separation among the excitation and the emission wavelengths. This offers the possibility to use the same nanoparticles on the same animal for both *in vivo* imaging and *ex vivo* microscopy and also an efficient use of the TPM microscopy technique. Fluorescence images of small living animals revealed that these nanoparticles can be used to detect the light emission over the autofluorescence background, offering also the possibility to investigate the integrity of the biological barriers. All these results suggest that this family of nanoparticles can present many advantages compared to commercial dyes. In particular, the optical properties of these nanoparticles and the tunability of their excitation and emission wavelengths further encourage the study of their functionalization with biomolecules for many different applications.

Chapter 7
Targeted label†

7.1 Introduction

Cancer remains a leading cause of death in the occidental world. Indeed, there is still no effective cure for some specific tumors and, more in general, for advanced tumors the scarcity of successful treatment options represents a serious limiting factor in patient management. Approximately 20% of colorectal cancer (CRC) patients present a metastatic disease at diagnosis, and 30-40% of patients with localized disease will ultimately develop metastases. Despite the introduction of novel therapeutic agents, combinations and protocols, as the tumor stage increases, the 5-year overall survival rates decline substantially.[1-3] The efficacy of curative surgical interventions can only be extended through an earlier detection of metastatic *foci*, which is dependent on both the sensitivity and specificity of the diagnostic tools.[3,4] To overcome the limits of current approaches, two strategies appear most promising: improving diagnostic protocols to allow detecting tumors in earlier stages and/or with higher specificity, and adopting new molecularly-targeted and personalized therapies to hit tumor cells with increasing efficiency and selectivity.

The recent developments in the design of nano-sized materials have provided powerful tools for high-potential perspectives in both strategies. Modular nanometric systems have proved to be versatile platforms to combine imaging and drug delivery for applications in the oncological field.[5] Among these, silica based nanoparticles are now emerging as an attractive strategy

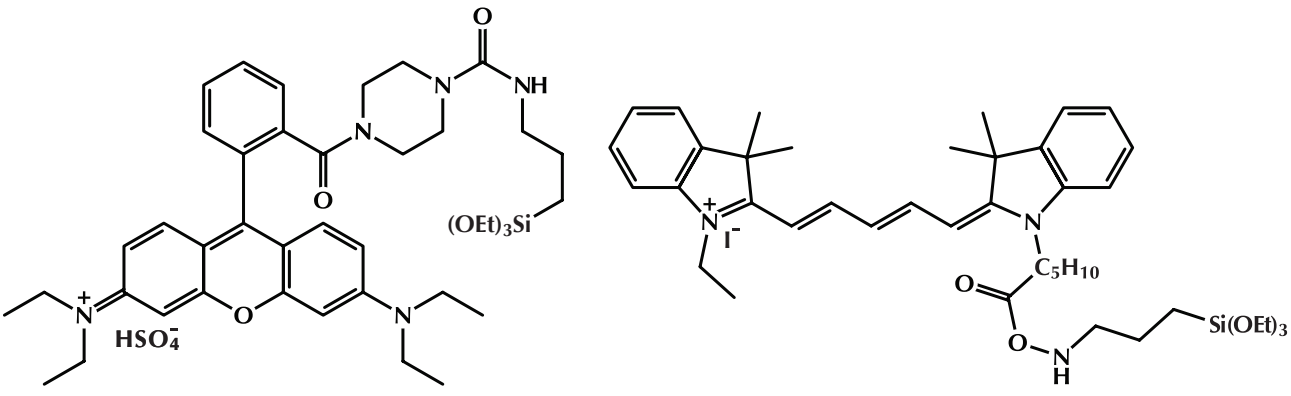

Rhod B Sil **C5 Sil**

Scheme 1 Molecular structures of the rhodamine derivative **Rhod B Sil** and of the polymethine dye **C5 Sil**.

†. This chapter is taken and adapted from: M. Soster, R. Juris, S. Bonacchi, D. Genovese, M. Montalti, E. Rampazzo, N. Zaccheroni, P. Garagnani, F. Bussolino, L. Prodi, S. Marchiò, *Small* **2012**, *submitted*.

1. J. B. O'Connell, M. A. Maggard, C. Y. Ko, *J. Natl. Cancer Inst.* **2004**, *96*, 1420.
2. B. M. Wolpin, R. J. Mayer, *Gastroenterology* **2008**, *134*, 1296.
3. J. S. Tomlinson, W. R. Jarnagin, R. P. DeMatteo, Y. Fong, P. Kornprat, M. Gonen, N. Kemeny, M. F. Brennan, L. H. Blumgart, M. D'Angelica, *J. Clin. Oncol.* **2007**, *25*, 4575.
4. D. J. Gallagher, N. Kemeny, *Oncology* **2010**, *78*, 237.
5. D. Majumdar, X.-H. Peng, D. M. Shin, *Curr. Top. Med. Chem.* **2010**, *10*, 1211.

Table 1 Morphological and photophysical properties of the different silica nanoparticles and their doping dyes.

Sample	Solvent	n° dyes[a]	λ abs[b]	ε[c]	λ em[b]	Φ[d]
Rhod B Sil	EtOH	–	562	$1.0 \cdot 10^5$	580	0.35
Rh@NPs	H_2O	4.5	570	$4.5 \cdot 10^5$	590	0.45
C5 Sil	EtOH	–	645	$2.5 \cdot 10^5$	655	0.32
C5@NPs	H_2O	3.0	650	$7.5 \cdot 10^5$	665	0.34
Rh+C5@NPs	H_2O	4.0[e] 3.0[f]	570[e] 650[f]	$4.0 \cdot 10^5$[e] $7.5 \cdot 10^5$[f]	590[e] 665[f]	0.04[e] 0.34[f]

[a] mean number of dyes per nanoparticle; [b] nm; [c] $M^{-1} \cdot cm^{-1}$; [d] rhodamine 6G in ehtanol (Φ = 0.94) was used as reference; [e] related to **Rhod B Sil**; [f] related to **C5**.

for cancer theragnostics, due to a favorable toxicological profile and biocompatibility *in vivo*, coupled to an inherent versatility of manipulation *in vitro*.[6]

7.2 Nanoparticles characterization

Here we report the design and testing of metastasis targeted silica nanoparticles doped with triethoxysilane functionalized fluorescent dyes **Rhod B Sil** and/or **C5 Sil**[7] (scheme 1) within a micelle of the triblock copolymer Pluronic® F127, resulting in a poly(ethylene glycol) (PEG) shell embedding a dye doped silica core (nanoparticles will be denoted as **Rh@NPs**, **C5@NPs**,

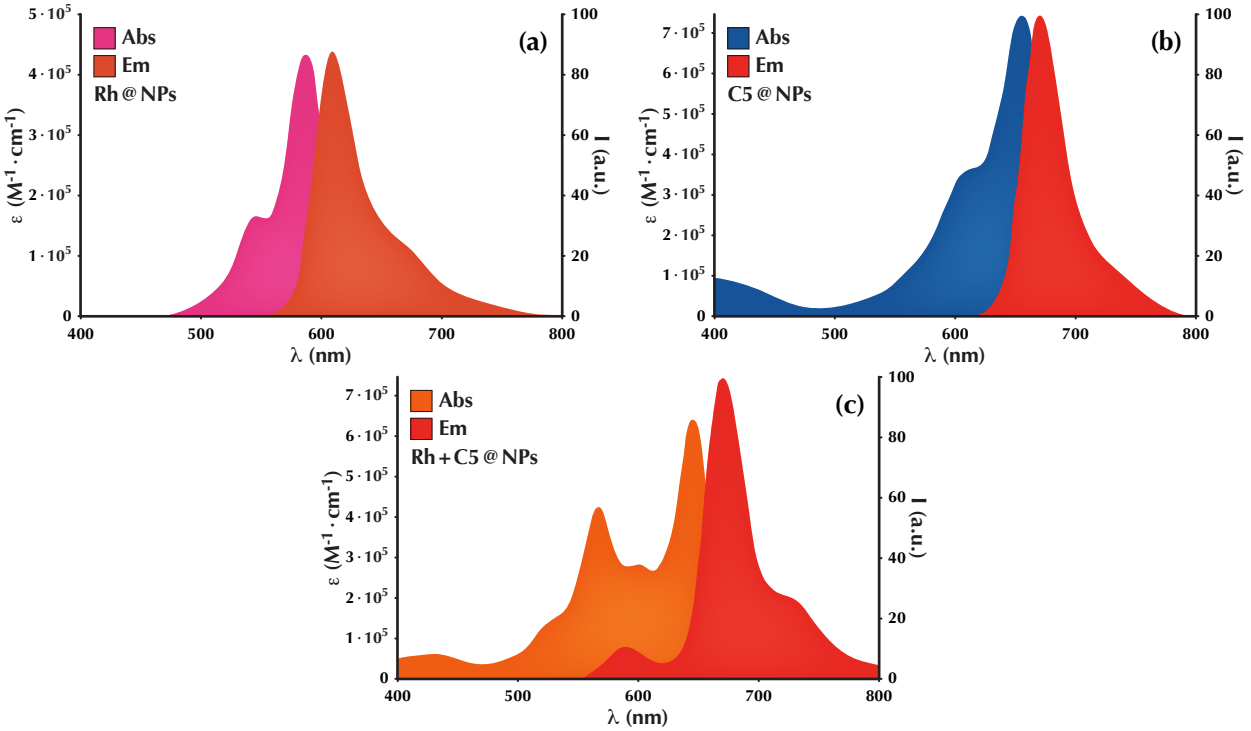

Figure 1 Absorption and emission spectra of (a) **Rh@NPs** (λ_{exc} = 514 nm), (b) **C5@NPs** (λ_{exc} = 633 nm), and (c) **Rh+C5@NPs** (λ_{exc} = 514 nm) in water.

6. S. Bonacchi, D. Genovese, R. Juris, M. Montalti, L. Prodi, E. Rampazzo, M. Sgarzi, N. Zaccheroni, *Top. Curr. Chem.* **2011**, *300*, 93.
7. The synthesis of **Rhod B Sil** is reported in reference 10. **C5 Sil** was prepared from the corresponding NHS ester, with 2 eq. of APTES, in DCM, stirred at room temperature overnight. The reaction mixture was then simply concentrated and used as such in the synthesis of nanoparticles.

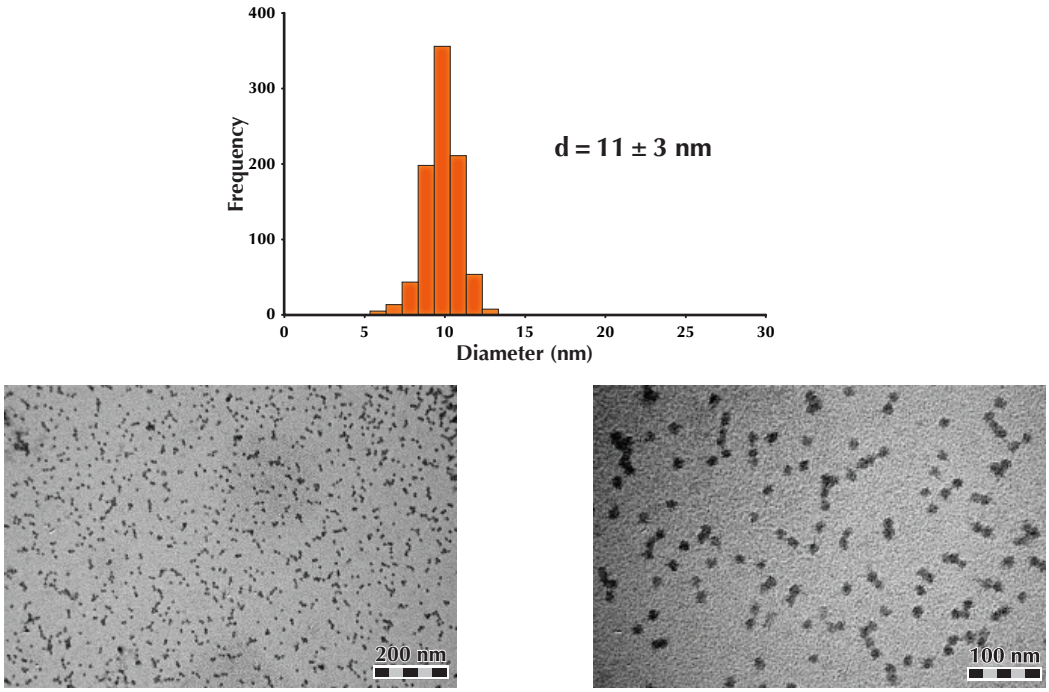

Figure 2 Size distribution of **Rh+C5@NPs** (above), and TEM pictures evidencing the nanoparticles silica core (below).

or **Rh+C5@NPs**).[89] The absorption and emission properties of **Rhod B Sil** and **C5 Sil** in single color nanoparticles, with the exception of a slight red-shift of λ_{max}, are the same of the free molecules (table 1), indicating the absence of interactions among the encapsulated dyes at the ground state at the chosen doping degrees. Remarkably, as a consequence of the entrapment in a rigid silica matrix, both dyes have increased fluorescence quantum yields. Dual color nanoparticles exhibit different fluorescence properties, due to the occurrence of an energy transfer (90% of efficiency) from **Rhod B Sil** to **C5 Sil**. This allows a large separation between the emission and the excitation wavelengths; as a consequence, when these nanoparticles are excited in the **Rhod B Sil** absorption band, the **Rhod B Sil** fluorescence decreases to 10%, with a concomitant increase in the **C5 Sil** emission.[10] The residual **Rhod B Sil** intensity is however sufficiently high to be exploited for imaging purposes, allowing a concomitant detection of the two fluorescence signals and background signal minimization.

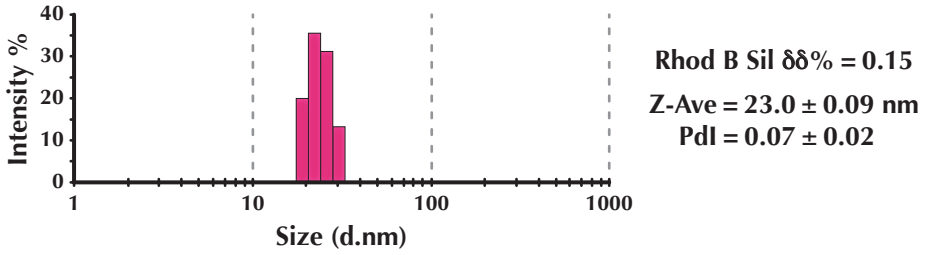

Figure 3 Dynamic light scattering diameter distribution of **Rh@NPs.**

8. S. Bonacchi, D. Genovese, R. Juris, M. Montalti, L. Prodi, E. Rampazzo, N. Zaccheroni, *Angew. Chem. Int. Ed.* **2011**, 50, 4056.
9. Synthesis of dye doped nanoparticles is described in detail in chapter 8 – Experimental section. These samples were prepared in 1 M acetic acid, with TMSCl as terminating agent, using 1.2 μmol of **Rhod B Sil**, and/or 0.8 μmol of **C5 Sil.**
10. E. Rampazzo, S. Bonacchi, R. Juris, M. Montalti, D. Genovese, N. Zaccheroni, L. Prodi, D. C. Rambaldi, A. Zattoni, P. Reschiglian, *J. Phys. Chem. B* **2010**, *114*, 14605.

The external PEG chains of Pluronic® F127 provide a standard of stealth polymer[11] for stable dispersion in physiological conditions and for prevention of uptake by the mononuclear phagocyte system, all features that render our nanoparticles a choice for *in vivo* applications. We derivatized the PEG tails with carbonyl groups, to enable covalent attachment of targeting ligands, *e.g.*, antibodies, proteins, or short peptides. The resulting nanoparticles have a core diameter of 11 ± 3 nm, as measured by transmission electron microscopy (TEM) (figure 2), and a hydrodynamic diameter of 23 nm with a polydispersity index (PdI) < 0.1 (figure 3). These features are reproducible among different preparations, independent from the embedded dye, and very stable (no aggregation, degradation or dye leakage even after several months of storage, data not shown).

7.3 Tissue binding assays

We surface-functionalized our nanoparticles with two peptides, namely **CGIYRLRS** and **CGVYSLRS**, that have been isolated in our laboratory as specific ligands for the microenvironment of human metastatic CRC. These peptide sequences were derived by comparative phage display biopanning on fresh surgical samples of hepatic metastases versus grossly normal liver biopsies of the same patients, and proved to be selective for both the stromal and the epithelial components of these pathologic tissues.[12]

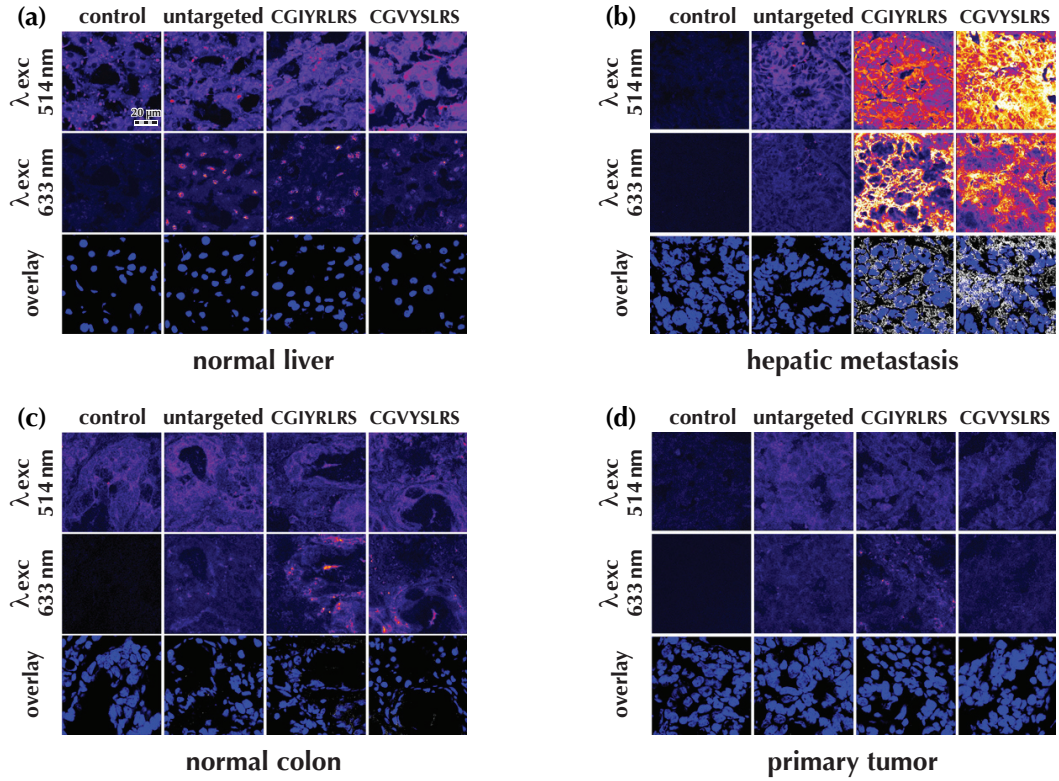

Figure 4 Targeted nanoparticles recognize human hepatic metastases *ex vivo*. 10 µm frozen sections of (a) matched (grossly) normal liver, (b) hepatic metastasis, (c) (grossly) normal colon, and (d) primary tumor were fixed in 4% formaldehyde, before being incubated with either untargeted, **CGIYRLRS-** or **CGVYSLRS-Rh+C5@NPs** for 4 hours at room temperature. After washing, the nanoparticles emitted fluorescence was analyzed by confocal microscopy, and the output was converted in a false color LUT Fire. The experiment was performed on specimens from 10 patients with metastatic CRC; exemplary images from tissues of patient #P85 are shown.

11. K. Knop, R. Hoogenboom, D. Fischer, U. S. Schubert, *Angew. Chem. Int. Ed.* **2010**, *49*, 6288.
12. F. Bussolino, S. Marchiò, PCT/EP2007/010428, **2007**.

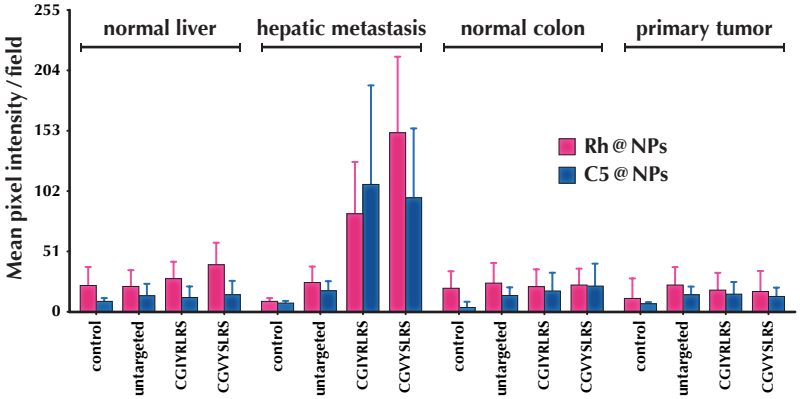

Figure 5 Quantification of nanoparticles binding is expressed as the intensity of emitted pixel following excitation at 514 nm (**Rhod B Sil**) and 633 nm (**C5**), and calculated as mean value of 5 images for each tissue.

We first investigated the binding properties of the deriving metastasis targeted, dual color nanoparticles *ex vivo* on human specimens of hepatic metastasis from the surgery. For this purpose, 10 µm sections of OCT-frozen human tissues were incubated with both control, untargeted, and peptide-targeted **Rh+C5@NPs**. The localization of specific fluorescent signals was evaluated by confocal microscopy (figure 4a-d), and quantified by the count of pixel intensities (figure 5). In these assays, both **CGIYRLRS**- and **CGVYSLRS-Rh+C5@NPs** showed binding selectivity for hepatic metastasis (figure 4b), compared to grossly-normal liver and colon, and to primary CRC. The concomitant presence of dyes with separate excitation/emission spectra allows an almost complete elimination of tissue background, through the identification of univocal signals by fluorescence overlay. In these *ex vivo* binding assays, imaging of colocalized **Rhod B Sil**/**C5 Sil** pixels revealed a sharp nanoparticle staining of epithelial cell membranes and stroma that was specifically associated with the hepatic metastasis tissues (see figure 4b, overlay).

7.4 Ex vivo *imaging*

We next investigated the capability of our peptide-targeted nanoparticles to home to hepatic metastasis *in vivo* in a clinically relevant mouse model of human metastatic CRC. For this purpose, non-obese diabetic/severe combined immunodeficient (NOD-SCID) mice were injected intrasplenically with the highly metastatic CRC cell line HCT-116m. In this well established model, 21 to 28 days after cell injection animals develop a pseudo-orthotopic primary tumor into the spleen and several secondary tumors into the liver.[13] During this time frame, we injected into the caudal vein either control or **CGIYRLRS**-targeted single or dual color nanoparticles, and let them circulate for increasing periods of time, starting from 1 hour. We observed a good reduction of unspecific fluorescence (*i.e.*, the signals of untargeted nanoparticles in target tissues, and/or of targeted nanoparticles in non-target tissues) after 6 hours, reaching an optimal signal to background ratio after 16-24 hours. A very similar outcome was obtained with the **CGVYSLRS**-nanoparticles (data not shown). The results of this experimental set up suggest that clearance of untargeted nanoparticles is paralleled by specific accumulation of targeted nanoparticles; the possibility of exploiting a wide time window for the diagnostic imaging of hepatic micrometastases is of further support for translation into clinical applications.

We evaluated the location *ex vivo* of single and dual color nanoparticles, observing in both cases a specific accumulation of targeted nanoparticles in hepatic metastases compared to surrounding

13. M. Bouvet, K. Tsuji, M. Yang, P. Jiang, A. R. Moossa, R. M. Hoffman, *Cancer Res.* **2006**, *66*, 11293.

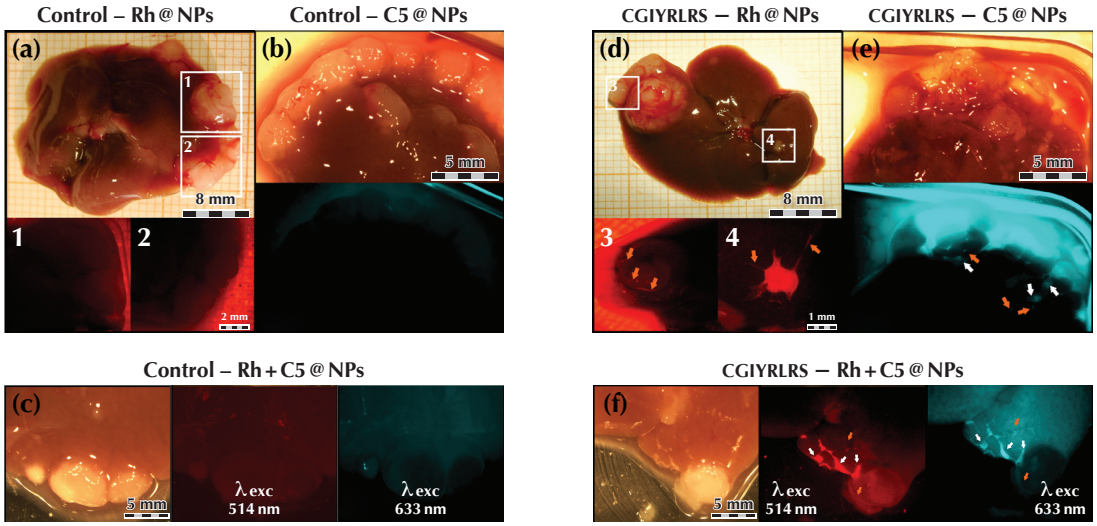

Figure 6 Targeted nanoparticles home to hepatic metastases *in vivo*. NOD-SCID mice bearing a primary spleen tumor and several liver metastases were injected with single [(a) control-**Rh@NPs**, (b) control-**C5@NPs**, (d) **CGIYRLRS-Rh@NPs**, and (e) **CGIYRLRS-C5@NPs**] or double color [(c) control-**Rh+C5@NPs** and (f) **CGIYRLRS-Rh+C5@NPs**]. After 16 hours, mice were euthanized and the explanted organs were photographed *in toto* with high-resolution CCD cameras connected to a fluorescence stereomicroscope. In (d), (e), and (f), orange arrows point at blood vessels crossing the hepatic metastasis; in (e) and (f), white arrows point at submillimetric metastatic *foci*.

normal tissues (figure 6d-f) and to untargeted nanoparticles (figure 6a-c). **CGIYRLRS-Rh@NPs** were visible exclusively in blood vessels of bigger masses (figure 6d, inset 3), even though they accumulated both in microvessels and in cancer cells in masses with a volume < 1-2 mm^3 (figure 6d, inset 4). The signal to background ratio obtained with the **CGIYRLRS-Rh@NPs** , although extremely specific, was generally low, probably due to scarce light penetration and/or relatively high tissue autofluorescence at the analyzed wavelengths. Conversely, the signal obtained with the **CGIYRLRS-C5@NPs** resulted both specific and highly intense, allowing the visualization of microvessels and even of submillimetric metastatic masses (figure 6e). Except for the strongly

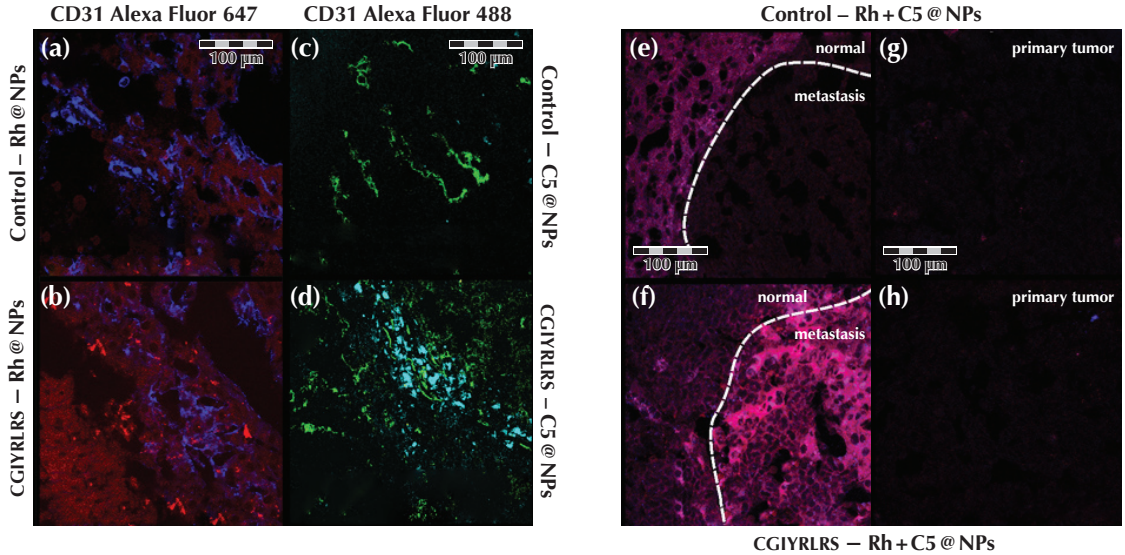

Figure 7 Samples of the same tissues as figure 6 were evaluated at the micrometric scale, by confocal analysis of the single [(a) control-**Rh@NPs**, (c) control-**C5@NPs**, (b) **CGIYRLRS-Rh@NPs**, and (d) **CGIYRLRS-C5@NPs**] or dual color [(e) control-**Rh+C5@NPs** and (f) **CGIYRLRS-Rh+C5@NPs**] nanoparticles emitted fluorescence. To visualize blood vessels, a staining for CD31 was superimposed to the signal of nanoparticles, and was revealed with the secondary (a, b) Alexa Fluor® 647 and (c, d) Alexa Fluor® 488 antibodies, for overlay with **Rh@NPs** and **C5@NPs**, respectively. In the case of dual color nanoparticles, a further control is visualized, *i.e.*, samples of primary tumors from mice injected with either (g) control-**Rh+C5@NPs** or (h) **CGIYRLRS-Rh+C5@NPs**.

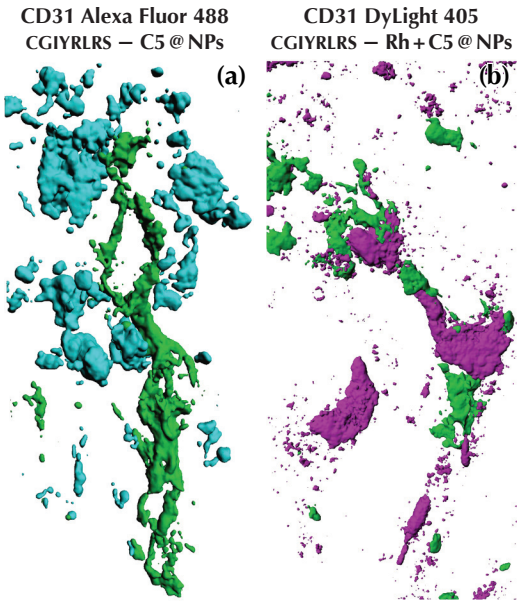

Figure 8 50 to 80 series of images superimposing CD31 staining with either **C5@NPs** [(a) particular of the field imaged in figure 7d] or **Rh+C5@NPs** [(b) particular of the field imaged in figure 7f, in which CD31 was revealed with the secondary DyLight™ 405 antibody] were composed to reconstruct 3D models using IMARIS software.

improved signaling efficiency, the accumulation of the dual color targeted nanoparticles was comparable to that of the single color nanoparticles (figure 6f).

A confocal microscopy analysis of explanted organs confirmed the specific presence of the single color nanoparticles into the hepatic metastases, with an accumulation of both **CGIYRLRS-Rh@NPs** (figure 7b) and **CGIYRLRS-C5@NPs** (**figure 7d**) in close proximity of blood vessels. In contrast, no specific emission was detected in metastatic tissues of mice injected with control nanoparticles (figure 7a and 7c). In the case of the dual color nanoparticles, the possibility of overlaying fluorescent signals in the channels of the two dyes allowed a precise identification of the nanoparticles over the tissue background, leading to univocal imaging of targeted nanoparticles in metastatic tissues compared to normal liver (figure 7f), primary splenic tumor (figure 7h), and to control nanoparticles (figure 7e and 7g).

We used IMARIS software to compose several z-stacks obtained by confocal microscopy and to reconstruct a 3D model of selected portions of hepatic metastases from animals injected with **CGIYRLRS-C5@NPs** (figure 8a) or **CGIYRLRS-Rh+C5@NPs** (figure 8b). These images clearly show that targeted nanoparticles extravasate from the fenestrate tumor blood vessels and clusterize in both endothelial/perivascular and nearby tumor epithelial cells and stroma, suggesting that specific molecular targets are easily accessible to our circulating nano-objects in this pathological microenvironment.

7.5 Conclusions

Different research groups have recently described the use of fluorescence based tracers during the surgery to improve the identification of pathologic tissues, *e.g.*, in prostate and gastric cancers to identify sentinel lymph nodes,[14,15] as well as in bladder,[16] and ovary cancers.[17] Preliminary data have also been reported in the diagnosis of externally accessible human cancers, such as the detection of superficial malignancies (non-melanoma skin tumors)[18] and the development of endoscopic fluorescence based imaging systems for CRC.[19] However, most results have been obtained with untargeted fluorescent compounds, in which case the recognition of a pathologic site is non specific, resulting only from the different physical features of tumoral versus healthy tissues. We here demonstrate that coupling specific molecular targeting to the distinctive fluorescent features of our nanoparticles leads to a significant improvement in both specificity and sensitivity of current diagnostic imaging, allowing visualization even of submillimetric metastases. The outer FDA approved PEG shell, yielding stable probes unaffected by the mononuclear phagocyte system, infers further valuable characteristics to our system. All the discussed experimental evidences demonstrate that our rationally designed modular nano-architectures have the characteristics for being translated into the clinical practice in the next future.

14. I. Miyashiro, N. Miyoshi, M. Hiratsuka, K. Kishi, T. Yamada, M. Ohue, H. Ohigashi, M. Yano, O. Ishikawa, S. Imaoka, *Ann. Surg. Oncol.* **2008**, *15*, 1640.
15. H. G. van der Poel, T. Buckle, O. R. Brouwer, R. A. Valdes Olmos, F. W. van Leeuwen, *Eur. Urol.* **2011**, *60*, 826.
16. M. A. D'Hallewin, A. R. Kamuhabwa, T. Roskams, P. A. De Witte, L. Baert, *BJU Int.* **2002**, *89*, 760.
17. G. M. van Dam, G. Themelis, L. M. Crane, N. J. Harlaar, R. G. Pleijhuis, W. Kelder, A. Sarantopoulos, J. S. de Jong, H. J. Arts, A. G. van der Zee, J. Bart, P. S. Low, V. Ntziachristos, *Nat. Med.* **2011**, *17*, 1315.
18. J. de Leeuw, N. van der Beek, W. D. Neugebauer, P. Bjerring, H. A. Neumann, *Lasers Surg. Med.* **2009**, *41*, 96.
19. V. Atlamazoglou, D. Yova, N. Kavantzas, S. Loukas, *Lasers Med. Sci.* **2001**, *16*, 253.

Part III

Experimental Section

Chapter 8
Experimental section

8.1 Materials & Methods

8.1.1 Chemicals

All reagents and solvents were used as received from commercial sources without further purification.

Boron trifluoride diethyl etherate, COMU® (≥ 97%), cresyl violet perchlorate, diethoxydimethylsilane (≥ 97%), *N*-(3-dimethylaminopropyl)-*N'*-ethylcarbodiimide (EDC, ≥ 97%), 2,4-dimethylpyrrole (≥ 97%), 3-ethyl-2,4-dimethylpyrrole (≥ 97%), *N*-hydroxysuccinimide (NHS, ≥ 98%), glutaric acid monomethyl ester chloride (≥ 98%), 1-hydroxybenzotriazole hydrate (HOBt, ≥ 97%), 4-methoxybenzaldehyde (≥ 98%), methyl adipoyl chloride (≥ 97%), methyl 4-chloro-4-oxobutyrate (≥ 97%), piperidine (≥ 99.5%), ruthenium(III) chloride hydrate ($RuCl_3 \cdot 3H_2O$, ≥ 99.98%), 4-(*tert*-butyloxy)benzaldehyde (≥ 97%), and tetraethyl orthosilicate (TEOS, ≥ 99%) were purchased from Aldrich.

Chlorotrimethylsilane (TMSCl, ≥ 99%), methanesulfonyl chloride (≥ 98%), and quinine sulfate (≥ 98%) were purchased from Fluka.

7-(Diethylamino)coumarin-3-carboxylic acid (DEAC, ≥ 98%), 2-(*N*-morpholino)ethanesulfonic acid hydrate (MES hydrate, ≥ 99.5%), Pluronic® F127, rhodamine 6G, rhodamine B, sodium chloride (NaCl, ≥ 99.5%), and sodium metaperiodate ($NaIO_4$, ≥ 99.5%) were purchased from Sigma.

Acetic acid (AcOH, ≥ 99.7%), acetonitrile (CH_3CN, ≥ 99.5%), (3-aminopropyl)triethoxysilane (APTES, ≥ 98%), carbon tetrachloride (CCl_4, ≥ 99.9%), cyclohexane (≥ 99.5%), dichloromethane (DCM, ≥ 99.9%), absolute dichloromethane (over molecular sieve, ≥ 99.5%), diethylether (Et_2O, ≥ 99.8%), *N*,*N*-diisopropylethylamine (DIPEA, ≥ 99.5%), dimethyl sulfoxide (≥ 99.5%), ethyl acetate (AcOEt, ≥ 99.5%), hydrochloric acid (HCl, fuming, 37%), lithium hydroxide (LiOH, ≥ 98%), methanol (MeOH, ≥ 99.8%), petroleum ether (bp 40-60 °C, ≥ 95%), potassium carbonate (K_2CO_3, ≥ 99%), sodium azide (NaN_3, ≥ 99.5%), sodium bicarbonate ($NaHCO_3$, ≥ 99.5%), sodium sulfate (Na_2SO_4, ≥ 99%), tetrahydrofuran (THF, ≥ 99%), absolute tetrahydrofuran (over molecular sieve, ≥ 99.5%), absolute toluene (over molecular sieve, ≥ 99.7%), *p*-toluensulfonic acid monohydrate (*p*TSA, ≥ 98.5%), triethylamine (TEA, ≥ 99.5%), and triphenylphosphine (Ph_3P, ≥ 99%) were purchased from Sigma-Aldrich.

Cyanine **C5 NHS ester** and **C7** were supplied by Cyanagen Srl (Bologna, Italy).

Cyanine IR-125 (indocyanine green) was purchased from Acros Organics.

DyLight™ 405 was purchased from BioLegend.

CGIYRLRS and **CGVYSLRS** peptides were purchased from New England Peptides.

Rat anti-CD31 antibody was purchased from BD Biosciences.

Quantum dots (Qtracker® 800, non-targeted, 2 mM solution – **QDs 800**), anti-rat secondary antibody Alexa Fluor® 647 and anti-rat secondary antibody Alexa Fluor® 488 were purchased from Invitrogen.

The synthesis and characterization of rhodamine B 4-((3-(triethoxysilyl)propyl)carbamoyl) piperazine amide (**Rhod B Sil**) has been reported elsewhere.[1]

A Milli-Q Millipore system was used for the purification of water (resistivity ≥ 18 MΩ·cm).

8.1.2 Purifications

Flash chromatography was performed on silica gel 60, 230-400 and 35-70 mesh. Thin layer chromatography (TLC) was carried out on silica gel supported on aluminum foils, containing a fluorescent indicator at 254 nm. All these products were purchased from Fluka.

Dialysis was performed against water at room temperature under gentle stirring with regenerated cellulose membrane dialysis tubing (molecular weight cut-off 12 kDa, average flat width 33 mm), purchased from Sigma.

After dialysis, all dye doped nanoparticles samples were passed through hydrophilic Durapore® membrane filters (0.45, 0.22 and 0.1 μm pore size) purchased from Millipore.

Ultrafiltration was carried out in a 75 mL stainless steel-glass solvent resistant stirred cell purchased from Millipore (47 mm filters). The ultrafiltration experimental setup included Amicon regenerated cellulose membranes (100 kDa cut-off) and an auxiliary reservoir (800 mL) equipped with a concentration selector valve.

8.1.3 NMR spectroscopy

Unless otherwise specified, ^{1}H-NMR spectra of all the fluorophores were recorded at 25 °C, in $CDCl_3$, on a Varian Mercury Plus 400 MHz spectrometer. ^{1}H-NMR spectra and ^{13}C-NMR spectra of the surfactants were recorded at 25 °C, in $CDCl_3$, on a Varian Gemini 300 MHz spectrometer. Chemical shifts are reported in δ from Me_4Si (δ = 0.00 ppm) or from $CDCl_3$ (δ = 7.26 ppm for ^{1}H-NMR or δ = 77.0 ppm for ^{13}C-NMR). Multiplicities are reported using the following abbreviations: s – *singlet*, d – *doublet*, t – *triplet*, q – *quartet*, m – *multiplet*, br – *broad*, or a suitable combination. All coupling constants *J* are expressed in Hz. In case of uncertainty, proton assignments were determined by means of two-dimensional ^{1}H,^{1}H-COSY experiments.

8.1.4 Photophysical measurements

UV-Vis absorption spectra were recorded at 25 °C by means of a Perkin-Elmer Lambda 45 spectrophotometer, while emission spectra were performed at 25 °C on a Perkin-Elmer LS 55 (chapter 3 and 4), or with an Edinburgh FLS920 equipped with a photomultiplier Hamamatsu R928P (chapter 5 and 6, for the 500-850 nm spectral range) or with an Edinburgh Instruments Ge detector (chapter 6, for the 800-1600 nm spectral range). Quartz cuvettes of 1 cm optical path length were used. Corrections for instrumental response, inner filter effects and phototube sensitivity were performed.[2,3]

8.1.4.1 Quantum yields

The luminescence quantum yields (uncertainty of ±15%) of nanoparticles were recorded on air-equilibrated solutions (absorbance < 0.1 in the whole spectral region to avoid auto-absorption), using the following equation:

---

1. E. Rampazzo, S. Bonacchi, R. Juris, M. Montalti, D. Genovese, N. Zaccheroni, L. Prodi, D. C. Rambaldi, A. Zattoni, P. Reschiglian, *J. Phys. Chem. B* **2010**, *114*, 14605.
2. A. Credi, L. Prodi, *Spectrochim. Acta, Part A* **1998**, *54*, 159.
3. M. Montalti, A. Credi, L. Prodi, M. T. Gandolfi, *Handbook of Photochemistry*, 3rd ed., **2006**, CRC Press (Boca Raton, FL).

$$\Phi_X = \Phi_{ST} \frac{F_X}{F_{ST}} \left(\frac{n_X}{n_{ST}} \right)^2 \quad [1]$$

where subscripts *ST* and *X* denote standard and test, respectively, Φ is the quantum yield, *F* is the integrated area under the corrected fluorescence spectrum, and *n* is the refractive index of the solvent.

Quinine sulfate in H_2SO_4 0.05 M ($\Phi = 0.53$),[3] rhodamine 6G in ethanol ($\Phi = 0.94$),[3] rhodamine B in ethanol ($\Phi = 0.49$),[4] cresyl violet perchlorate in methanol ($\Phi = 0.54$),[3] and cyanine IR-125 in dimethyl sulfoxide ($\Phi = 0.13$)[5] were used as a reference.

8.1.4.2 Anisotropy

Fluorescence anisotropy measurements were performed on an Edinburgh FLS920 equipped with Glan-Thompson polarizers. Anisotropy measurements were collected using an L-format configuration and all data were corrected for polarization bias using the G-factor. Four different spectra were acquired for each sample combining different orientation of the excitation and emission polarizers: I_{VV}, I_{VH}, I_{HH}, I_{HV} (where *V* stands for vertical and *H* for horizontal; the first subscript is referred to the excitation and the second to the emission). The spectra were used to calculate the G-factor and the anisotropy *r*, which are given by:[6]

$$G = \frac{I_{HV}}{I_{HH}} \quad [2]$$

$$r = \frac{I_{VV} - G I_{VH}}{I_{VV} + 2 G I_{VH}} \quad [3]$$

8.1.5 Particles size distribution

8.1.5.1 Dynamic light scattering

The determination of the nanoparticles hydrodynamic diameter distributions was carried out through dynamic light scattering (DLS) measurements employing a Malvern Nano ZS instrument with a 633 nm laser diode. Samples were housed in disposable polystyrene or quartz cuvettes of 1 cm optical path length, using water as suspendant. The width of the DLS hydrodynamic diameter distribution is indicated by the polydispersity index (PdI). In case of a mono-modal distribution (Gaussian) calculated by means of cumulant analysis, $PdI = (\sigma / Z\text{-AVE})^2$, where σ is the width of the distribution and Z-AVE is average diameter of the particles population.

8.1.5.2 Transmission electron microscopy

Transmission electron microscopy (TEM) experiments were performed on a Philips CM 100 transmission electron microscope operating at 80 kV. A holey carbon foil supported on conventional copper microgrids was dried up under vacuum after deposition of a drop of nanoparticles suspension diluted with water (1:50, that is, 0.40 μM). The size distribution was obtained analyzing an image with a block of several hundreds of nanoparticles.

4. K. G. Casey, E. L. Quitevis, *J. Phys. Chem.* **1988**, *92*, 6590.
5. S. A. Soper, Q. J. Mattingly, *J. Am. Chem. Soc.* **1994**, *116*, 3744.
6. J. R. Lakovicz, *Principles of fluorescence spectroscopy*, 3rd ed., **2006**, Springer (New York, NY).

8.1.6 Live cell fluorescence imaging – Chapter 5

8.1.6.1 Preparation and staining of cell cultures

Neuroblastoma SHSY5Y (purchased from Lonza) cells were cultured in Dulbecco's Modified Eagle Medium (DMEM, Lonza), supplemented with 10% Fetal Bovine Serum (FBS, Lonza) glutamine (2 mM) and penicillin/streptomycin (50 µg/mL).

Cells were plated on 35 mm glass bottom culture dishes (WillCo Wells), then incubated during 24 hours at 37 °C in 5% CO_2 atmosphere. For the experiments with exogenous copper addition, a parallel series of samples was incubated – over the total incubation time – for 5 hours (37 °C and 5% CO_2) with $CuCl_2$ supplemented DMEM. The $CuCl_2$concentrations tested were 20, 50, and 100 µM.

Immediately before the experiments, cells were washed with PBS buffer, incubated 5 minutes at 25 °C with the probe solutions (free **1**, free nanoparticles, **1@NPs** – 1:1 molar ratio) or just PBS (control sample), washed with PBS, and imaged. The probe solution concentrations tested were $10 \cdot 10^{-6}$ M, $5 \cdot 10^{-6}$ M, $3 \cdot 10^{-6}$ M.

8.1.6.2 Fluorescence microscopy imaging

Observations were carried out by fluorescence microscopy, both with a confocal laser scanning microscope (LSM, Olympus FV1000 Fluoview) equipped with an oil immersion objective (60x) and with an Axioskop2 epifluorescence microscope (Carl Zeiss, Jena, Germany), equipped with a digital camera (micro-CCD). For LSM images acquisition, the excitation was carried out with the HeNe laser ($\lambda_{exc} = 543$ nm) and emitted light was detected at 572 nm. For epifluorescence imaging the following filters were used: DAPI ($\lambda_{exc} = 359$ nm, $\lambda_{em} \approx 461$ nm), FITC ($\lambda_{exc} = 495$ nm, $\lambda_{em} \approx 521$ nm) and TRITC ($\lambda_{exc} = 552$ nm, $\lambda_{em} \approx 578$ nm).

8.1.7 *In vivo* imaging – Chapter 6

8.1.7.1 Total body imaging

Optical properties of the nanoparticles solutions were investigated in the 575-650 nm range by using an exciting radiation in the 500-550 nm interval (DsRed/DsRed filters), and in the 810-875 nm range by using an exciting radiation in the 710-760 nm region (ICG/ICG filters). Visible and NIR fluorescence images of small living animals were acquired using an optical imager (IVIS 200, Caliper, Alameda, USA) equipped with a CCD camera cooled at –90 °C. Images were acquired with: exposure time = 1 s, binning = 8 and aperture stop $f = 2$.

Each of the three groups of $n = 6$ of Nu/Nu mice was treated with **Rh@NPs**, **C7@NPs**, and **Rh+C7@NPs**; $n = 6$ Nu/Nu mice were kept as the control group and treated with physiological solution. Anesthetized (isoflurane 2%) mice were put in prone position on the heated stage of the instrument. Animal treatments were approved by the Institutional Ethical Committee (CIRSAL) according to the regulations of the Italian Ministry of Health and to the European Communities Council (86/609/EEC) directive.

Images were acquired before and after (continuously for 3 h) tail vein injection of 10 µL per g of body weight of nanoparticles solutions. Different dilutions in physiological solution were tested to obtain the lower detectable signal in the DsRed/DsRed range over the fluorescent background in *in vivo* experiments. The optimal dilution resulted in a nanoparticle concentration of 2 µM.

Three hours after injection the animals were perfused with PBS. The extracted organs of $n = 3$ animals for each group were acquired with the following parameters: exposure time = 1 s, binning = 8 and $f = 1$.

8.1.7.2 *In vivo* microscopy

Microscopic imaging was performed by a two-photon microscope DM-6000 CS (Leica). The nanoparticles were excited by a Chameleon ULTRA II laser (Coherent) at 800 nm and visualized with a 20x objective (water immersed, numerical aperture 1) in the range 560-624 nm. The LAS AF (Leica Application Suite Advance Fluorescence, Leica) software was used during realtime acquisition to process, archive and analyze the image data. A tumor bearing Balb-C mouse was treated by intravenous injection of 30 ml of **Rh+C7@NP**s 4 μM in PBS. It was anesthetized with an intraperitoneal injection of ketamine (100 $mg \cdot kg^{-1}$) and xylazine (15 $mg \cdot kg^{-1}$). Deeper anesthesia has been obtained with isoflurane. An aseptic middle abdominal incision of the skin was made to allow the derma to exteriorize the rectal tumor. The mouse positioned on the stabilizing device was maintained at 37 °C using a thermostatic blanket system (Stoelting) and placed on the microscope. Three anatomical regions were visualized: tumor, ear and derma.

8.1.8 Tissue binding assay and *ex vivo* imaging – Chapter 7

8.1.8.1 Cell cultures and human samples

A highly metastatic variant of HCT-116 cells (ATCC CCL-247), namely HCT-116m, was provided by Dr. Alberto Bardelli (IRCC, Candiolo, Italy). Cells were maintained in Iscove's Modified Dulbecco's Medium (IMDM) supplemented with 10% Fetal Calf Serum (FCS). Fresh samples of grossly normal liver and colon, of primary CRC, and of hepatic metastasis secondary to CRC were collected by the Unit of Surgical Oncology at the IRCC. Collection and manipulation of human samples were approved by the Institute's Ethical Committee, and written informed consent was obtained from all patients in accordance with the Declaration of Helsinki.

8.1.8.2 Nanoparticles overlay assays, histochemistry and 3D tissue reconstructions

OCT-frozen human tissue specimens were cut in 10 μm sections. For overlay experiments nanoparticles (1011/μL) were incubated with the tissue sections for 4 hours at room temperature, followed by 3 washes in Tris Buffered Saline in the presence of 0.1% Tween® 20 (TBS-T). Specific tissue binding, evaluated as emitted fluorescent signal, was detected with a DMIRE2 confocal microscope (Leica Microsystems, Milan, Italy). For prompt visualization of quantified signals, images were converted into a false color LUT Fire scale. Colocalized pixels were identified by the use of ImageJ software (National Institute of Health, Bethesda, MA). To evaluate the homing of metastasis targeted nanoparticles *in vivo*, nanoparticles images were superimposed to blood vessel staining performed with a CD31-specific antibody that was revealed by either Alexa Fluor® 647 (overlay with **Rh@NPs**), Alexa Fluor® 488 (overlay with **C5@NPs**), or DyLight™ 405 (overlay with **Rh+C5@NPs**) secondary antibodies. To reconstruct the 3D models of nanoparticles and tumor vessels, 50 to 80 confocal image series were composed using IMARIS software v. 6.3.1 (Bitplane Scientific Software, Zurich, Switzerland).

8.1.8.3 *Ex vivo* experiments

Six-week female NOD-SCID mice were purchased from Charles River (Lecco, Italy). Experiments involving animals were reviewed and approved by the Institute's ethical committee, and by the Italian Ministry of Health. Eight animals/group were subjected to intraperitoneal anaesthesia with a mixture of xylazine (Xilor®, BI098, Milan, Italy; 0.75 mg/mL) and tiletamine-zolazepam (Zoletil®, Virbac, Milan, Italy; 1 mg/mL each), in physiological solution. Once the mice were profoundly asleep, a midline incision was performed, the spleen was exposed, and HCT-116m cells were injected ($2 \cdot 10^6$ in 50 μL of IMDM medium). The wound was closed by a double suture

and each animal was given caprofen (Rymadil®, Pfizer, Milan, Italy; 0.1 mg) in physiological solution, allowing post-operative pain relief and rehydration. Mice were strictly monitored until completely awake, and oral Ampicillin was administered for 5 days following the surgery. At day 21-28, mice were injected intravenously with nanoparticles ($5 \cdot 10^{12}$ in 200 µL of saline solution). To evaluate nanoparticle homing, mice were euthanized after 16 hours, and organs were photographed with a MZ16FA fluorescence stereomicroscope equipped with a DFC420C (**Rh@NPs**) and a DFC350FX (**C5@NPs**) digital camera (Leica).

8.2 Fluorophores synthesis

8.2.1 Formation of the *s*-indacene system

By varying the starting materials – *i.e.*, the pyrrole and the acyl chloride, a small library of molecules has been synthesized.

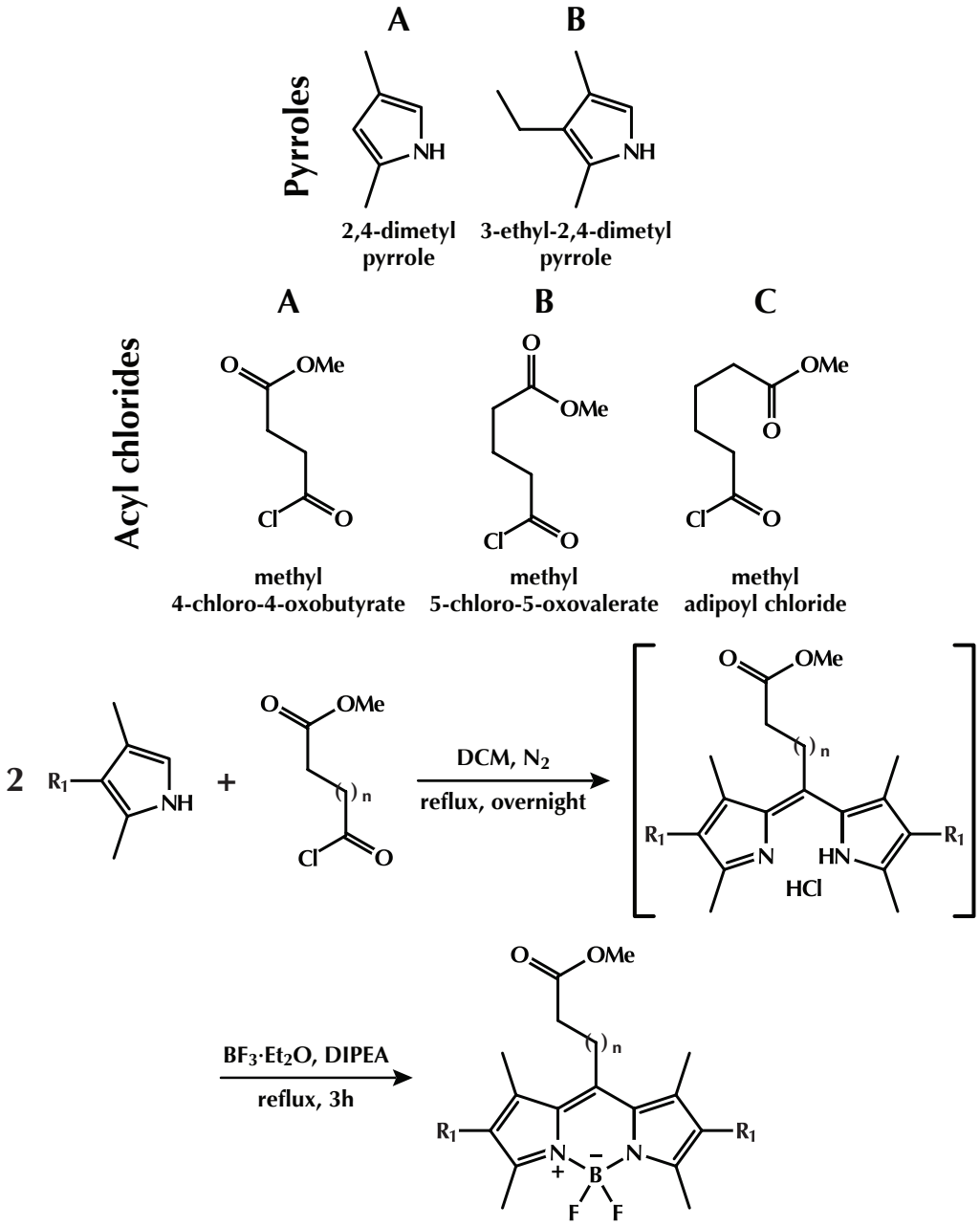

Scheme 1 Molecular structures of the starting materials and synthesis of the BODIPY methyl esters.

BODIPY molecules synthesized starting from pyrrole A have been labeled as **TM** (which stands for **T**etra**M**ethyl – *i.e.*, the substituents on the indacene system – hence R_1 = H), while those from pyrrole B have been tagged **DE** (which indicates the extra **DiE**thyl residues and R_1 = Et). After that designation, the following letter represents the length of the alkyl chain at the 8-position connecting the ester moiety (whose presence is denoted by **OMe**); namely, **E** for **E**thyl (n = 1) – from acyl chloride A, **P** for **P**ropyl (n = 2) – from acyl chloride B, and **B** for **B**utyl (n = 3) – from acyl chloride C.

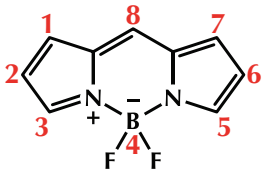

Scheme 2 IUPAC numbering system for BODIPY dyes.

8.2.1.1 Synthetic procedure[7]

A three-necked flask, equipped with a reflux condenser and an addition funnel, is dried with a heat gun under a flow of nitrogen. Then, DCM (1.2 mL per mmol of pyrrole) and a pyrrole (1 eq.) are added inside the flask, while an acyl chloride (1 eq.) diluted in DCM (0.6 mL per mmol of pyrrole) is added dropwise through the addition funnel. The reaction mixture is heated under reflux overnight, after which it is allowed to cool to room temperature. After that, DIPEA (2.2 eq.) is added dropwise through a syringe and, after 15 minutes, boron trifluoride diethyl etherate (3.3 eq.) is added in the same way. Next, the reaction mixture is heated under reflux for 3 hours, after which is allowed to cool to room temperature, diluted with DCM and a 0.1 M solution of hydrochloric acid and extracted three times. The combined organic phases are dried over sodium sulfate, concentrated with the rotary evaporator and desiccated in vacuum, affording a solid substance. The crude product is purified by means of flash chromatography on silica gel; the appropriate fractions of the eluate are then concentrated with the rotary evaporator and desiccated in vacuum.

8.2.1.2 Characterization data

TM-E OMe

PYRROLE A – ACYL CHLORIDE A

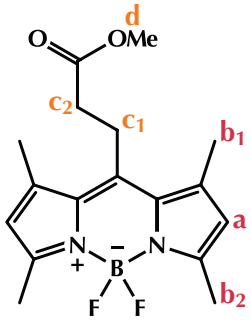

- *Name:* 4,4-difluoro-8-(3-methoxy-3-oxopropyl)-1,3,5,7-tetramethyl-3a,4a-diaza-4-bora-*s*-indacene;
- *Chemical formula:* $C_{17}H_{21}BF_2N_2O_2$;

7. Adapted from: (a) M. Shah, K. Thangraj, M. L. Soong, L. Wolford, J. H. Boyer, I. R. Politzer, T. G. Pavlopoulos, *Heteroat. Chem.* **1990**, *1*, 389; (b) J. H. Boyer, A. M. Haag, G. Sathyamoorthi, M.-L. Soong, K. Thangaraj, *Heteroat. Chem.* **1993**, *4*, 39.

- *Molecular weight:* 334.17;
- *Flash chromatography:* cyclohexane/Et_2O gradient, from 9/1 to 8/2;
- *Yield:* 25%;
- *Appearance:* orange solid;
- *^{1}H-NMR:* 6.05 (s, 2H, **a**); 3.72 (s, 3H, **d**); 3.31-3.27 (m, 2H, **c_1**); 2.61-2.57 (m, 2H, **c_2**); 2.50 (s, 6H, **b_2**); 2.42 (s, 6H, **b_1**).

TM-P OMe

PYRROLE A – ACYL CHLORIDE B

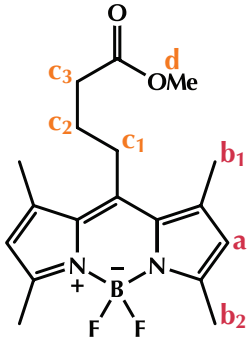

- *Name:* 4,4-difluoro-8-(4-methoxy-4-oxobutyl)-1,3,5,7-tetramethyl-3a,4a-diaza-4-bora-*s*-indacene;
- *Chemical formula:* $C_{18}H_{23}BF_2N_2O_2$;
- *Molecular weight:* 348.20;
- *Flash chromatography:* cyclohexane/Et_2O gradient, from 8/2 to 6/4;
- *Yield:* 63%;
- *Appearance:* orange solid;
- *^{1}H-NMR:* 6.04 (s, 2H, **a**); 3.68 (s, 3H, **d**); 3.01-2.97 (m, 2H, **c_1**); 2.51-2.47 (m, 8H, **b_2**-**c_3**); 2.41 (s, 6H, **b_1**); 1.98-1.91 (m, 2H, **c_2**).

TM-B OMe

PYRROLE A – ACYL CHLORIDE C

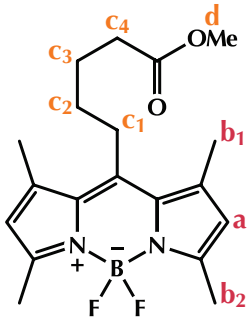

- *Name:* 4,4-difluoro-8-(5-methoxy-5-oxopentyl)-1,3,5,7-tetramethyl-3a,4a-diaza-4-bora-*s*-indacene;
- *Chemical formula:* $C_{19}H_{25}BF_2N_2O_2$;
- *Molecular weight:* 362.22;
- *Flash chromatography:* DCM/cyclohexane/Et_2O gradient, from 2/7/1 to 2/6/2;
- *Yield:* 66%;
- *Appearance:* orange solid;
- *^{1}H-NMR:* 6.03 (s, 2H, **a**); 3.65 (s, 3H, **d**); 2.97-2.92 (m, 2H, **c_1**); 2.49 (s, 6H, **b_2**); 2.40 (s, 6H, **b_1**); 2.37 (t, *J*=7.0, 2H, **c_4**); 1.84-1.77 (m, 2H, **c_3**); 1.69-1.60 (m, 2H, **c_2**).

DE-E OMe

PYRROLE B – ACYL CHLORIDE A

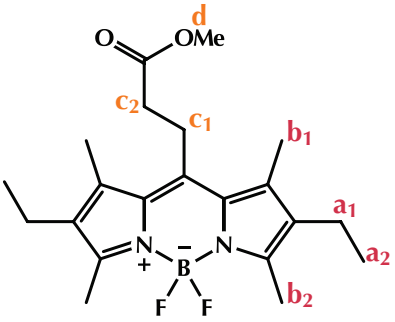

- *Name:* 2,6-diethyl-4,4-difluoro-8-(3-methoxy-3-oxopropyl)-1,3,5,7-tetramethyl-3a,4a-diaza-4-bora-*s*-indacene;
- *Chemical formula:* $C_{21}H_{29}BF_2N_2O_2$;
- *Molecular weight:* 390.27;
- *Flash chromatography:* cyclohexane/Et_2O gradient, from 95/5 to 85/15;
- *Yield:* 29%;
- *Appearance:* deep orange solid;
- *^{1}H-NMR:* 3.73 (s, 3H, **d**); 3.37-3.32 (m, 2H, **c_1**); 2.62-2.57 (m, 2H, **c_2**); 2.48 (s, 6H, **b_2**); 2.38 (q, *J*=7.6, 4H, **a_1**); 2.34 (s, 6H, **b_1**); 1.03 (t, *J*=7.6, 6H, **a_2**).

DE-P OMe

PYRROLE B – ACYL CHLORIDE B

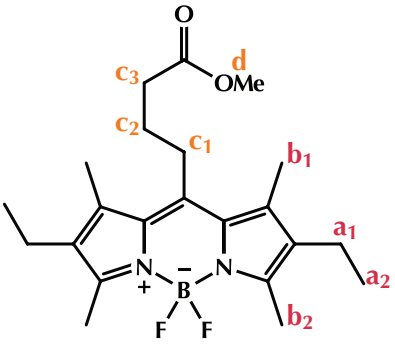

- *Name:* 2,6-diethyl-4,4-difluoro-8-(4-methoxy-4-oxobutyl)-1,3,5,7-tetramethyl-3a,4a-diaza-4-bora-*s*-indacene;
- *Chemical formula:* $C_{22}H_{31}BF_2N_2O_2$;
- *Molecular weight:* 404.30;
- *Flash chromatography:* cyclohexane/Et_2O gradient, from 85/15 to 8/2;
- *Yield:* 52%;
- *Appearance:* deep orange solid;
- *^{1}H-NMR:* 3.69 (s, 3H, **d**); 3.05-3.01 (m, 2H, **c_1**); 2.51-2.48 (m, 8H, **b_2**-**c_3**); 2.38 (q, *J*=7.5, 4H, **a_1**); 2.38 (s, 6H, **b_1**); 1.99-1.91 (m, 2H, **c_2**); 1.03 (t, *J*=7.5, 6H, **a_2**).

DE-B OMe

PYRROLE B – ACYL CHLORIDE C

- *Name:* 2,6-diethyl-4,4-difluoro-8-(5-methoxy-5-oxopentyl)-1,3,5,7-tetramethyl-3a,4a-diaza-4-bora-*s*-indacene;
- *Chemical formula:* $C_{23}H_{33}BF_2N_2O_2$;
- *Molecular weight:* 418.33;

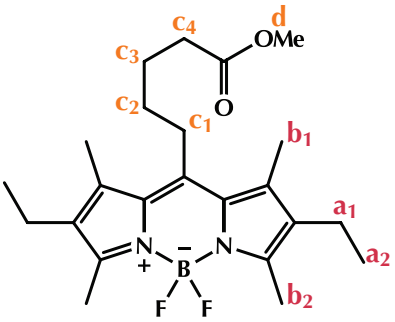

- *Flash chromatography:* cyclohexane/Et_2O gradient, from 95/5 to 75/25;
- *Yield:* 71%;
- *Appearance:* deep orange solid;
- *^{1}H-N MR:* 3.66 (s, 3H, **d**); 3.01-2.97 (m, 2H, **c_1**); 2.47 (s, 6H, **b_2**); 2.41-2.35 (m, 6H, **a_1**-**c_4**); 2.32 (s, 6H, **b_1**); 1.85-1.78 (m, 2H, **c_3**); 1.69-1.61 (m, 2H, **c_2**); 1.03 (t, J=7.4, 6H, **a_2**).

8.2.1.3 Remarks on the synthesis

The molecules with an ethyl chain at the 8-position seem to have the tendency to decompose during the purification by means of flash chromatography (a red, non fluorescent band always precedes the yellow/orange, fluorescent band of the product – even if a pure fraction is passed through the column again): in fact, the yields for these compounds are about half less than those bearing a propyl or a butyl chain. At a lesser extent, this phenomenon seems to occur also in the subsequent synthetic steps.

8.2.2 Extension of the aromatic conjugation

Methyl substituents at the 3- and 5-position are acidic enough to react with electron-rich aldehydes in a Knoevenagel condensation (scheme 3),[8] allowing the expansion of the π-conjugation and thus shifting both the absorption and emission maxima of the resulting molecules towards the red.

Monoadducts are labeled **mS**, while distyryl molecules are denoted with **dS**; the letter that follows (**A** – R_2 = Me, or **B** – R_2 = *t*-Bu) indicates the type of aldehyde which has been used in the condensation.

8.2.2.1 Synthetic procedure[9]

In a two-necked flask, equipped with a Dean-Stark apparatus, a methyl ester functionalized dye (1 eq.), a benzaldehyde (0.9 eq to obtain mainly the monosubstituted product, 4 eq. to get mainly the distyryl adduct or 1.5 eq. to obtain approximately the same mmol of both), piperidine (20 eq.) and *p*TsA (0.4 eq.) are dissolved in toluene (0.1 mL per mg of dye) and heated to

Table 1 Reaction conditions for the Knoevenagel condensation.

Product	n	R_1	R_2	Aldehyde	Equivalents	Days of reflux	Major Adduct
DE-P mSA OMe	2	Et	Me	A	0.9	1	mono
DE-B mSA OMe	3	Et	Me	A	1.5	7	mono
TM-P dSB OMe	2	H	*t*-BuO	B	4.0	3	di

8. E. Knoevenagel, *Ber. Dtsch. Ch em. Ges.* **1898**, *31*, 2596.
9. Adapted from: R. Ziessel, T. Bura, J.-H. Olivier, *Synlett* **2010**, 2304.

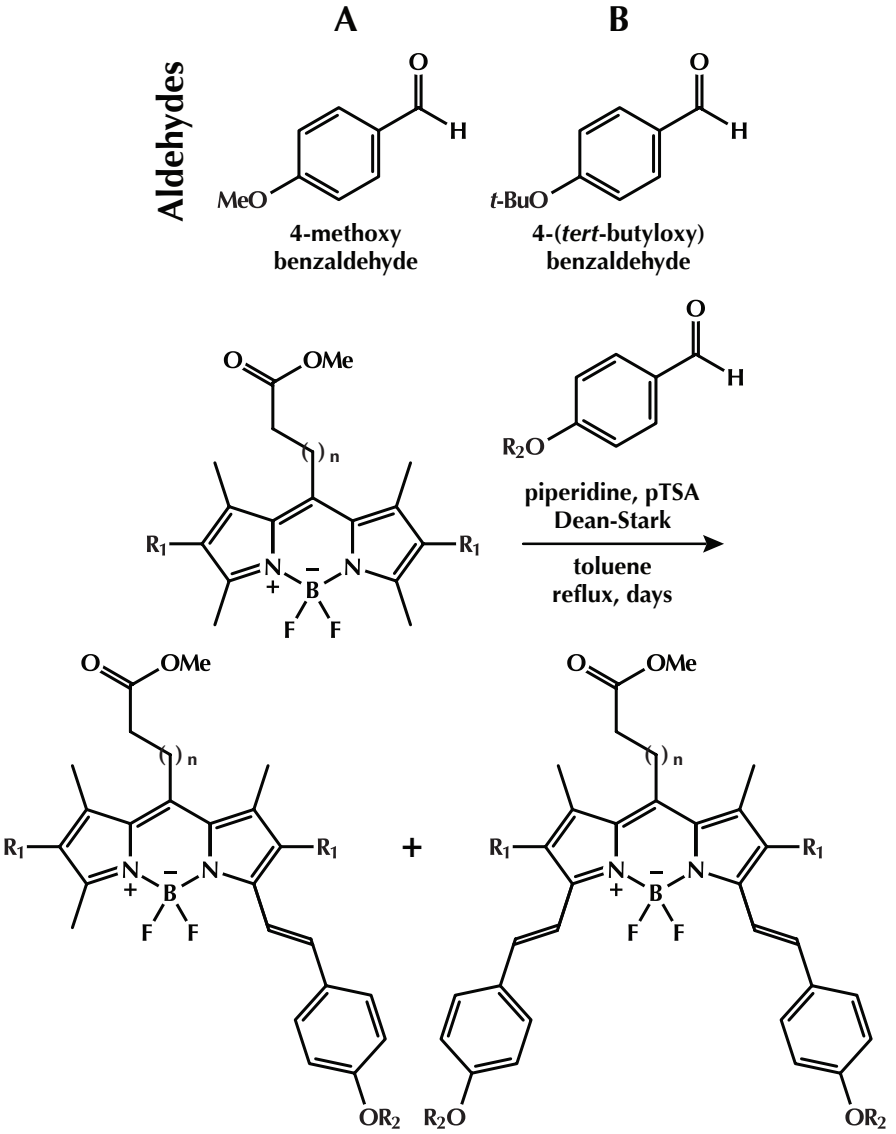

Scheme 3 Molecular structures of the aldehydes used in the Knoevenagel condensation and synthesis of the mono- and distyryl adducts.

reflux for several days. The reaction is monitored by TLC every day and stopped when no further progress is detected. At this point, it is allowed to cool to room temperature, then diluted with DCM and a 0.1 M solution of hydrochloric acid and finally extracted three times with DCM. The combined organic phases are dried over sodium sulfate, concentrated with the rotary evaporator and desiccated in vacuum, affording a solid substance. The crude product is purified by means of flash chromatography on silica gel; the appropriate fractions of the eluate are then concentrated with the rotary evaporator and desiccated in vacuum.

8.2.2.2 Characterization data

DE-P mSA OMe

- *Name:* (*E*)-2,6-diethyl-4,4-difluoro-8-(4-methoxy-4-oxobutyl)-5-(4-methoxystyryl)-1,3,7-trimethyl-3a,4a-diaza-4-bora-*s*-indacene;
- *Chemical formula:* $C_{30}H_{37}BF_2N_2O_3$;
- *Molecular weight:* 522.43;
- *Flash chromatography:* petroleum ether/AcOEt gradient, from 95/5 to 7/3;
- *Yield:* 10%;

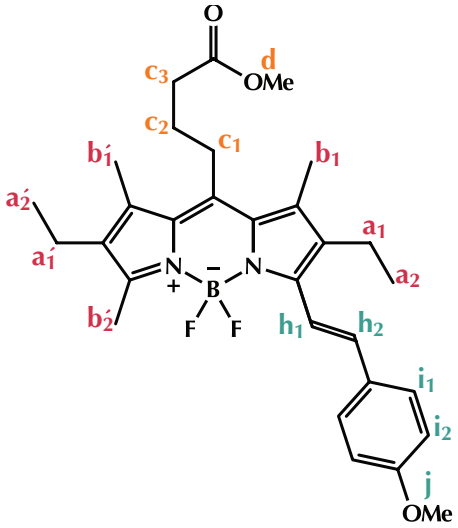

- *Appearance:* golden solid;
- *^{1}H-NMR:* 7.55 (d, *J*=17.0, 1H, h_2); 7.51 (d, *J*=8.8, 2H, i_1); 7.10 (d, *J*=17.0, 1H, h_1); 6.88 (d, *J*=8.8, 2H, i_2); 3.82 (s, 3H, **j**); 3.69 (s, 3H, **d**); 3.10-3.05 (m, 2H, c_1); 2.67 (q, *J*=7.5, 2H, a_1); 2.52-2.49 (m, 5H, b_2́-c_3); 2.43-2.35 (m, 8H, a_1́-b_1-b_1́); 2.00-1.92 (m, 2H, c_2); 1.20 (t, *J*=7.5, 3H, a_2); 1.04 (t, *J*=7.6, 3H, a_2́).

DE-B mSA OMe

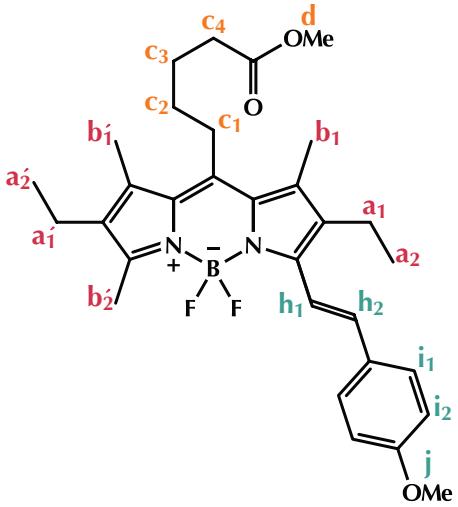

- *Name:* (*E*)-2,6-diethyl-4,4-difluoro-8-(5-methoxy-5-oxopentyl)-5-(4-methoxystyryl)-1,3,7-trimethyl-3a,4a-diaza-4-bora-*s*-indacene;
- *Chemical formula:* $C_{31}H_{39}BF_2N_2O_3$;
- *Molecular weight:* 536.46;
- *Flash chromatography:* petroleum ether/AcOEt gradient, from 95/5 to 75/25;
- *Yield:* 14%;
- *Appearance:* golden solid;
- *^{1}H-NMR:* 7.55 (d, *J*=16.8, 1H, h_2); 7.51 (d, *J*=8.8, 2H, i_1); 7.10 (d, *J*=16.8, 1H, h_1); 6.88 (d, *J*=8.8, 2H, i_2); 3.82 (s, 3H, **j**); 3.67 (s, 3H, **d**); 3.06-3.01 (m, 2H, c_1); 2.67 (q, *J*=7.5, 2H, a_1); 2.52 (s, 3H, b_2́); 2.43-2.32 (m, 10H, a_1́-b_1-b_1́-c_4); 1.87-1.79 (m, 2H, c_3); 1.71-1.64 (m, 2H, c_2); 1.21 (t, *J*=7.5, 3H, a_2); 1.04 (t, *J*=7.8, 3H, a_2́).

TM-P dSB OMe

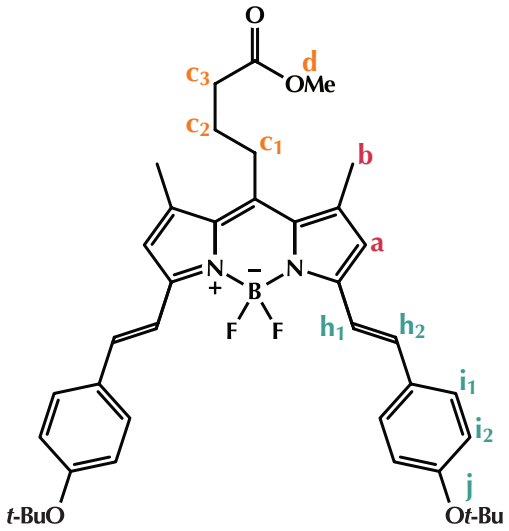

- *Name:* 3,5-bis((*E*)-4-(*tert*-butoxy)styryl)-4,4-difluoro-8-(4-methoxy-4-oxobutyl)-1,7-dimethyl-3a,4a-diaza-4-bora-*s*-indacene;
- *Chemical formula:* $C_{40}H_{47}BF_2N_2O_4$;
- *Molecular weight:* 668.62;
- *Flash chromatography:* first column – petroleum ether/AcOEt gradient, from 9/1 to 6/4; second column – cyclohexane/DCM gradient, from 4/6 to 0/10;
- *Yield:* 22%;
- *Appearance:* bronze solid;
- *^{1}H-NMR:* 7.59 (d, *J*=16.4, 2H, **h_2**); 7.52 (dd, *J*=2.0, *J*=6.8, 4H, **i_1**); 7.19 (d, *J*=16.4, 2H, **h_1**); 6.99 (dd, *J*=2.0, *J*=6.8, 4H, **i_2**); 6.69 (s, 2H, **a**); 3.69 (s, 3H, **d**); 3.07-3.02 (m, 2H, **c_1**); 2.03-1.95 (m, 2H, **c_2**); 2.53-2.49 (m, 8H, **b**-**c_3**); 1.41 (s, 9H, **j**); 1.37 (s 9H, **j´**).

8.2.2.3 Remarks on the synthesis

By adjusting the reaction conditions (*i.e.*, the equivalents of aldehyde and the days of reflux), it is possible to choose between the monosubstituted species or the disubstituted adduct as the major product, but they can never be obtained exclusively; moreover, the reaction never reaches completion, so the crude always contains a certain amount of starting material as well. Extra care should be given during purification by means of flash chromatography, considering that the three products have similar polarity and that the distyryl product in particular tends to be well soluble only in dichloromethane.

8.2.3 Deprotection of the methyl ester

There are two viable methods for removing the ester moiety: saponification with potassium carbonate or lithium hydroxide. The latter reagent is more reactive and it requires shorter reaction times, but there is a slight risk of degrading the indacene ring.

The designation of the molecules changes simply from **OMe** to **OH**. These reactions can be applied not only to the simplest BODIPY molecules (*i.e.*, $R_3=R_4=H$), but also to monoadducts ($R_3=H$, R_4=4-alkoxystyryl) and to diadducts ($R_3=R_4$=4-alkoxystyryl).

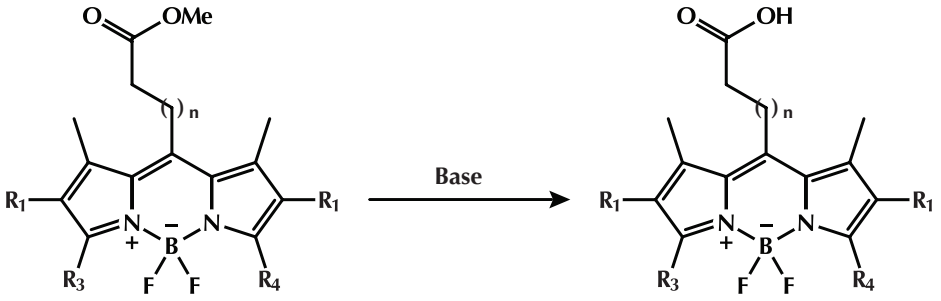

Scheme 4 Deprotection of the ester moiety.

8.2.3.1 Synthetic procedures

Method A – K_2CO_3:[10] in a one-necked flask, a methyl ester functionalized dye (1 eq.) is dissolved in a mixture of methanol and THF (1/1, v/v, 0.2 mL/mg). In the meantime, potassium carbonate (5 eq.) is dissolved in water (0.1 mL/mg of dye) and added to the flask. After the reaction mixture is stirred overnight, it is diluted with DCM and a 0.1 M solution of hydrochloric acid and extracted three times with DCM. The combined organic phases are dried over sodium sulfate, concentrated with the rotary evaporator and desiccated in vacuum, affording a solid substance. The crude product may be used without further purification. It is recommended to attempt purification only in small amounts, for spectrometric identification, by means of flash chromatography on silica gel.

Method B – LiOH:[11] in a one-necked flask, a methyl ester functionalized dye (1 eq.) is stirred until complete dissolution in THF (0.2 mL/mg). In the meantime, lithium hydroxide (5 eq.) is dissolved in water (0.04 mL/mg of dye) and added to the flask. After the reaction mixture is stirred from 2 to 4 hours, it is diluted with DCM and a 0.1 M solution of hydrochloric acid and extracted three times with DCM. The combined organic phases are dried over sodium sulfate, concentrated with the rotary evaporator and desiccated in vacuum, affording a solid substance.

Table 2 Reaction conditions for the ester cleavage.

Product	n	R_1	R_3	R_4	Method	Base	Time
TM-E OH	1	H	Me	Me	A	K_2CO_3	overnight
TM-P OH	2	H	Me	Me	B	LiOH	2 hours
TM-B OH	3	H	Me	Me	B	LiOH	4 hours
DE-E OH	1	Et	Me	Me	B	LiOH	2 hours
DE-P OH	2	Et	Me	Me	B	LiOH	2 hours
DE-B OH	3	Et	Me	Me	A	K_2CO_3	overnight
DE-P mSA OH	2	Et	Me	4-methoxystyryl	B	LiOH	2 hours
DE-B mSA OH	3	Et	Me	4-methoxystyryl	B	LiOH	6 hours
TM-P dSB OH	2	H	4-(*t*-BuO)styryl	4-(*t*-BuO)styryl	B	LiOH	2 hours

10. Adapted from: K. L. Kaestle, M. K. Anwer, T. K. Audhya, G. Goldstein, *Tet. Lett.* **1991**, *32*, 327.
11. Adapted from: E. J. Corey, I. Székely, C. S. Shiner, *Tet. Lett.* **1977**, *18*, 3529.

8.2.3.2 Characterization data

TM-E OH

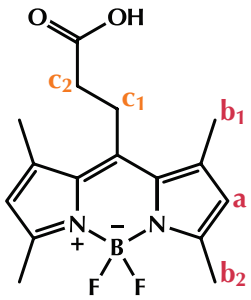

- *Name:* 8-(2-carboxyethyl)-4,4-difluoro-1,3,5,7-tetramethyl-3a,4a-diaza-4-bora-*s*-indacene;
- *Chemical formula:* $C_{16}H_{19}BF_2N_2O_2$;
- *Molecular weight:* 320.14;
- *Flash chromatography:* cyclohexane/AcOEt gradient, from 7/3 to 1/1;
- *Crude yield:* 104%;
- *Appearance:* orange solid;
- *^{1}H-NMR:* 6.06 (s, 2H, **a**); 3.33-3.29 (m, 2H, **c_1**); 2.67-2.63 (m, 2H, **c_2**); 2.51 (s, 6H, **b_2**); 2.43 (s, 6H, **b_1**).

TM-P OH

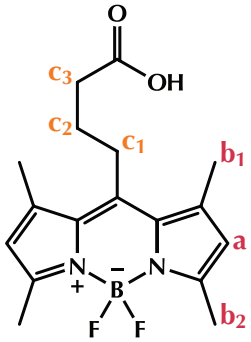

- *Name:* 8-(3-carboxypropyl)-4,4-difluoro-1,3,5,7-tetramethyl-3a,4a-diaza-4-bora-*s*-indacene;
- *Chemical formula:* $C_{17}H_{21}BF_2N_2O_2$;
- *Molecular weight:* 334.17;
- *Flash chromatography:* cyclohexane/AcOEt gradient, from 8/2 to 1/9;
- *Crude yield:* 100%;
- *Appearance:* orange solid;
- *^{1}H-NMR:* 6.04 (s, 2H, **a**); 3.04-2.99 (m, 2H, **c_1**); 2.54 (t, *J*=7.2, 2H, **c_3**); 2.50 (s, 6H, **b_2**); 2.41 (s, 6H, **b_1**); 2.00-1.92 (m, 2H, **c_2**).

TM-B OH

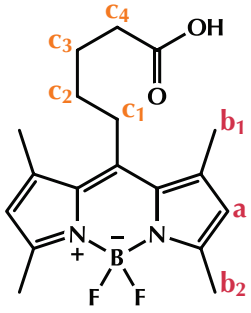

- *Name:* 8-(4-carboxybutyl)-4,4-difluoro-1,3,5,7-tetramethyl-3a,4a-diaza-4-bora-*s*-indacene;
- *Chemical formula:* $C_{18}H_{23}BF_2N_2O_2$;
- *Molecular weight:* 348.20;
- *Flash chromatography:* cyclohexane/AcOEt gradient, from 8/2 to 1/1;
- *Crude yield:* 111%;
- *Appearance:* orange solid;
- *^{1}H-NMR:* 6.03 (s, 2H, **a**); 2.97-2.93 (m, 2H, **c_1**); 2.49 (s, 6H, **b_2**); 2.44-2.40 (m, 8H, **b_1**-**c_4**); 1.85-1.78 (m, 2H, **c_3**); 1.71-1.63 (m, 2H, **c_2**).

DE-E OH

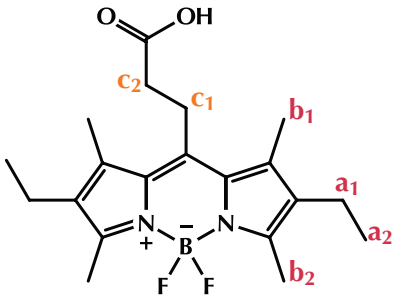

- *Name:* 8-(2-carboxyethyl)-2,6-diethyl-4,4-difluoro-1,3,5,7-tetramethyl-3a,4a-diaza-4-bora-*s*-indacene;
- *Chemical formula:* $C_{20}H_{27}BF_2N_2O_2$;
- *Molecular weight:* 376.25;
- *Flash chromatography:* cyclohexane/AcOEt gradient, from 8/2 to 6/4;
- *Crude yield:* 108%;
- *Appearance:* deep orange solid;
- *^{1}H-NMR:* 3.39-3.35 (m, 2H, **c_1**); 2.69-2.64 (m, 2H, **c_2**); 2.49 (s, 6H, **b_2**); 2.39 (q, *J*=7.7, 4H, **a_1**); 2.35 (s, 6H, **b_1**); 1.04 (t, *J*=7.7, 6H, **a_2**).

DE-P OH

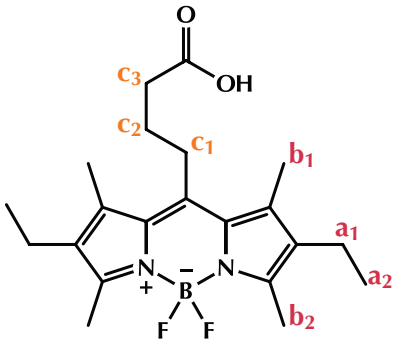

- *Name:* 8-(3-carboxypropyl)-2,6-diethyl-4,4-difluoro-1,3,5,7-tetramethyl-3a,4a-diaza-4-bora-*s*-indacene;
- *Chemical formula:* $C_{21}H_{29}BF_2N_2O_2$;
- *Molecular weight:* 390.27;
- *Flash chromatography:* cyclohexane/AcOEt gradient, from 7/3 to 2/8;
- *Crude yield:* 93%;
- *Appearance:* deep orange solid;
- *^{1}H-NMR:* 3.08-3.04 (m, 2H, **c_1**); 2.54 (t, *J*=7.2, 2H, **c_3**); 2.48 (s, 6H, **b_2**); 2.38 (q, *J*=7.5, 4H, **a_1**); 2.33 (s, 6H, **b_1**); 2.01-1.93 (m, 2H, **c_2**); 1.03 (t, *J*=7.5, 6H, **a_2**).

DE-B OH

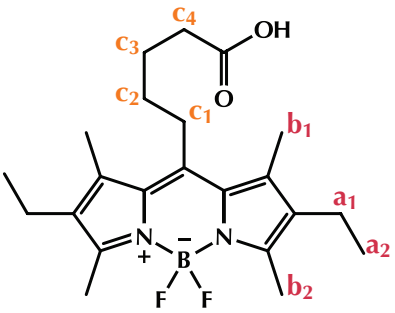

- *Name:* 8-(4-carboxybutyl)-2,6-diethyl-4,4-difluoro-1,3,5,7-tetramethyl-3a,4a-diaza-4-bora-*s*-indacene;
- *Chemical formula:* $C_{22}H_{31}BF_2N_2O_2$;
- *Molecular weight:* 404.30;
- *Flash chromatography:* not performed;
- *Crude yield:* 104%;
- *Appearance:* deep orange solid;
- *^{1}H-NMR:* 3.02-2.98 (m, 2H, c_1); 2.47 (s, 6H, b_2); 2.45-2.35 (m, 6H, a_1-c_4); 2.32 (s, 6H, b_1); 1.86-1.79 (m, 2H, c_3); 1.72-1.64 (m, 2H, c_2); 1.03 (t, J=7.4, 6H, a_2).

DE-P mSA OH

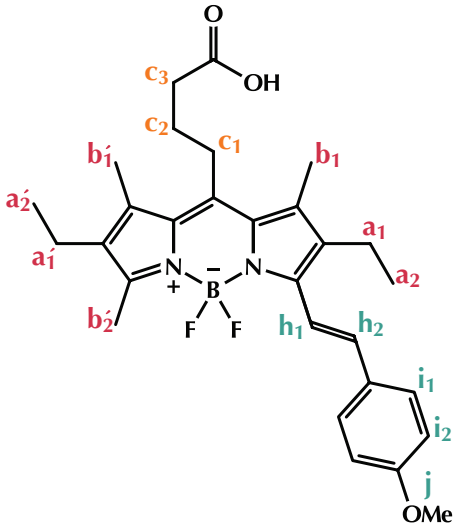

- *Name:* (*E*)-8-(3-carboxypropyl)-2,6-diethyl-4,4-difluoro-5-(4-methoxystyryl)-1,3,7-trimethyl-3a,4a-diaza-4-bora-*s*-indacene;
- *Chemical formula:* $C_{29}H_{35}BF_2N_2O_3$;
- *Molecular weight:* 508.41;
- *Flash chromatography:* not performed;
- *Crude yield:* 101%;
- *Appearance:* golden solid;
- *^{1}H-NMR:* not recorded.

DE-B mSA OH

- *Name:* (*E*)-8-(4-carboxybutyl)-2,6-diethyl-4,4-difluoro-5-(4-methoxystyryl)-1,3,7-trimethyl-3a,4a-diaza-4-bora-*s*-indacene;
- *Chemical formula:* $C_{30}H_{37}BF_2N_2O_3$;
- *Molecular weight:* 522.43;

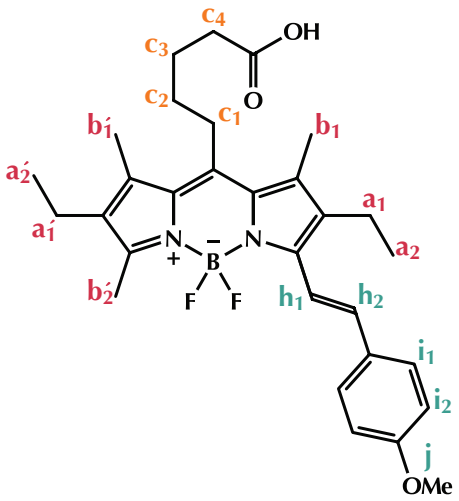

- *Flash chromatography:* not performed;
- *Crude yield:* 105%;
- *Appearance:* golden solid;
- *^{1}H-NMR:* 7.55 (d, *J*=16.6, 1H, h_2); 7.50 (d, *J*=8.6, 2H, i_1); 7.10 (d, *J*=16.6, 1H, h_1); 6.88 (d, *J*=8.6, 2H, i_2); 3.82 (s, 3H, **j**); 3.07-3.02 (m, 2H, c_1); 2.67 (q, *J*=7.7, 2H, a_1); 2.52 (s, 3H, b_2'); 2.46-2.39 (m, 4H, a_1'-c_4); 2.36 (s, 3H, b_1); 2.34 (s, 3H, b_1'); 1.86-1.81 (m, 2H, c_3); 1.72-1.68 (m, 2H, c_2); 1.20 (t, *J*=7.7, 3H, a_2); 1.04 (t, *J*=7.6, 3H, a_2').

TM-P dSB OH

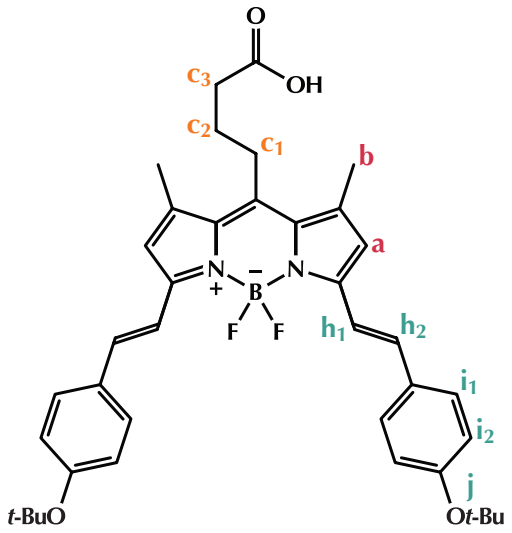

- *Name:* 3,5-bis((*E*)-4-(*tert*-butoxy)styryl)-8-(3-carboxypropyl)-4,4-difluoro-1,7-dimethyl-3a,4a-diaza-4-bora-*s*-indacene;
- *Chemical formula:* $C_{39}H_{45}BF_2N_2O_4$;
- *Molecular weight:* 654.59;
- *Flash chromatography:* cyclohexane/AcOEt gradient, from 8/2 to 2/8;
- *Crude yield:* 106%;
- *Appearance:* bronze solid;
- *^{1}H-NMR:* 7.58 (d, *J*=16.2, 2H, h_2); 7.52 (d, *J*=8.8, 4H, i_1); 7.20 (d, *J*=16.2, 2H, h_1); 6.99 (d, *J*=8.8, 4H, i_2); 6.69 (s, 2H, **a**); 3.09-3.05 (m, 2H, c_1); 2.56 (t, *J*=7.2, 2H, c_3); 2.49 (s, 6H, **b**); 2.03-1.98 (m, 2H, c_2); 1.37 (s, 18H, **j**).

8.2.3.3 Remarks on the synthesis

The crude product is pure enough to be used in the next step without further purification. Flash chromatography on silica gel of molecules containing carboxylic acids is often troublesome and can lead to a substantial loss of product. If purification is needed for an accurate spectrometric identification, it is recommended to attempt it only in small amounts.

8.2.4 Triethoxysilane functionalization

The triethoxysilane function is introduced via a coupling reaction between the carboxylic moiety of the dye and the amino group of APTES. In an optimization step, several coupling agents were tested: from those experiments 1-hydroxybenzotriazole and COMU® resulted to be the best reagents in DCM.

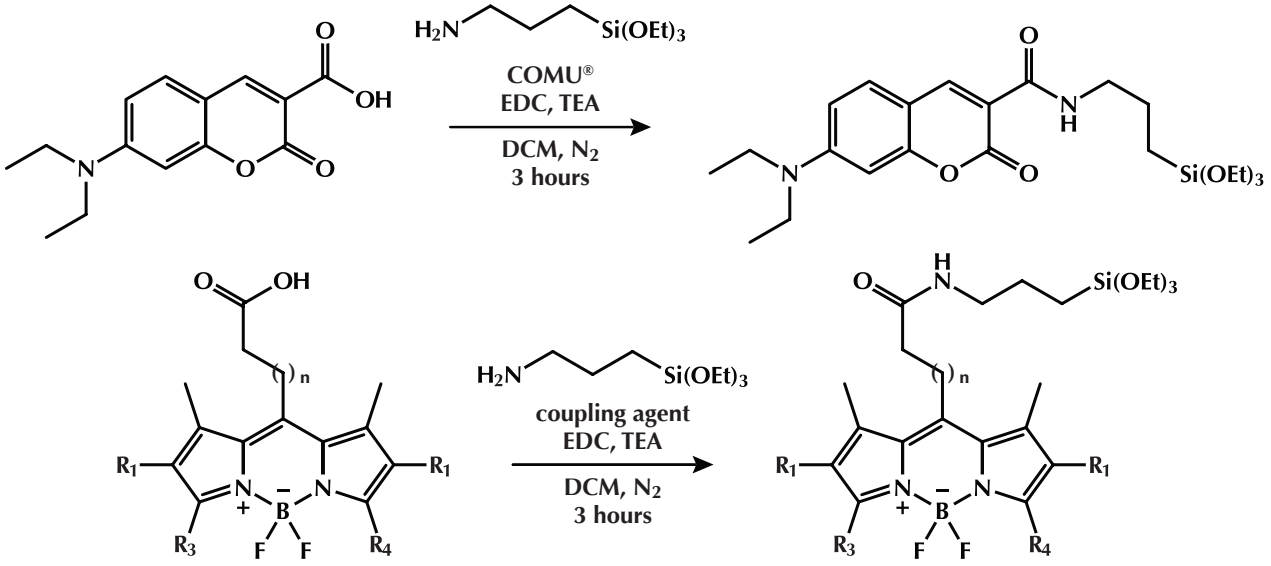

Scheme 5 Coupling between fluorophores and APTES.

Table 3 Reaction conditions for the triethoxysilane derivatization of BODIPY dyes.

Product	n	R_1	R_3	R_4	Coupling agent	Solvent
TM-E Sil	1	H	Me	Me	COMU®	DCM
TM-P Sil	2	H	Me	Me	COMU®	THF[a]
TM-B Sil	3	H	Me	Me	COMU®	DCM
DE-E Sil	1	Et	Me	Me	HOBt	DCM
DE-P Sil	2	Et	Me	Me	COMU®	DCM
DE-B Sil	3	Et	Me	Me	HOBt	DCM
DE-P mSA Sil	2	Et	Me	4-methoxystyryl	COMU®	DCM
DE-B mSA Sil	3	Et	Me	4-methoxystyryl	HOBt	DCM
TM-P dSB Sil	2	H	4-(*t*-BuO)styryl	4-(*t*-BuO)styryl	HOBt	DCM

[a] The compound is insoluble in DCM.

As regards the nomenclature of these molecules, the designation **OH** changes to **Sil**; DEAC becomes **DEAC Sil.**

8.2.4.1 Synthetic procedure

A two-necked flask is dried with a heat gun under a flow of nitrogen. Then, DCM (0.4 mL/mg of dye), a carboxylic-functionalized dye (1 eq.), APTES (2 eq.), TEA (2 eq.), EDC (1.5 eq.), and the coupling agent (1.5 eq.) are mixed together and stirred at room temperature for 90 minutes; after that, an additional amount of EDC (1.5 eq.) and coupling agent (1.5 eq.) is added. Finally, the solvent is removed under reduced pressure with a rotary evaporator. The powder is purified by means of flash chromatography on silica gel; the appropriate fractions of the eluate are then concentrated with the rotary evaporator and desiccated in vacuum, affording a solid substance.

8.2.4.2 Characterization data

DEAC Sil

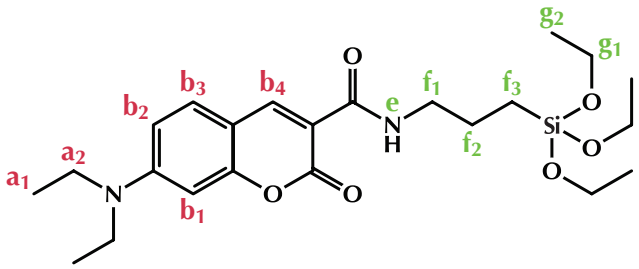

- *Name:* 7-(diethylamino)-*N*-(3-(triethoxysilyl)propyl)-coumarin-3-carboxamide;
- *Chemical formula:* $C_{23}H_{36}N_2O_6Si$;
- *Molecular weight:* 464.63;
- *Flash chromatography:* cyclohexane/AcOEt gradient, from 6/4 to 4/6;
- *Yield:* 85%;
- *Appearance:* yellow solid;
- *^{1}H-NMR:* 8.83-8.79 (brs, 1H, **e**), 8.68 (s, 1H, **b_4**), 7.40 (d, J=8.8, 1H, **b_3**), 6.62 (dd, J=2.4, J=8.8, 1H, **b_2**), 6.48 (d, J=2.4, 1H, **b_1**), 3.80 (q, J=6.9, 6H, **g_1**), 3.46-3.39 (m, 6H, **a_2**-**f_1**), 1.75-1.67 (m, 2H, **f_2**), 1.23-1.19 (m, 15H, **a_1**-**g_2**), 0.68 (t, J=8.4, 2H, **f_3**).

TM-E Sil

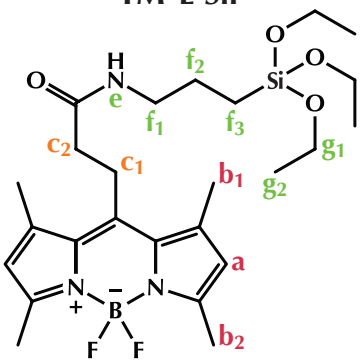

- *Name:* 4,4-difluoro-1,3,5,7-tetramethyl-8-(3-oxo-3-((3-(triethoxysilyl)propyl)amino) propyl)-3a,4a-diaza-4-bora-*s*-indacene;
- *Chemical formula:* $C_{25}H_{40}BF_2N_3O_4Si$;
- *Molecular weight:* 523.50;
- *Flash chromatography:* cyclohexane/AcOEt gradient, from 9/1 to 1/1;
- *Yield:* 62%;
- *Appearance:* orange solid;

- *^{1}H-NMR:* 6.03 (s, 2H, **a**); 5.82 (brs, 1H, **e**); 3.79 (q, *J*=7.1, 6H, **g_1**); 3.33-3.29 (m, 2H, **c_1**); 3.27-3.22 (m, 2H, **f_1**); 2.49 (s, 6H, **b_2**); 2.42 (s, 6H, **b_1**); 2.41-2.38 (m, 2H, **c_2**); 1.65-1.57 (m, 2H, **f_2**); 1.20 (t, *J*=7.1, 9H, **g_2**); 0.60 (t, *J*=8.0, 2H, **f_3**).

TM-P Sil

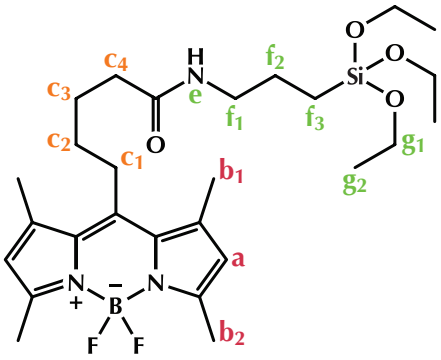

- *Name:* 4,4-difluoro-1,3,5,7-tetramethyl-8-(4-oxo-4-((3-(triethoxysilyl)propyl)amino) butyl)-3a,4a-diaza-4-bora-*s*-indacene;
- *Chemical formula:* $C_{26}H_{42}BF_2N_3O_4Si$;
- *Molecular weight:* 537.52;
- *Flash chromatography:* cyclohexane/AcOEt gradient, from 7/3 to 1/9;
- *Yield:* 49%;
- *Appearance:* orange solid;
- *^{1}H-NMR:* 6.03 (s, 2H, **a**); 5.88 (brs, 1H, **e**); 3.80 (q, *J*=7.0, 6H, **g_1**); 3.26-3.22 (m, 2H, **f_1**); 3.02-2.98 (m, 2H, **c_1**); 2.49 (s, 6H, **b_2**); 2.41 (s, 6H, **b_1**); 2.31 (t, *J*=7.2, 2H, **c_3**); 1.99-1.91 (m, 2H, **c_2**); 1.66-1.58 (m, 2H, **f_2**); 1.20 (t, *J*=7.0, 9H, **g_2**); 0.62 (t, *J*=8.0, 2H, **f_3**).

TM-B Sil

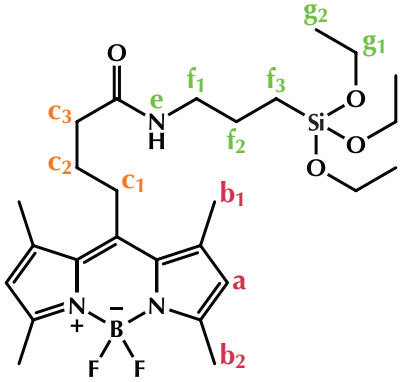

- *Name:* 4,4-difluoro-1,3,5,7-tetramethyl-8-(5-oxo-5-((3-(triethoxysilyl)propyl)amino)pen tyl)-3a,4a-diaza-4-bora-*s*-indacene;
- *Chemical formula:* $C_{27}H_{41}BF_2N_3O_4Si$;
- *Molecular weight:* 551.55;
- *Flash chromatography:* cyclohexane/AcOEt gradient, from 8/2 to 1/1;
- *Yield:* 63%;
- *Appearance:* orange solid;
- *^{1}H-NMR:* 6.03 (s, 2H, **a**); 5.71 (brs, 1H, **e**); 3.66 (q, *J*=7.0, 6H, **g_1**); 3.24-3.19 (m, 2H, **f_1**); 2.97-2.93 (m, 2H, **c_1**); 2.49 (s, 6H, **b_2**); 2.39 (s, 6H, **b_1**); 2.18 (t, *J*=7.2, 2H, **c_4**); 1.86-1.78 (m, 2H, **c_3**); 1.67-1.56 (m, 4H, **c_2**-**f_2**); 1.20 (t, *J*=7.0, 9H, **g_2**); 0.60 (t, *J*=8.0, 2H, **f_3**).

DE-E Sil

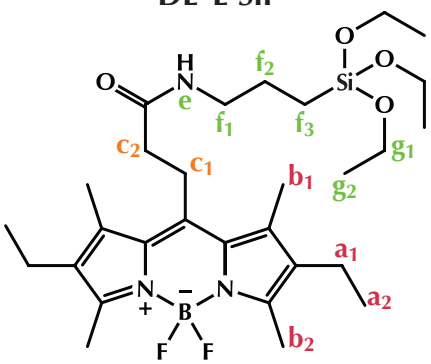

- *Name:* 2,6-diethyl-4,4-difluoro-1,3,5,7-tetramethyl-8-(3-oxo-3-((3-(triethoxysilyl)propyl) amino)propyl)-3a,4a-diaza-4-bora-*s*-indacene;
- *Chemical formula:* $C_{29}H_{48}BF_2N_3O_4Si$;
- *Molecular weight:* 579.60;
- *Flash chromatography:* cyclohexane/ AcOEt gradient, from 95/5 to 7/3;
- *Yield:* 52%;
- *Appearance:* deep orange solid;
- *^{1}H-NMR:* 5.80 (brs, 1H, **e**); 3.80 (q, *J*=7.1, 6H, $\mathbf{g_1}$); 3.39-3.34 (m, 2H, $\mathbf{c_1}$); 3.29-3.24 (m, 2H, $\mathbf{f_1}$); 2.44-2.37 (m, 6H, $\mathbf{a_1}$-$\mathbf{c_2}$); 2.48 (s, 6H, $\mathbf{b_2}$); 2.35 (s, 6H, $\mathbf{b_1}$); 1.65-1.57 (m, 2H, $\mathbf{f_2}$); 1.20 (t, *J*=7.1, 9H, $\mathbf{g_2}$); 1.04 (t, *J*=7.6, 6H, $\mathbf{a_2}$); 0.61 (t, *J*=8.0, 2H, $\mathbf{f_3}$).

DE-P Sil

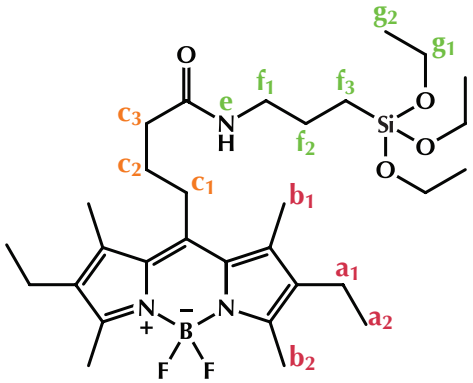

- *Name:* 2,6-diethyl-4,4-difluoro-1,3,5,7-tetramethyl-8-(4-oxo-4-((3-(triethoxysilyl)propyl) amino)butyl)-3a,4a-diaza-4-bora-*s*-indacene;
- *Chemical formula:* $C_{30}H_{50}BF_2N_3O_4Si$;
- *Molecular weight:* 593.63;
- *Flash chromatography:* cyclohexane/AcOEt gradient, from 9/1 to 3/7;
- *Appearance:* deep orange solid;
- *Yield:* 46%;
- *^{1}H-NMR:* 5.81 (brs, 1H, **e**); 3.80 (q, *J*=7.0, 6H, $\mathbf{g_1}$); 3.29-3.22 (m, 2H, $\mathbf{f_1}$); 3.06-3.02 (m, 2H, $\mathbf{c_1}$); 2.47 (s, 6H, $\mathbf{b_2}$); 2.37 (q, *J*=7.4, 4H, $\mathbf{a_1}$); 2.33-2.29 (m, 8H, $\mathbf{b_1}$-$\mathbf{c_3}$); 1.99-1.91 (m, 2H, $\mathbf{c_2}$); 1.66-1.58 (m, 2H, $\mathbf{f_2}$); 1.20 (t, *J*=7.0, 9H, $\mathbf{g_2}$); 1.02 (t, *J*=7.4, 6H, $\mathbf{a_2}$); 0.62 (t, *J*=8.2, 2H, $\mathbf{f_3}$).

DE-B Sil

- *Name:* 2,6-diethyl-4,4-difluoro-1,3,5,7-tetramethyl-8-(5-oxo-5-((3-(triethoxysilyl)propyl) amino)pentyl)-3a,4a-diaza-4-bora-*s*-indacene;
- *Chemical formula:* $C_{31}H_{52}BF_2N_3O_4Si$;

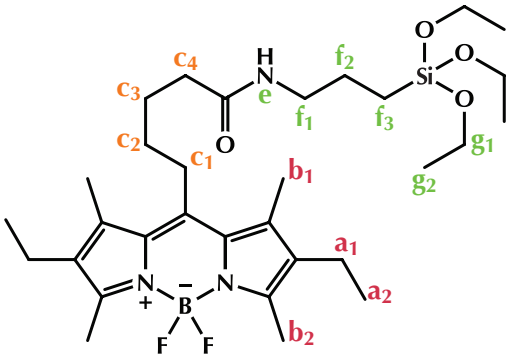

- *Molecular weight:* 607.66;
- *Flash chromatography:* cyclohexane/AcOEt gradient, from 9/1 to 3/7;
- *Yield:* 63%;
- *Appearance:* deep orange solid;
- *^{1}H-NMR:* 5.70 (brs, 1H, **e**); 3.79 (q, *J*=7.1, 6H, **g_1**); 3.25-3.20 (m, 2H, **f_1**); 3.01-2.97 (m, 2H, **c_1**); 2.47 (s, 6H, **b_2**); 2.38 (q, *J*=7.4, 4H, **a_1**); 2.31 (s, 6H, **b_1**); 2.19 (t, *J*=7.4, 2H, **c_4**); 1.86-1.79 (m, 2H, **c_3**); 1.67-1.56 (m, 4H, **c_2**-**f_2**); 1.20 (t, *J*=7.1, 9H, **g_2**); 1.02 (t, *J*=7.4, 6H, **a_2**); 0.61 (t, *J*=7.8, 2H, **f_3**).

DE-P mSA Sil

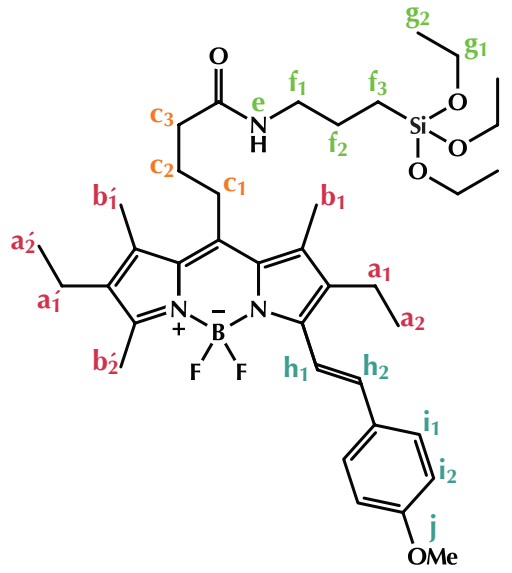

- *Name:* (*E*)-2,6-diethyl-4,4-difluoro-5-(4-methoxystyryl)-1,3,7-trimethyl-8-(4-oxo-4-((3-(triethoxysilyl)propyl)amino)butyl)-3a,4a-diaza-4-bora-*s*-indacene;
- *Chemical formula:* $C_{38}H_{56}BF_2N_2O_3Si$;
- *Molecular weight:* 711.76;
- *Flash chromatography:* petroleum ether/AcOEt gradient, from 1/1 to 3/7;
- *Yield:* 51%;
- *Appearance:* golden solid;
- *^{1}H-NMR:* 7.55 (d, *J*=16.6, 1H, **h_2**); 7.50 (d, *J*=8.8, 2H, **i_1**); 7.09 (d, *J*=16.6, 1H, **h_1**); 6.88 (d, *J*=8.8, 2H, **i_2**); 5.81 (brs, 1H, **e**); 3.82-3.77 (m, 9H, **g_1**-**j**); 3.27-3.22 (m, 2H, **f_1**); 3.10-3.06 (m, 2H, **c_1**); 2.66 (q, *J*=7.6, 2H, **a_1**); 2.52 (s, 3H, **b_2'**); 2.42-2.35 (m, 8H, **a_1'**-**b_1**-**b_1'**); 2.31 (t, *J*=7.2, 2H, **c_3**); 1.99-1.93 (m, 2H, **c_2**); 1.66-1.58 (m, 2H, **f_2**); 1.24-1.18 (m, 12H, **a_2**-**g_2**); 1.03 (t, *J*=7.8, 3H, **a_2'**); 0.62 (t, *J*=8.0, 2H, **f_3**).

DE-B mSA Sil

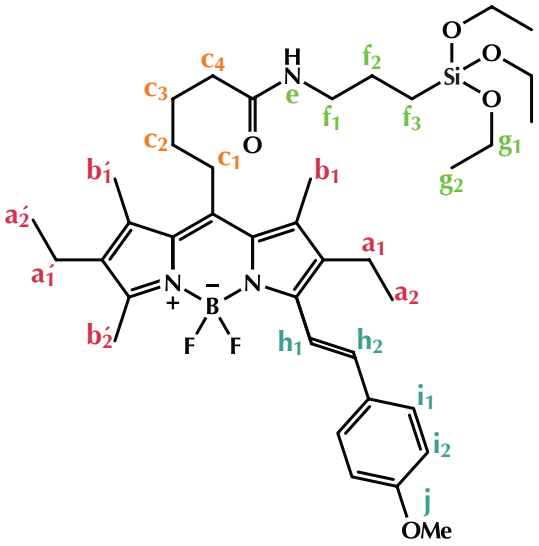

- *Name:* (*E*)-2,6-diethyl-4,4-difluoro-5-(4-methoxystyryl)-1,3,7-trimethyl-8-(5-oxo-5-((3-(triethoxysilyl)propyl)amino)pentyl)-3a,4a-diaza-4-bora-*s*-indacene;
- *Chemical formula:* $C_{39}H_{58}BF_2N_3O_5Si$;
- *Molecular weight:* 725.79;
- *Flash chromatography:* cyclohexane/AcOEt gradient, from 8/2 to 2/8;
- *Yield:* 52%;
- *Appearance:* golden solid;
- *^{1}H-NMR:* 7.55 (d, *J*=16.6, 1H, h_2); 7.50 (d, *J*=8.8, 2H, i_1); 7.09 (d, *J*=16.6, 1H, h_1); 6.88 (d, *J*=8.8, 2H, i_2); 5.72 (brs, 1H, e); 3.81-3.77 (m, 9H, g_1-j); 3.25-3.20 (m, 2H, f_1); 3.05-3.01 (m, 2H, c_1); 2.67 (q, *J*=7.6, 2H, a_1); 2.51 (s, 3H, b_2'); 2.39 (q, *J*=7.6, 2H, a_1'); 2.35 (s, 3H, b_1); 2.33 (s, 3H, b_1'); 2.20 (t, *J*=7.6, 2H, c_4); 1.87-1.80 (m, 2H, c_3); 1.67-1.56 (m, 2H, c_2-f_2); 1.24-1.18 (m, 12H, a_2-g_2); 1.04 (t, *J*=7.6, 3H, a_2'); 0.61 (t, *J*=8.0, 2H, f_3).

TM-P dSB Sil

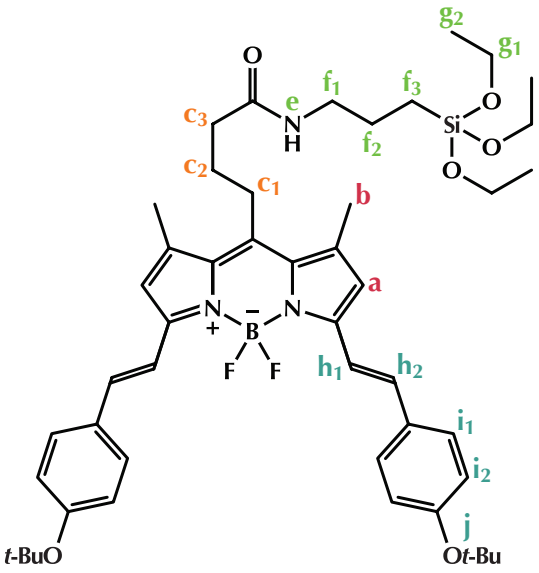

- *Name:* 3,5-bis((*E*)-4-(*tert*-butoxy)styryl)-4,4-difluoro-1,7-dimethyl-8-(4-oxo-4-((3-(triethoxysilyl)propyl)amino)butyl)-3a,4a-diaza-4-bora-*s*-indacene;
- *Chemical formula:* $C_{48}H_{66}BF_2N_3O_6Si$;

- *Molecular weight:* 857.95;
- *Flash chromatography:* cyclohexane/AcOEt gradient, from 6/4 to 1/9;
- *Yield:* 73%;
- *Appearance:* bronze solid;
- *^{1}H-NMR:* 7.58 (d, *J*=16.2, 2H, h_2); 7.52 (d, *J*=8.8, 4H, i_1); 7.19 (d, *J*=16.2, 2H, h_1); 6.99 (d, *J*=8.8, 4H, i_2); 6.67 (s, 2H, **a**); 5.80 (brs, 1H, **e**); 3.80 (q, *J*=7.0, 6H, g_1); 3.27 - 3.23 (m, 2H, f_1); 3.08-3.03 (m, 2H, c_1); 2.49 (s, 6H, **b**); 2.32 (t, *J*=6.6, 2H, c_3); 2.03-1.95 (m, 2H, c_2); 1.66 - 1.59 (m, 2H, f_2); 1.37 (s, 18H, **j**); 1.20 (t, *J*=7.0, 9H, g_2); 0.62 (t, *J*=8.0, 2H, f_3).

8.2.4.3 Remarks on the synthesis

Even though all the triethoxysilane synthesized seem to be well stable and easily handleable, this functional group is quite sensitive to moisture and exposure to air should be minimized as possible, in order to avoid unwanted and uncontrolled hydrolysis. As soon as the compound is isolated and dried under vacuum, it must be rapidly frozen at –20 °C.

8.3 Pluronic® F127 derivatization

8.3.1 Dimesyl derivative

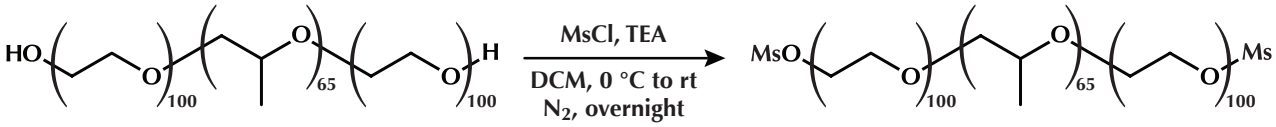

Scheme 6 Mesylation of Pluronic® F127.

- *Synthetic procedure:*[12] a two-necked flask is dried with a heat gun under a flow of nitrogen. Then, 12.6 g of Pluronic® F127 (1.0 mol) is solubilized in 50 mL of anhydrous DCM and cooled to 0 °C. Next, 280 µL of TEA (2.0 mmol) and 155 µL of methanesulfonyl chloride (2.0 mmol) are added. The reaction mixture is kept under stirring at 0 °C for 3 hours and then at room temperature overnight. The suspended solid is filtered away and the collected solution is dried under reduced pressure with a rotary evaporator and desiccated in vacuum, affording a white solid substance (yield: 99%).

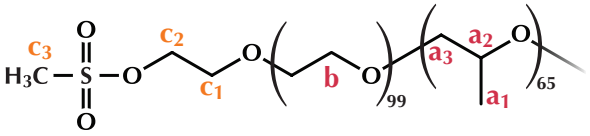

- *^{1}H-NMR:* 4.38-4.35 (m, 4H, c_2), 3.87-3.84 (m, 4H, c_1), 3.63-3.61 (m, **b**) + 3.57-3.46 (m, a_3) + 3.41-3.35 (m, a_2) ≈ 1000H, 3.07 (s, 6H, c_3), 1.13-1.10 (m, ~195H, a_1).
- *^{13}C-NMR:* 75.0, 74.9, 74.8, 72.9, 72.6, 72.5, 72.3, 70.1, 69.0, 68.6, 17.1, 16.9.

8.3.2 Diazide derivative

- *Synthetic procedure:*[12] in a three-necked flask, equipped with a reflux condenser, 10.2 g of dimesyl derivative (0.8 mmol) and 156 mg of sodium azide (2.4 mmol) are solubilized in 50 mL of acetonitrile and heated under reflux for 48 hours. The solvent is removed under reduced pressure with a rotary evaporator. The obtained solid is redispersed with a 5% aqueous solution of sodium bicarbonate, then saturated with solid sodium chloride and extracted 6 times with DCM. The combined organic phases are dried over sodium sulfate,

12. Adapted from: L. Bromberg, M. Temchenko, *Langmuir* **1999**, *15*, 8633.

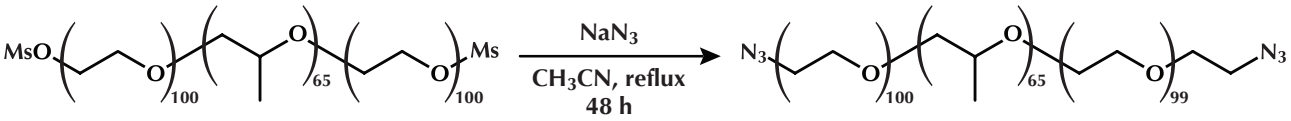

Scheme 7 Formation of the diazide derivative.

concentrated with the rotary evaporator and desiccated in vacuum, affording a white solid substance. Purification is carried out by means of dialysis against water (yield: 89%).

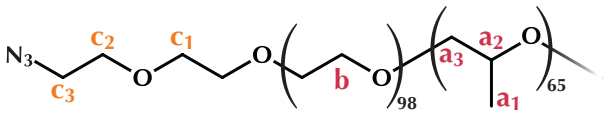

- *^{1}H-NMR:* 3.86-3.82 (m, 4H, c_1), 3.61-59 (m, **b**) + 3.53-3.45 (m, a_3) + 3.38-3.33 (m, a_2) ≈ 1000H, 2.38 (m, 4H, c_3), 1.11-1.08 (m, ~195H, a_1).[13]
- *^{13}C-NMR:* 75.0, 74.8, 74.6, 72.8, 72.5, 72.4, 70.1, 50.2, 17.0, 16.9.
- *IR (NaCl, thin solid film):* 2245 cm^{-1} (azide asymmetric stretching).

8.3.3 Diamine derivative

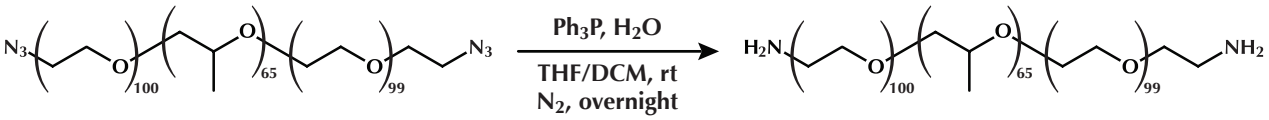

Scheme 8 Reduction of the azide moiety to amine.

- *Synthetic procedure:*[12] a two-necked flask is dried with a heat gun under a flow of nitrogen. Then, 500 mg of Pluronic® F127 diazide (0.04 mmol) and 31 mg of triphenylphosphine (0.12 mmol) are dispersed in 5.0 mL of anhydrous THF. The minimum necessary amount of anhydrous DCM is added in order to obtain an homogeneous solution. The reaction mixture is stirred overnight. Next, 1.0 mL of water is added and the stirring continued for 4 hours. After that, the organic solvent is removed under reduced pressure with a rotary evaporator. The reaction mixture is then diluted with a 5% aqueous solution of sodium bicarbonate, saturated with solid sodium chloride and extracted 6 times with DCM. The combined organic phases are dried over sodium sulfate, concentrated with the rotary evaporator and desiccated in vacuum, affording a white solid substance. Purification is carried out by means of dialysis against water (yield: 82%).[14]

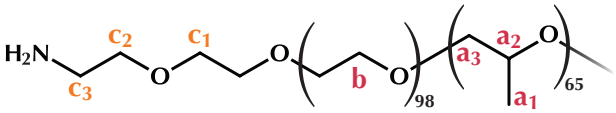

- *^{1}H-NMR:* 3.83-3.80 (m, 4H, c_1), 3.60-3.58 (m, **b**) + 3.52-3.50 (m, a_3) + 3.36-3.33 (m, a_2) ≈ 1000H, 2.64 (s, c_3), 1.09-1.08 (m, ~195H, a_1).[13,]
- *^{13}C-NMR:* 75.0, 74.9, 74.7, 72.9, 72.6, 72.5, 70.1, 68.2, 17.0, 16.9.

13. c_2 is probably hidden under the Pluronic® F127 chains around 3.5 ppm.
14. Besides NMR spectroscopy, amine has been confirmed by the disappearance of the azide peak in the IR spectrum and by means of fluorimetric determination with fluorescamine (data not shown). For the fluorescamine experiment see: (a) M. Weigele, S. L. DeBernardo, J. P. Tengi, W. Leimgruber, *J. Am. Chem. Soc.* **1972**, *94*, 5927; (b) S. Udenfriend, S. Stein, P. Böhlen, W. Dairman, W. Leimgruber, M. Weigele, *Science* **1972**, *178*, 87; (c) R. Adamou, A. Coly, S. E. Douabalé, M. L. Ould Cheikh Ould Saleck, M. D Gaye-Seye, A. Tine, *J. Fluoresc.* **2005**, *15*, 679.

8.3.4 Dicarboxylic acid derivative

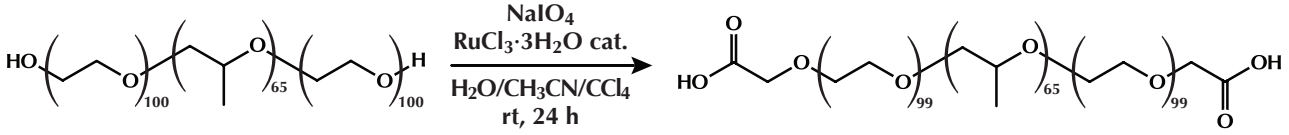

Scheme 9 Oxidation of the hydroxyl ends of Pluronic® F127.

- *Synthetic procedure:*[15] in a three-necked flask , 12.60 g of Pluronic® F127 (1.0 mmol) is solubilized in 60 mL of water. Then, 1.76 g of sodium metaperiodate (8.2 mmol) are added, along with 24 mL of acetonitrile and 21 mL of carbon tetrachloride. Next, 11.5 mg of ruthenium(III) chloride hydrate (44 µmol, 4.4% in mol) are added to the resulting biphasic pasty solution and the reaction mixture is kept under vigorous magnetic stirring for about 20 hours at room temperature. The reaction mixture is then diluted with water, saturated with solid sodium chloride and extracted 6 times with DCM. The combined organic phases are dried over sodium sulfate, concentrated with the rotary evaporator and desiccated in vacuum, affording a white solid substance. Purification is carried out by means of dialysis against water (yield: 77%).

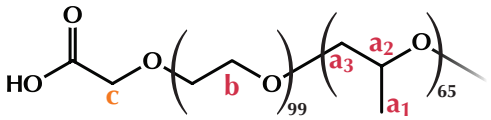

- *^{1}H-NMR:* 4.05 (s, 4H, **c**); 3.54-3.52 (m, **b**) + 3.45-3.43 (m, $\mathbf{a_3}$) + 3.32-3.29 (m, $\mathbf{a_2}$) ≈ 1000H, 1.10-1.08 (m, ~195H, $\mathbf{a_1}$).
- *^{13}C-NMR:* 75.2, 75.0, 74.8, 73.0, 72.6, 70.2, 17.1.
- *IR (NaCl, thin solid film):* 1735 cm^{-1} (carboxylic acid carbonyl stretching).

8.4 Nanoparticles synthesis

The synthesis of nanoparticles can be carried out in different aqueous media – 0.85 M hydrochloric acid or 1 M acetic acid – depending on the particular requirements some molecules may have. In table 1 the parameters that are influenced by the type solvent employed are listed.

In a typical preparation, 100 mg of Pluronic® F127 (8.0 µmol)[16] and the required amount of triethoxysilane fluorophore[17] are weighed in two separate scintillation vials. Next, the fluorophore is dissolved in a controlled amount of DCM and added to the surfactant. When the resulting solution is clear, the solvent is evaporated under a gentle flow of nitrogen. Finally, the sample is kept under vacuum for several hours to ensure a complete desiccation and then stored at -20 °C.

The following day, after the sample is allowed to thaw, sodium chloride and 1.57 mL of solvent are added and the vial is stirred with a vortex mixer for 1 hour. After that, the sample is transferred into a heating bath set at 25 °C and the silica precursor (0.8 mmol) is added. Finally, after a specified time interval (Δt), the condensation terminating agent is added (0.08 mmol) and the reaction is kept under stirring for at least 48 hours.

15. Adapted from: P. H. J. Carlsen, T. Katsuki, V. S. Martin, K. B. Sharpless, *J. Org. Chem.* **1981**, *46*, 3936.
16. In case of functionalized nanoparticles, 8.0 µmol is the total quantity of surfactant employed, taking into account the commercial Pluronic® F127 plus the derivatized one.
17. The exact amounts of triethoxysilane dyes used in each synthesis are listed in the tables of chapter 3; see also note 16 of chapter 5, note 20 of chapter 6, and note 9 of chapter 7.

Table 4 Reaction conditions in the synthesis of nanoparticles.

Solvent	Silica precursor	µL	Terminating agent	Δt (min)	NaCl (mg)	NaCl (M)
HCl 0.85 M	**TEOS**	179	TMSCl	180	68.6	0.75
	TEOS	179	DEDMS	90	68.6	0.75
AcOH 1 M	**TEOS**	179	TMSCl	180	68.6	0.75
	TEOS	179	DEDMS	90	68.6	0.75

A controlled amount of crude solution – usually 1.5 mL – is dialyzed against water for at least 24 hours with four changes of water. The sample is then collected, diluted to a known quantity – typically 5 mL – and passed at least twice through hydrophilic membrane filters with a 0.45, 0.22 and 0.1 µm pore size.

The molar absorption coefficients of the nanoparticles listed in chapter 3 are based on the fact that their concentration has been previously determined.[1] These values take into account also the possible leaching of fluorophore, by comparing the absorption spectra before and after purification.

8.4.1 Peptide bioconjugation

To obtain peptide-targeted nanoparticles, MES buffer pH 6.0 (0.2 M, 40 µL), EDC·HCl (1.2 µmol, corresponding to 20 eq. of the carboxylic acid moieties) and NHS (1.2 µmol) were mixed with the nanoparticles solution (250 µL), which was kept under stirring for 3 hours at room temperature. 10x Dulbecco's Phosphate Buffered Saline (DPBS, 240 µL) was added and pH was adjusted to 7.2. Finally, **CGIYRLRS** or **CGVYSLRS** synthetic peptide (0.61 µmol, 10 eq.) was added, and the stirring continued overnight at room temperature. Purification of peptide-targeted nanoparticles was performed by dialysis.